DGK Veröffentlichungen der DGK
Ausschuss Geodäsie der Bayerischen Akademie der Wissenschaften

Reihe C | Dissertationen | Heft Nr. 887

Stephan M. Palm

Mapping of urban scenes by single-channel mmW FMCW SAR on circular flight and curved car trajectories

München 2022

Bayerische Akademie der Wissenschaften

ISSN 0065-5325 | ISBN 978-3-7696-5299-4

Diese Arbeit ist gleichzeitig als E-Dissertation auf mediaTUM veröffentlicht:
https://mediatum.ub.tum.de/1618641, München 2021

DGK Veröffentlichungen der DGK

Ausschuss Geodäsie der Bayerischen Akademie der Wissenschaften

Reihe C Dissertationen Heft Nr. 887

Mapping of urban scenes by single-channel mmW FMCW SAR on circular flight and curved car trajectories

Vollständiger Abdruck
der von der TUM School of Engineering and Design
der Technischen Universität München
zur Erlangung des akademischen Grades eines
Doktor-Ingenieurs (Dr.-Ing.)
genehmigten Dissertation

von

Dipl.-Ing. Stephan M. Palm

München 2022

Bayerische Akademie der Wissenschaften

ISSN 0065-5325 ISBN 978-3-7696-5299-4

Diese Arbeit ist gleichzeitig als E-Dissertation auf mediaTUM veröffentlicht:
https://mediatum.ub.tum.de/1618641, München 2021

Adresse der DGK:

Ausschuss Geodäsie der Bayerischen Akademie der Wissenschaften (DGK)

Alfons-Goppel-Straße 11 ● D – 80 539 München

Telefon +49 – 89 – 23 031 1113 ● Telefax +49 – 89 – 23 031 - 1283 / - 1100

e-mail post@dgk.badw.de ● http://www.dgk.badw.de

Prüfungskommission:

Vorsitzender:	Prof. Dr. Roland Pail
Prüfer der Dissertation:	1. Prof. Dr.-Ing. Uwe Stilla
	2. Prof. Dr.-Ing. Uwe Sörgel
	3. Prof. Dr.-Ing. Joachim Ender

Die Dissertation wurde am 10.08.2021 bei der Technischen Universität München eingereicht
und durch die TUM School of Engineering and Design am 13.12.2021 angenommen

---

ISSN 0065-5325 ISBN 978-3-7696-5299-4

Abstract

The image-based acquisition of the current situation in urban areas is of great importance for various applications. Due to the independence of weather and daylight conditions, SAR is very suitable for time-independent scene acquisition. Typically, a scene is recorded from single-channel or multi-channel sensors from a single or several temporally shifted aspect angles along linear trajectories. This thesis presents new mapping methods for comprehensive ultra-high-resolution images of urban scenes by operating a mmW SAR along circular flight trajectories (CSAR) and curved car trajectories.

For the acquisition of a comprehensive data set with an airborne mmW SAR sensor on circular trajectories, a method for a beam-stabilized sensor concept is presented. An optimized focusing method for the particular geometry and high carrier frequency is described, and a Video-CSAR method (ViCSAR) for the optimized visualization of many registered views by processing overlapping subapertures is proposed. The maximum resolution in the center and at the edges of the illuminated scene is derived that allows sharp imaging of objects of a certain height.

For the reconstruction of 3d information of individual objects from single-channel CSAR data, the determined aspect-dependent movement of scattering centers above the focussing plane in the ViCSAR amplitude image sequences is evaluated. In contrast, another method is described that focuses the data on different reference heights while the circular trajectory is divided into circular arcs of larger subapertures. The 3d information is extracted by means of a proposed kurtosis and a spectral operator from the amplitude images. Two alternative approaches are presented for the fusion of a georeferenced 3d point cloud that allows a 360° view of the scene. Based on the point cloud, the data is refocused, and several aspect views are merged into a single high-resolution SAR image. For carborne SAR acquisitions (mobile mapping), a method optimizing the focusing of street and facade surfaces is proposed.

For the validation of the CSAR and mobile mapping methods, for the first time, experimental measurements along circular flight trajectories with an ultralight aircraft (94 GHz FMCW SAR) over suburban areas and a reflector field, and measurements along curved street trajectories with a van (300 GHz FMCW SAR) in the rural area and on a test field were carried out.

The results demonstrate that from single-channel W-band CSAR data, both high-resolution SAR images with an azimuth resolution of up to approx. 1 cm (corresponds to a coherent integration of up to 10°) and 3d point clouds can be derived. The point cloud was validated with LiDAR measurements and indicates that height accuracies of isolated point objects of up to 10 cm are feasible. From the circular flight trajectories, both roofs and parts of facades could be reconstructed by 3d point clouds. ViCSAR allows not only a 360° scene and signature acquisition of backscatterers but also the visualization of moving objects based on the movement of their shadows in the image sequence. The movement of smaller cars and even individual people can be observed.

By mobile mapping of streets and facades, images with a resolution of up to 5 mm could be generated. In the process, structures of objects such as paving stones, clinker bricks, or small cracks in road surfaces become visible. The application of the extremely small wavelengths proved to be beneficial due to the diffuse scattering characteristics in the mapping of street details and only makes the detection of moving objects based on their radar shadows on streets possible.

Kurzfassung

Die bildliche Erfassung der aktuellen Situation urbaner Gebiete ist für verschiedene Anwendungen von hoher Bedeutung. Für eine zeitunabhängige Szenenerfassung ist der Einsatz eines SAR-Systems aufgrund der Beleuchtungs- und Wetterunabhängigkeit sehr gut geeignet. Typischerweise wird eine Szene durch ein- oder mehrkanalige Sensoren aus einem einzelnen oder mehreren zeitlich versetzten Aspektwinkeln entlang linearer Trajektorien aufgenommen. Diese Arbeit präsentiert neue Mapping-Verfahren zu umfassenden ultra-hochaufgelösten Abbildungen urbaner Szenen durch ein mmW SAR entlang zirkularer Flugtrajektorien (CSAR) sowie entlang gekrümmter Fahrzeugtrajektorien.

Zur Aufnahme eines umfassenden Datensatzes mit einem flugzeuggetragenen mmW SAR-Sensors auf kreisförmigen Trajektorien wird ein Verfahren für ein beamstabilisiertes Sensorkonzept präsentiert. Es wird eine optimierte Fokussierungsmethode für die spezielle Geometrie und Trägerfrequenz beschrieben sowie ein Video-CSAR-Verfahren (ViCSAR) zur optimierten Darstellung vieler registrierter Ansichten durch Prozessierung überlappender Subaperturen vorgeschlagen. Die maximale Auflösung im Zentrum sowie an den Rändern der beleuchteten Szene wird hergeleitet, um Objekte bestimmter Höhe noch scharf abzubilden.

Zur Rekonstruktion von 3D-Informationen einzelner Objekte aus einkanaligen CSAR-Datensätzen werden in einem Verfahren sowohl theoretisch als auch experimentiell die ermittelte aspektabhängige Bewegung von Streuzentren oberhalb der Fokussierungsebene in den ViCSAR-Amplitudenbildsequenzen ausgewertet. Im Gegensatz dazu wird ein weiteres Verfahren beschrieben, welches die Daten auf unterschiedlichen Referenzhöhen fokussiert, wobei die zirkulare Trajektorie in Kreisbögen größerer Subaperturen unterteilt wird und die 3D-Informationen mittels eines vorgeschlagenen Kurtosis- und eines spektralen Operators aus den Amplitudenbildern extrahiert wird. Zur Fusion einer georeferenzierten 3D-Punktwolke, die eine 360°-Betrachtung der Szene erlaubt, werden zwei alternative Ansätze vorgestellt. Basierend auf der Punktwolke wird eine Refokussierung der Daten und die Fusion mehrerer Ansichten in einem einzigen hochaufgelösten SAR-Bild durchgeführt. Für fahrzeuggetragende SAR-Aufnahmen (Mobile-Mapping) wird ein Verfahren zur Optimierung der Fokussierung von Straßen- und Fassadenoberflächen vorgestellt.

Für die Validierung der CSAR- und Mobile-Mapping-Verfahren wurden erstmalig experimentelle Messflüge entlang zirkularer Flugtrajektorien mit einem Ultraleichtflugzeug (94 GHz FMCW SAR) über vorstädtischem Bereich und einem Reflektorfeld, sowie Messfahrten entlang gekrümmter Straßentrajektorien mit einem Van (300 GHz FMCW SAR) im dörflichen Bereich und einem Testfeld unternommen.

Die Ergebnisse zeigen, dass von CSAR-Datensätzen im einkanaligen W-Band sowohl fokussierte hochaufgelöste SAR-Bilder mit bis zu ca. 1 cm Azimut-Auflösung (entspricht einer kohärenten Integration von bis zu 10°) sowie 3D-Punktwolken abgeleitet werden können. Die Punktwolke wurde mit LiDAR-Messungen validiert und zeigt, dass Höhengenauigkeiten von isolierten punktförmigen Objekten bis zu 10 cm möglich sind. Aus den kreisförmigen Befliegungen konnten sowohl Dächer als auch Teile von Fassaden durch 3D-Punktwolken rekonstruiert werden. ViCSAR erlaubt neben einer 360° Szenen- und Signaturerfassung von Rückstreuern auch die Visualisierung von bewegten Objekten anhand der Bewegung ihrer Schatten in der Bildsequenz. Es kann sowohl die Bewegung kleinerer Fahrzeuge wie auch einzelner Personen beobachtet werden.

Beim Mobile-Mapping von Straßen und Fassaden konnten Bilder mit bis zu 5 mm Auflösung erstellt werden. Dabei werden Strukturen von Objekten wie Pflaster- oder Klinkersteine oder Risse in Straßenoberflächen sichtbar. Die Verwendung der extrem kleinen Wellenlängen erwies sich durch das diffuse Streuverhalten bei der Abbildung von den Straßendetails als vorteilhaft und ermöglichte erst das Erkennen von bewegten Objekten anhand ihrer Radarschatten auf Straßen.

Contents

List of Abbreviations

Abbreviation	Description	Page
AGL	Above ground level	82
ALS	Airborne laser scanning	17
CSAR	Circular synthetic aperture radar	19
CSSAR	Circular stripmap synthetic aperture radar	19
DDS	Direct digital synthesis	31
DEM	Digital elevation model	17
DInSAR	Differential synthetic aperture radar interferometry	19
DSM	Digital surface model	17
dGPS	Differential GPS	81
FFT	Fast Fourier transform	47
FMCW	Frequency modulated continuous wave	22
GMT	Ground moving target	84
GMTI	Ground moving target indication	136
GPS	Global positioning system	79
HPA	High power amplifier	31
IF	Intermediate frequency	31
IMU	Inertial measurement unit	39
INS	Inertial navigation system	79
InSAR	Synthetic aperture radar interferometry	19
IRF	Impulse response function	41
ISAR	Inverse synthetic aperture radar	18
Ku	Kurtosis operator	105
LiDAR	Light detection and ranging	17
LFM	Linear frequency modulation	30
LNA	Low noise amplifier	31
LoS	Line of sight	37
mmW	Millimeter-wave	17
MIRANDA	Millimeter radar using analog and digital approach	79
MRM	Mobile radar mapping	21
PDF	Probability density function	70
PRF	Pulse repetition frequency	79
PSF	Point spread function	97
PSI	Persistent scatterer interferometry	19
PSLR	Peak sidelobe ratio	62
RCS	Radar cross-section	29
RF	Radio frequency	21
SAR	Synthetic aperture radar	17
SCR	Signal to clutter ratio	56
SNR	Signal to noise ratio	30
SP	Image spectrum operator	105
SRF	Sweep repetition frequency	31
TBP	Time-bandwidth product	30
TomoSAR	Synthetic aperture radar tomography	19
UAV	Unmanned aerial vehicle	16

Abbreviation	Description	Page
UWB	Ultra wideband	21
ViCSAR	Video circular synthetic aperture radar	24
ViSAR	Video synthetic aperture radar	19
WGS84	World geodetic system 1984	53
WM	Weighted mean operator	105

List of Figures

List of Tables

1 Introduction

Urban areas are characterized by a high population and building density and are often central to the political, social, and economic development of a region. It is estimated that between 50 -80 % of the Gross Domestic Product (GDP) in most countries of the world is generated in cities while some countries like the United States generate as much as 90 % of GDP in metropolitan areas [Weiss, 2001]. Due to the urbanization of the worldwide population over the past decades, over 55% of the population now live in urban areas and 60% of the people are forecast to live in these regions by 2030 [Nations, 2019]. Area-wide and up-to-date acquisition of spatial information of urban areas is therefore vital to capture temporal changes. This includes information of areas as diverse as entire city districts, traffic infrastructure, individual buildings, tree population, or the condition of road surfaces. Further applications are the monitoring of traffic flow or the monitoring of infrastructure that is of particular interest.

1.1 Motivation

Monitoring the fast progressive change in urban areas is of interest for many disciplines, like urban planning, environmental risk management, or updating the mapping by 3d city models [Gamba & Herold, 2009; Lv et al., 2016]. Remote sensing can play a significant role in these scenarios and can provide a variety of information [de Paul, 2007]. For collecting the required information, remote sensing uses technology that records the backscattered or emitted energy in the form of electromagnetic radiation from objects on the Earth's surface. The collected data are then generally processed into digital image data. The most important criteria to evaluate the potential of these data are (i) the spatial, (ii) spectral, (iii) radiometric, and (iv) temporal resolution of the image material. The first characteristic describes the ability to represent two spatially adjacent objects on the Earth's surface separately and thus make them distinguishable. The second describes the electromagnetic bandwidth that is covered by the sensor. The third defines the sensor's sensitivity and the associated energy differences, which can still be measured. At the same time, the temporal resolution describes the smallest time interval between two measurements of any object on the surface.

Remote sensing platforms

Various carrier platforms are operated in remote sensing for data acquisition. Depending on the application and the accessibility of the scene, the use of satellites, spacecraft, airplanes or helicopters is established. While remote sensing satellites have the great advantage of being able to collect extensive information from large areas at regular intervals from basically every place on Earth [Guo et al., 2016], the spatial resolution of the data from spaceborne optical sensors is typically lower than that of the data from airplanes since the distance to the Earth's surface is significantly larger. In addition, the temporal resolution of spaceborne data depends on the satellite's orbit. On geostationary orbit, it can be in the order of several minutes. On low Earth orbit, typically, several days while sun synchronized orbiting satellites visit the same area on an

exact daily basis. Satellites equipped with radar sensors typically orbit the Earth on a near-polar orbit.

The advantage of airborne carrier platforms is their mobilization flexibility [Fu et al., 2020]. In contrast to satellites, they can, in principle, collect information from any aspect or elevation angle that can be very advantageous in urban areas. In addition, the sensors are typically much cheaper to maintain and can be replaced relatively easily by an improved or updated version. In the case of non-time-critical data acquisition, favorable weather and sunlight conditions can be exploited. On the other side, bad weather conditions can limit the operation of such carriers. In recent years, there has also been growing interest in miniaturized flight platforms that led to the establishment of carriers such as small aircraft or unmanned aerial vehicles (UAVs). These platforms offer economic advantages, particularly as the purchase and operation are at a relatively low cost. Further, they offer a high degree of flexibility and can provide high temporal resolution. The area of the collected data is typically significantly smaller or often with a focus only on a spotlighted, small region of interest. Besides the limited usability in adverse weather conditions, they usually only provide a restricted payload and output power. Therefore, they require a miniaturized and lightweight sensor system with low power consumption. These properties typically limit these carriers to operate sensors with relatively short or medium-range applications.

In the field of mobile mapping, the operation of sensors on vehicles such as cars, vans, or trucks is established, while the use of cameras and laser sensors is state of the art technology [Paparoditis et al., 2012; Gehrung et al., 2017]. Commercial optical and laser sensors can map the entire street environment in very high resolution [Borgmann et al., 2021; Kremer & Hunter, 2007; Ellum & El-Sheimy, 2002], while radar sensors have been rarely applied. Typical applications require the acquisition of data with very high spatial resolution and detailed information in a short or medium range to the sensor. Here, camera-based applications such as Google Street View are known by many users. Moving the sensor along a street also leads to new data acquisition geometries, such as the collection of facade information from a more vertical view or the precise data collection of road surfaces at close distances.

Remote sensing sensors

Sensors are classified as passive if they measure natural radiation such as sunlight and active if they function themselves as a radiation source and measure the backscattered reflection. Further, they are differentiated in the covered bandwidth of the electromagnetic spectrum.

Passive sensors

Passive sensors are, in particular, cameras that collect information in the electromagnetic field of optical light up to the mid-infrared spectrum (0.3 μm to 14 μm wavelength). These sensors have been in use in remote sensing for many decades on all platforms. The main difference between panchromatic, multispectral and hyperspectral cameras is the width and the number of measured frequency bands to collect information of the scene. Panchromatic sensors usually collect a single but large frequency band of visible light. Instead, multi- and hyperspectral cameras cover a more significant number of narrower frequency bands (up to several hundred) up to the mid and far-infrared spectrum to increase the spectral resolution. As hyperspectral imaging can give information about gases, liquids, and solids, there are still a growing number of applications that are currently evolving concerning this remote sensing technique [Madry & Pelton, 2013].

Passive imaging radar typically uses the frequency spectrum of digital broadcast signals or, recently, even radio-astronomical sources [Ulander et al., 2017; Peters et al., 2021]. However, the

data still has limited spatial resolution and is currently mainly applied for military remote sensing applications.

Active sensors

Commonly applied active sensors are laser and radar. Laser scanning systems enable the acquisition of large and very precise 3d data sets. The principle of light detection and ranging (LiDAR) can be applied from airborne carriers or vehicles in the context of mobile mapping. Airborne laser scanning (ALS) emits light, collects the reflected radiation, and can thus scan the Earth's surface very precisely. During the last decades, ALS has therefore proven to be a very effective and accurate way to derive digital elevation (DEM) or digital surface models (DSM). Besides the high measurement accuracy, further advantages are the potential penetration of vegetation and the high density of measurement points also in areas of application where the surface has low roughness. Although the laser is independent of daylight conditions, fog and clouds can only be penetrated to a limited extent, if at all. A selection of laser and camera systems in operation on airborne or satellite platforms is shown in [Ehlers, 2005; Fu et al., 2020].

The synthetic aperture radar (SAR) principle has also become an essential tool for remote sensing of the Earth's surface during the last decades. As an active remote sensing system, radar provides its own illumination and can therefore be well operated independently of daylight conditions. Its principle is based on the emission of electromagnetic waves in a defined frequency band to illuminate the region of interest. The waves interfere with the Earth's surface, and a small part of the transmission power is reflected back to the receiver as an echo signal. At the same time, its characteristics, e.g., amplitude, phase, or frequency spectrum, can already indicate properties of the illuminated area. The backscattered echos are then collected and further processed to derive a two-dimensional reflectivity map of the region. For achieving imaging with reasonable resolution, the build-up of a synthetic aperture is required. Compared to optical sensors that exploit reflectivity effects of the Earth's surface caused by chemical characteristics, backscattering effects in the microwave domain are caused by physical properties. These are geometrical and dielectric properties, and the surface roughness primarily affected by surface moisture.

Although SAR images are therefore generally considered to be more difficult to interpret, the principle of radar imaging shows several specific advantages compared to optical or infrared systems. Besides the independence of daylight conditions, radar imaging techniques can also be applied during adverse weather conditions, e.g., smog, cloud coverage, or rain. This is due to the considerably larger wavelength in the microwave and millimeter-wave (mmW) domain compared to optical light. However, it must be mentioned that the atmospheric attenuation of the radar signal increases at very high frequencies and high humidity that reduces the observable range of mmW radars [Altshuler & Marr, 1988].

Further, temporally repeated data collection of a specific area using the same geometry will provide comparable results that are not affected by changing weather- or sunlight conditions which is beneficial for change detection applications. Moreover, physical properties such as the backscattering coefficient of the observed surface can be derived. Compared to optical or laser sensors, the achievable spatial resolution does not depend on the distance to the object. Last but not least, the large frequency diversity with radar systems operating from 1 m wavelength down to 1 mm wavelength offers a variety of specific applications. Long wavelengths (e.g., L- or P-band) have typically long-range capability and can penetrate volume scatterers such as the foliage of trees and even ground to some degree. Systems operating at shorter wavelengths (X-, Ku-, Ka, or W-band) can generate larger frequency bandwidths that result in higher spatial resolution, resolve smaller objects, and can map the canopies of vegetation [Schmitt & Stilla, 2014b,a; Magnard et al., 2016]. The shorter the wavelength, the smaller in length the synthetic aperture can be built up,

yielding the same azimuth resolution. However, the flight path measurement must be all the more precise.

Nowadays, single-channel and multi-channel SAR sensors are operated from satellites and all kinds of airborne platforms. Spaceborne systems like Terra-SAR-X, Radarsat-2, COSMO/Skymed, or sensors launched within the german defense program 'SAR-Lupe' can generate images of urban areas with decimeter resolution. Carborne SAR experiments have also been carried out for several decades [Ender, 1993] but not in the field of mobile mapping, yet.

1.2 Challenges of urban remote sensing with SAR

Urban remote sensing by SAR has reached great attention in the scientific community. Conferences like IGARSS or the biennial JURSE-Joint Urban Remote Sensing Event, see e.g., [Stilla et al., 2011], have organized special tracks for contributions using SAR. Although SAR images are generally regarded to show a more difficult interpretability, during the last two decades, airborne and satellite carried SAR sensors have reached resolutions in the decimeter domain or better that makes these data much more applicable for an adequate description of urban scenes [Stilla, 2012].

Yet, mapping urban scenes with SAR sensors is associated with specific challenges. A high radiometric resolution is required as urban scenes, on the one hand, are characterized by many man-made objects that often show selectively high backscattering characteristics. Simultaneously, on the other hand, streets or areas covered with vegetation typically show very smooth and low backscattering amplitude levels. These areas then tend to be overexposed and show high sidelobes. Further, the side-looking geometry of the SAR sensor causes shadowing and overlay effects that lead to gaps in the reconstruction of the urban environment and often to misinterpretation [Stilla et al., 2003]. While mapping large urban areas is most efficient using the classic method of processing approximately linear flight tracks, other applications require a more detailed view of smaller, specific objects. Real-time SAR processing can even enable such important objects to be detected during flyby [Palm et al., 2014]. This feature would make it possible, for example, to detect a conspicuous object during the flight and to collect detailed information immediately. This may not only be of interest for military or security applications, but also for damaging events such as the collapse of a building, fire or flooding.

For reducing the mentioned overlay and shadowing effects of the collected information, data acquisition from multiple complementary aspects and subsequent fusion has proven to be very beneficial to fill scene information that is occluded in a single aspect view [Thiele et al., 2006; Schmitt & Stilla, 2011, 2014b]. However, in unknown urban areas, it is challenging to investigate the best line of sight in advance [Stilla & Hedman, 2010], [Schmitt & Stilla, 2011]. To acquire as much information as possible of a defined area, it seems reasonable to consider as many lines of sight as possible to fill the information gaps. These multiple views are achievable by performing circular flight trajectories (hyper-aspect or full-aspect) over the scene of interest. This procedure is similar to the method of inverse synthetic aperture radar (ISAR), which derives the signatures of objects, whereby the object turns in a controlled way on a circle and is measured by the radar from a fixed position [Essen et al., 2008]. ISAR works well for small objects, vehicles, trucks, or tanks but is not possible with buildings or even larger objects. However, in the context of urban remote sensing, knowledge of a building's or object's signature would greatly benefit improving the classification or the detection of changes. Particularly concerning the appearance of objects in SAR images that typically tend to depend less on the selected elevation angle but much more on the aspect angle.

Thus, circular synthetic aperture radar (CSAR) has become of particular interest due to the ability to image and continuously monitor a scene from an extensive aspect interval [Soumekh,

1996; Axelsson, 2004; Ertin et al., 2006; Cantalloube et al., 2007]. In CSAR, the radar sensor typically follows a 360° circular trajectory while continuously spotlighting the area of interest. This imaging geometry is different from circular stripmap SAR (CSSAR) [Li et al., 2017]. Although CSSAR is suitable for wide-area surveillance and reconnaissance due to the broad coverage compared to CSAR, there is a specific revisit time of usually several minutes. Further, the scene is illuminated only from a limited aspect angle. However, both forms of data acquisition cannot be performed by spaceborne platforms but rely on more flexible airborne carrier platforms.

Compared to SAR from linear trajectories, the CSAR acquisition geometry provides many unique features for new imaging techniques [Moreira et al., 2013]. Observers can gain information on broad angular scattering characteristics at very high resolution and obtain a favorable viewing angle for object identification [Froelind et al., 2008; Palm et al., 2016c]. Imaging the scene from multiple views offers the possibility to fuse the generated aspect views to extract additional value. This brings new challenges such as the joint representation of the many aspect views, a suitable fusion strategy, or the question of an optimal length of subapertures in urban areas. Based on the concept of Video-SAR (ViSAR) proposed by Sandia National Laboratory in 2003 [Wells et al., 2003; Damini et al., 2010; Kim et al., 2018], it would, for example, be of great interest to what extent a successive situation assessment of an urban scene with data acquired from a circular trajectory can be provided.

A further CSAR characteristic is that, unlike SAR from linear trajectories, the azimuth resolution is highly dependent on knowing the actual elevation of objects in the scene, as indicated by Cantalloube & Colin [2006]; Cantalloube [2018]. In return, it offers the possibility of a 3d scene reconstruction with single-channel data. This is valuable since, besides multi-aspect urban scene imaging, collecting 3d information is of great interest to reconstruct an urban scene.

1.3 State of the art

3d urban mapping

Extracting 3d information over urban areas is an active research field derived by interferometric, radargrammetric, and tomographic techniques. Cross-track SAR Interferometry (InSAR) coherently evaluates the received echos from multiple acquisitions over the same area of interest taken along different sensor trajectories separated orthogonally to both the line of sight and the track direction (baseline) [Massonnet & Rabaute, 1993]. Radargrammetry (stereo SAR) uses a much larger baseline and non-coherently evaluates amplitude images acquired of the same scene with different incidence angles. 3d extraction then typically relies on matching strong scatterer returns with high SNR [Goel & Adam, 2012; Soergel et al., 2009]. The advantage is that such measurements can also be carried out with a single-channel sensor concept, and there are no errors due to phase unwrapping. Still, it comes to the cost of a relatively limited height resolution.

While first InSAR techniques were based on the evaluation of only one interferogram, differential InSAR (DInSAR) techniques evaluating multi-baseline images with a temporal separation can detect displacement changes with subcentimeter accuracy [Ferretti et al., 2000]. In particular, methods based on persistent scatterer interferometry (PSI), mainly applied from satellite SAR sensors, have proven to be very effective in monitoring small deformations of strong scatterers of buildings [Gernhardt & Bamler, 2012]. As InSAR and DInSAR techniques assume a dominant scatterer model within a range/azimuth resolution cell, reliable results are not provided in areas with layover or volume scattering characteristics [Rambour et al., 2020].

Tomographic SAR (TomoSAR) can be regarded as an extension towards multidimensional imaging. Unlike InSAR techniques, a reconstruction of a three-dimensional scattering distribution

along the vertical axis is possible by arranging a second synthetic aperture in elevation direction [Reigber & Moreira, 2000; Reigber et al., 2015]. This allows for scatterer unmixing of multiple targets that are present in a single range/azimuth resolution cell. Unmixing scatterers in urban areas can be realized by spectral analysis methods such as conventional beamforming, capon beamforming, multiple signal classification, or weighted subspace fitting [Rambour et al., 2020]. More recently, compressive sensing (CS) approaches have also successfully been applied while its advantage is that the number of measurements can be reduced and the achievable spatial resolution given a defined set of baselines is enhanced [Budillon et al., 2011]. Analog to DInSAR, by exploiting multi-baseline and multi-temporal data acquisitions, it is further possible to extract 4d data (3d plus deformations) or even 5d data (3d plus deformations plus thermal dilation) of urban scenes [Budillon et al., 2017].

Experiments performed with multi-view satellite data evaluating TerraSAR-X spotlight images from ascending and descending orbits show the great potential these techniques have in terms of reconstructing 3d building models [Zhu & Shahzad, 2014]. The reconstruction of a digital surface model (DSM) of an urban scene from multi-baseline and multi-aspect InSAR data acquired from multiple linear airborne flight tracks in Ka-band was presented by Schmitt & Stilla [2014b]. The authors apply a maximum-likelihood estimation procedure by evaluating the joint probability density function of both multi-baseline InSAR and multi-aspect data to extract a dense DSM over an urban area of Munich, thus demonstrating the great benefit of multi-aspect fusion.

On a different field, analysis on visualization of moving objects in single-channel SAR data is presented by Wang et al. [2017]. The authors evaluate Ka-band stripmap SAR images where a simulated moving target shadow was added to the images while the relationship between detection probability and shadow-to-clutter noise ratio of moving objects is analyzed.

CSAR data acquisitions at different wavelengths

In the last two decades, multiple single- and multi-pass CSAR experiments were performed with long-range pulsed radar systems on airborne platforms. The applied radar frequency bands range from VHF/UHF-band by FOI-Sweden [Frölind et al., 2012] to P-, L- and X-band by ONERA-France [Cantalloube et al., 2007; Cantalloube & Nahum, 2010; Ruault du Plessis & Dreuillet, 2013], AFRL-USA (Gotcha data set) [Ertin et al., 2007], NRSCC-China [Lin et al., 2012] and DLR-Germany [Ponce et al., 2011]. Most data sets were collected over natural landscapes, airport areas, and parking spaces. By applying autofocus methods, the processed images from these experiments show the very high spatial resolution due to the acquisition geometry, in some cases even generating imagery with $\frac{\lambda}{4}$ resolution by focusing on a high resolution laser DEM in L-band by DLR [Ponce et al., 2014]. The DLR data set used a luneberg lens as a reference, while the measured phase error in the frequency domain was then converted into trajectory errors. At ONERA, three corner reflectors, each at the image's border, were evaluated while an inversion of the phase histories then corrected the flight path.

3d extraction using CSAR data

Processing CSAR data [Ponce et al., 2011] and extracting 3d information in this acquisition geometry is an active research field [Zhou et al., 2015]. Instead of providing a stack of images of the same area collected with different incidence angles, data sets collected in CSAR mode provide views of large aspect intervals. While tomographic methods are thus linked to the broad angular backscattering stability of single targets [Pinheiro et al., 2009], radargrammetric algorithms have the problem of wide angular matching of equal scatterer information [Palm et al., 2012]. Both potentials are thus limited in real-world scenarios, especially in urban scenes, as scatterers tend to

be anisotropic and matching equal scatterer information from far distant aspects is challenging. Moreover, a highly directive scatterer will show no height resolving ability.

For enhancing directive scatterers' weak tomographic imaging capability, Lin et al. [2011] presents a theoretical study that takes advantage of the coherence and nonzero interferometric phase difference of InSAR data to remove focused scatterers at wrong elevation. Other studies take advantage of using multiple circular apertures placed at different heights [Zhu et al., 2016; Ertin et al., 2008; Austin et al., 2011; Marston & Kennedy, 2016]. Fully polarimetric 3d imaging results with single-pass airborne L-band data have been demonstrated in [Ponce et al., 2014] showing the CSAR tomography of an isolated, isotropic target and the tomogram of a tree, thereby obtaining its polarimetric backscattering profile. This research, in particular, demonstrated the new possibilities for monitoring vegetated areas taking advantage of the penetration capacity of low radar frequencies.

Again at L-band, the concept of holographic SAR tomography (HoloSAR) from multi-pass circular data is presented by Ponce et al. [2016]. Maximum resolution can thus be achieved by a complete projection of each circle in a volume and subsequent coherent summation resulting in a full 3d volume representation of objects. By evaluating 19 circular flight paths at different heights, a fully polarimetric 3d backscattering of a forested area was retrieved. Again, such applications need penetration capacity and phase stability over the entire circular trajectory, which is more realistic at lower frequencies.

In the context of 3d urban scene mapping, promising results with X-band data over the city of Nimes were presented by Palm et al. [2012] by a radargrammetric matching strategy dividing the single-pass circular acquisition into small angular regions. To extract height information, the authors evaluate the sum of the correlation coefficients by matching the central images of each region with images in a defined aspect interval using different height hypotheses. Further, the extraction of a 3d shape of a single vehicle was presented by Chen et al. [2017] using a 360° non-coherent summation of subaperture amplitude images from the single-pass CSAR Gotcha data set in X-band. First, the authors extracted the basic outline from the image, and then the 3d information was estimated from the layover using 'a priori' information. Zhang et al. [2018] present a radargrammetric approach to derive a DEM over a parking space area based on low-rank and sparse matrix decomposition that was also evaluated with the Gotcha data set in X-band. Their method efficiently determines the shifts between images in a 3d image stack, while this approach also relies on cross-correlation criteria to determine the offset.

Mobile radar mapping

In the context of mobile radar mapping (MRM), current carborne applications that are investigated are topography mapping in Ku-band [Frey et al., 2018] or automotive applications like parking lot detection [Feger et al., 2017]. High-resolution mobile radar mapping has not been investigated, yet. One problem is that the used wavelengths known from airborne or satellite SAR in P-, L-, X-, Ku- or Ka-band have a relatively low spatial resolution in cross-range. It is technically not feasible to generate sufficient radio frequency (RF) bandwidth in these frequency bands for a subcentimeter scale mapping of objects on roads or facades. Even with low resolution, these wavelengths are too large compared to the surface roughness of asphalt, e.g., which then shows rather specular behavior. Ultra-wideband (UWB) radars might be interesting for these applications. They have low output power and high resolution focusing capacity [Oloumi et al., 2016; Vu et al., 2010]. However, these radars typically also work in the domain of 1 to 15 GHz, which still is a relatively large wavelength compared to the investigated surface roughness.

1.4 New potential by compact sensors at very high frequencies

The methods summarized in Section 1.1 and 1.3 demonstrate the tremendous progress in urban scene reconstruction during the last two decades. Yet, urban areas remain a challenging area for radar remote sensing, and comprehensive mapping of these areas has not been finally solved. One factor that currently limits the scope of application is that most of the presented methods are still very complex and time-consuming to operate, both in terms of the complexity of the data processing chain, the operation of the SAR sensor system, and the acquisition of the data. For example, multi-baseline InSAR methods require a multichannel SAR system with correspondingly large amounts of data or several staggered flight paths of the scene at slightly different heights and - if possible - multiple aspects. TomoSAR approaches show great potential in generating large DSMs of urban scenes, but they need sizeable multi-temporal image data set acquired by repeat-pass platforms. Collecting these data set is very expensive and time-consuming and can easily take several months from current satellite platforms.

The operation of airborne CSAR sensors in the literature so far has been mainly carried out from larger aircraft with a research focus on high-resolution imaging and 3d extraction of smaller objects on the ground or volume representation of vegetated areas. Mapping urban scenes have so far been less of a focus. In addition, up to now, relatively low carrier frequencies like UHF-, P-, L-, and X-band have been investigated in this acquisition geometry. Still, they might not be the best choice for urban scene mapping or monitoring. Multi-aspect fusion of Ka-band InSAR data has already shown the potential that higher frequency domains might have for urban reconstruction.

Applications that require a fast and comprehensive scene evaluation of a local urban area have also received little attention. The SAR system can play to its full strength in these scenarios since it does not depend on daylight or favorable weather conditions. To perform such time-critical applications in a feasible and economically sensible way, a compact SAR sensor on a flexible carrier platform while simultaneously offering high-resolution imaging and comprehensive scene acquisition would be beneficial. These flexible and rather 'cheap' platforms might be small aircraft or unmanned drones. Such carriers usually have restricted payloads and limited output power that requires a reduction of the airborne SAR sensor in weight, size, and output power [Kinghorn & Nejman, 2009; Otten et al., 2014].

In the course of modern semiconductor technology, very compact and therefore lightweight mmW frequency modulated continuous wave (FMCW) radar systems can be designed at very high carrier frequencies that allows the operation of these remote sensing sensors on such cost-efficient carrier platforms. In contrast to pulsed radar systems, FMCW radars radiate their energy steadily over a much more extended time. They, therefore, require significantly less output power, typically in the range of several watts. As a result, large RF bandwidths can be emitted over a relatively constant power level. In addition, there is no need to sample the entire RF bandwidth, which can be technically very complex with large signal bandwidths and requires weight and room. Thus, the small size and weight of the sensor would possibly allow the system's installation in a small mechanical mount or gimbal unit, which makes such a system ideally suited for more ambitious flight trajectories over urban scenes.

The use of extremely high carrier frequencies from 94 GHz (W-band) up to 300 GHz to map and monitor urban scenes while simultaneously operating on circular trajectories might therefore be a new promising field of research. Compared to X-band, this would correspond to applying a ten times smaller wavelength as previously carried out CSAR experiments in the literature. These small wavelengths may possibly interact very beneficial with the many fine-scale objects in urban areas. Operated in a minor complex configuration in single-channel and single-path mode, it allows a complete 360° full aspect data acquisition, a probably very high image resolution, and

to some extent, 3d reconstruction of the scene by applying radargrammetric methods. Besides generating and transmitting large frequency bandwidths in W-band, a further advantage is that a minor aspect angle interval is required to build up equal azimuth bandwidth in proportion to the increase in frequency. While operating in CSAR mode, this advantage can be used to generate significantly more images or 'views' of the object showing the scene from a slightly different aspect angle interval. This might be beneficial in urban areas since objects are often shaded or hidden by buildings or vegetation over large angular intervals, and the 'visible' aspect area might be small. Finding a favorable viewing angle to a specific object becomes then much more accessible.

Also, in the context of mobile radar mapping, the physical properties of extremely high radar frequencies might be promising to open a new field of research. Up to now, mobile mapping with cameras and laser sensors is state of the art, while SAR sensors have only been applied to a minimal extent. However, by operating compact and leading-edge FMCW radars and further increasing the frequency band from W-band to the lower terahertz domain, the spatial resolution in the subcentimeter domain becomes more suitable for mobile mapping applications. By now, the high resolution and penetration capacity of the lower terahertz band or submillimeter-wave frequency region has mainly been applied in security applications [Krozer et al., 2010; Cooper et al., 2008, 2011] or by demonstrating ISAR measurements [Dzwonkowski, 2016]. To the author's knowledge, carborne mobile mapping experiments to measure streets and close infrastructure in these wavelengths have not been investigated, yet.

1.5 Objective of the thesis

This thesis presents new mapping methods for comprehensive ultra-high-resolution images of urban scenes by operating a single-channel and single-pass mmW SAR along circular flight and curved car trajectories. More specifically, it aims to contribute to the following scientific questions:

a) What spatial resolution can be achieved over an illuminated urban area without autofocus methods on a circular trajectory with a W-band SAR on a small aircraft?

b) How can a joint representation of the 360° full-aspect SAR imaging be realized and represented significantly?

c) How can the potentially large azimuth bandwidth, which increases rapidly over a small aspect interval, be exploited to extract 3d information, and which accuracy can be achieved with such a radargrammetric evaluation of single-channel, single-pass data to obtain a 3d point cloud?

d) To what extent can SAR measurements in the lower terahertz frequency domain from a carborne mobile radar mapping system be processed, and which details of the urban scene can be resolved?

In this context, the demonstration of the operational feasibility of full aspect data acquisition and CSAR imaging in the W-band domain shall be investigated. As there was neither a W-band CSAR data set nor a sensor constellation that was able to acquire such a complete aspect data set on an airborne platform in the literature, experimental investigations were at first made to evaluate the requirements that would be placed on such a sensor concept if operated with current state technology. This work also includes parts of the sensor concept design for carrying out experimental measurements in W-band in this specific geometry. These are, in particular, the creation of an automatic beam steering procedure to fix the radar beam on an arbitrary ground

target while operating the sensor from a small carrier platform. This involves the evaluation of the influence of such a sensor stabilization on the CSAR processing. A further, more general contribution of this thesis is to indicate the potential advantage that the application of mmW can offer in urban mapping.

1.6 Structure of the thesis

To answer the above questions, the thesis is structured in the following way:

In Chapter 2, the basic principles and definitions of SAR on linear and circular trajectories are briefly outlined. Further, the physical and atmospheric characteristics associated with millimeter waves are summarized. Subsequently, the basic concept of an FMCW radar is described that is applied to acquire the data set.

In Chapter 3, the design of a required sensor constellation is described that is capable of acquiring experimental W-band CSAR data sets over urban scenes. It derives the specifications and the design of a developed real-time beam steering concept that can continuously illuminate a fixed target region on the ground while operating the sensor on a small aircraft.

In Chapter 4, the CSAR processing of the radar data, the design of different image geometries, and the composition of the geocoded image stack are presented in Sections 4.1 and 4.2. It further analyzes an optimal coherent integration interval in urban scenes by examining the accurate projection of high targets in CSAR geometry in Section 4.3. Finally, based on this analysis, a joint representation of the data is derived in the form of Video-CSAR (ViCSAR) in Section 4.4.

In Chapter 5, a methodology to extract 3d scene information by non-coherently evaluating CSAR amplitude image sequences is presented in Section 5.1. The main focus is on the proposed methods in Section 5.2 that generate a global 3d point cloud by extracting 3d information over larger coherent apertures and subsequent fusion, thereby revealing the urban scene from 360°. Finally, a refocusing strategy that exploits the 3d information from the generated point cloud and improves the image resolution and interpretability by reducing shadowed regions is presented in Section 5.3.

In Chapter 6, a method to adapt the focusing geometry for ultra-high-resolution carborne mobile street mapping is presented in Section 6.1. A further adaptation to focus and map facades in the close vicinity of streets is demonstrated in Section 6.2.

In Chapter 7, the experimental setups of the different airborne and carborne campaigns, the operated FMCW radar sensors and carrier platforms, and the specific characteristics of the acquisition geometries and data processing are presented.

In Chapter 8, the results of the investigated experiments and the corresponding discussion of the outcome are presented. In Section 8.1, the evaluation of the beam steering mode is presented. In Section 8.2, the results of the urban mapping in very high resolution and ViCSAR mode are shown. In Section 8.3, the results on the measurement to derive the spatial resolution are presented. In Section 8.4, the extraction of 3d urban scene information and the generated point clouds of the urban scene are demonstrated. In Section 8.5, the generation of a shadow-reduced view and the fusion of information acquired from different aspects in a single SAR image in high resolution is presented. Finally, in Section 8.6, the results of the urban mobile mapping experiments are shown.

Chapter 9 concludes this thesis, discusses possible applications, and shows potential for future research directions of this work.

2 Fundamentals

This Chapter briefly outlines the basic principle and definitions of SAR on linear and circular trajectories. Further, it summarizes physical and atmospheric characteristics that are associated with millimeter waves. Subsequently, the basic concept of a frequency modulated continuous wave (FMCW) radar is described that is applied to acquire the data set. At last, the signal model of a stationary target that is received by an FMCW radar is presented.

2.1 Synthetic aperture radar

In optics, the meaning of the word aperture denotes the opening or its diameter through which rays of light are transmitted or received. Analog, synthetic aperture radar (SAR) describes the methodology of moving the radar sensor on a measured trajectory, thus synthesizing an antenna with a large aperture by the computer in retrospect. The principle was introduced by Carl A. Wiley of Goodyear Aircraft Company in 1951 [Wiley, 1954]. Focusing the radar raw data requires a fully coherent radar system and a very precise measurement of the flight path synchronized with the radar data. The accuracy of the flight path measurement has to be in the order of a fraction of the emitted wavelength. Otherwise, coherent processing of the radar raw data in the flight direction is impossible. Thus, the azimuth resolution of the reflectivity map would be limited to the size of the physical footprint of the radar beam. As a result, the spatial resolution of such data would be far too low for applications in urban remote sensing.

As the methodology of SAR and various processing algorithms are presented in detail in the literature, see, e.g. [Curlander & McDonough, 1991; Cumming & Wong, 2005], only the basic concept and definitions relevant for the further understanding of this thesis are introduced. Additional geometrical effects such as shadowing or foreshortening of objects that occur in SAR images are explained in detail by Lillesand et al. [2004].

SAR on linear trajectories

The basic stripmap SAR concept assumes that the radar is moved on a preferably linear trajectory and a constant height h_z while illuminating the scene of interest in a side-looking geometry with a depression or elevation angle ϵ or θ, respectively, see Fig. 2.1a. The footprint of the radar beam on the surface - the swath width - is then defined by the 3 dB beam width of the antenna. Commonly, the beam width in elevation ϱ is chosen to be significantly larger than the beam width in azimuth. With L the antenna length in azimuth, λ the wavelength and $\beta = \lambda/L$ the azimuth beam width, the length L_s of the synthetic aperture can then be derived by $L_s = \frac{r \cdot \lambda}{L}$ with r being the slant range distance to the target. Sampling the received echos is performed at fast time t while the temporal distance between two emitted pulses is defined by slow time T. Thus, T typically corresponds to the inverse of the pulse repetition frequency (PRF).

While the range resolution δ_x is dependent on the emitted RF bandwidth B with $\delta_x = \frac{c_0}{2 \cdot B}$, c_0 the speed of light, the azimuth resolution δ_y depends on the length of the synthetic aperture

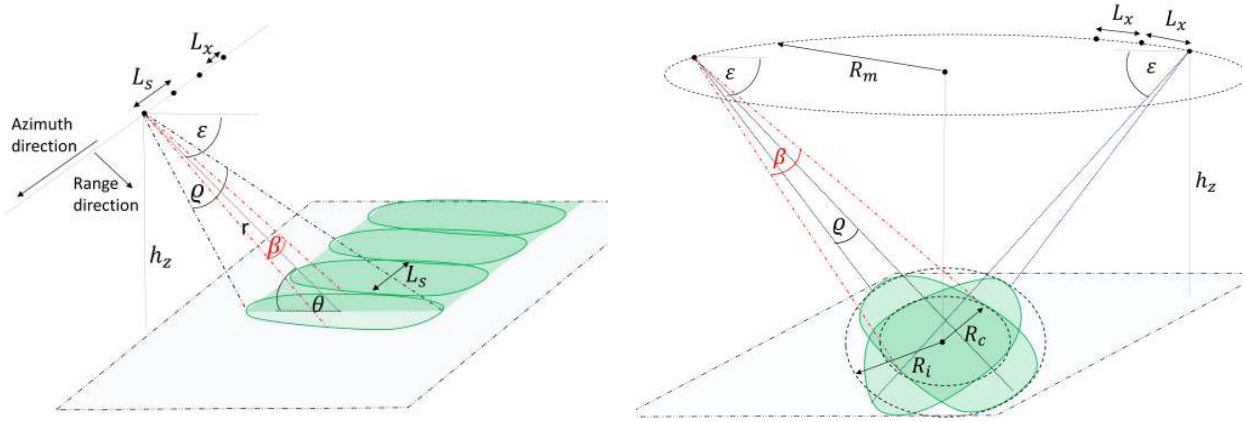

(a) (b)

Figure 2.1: Visualization of the basic SAR and CSAR geometry. a) SAR on a linear trajectory, (b) SAR on a circular trajectory.

that has been coherently processed. Analog, collecting echos over a larger angular aspect interval generates a more considerable amount of azimuth bandwidth that can coherently be processed. A maximum azimuth resolution of $\delta_y = L/2$ can be achieved by processing the total length L_s.

Processing only a smaller portion of the available azimuth bandwidth is called subaperture processing. This kind of processing method can be beneficial for various reasons. First, it may be technically only feasible to measure a portion of the flight path of a large synthetic aperture in the accuracy of a fraction of the wavelength. This is particularly true if the carrier frequency of the sensor is very high and the carrier platform smaller, more susceptible to wind, and therefore more turbulent in the air. Considering that the requirements for measuring flight path accuracy in W-band are ten times higher than in X-band, the build-up of large coherent apertures without autofocus algorithms is challenging. Second, the target may have only a small angular persistence or small angular visibility. Third, specific applications require reduced illumination time to process a single image.

The azimuth resolution δ_y with respect to the processed aspect interval φ_{az} for subaperture processing can then be approximated by the linear relationship

$$\delta_y = \frac{r \cdot \lambda}{2L_x} = \frac{r \cdot \lambda}{4r \cdot tan(\frac{\varphi_{az}}{2})} = \frac{c_0}{4f_0 \cdot tan(\frac{\varphi_{az}}{2})} \tag{2.1}$$

with $B_A = 2f_0 \cdot tan(\frac{\varphi_{az}}{2})$ the resulting azimuth bandwidth, f_0 the carrier frequency and L_x the length of the subaperture. Depending on the favored resolution, the length of coherent apertures in W-band or even at higher frequencies can then be reduced to only several meters, still resulting in SAR images that show decimeter resolution.

If the same scene content processed from multiple subapertures is additionally non-coherently superposed in a single SAR image, this is known as multilook processing. An example of a mmW SAR image of an industrial complex acquired from a linear trajectory is presented in Fig. 2.2.

SAR on circular trajectories

The basic geometry of SAR on circular trajectories is indicated in Fig. 2.1b. In this geometry, the sensor ideally follows a circular trajectory with a radius R_m while the radar beam is preferably fixed on the center of the circle. Typically, the illuminated surface area can then be separated in a

Figure 2.2: Ka-band SAR image acquired on a linear trajectory showing an industrial complex and several parking areas in Woerth, Germany. Resolution is 25 cm. More sensor and processing specifications are presented in [Palm et al., 2016c].

center area with size $\pi \cdot R_c^2$ and an area outside the center with size $\pi \cdot (R_i - R_c)^2$. The center area is illuminated in full aspect mode, and a 360° data set of this region can be acquired. Only a more minor angular part is acquired from the area outside the circle, typically one angular interval in near and one in far range from the opposite direction. Since the center area is illuminated over 360°, the length of the synthetic aperture for targets located there is $L_s = 2\pi \cdot R_m$.

However, since urban areas are characterized by scatterers that show rather a short angular visibility, the processing of subapertures is beneficial. Dividing the complete 360° spectral information into multiple small, overlapping circular segments allows the generation of numerous views from slightly different aspect angles with reduced resolution capacity.

Knowledge of the exact absolute height of scatterers is essential to avoid blurring and azimuth smearing in the final CSAR images [Cantalloube, 2018]. This behavior is different from stripmap or spotlight SAR on linear trajectories, where the platform has a linear motion while forming the synthetic aperture. Incorrect height information in this geometry does not lead to blurring in the processing as there is no loss of coherency. Although the scatterer will be displaced in the image geometry, the compression rate will not suffer [Duersch & Long, 2015]. The potential point targets of interest that satisfy the expected slant range history and elevation lie on a hyperbolic curve. Rotational symmetry applies, and each range/elevation solution will produce a well-focused point target. In CSAR, only objects at reference height are imaged in focus.

2.2 Millimeter-wave characteristics

Since radar remote sensing is commonly associated with systems in the P-, L-, C- or X-band domain, several mmW characteristics need to be taken into account that will be briefly introduced whereby the focus is on frequencies at and above the W-band. The electromagnetic spectrum of the W-band ranges from 75 to 110 GHz corresponding to a wavelength of $2.7 - 4.0$ mm.

Technological, the capability of very compact sensor design and the very high achievable spatial resolution in both dimensions range and azimuth is of great benefit. In proportion to the smaller wavelength, shorter synthetic apertures in length are required to generate large azimuth bandwidth compared to established wavelengths. On the contrary, the accuracy of the flight path

measurements has to be in one order of magnitude more precisely than in X-band to perform the required motion compensation steps. Apart from this, by now, the most limiting factor is the low output power of broadband power amplifier in the W-band or at frequencies in the lower terahertz domain. The low output power and the relatively high atmospheric attenuation have restricted W-band SAR applications until now to operate on linear trajectories at low altitude using antennas with high gain in azimuth [Stanko et al., 2011].

Atmospheric attenuation

SAR applications in this wavelength domain typically use the atmospheric transmission window around 94 GHz. Still, they are nevertheless restricted to medium ranges (< 10 km) due to the high propagation losses, as indicated in Fig. 2.3. The main reason for the different propagation properties is resonance absorption caused by molecules in the atmosphere, particularly oxygen and vapor [Skolnik, 1980]. Propagation measurements in W-band to validate path attenuation models indicate that the best results were obtained by deriving the attenuation with Mie scattering propagation models for rain [García-Rubia et al., 2013] and for fog and clouds [Liebe et al., 1989]. The extent to which W-band remote sensing can image the Earth's surface in adverse weather conditions depends primarily on the density and size of the water droplets in the atmosphere. Significant drop sizes in the order of the electromagnetic wavelength act as antennae and absorb the energy of the electromagnetic resonance wave. In contrast, the small particle size of smoke, for instance, shows a low attenuation [Schmitt et al., 2013]. Thus, W-band can penetrate most weather conditions as long as the water droplets' density and size are not excessively high.

Roughness characteristics

The surface roughness is an essential characteristic of the scattering behavior of electromagnetic waves. The extent to which a surface appears rough or relatively smooth is not an intrinsic attribute but depends on the incidence angle and the emitted wavelength λ. In general, a surface that is considered to be more rough shows more diffuse or incoherent scattering characteristics, while a smooth surface shows more directional or coherent scattering. The surface roughness in natural environment varies typically from medium to high which means that there typically exists

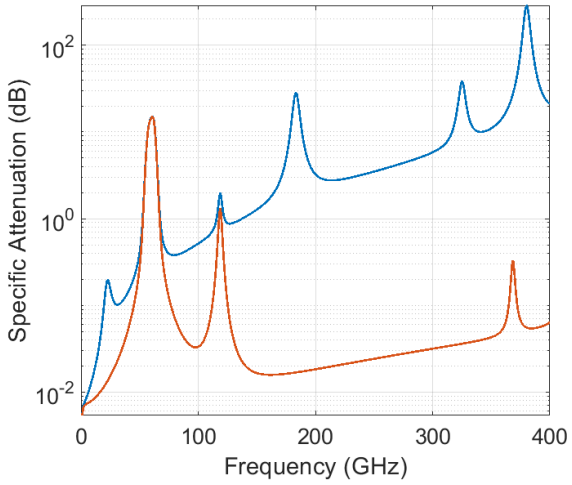

Figure 2.3: Atmospheric attenuation spectrum from 1 to 400 GHz for an atmospheric pressure of 101.300 kPa and a temperature of 15°. (blue) Vapor density of 7.5 $\frac{g}{m^3}$. (red) Dry air. From [Altshuler & Marr, 1988].

a minor coherent scattering component which is reflected away from a monostatic radar and a major diffuse component.

The Rayleigh- or Fraunhofer roughness criteria [Matzler et al., 2006] are often used to determine whether a surface is rather rough or smooth in a specific frequency range and angle of incidence θ_i. Both state that the phase difference $\Delta\Phi$ between two reflected waves in the immediate vicinity should not exceed $\frac{\pi}{2}$ or even $\frac{\pi}{8}$, respectively, as the reflected waves are then no longer in phase and become incoherent. $\Delta\Phi$ in this context means nothing other than the path difference of two reflected waves caused by the standard deviation of the surface height variation δh with

$$\Delta\Phi = \frac{4\pi}{\lambda} \cdot \delta h \cdot \cos(\theta_i) \tag{2.2}$$

yielding

$$\delta h < \frac{\lambda}{8 \cdot \cos(\theta_i)} \qquad or \qquad \delta h < \frac{\lambda}{32 \cdot \cos(\theta_i)} \tag{2.3}$$

Compared to established SAR wavelength domains, a smooth surface at 3.2 mm wavelength in W-band or even with 1.0 mm wavelength at 300 GHz with $\theta_i = 45°$ would correspond to an root mean square (RMS) surface height variation of < 0.14 mm or < 0.04 mm, respectively. This indicates that in these high-frequency wavebands, natural and urban surfaces except for a few artificial objects are to be categorized as rough, leading to a diffuse scattering of even fine-scale objects. Further, it has been shown that the W-band radar cross-section (RCS) is almost independent of the angle of incident from rough surfaces. At the same time, this is not the case for larger millimeter wavelengths (Ka-band) [Yamaguchi et al., 1997].

While focusing the data in the context of SAR processing, the diffuse scattering within a synthetic aperture leads to coherent averaging that is similar to the process of multilook processing and lowers the speckle effect of homogeneous surfaces [Schmitt et al., 2013]. The diffuse scattering can therefore be of great benefit in urban scenes as these regions are currently more characterized by surfaces that appear less rough and typically show more specular or point scattering behavior. More details on these phenomena are presented by Soergel [2010].

2.3 FMCW radar sensors

Frequency modulated continuous wave (FMCW) radars transmit electromagnetic waves whose frequencies change periodically over long time periods. Although considerable progress has been made concerning the design of the sensors and the various modulation methods, the fundamental concept is still based on the first demonstrated radar, presented by the engineer Christian Huelsmeyer in 1904 [Huelsmeyer, 1905]. This first radar was demonstrated publicly from a bridge over the Rhine in Cologne to detect ships and would nowadays be classified as a continuous wave (CW) radar. Due to the lack of frequency modulation, this first radar was generally not able to measure ranges. Still, a coarse measurement was possible by a trigonometric evaluation of the antenna's directivity. In this thesis, only the most essential characteristics of FMCW are to be introduced. For further information, the reader is referred to [Meta, 2006].

Comparison to pulsed radar sensors

Nowadays, long-range SAR remote sensing from spaceborne or large airborne platforms is dominated by pulsed radar sensors. In principle, these sensors transmit an extremely short, high-power, and typically frequency-modulated pulse and then wait for the incoming echo. The distance of the reflected objects is determined by measuring the time of flight, while there is a long latency period between two transmitted pulses, see Fig. 2.4. An important term in this context is the

time-bandwidth product (TBP) which describes the product of pulse duration T and its frequency bandwidth B. For an unmodulated pulse, TBP equals 1, while for a frequency-modulated pulse, it can reach values well over $10,000$. The TBP is thus a measure of the pulse compression rate. Furthermore, it indicates the factor by which a frequency-modulated signal improves the range resolution and the signal to noise ratio (SNR) compared to a signal that is only pulse-modulated with the same time duration.

Pulsed radars are thus able to cover large distances and show high sensitivity with only marginal overcoupling. On the other hand, they need high output power as the full pulse power must be transmitted over an extremely short period of time. Further, the receive signal can be down-converted by an adjustable signal form and bandpass filtered to reduce the sampling frequency similar to FMCW techniques. However, if the receive signal is not down-converted, the entire RF bandwidth must be sampled. This is a technically very challenging task for very broadband sensors that may transmit several gigahertz.

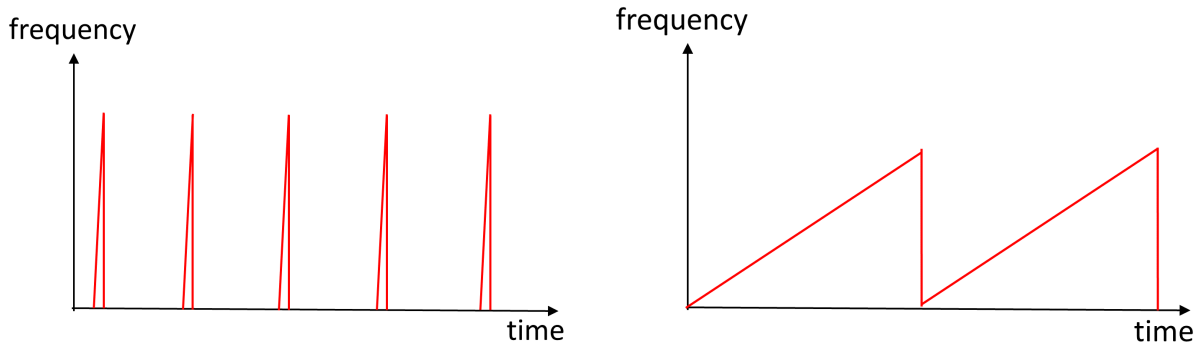

(a) (b)

Figure 2.4: Signal transmission of frequency modulated pulses over time. Schematic representation. a) Pulsed radar, b) FMCW radar.

FMCW mode of operation

FMCW radars continuously emit signals and simultaneously receive the echo. To measure distances of objects in close- or mid-range applications, sawtooth or triangular functions are often generated that show a linear frequency modulation (LFM) over time. The frequency modulation enables a time relationship between the transmitted signal and the target echo. The basic idea to measure distances with these systems is to evaluate an indirect transmit time measurement via the frequency change of the transmitter. While the radar continuously transmits a signal with a modulated linear chirp, the received echo from the object is time-shifted from the original transmitted frequency. In dechirp-on-receive systems, the received frequency is instantaneously mixed with the current transmit frequency. This results in a beat signal that ideally consists of a single frequency for one object and thus shows a very narrow bandwidth, see Fig. 2.5. By this operation, the frequency shift that is analog to a time shift can be determined. Based on the knowledge of the radar's modulation parameters, the transmit time t_r can be determined that is proportional to the distance of the object. In other words, the sampled beat signal or intermediate frequency (IF) is proportional to the object's distance.

For this reason, the modulation of the transmission frequency must be precisely linear to have accurate distance measurements. Any non-linearity worsens the distance measurement or range resolution since the bandwidth of the beat signal increases. From Fig. 2.5, the distance r to an

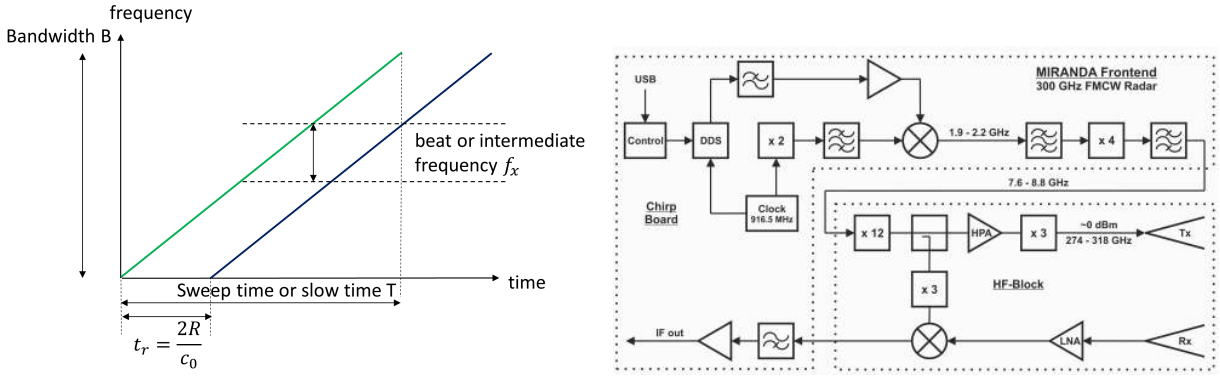

Figure 2.5: FMCW principle and front-end design. a) Basic FMCW principle with one target. Transmit signal (green), receive signal (blue), b) FMCW radar block diagram using the example of the 300 GHz MIRANDA radar from [Palm et al., 2016a].

arbitrary target can then be derived by

$$r = \frac{c_0 T f_x}{2B} = \frac{c_0 \cdot f_x}{2(\frac{d(f)}{d(t)})} = \frac{c_0 \cdot f_x}{2k_T} \tag{2.4}$$

with f the emitted frequency, f_x the IF, t the fast time (sampling time), T the slow time, and $\frac{d(f)}{d(t)} = \frac{B}{T} = k_T$ the chirp rate or frequency deviation.

Due to the continuous signal transmission, the output power of FMCW radars can be distributed over a much more extended period which results in significantly less output power requirements compared to pulsed radars. Further advantages are the measurement of targets at very close ranges, and the sampling of the RF bandwidth can be carried out in significantly lower frequency bands. On the other hand, the distance is rather limited to mid-range applications and lower sensitivity (overcoupling).

The high-frequency signal generation of an FMCW sensor is indicated using the example of a 300 GHz radar in Fig. 2.5b. Based on a direct digital synthesis (DDS) circuit, periodic and band-limited signals of nearly any frequency resolution can be generated. The corresponding output signal is then multiplied and filtered over several stages and finally amplified by a high power amplifier (HPA) before being emitted via the transmitting antenna. In turn, the received signal is amplified by a low noise amplifier (LNA), mixed with the instantaneous transmit frequency, and then digitally sampled.

Signal model of a stationary single target

Using an FMCW radar as SAR sensor, typically, continuous linear chirps $s_e(t)$ of the form

$$s_e(t) = \exp(-(j2\pi f_0 t + j\pi k_T t^2)), t \leq T \tag{2.5}$$

are transmitted in a side-looking geometry to illuminate the region of interest. Again, $k_T = \frac{B}{T}$ is the chirp rate, j the imaginary number, and slow time T the sweep duration, which is close or equal to the inverse of the sweep repetition frequency (SRF) in FMCW systems. The echoed signal $s_R(t)$ of a single radar chirp can then be described as the complex weighted, time shifted transmit signal

$$s_R(t) = \int_R \alpha(\mathbf{x}) \cdot s_e \left(t - \frac{2r\left(\mathbf{x}, \vec{\mathbf{x}}_s(t)\right)}{c_0} \right) d\mathbf{x} \tag{2.6}$$

with α as the target's complex reflectivity, the sensor's position $\vec{\mathbf{x}}_s(t)$ at fast time t and consequently the distance between sensor and region $r\left(\mathbf{x}, \vec{\mathbf{x}}_s(t)\right)$ with $\mathbf{x} \in \mathrm{R}^3$.
In dechirp-on-receive systems, the receive signal $s_R(t)$ is then mixed with the instantaneous transmit signal $s_e(t)$ or mixed with a time-shifted copy $s_e(t - t_d)$ with t_d the delay time. Neglecting amplitude information and assuming $\alpha = 1$, the generated IF signal $s_r(t)$ for an ideal volumetric point scatterer at position $\vec{\mathbf{x}}_p \in \mathbf{x}$ is then the sampled version of a sinusoidal function of the form

$$\begin{aligned} s_r(t) = \; & \exp\left\{j2\pi f_0 t_r(t)\right\} \exp\left\{-j\pi k_T (t_r(t))^2\right\} \\ & \cdot \exp\left\{j2\pi t \left[k_T t_r(t) - f_{R0}\right]\right\}, t \leq T, \end{aligned} \tag{2.7}$$

with $t_r(t)$ the fast time dependent two way time delay $\frac{2r(\vec{\mathbf{x}}_p, \vec{\mathbf{x}}_s(t))}{c_0}$. The sampled version of $s_r(t)$ then represents one column of the two dimensional SAR raw data set.

The intermediate frequency $f_{\mathbf{x}}(t)$ of the sinusoidal function is determined in the third term with $f_{\mathbf{x}}(t) = k_T t_r(t) - f_{R0}$, f_{R0} being the radar mid-range frequency shift, see deramping in [Gurgel & Schlick, 2009]. In contrast to pulsed radars, FMCW allows the direct use of an FFT operation to achieve range compression. In this context, it is essential to emphasize again that both the phase terms and the IF term of $s_r(t)$ are fast time-dependent if the radar sensor is moved while collecting the SAR data. The IF signal results in a clean sinusoidal oscillation only in the case of a stationary radar and a stationary target.

A visualization of a linear chirped transmit signal $s_e(t)$ (see equation 2.5), receive signal $s_e(t - t_d)$ (see equation 2.6) and the resulting IF signal $s_r(t)$ (see equation 2.7) is illustrated in Fig. 2.6. The significantly reduced sampling frequency to digitize the IF signal is clearly indicated.

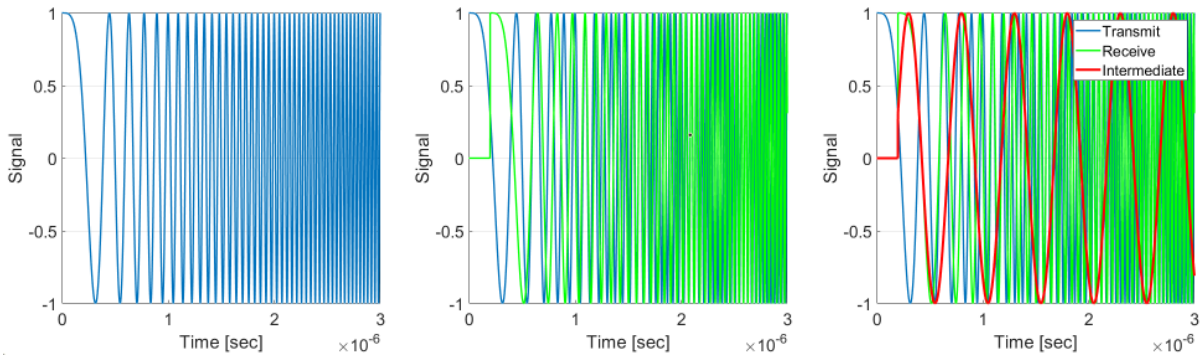

Figure 2.6: Simulation of a stationary configuration with a fixed target at 30 m distance. Illustrated is the first 3% of the signal with a length of 100 μs. f_0 is 94 GHz and B = 1 GHz. a) Transmit signal (blue), b) transmit and time-shifted receive signal (green), c) IF signal (red). The sampled IF represents the raw signal of the SAR processing chain.

3 Beam adjusted sensor concept for CSAR data acquisition

Evaluating a circular data set of an urban scene requires developing a sensor constellation capable of acquiring it. Therefore, such a system's essential parameters and requirements should be determined. This includes an evaluation of potential challenges that have to be solved that may restrict a comprehensive data acquisition. This Chapter describes essential parameters to determine optimal flight configurations in CSAR mode. Further, it presents the design of a developed real-time beam steering concept to acquire full aspect W-band CSAR data sets operationally.

3.1 Challenges operating a W-band CSAR

In CSAR, (i) the main lobe of the radar shall remain permanently directed to the specific target area. In addition, (ii) the sensor ideally illuminates a large urban surface area and (iii) emits high RF bandwidths. Simultaneously, (iv) it shall provide sufficient output power to be able to process the high-resolution SAR images with acceptable SNR. From a purely technological point of view, such an airborne system that is able to acquire a 360° data set of an area with a sufficient diameter on the surface places severe demands. One significant aspect is that the output power of W-band radar systems is still very limited [Lewark et al., 2015]. Acquiring a circular data set must therefore occur on significantly smaller radii, as the distance to the target scene is much shorter compared to typical X- or P-band CSAR experiments known from the literature [Palm et al., 2012].

Broadband, high-performance, and semi-conductor-based amplifiers in W-band currently have output powers of 24-30 dBm [Thome et al., 2018]. Following the radar equation, SAR sensors operating at these frequencies typically use antennas that have very high gain in azimuth, such as slotted antennas with $1° - 1.5°$ beam width [Caris et al., 2015]. These sensors' narrow beam width (pencil beam) only allows a limited area on the surface to be illuminated simultaneously. Operating these sensors on linear trajectories in stripmap mode is unproblematic since the surface area is continuously scanned in the width of the elevation angle, whereby the buildup of a large azimuth bandwidth is limited. However, this configuration is not very suitable for data acquisition on circular trajectories. In this geometry, a large, ideally symmetrical region must be continuously illuminated that allows the acquisition of a 360° data set of the surface. Cassegrain or horn antennas are typically better suited.

In principle, data collection is also possible with high-gain antennas. Still, the spot's position on the surface is even more highly dependent on aligning the target beam precisely. Even small angular deviations would cause the beam to drift out of the target region. A reasonable solution to reduce angular dependence is to use antennas with less gain. To illustrate this with an example, operating a 10° horn antenna instead of a 1.5° slotted antenna decreases the antenna gain by 6 dB in one dimension and 12 dB considering the receiving antenna. Consequently, the range of the

sensor further decreases that requires a reduction of the flight height. Since the elevation angle θ cannot be chosen arbitrarily small to avoid long shadow formation, especially in urban scenes, the reduced flight altitude inevitably leads to smaller flight radii.

Further, the maximum Doppler frequency f_d and thus the sensor's PRF or SRF is also directly related to the wide azimuth beam width β and the airspeed $\vec{v}_s$ by

$$f_d = \frac{2 \cdot |\vec{v}_s|}{\lambda} \cdot \cos\left(\frac{\pi}{2} - (\frac{\beta}{2} + \beta_d)\right) \tag{3.1}$$

with β_d the expected drift angle in CSAR mode. Applying the Nyquist-Shannon-criterion, with moderate $|\vec{v}_s|$ of only 35 m/s, a horn antenna of $\beta = 10°$ and expected $\beta_d = 5°$, this already results in a very high PRF mode of PRF $= 2 \cdot 1.3 \cdot f_d \approx 10$ kHz. Considering the simultaneous transmission of high RF bandwidths, it is obvious that technical limits are rapidly reached since both the IF sampling frequency and the amount of sampled data increase proportionally to the higher PRF.

Flying at a relatively low altitude on small radii at only moderate speed is difficult to be realized on a larger aircraft. Therefore, small aircraft or UAVs are much better suited to these requirements, but on the other side, these platforms are more sensitive to thermal lift and have low wing loading. With small aircraft, following an exact circular trajectory on a narrow radius with a fixed roll angle becomes typically more challenging as the flight attitude is more unstable than larger radii. The challenge is that the platform in data acquisition mode has to follow an exact circular path over the ground while constantly keeping the antenna pointing to the circle's center. But this is synonymous with the problem that the direction of the wind vector hitting the platform permanently changes (headwind, crosswind, tailwind). As a result, the pilot must compensate these effects with frequent aileron movements (rolling). These corrections typically also lead to a platform drift (yaw rotation), and the platform no longer moves tangentially to the defined circular path. Even if the aircraft were to fly a perfect circle, the radar would additionally have to be installed in the center of rotation, which is generally not the case. Contrariwise, the radar is often mounted on the aircraft's wing.

3.2 Determination of optimal flight configurations

To evaluate a suitable flight configuration of a W-band sensor in CSAR mode over urban area, the maximum range and illuminated region of such a sensor given current technology should be roughly estimated. The derivation shall be the basis for subsequent experimental studies and provide a perspective for applications.

Maximum range, swath width and optimal sensor installation

From [Cumming & Wong, 2005], the received power P_r as a function of the emitted power P_e is given by the radar equation by

$$P_r = P_e \cdot \frac{G^2 \sigma \lambda^2}{(4\pi)^3 \cdot r^4} \tag{3.2}$$

with G the antenna gain, σ the target's RCS and the range r. Atmospheric attenuation is neglected. By knowing that β is approximated by $\beta = \frac{\lambda}{L}$ with L the antenna length, and $G = \frac{4\pi \cdot L}{\lambda \cdot \varrho}$, with ϱ the antenna beam width in elevation, P_r yields

$$P_r = P_e \cdot \frac{L^2 \cdot \sigma}{(4\pi) \cdot \varrho^2 \cdot r^4}. \tag{3.3}$$

For further analysis, it is crucial how large the selected resolution cells on the ground are chosen and how long the synthetic aperture can be coherently integrated. In CSAR mode, in theory, the whole 360° trajectory can be regarded as the synthetic aperture. However, considering no autofocus routines and real, non-isotropic targets, this becomes unrealistic.

Maximum range in stripmap mode

Considering stripmap SAR mode and assuming the ability to coherently integrate a fraction $1/n$, $n \in \mathbb{N}$ of the full synthetic aperture defined by the antenna beam width and simultaneously providing sufficient RF bandwidth, the maximum resolution corresponds to $\delta_x = \delta_y = \frac{L}{2} \cdot n$ with δ_x, δ_y the range and azimuth resolution, respectively. The RCS of each pixel or resolution cell can then be described by $\sigma = \delta_x \cdot \delta_y \cdot \sigma_0 = (\frac{L}{2} \cdot n)^2 \cdot \sigma_0$. The energy $W_r = P_r \cdot T_s$ that is collected over the integration time $T_s = \frac{\lambda \cdot r}{L \cdot |\vec{\mathbf{v}}_s| \cdot n}$ equals

$$W_r = \frac{P_e \cdot L^3 \cdot \sigma_0 \cdot \lambda \cdot n}{16\pi \cdot \varrho^2 \cdot |\vec{\mathbf{v}}_s| \cdot r^3}. \tag{3.4}$$

To achieve good image contrast, the collected energy of each pixel should provide an SNR of at least 10, yielding $W_r \geq 10 \cdot k \cdot T_K \cdot N$. The maximum range r_{max} of the sensor then depends on the sensor's noise figure N and the specific RCS of the target area and can be derived by

$$r_{max} = L \cdot \sqrt[3]{\frac{P_e \cdot \sigma_0 \cdot \lambda \cdot n}{16\pi \cdot \varrho^2 \cdot |\vec{\mathbf{v}}_s| \cdot 10 k T_K N}} \tag{3.5}$$

with $k = 1.38 \cdot 10^{23} Ws/K$ and T_K the temperature.

Giving a further example, r_{max} shall be evaluated for grassland where experimental studies showed that grass has approximately an RCS of $-10\,dBm^2/m^2$. Let's further assume that the sensor transmits a RF bandwidth of 1 or 2 GHz. Applied to a high-performance W-band sensor with output power of 29 dBm (0.8 W), a 10° beam width (azimuth/elevation) and a noise figure of $N = 25$ installed on a small aircraft with typical airspeed of $|\vec{\mathbf{v}}_s| = 35$ m/s, this corresponds to $r_{max} = 660$ m for 7.5 cm resolution cells (2 GHz) and $r_{max} = 830$ m for 15 cm resolution cells (1 GHz), respectively. Processing the entire synthetic aperture of 10° in a 1 cm resolution cell would limit the range r_{max} to 330 m.

Maximum range in CSAR mode

In CSAR mode, the integration time T_s and also the spatial resolution δ_y is not limited by the azimuth beam width or the size L of the antenna. From Fig. 3.1a, T_s is dependent on the integration interval φ_{az} and the radius R_m of the circular path with $T_s = \frac{R_m \cdot \varphi_{az}}{|\vec{\mathbf{v}}_s|} = \frac{r \cdot \cos\theta \cdot \varphi_{az}}{|\vec{\mathbf{v}}_s|}$. For the maximum range r_{max} it follows:

$$r_{max} = \sqrt[3]{\frac{P_e \cdot L^2 \cdot \delta_y(\varphi_{az}) \cdot \delta_x(\varphi_{az}, B) \cdot \sigma_0 \cdot \cos(\theta) \cdot \varphi_{az}}{4\pi \cdot \varrho^2 \cdot |\vec{\mathbf{v}}_s| \cdot 10 k T_K N}} \tag{3.6}$$

with $\delta_y(\varphi_{az})$, $\delta_x(\varphi_{az}, B)$ being the maximum resolution that is achievable with the corresponding integration interval φ_{az} and the RF bandwidth B, see Section 4.1.2. With a specific optimal flight velocity $|\vec{\mathbf{v}}_s|$ of the aircraft, the steeper the elevation angle θ is chosen, the shorter the integration time for φ_{az} and the lower the collected energy W_r. However, it should be noted, that in most countries, including Germany, a certain minimum flight height is compulsory over urban areas.

Since the spatial resolution is no longer restricted to L/2 and by further knowing that in the case of a symmetrical antenna it also holds $\varrho = \frac{\lambda}{L}$ the length of the antenna affects equation 3.6

by the power of 4. Halving the antenna beam width in both dimensions would correspond to an increase of r_{max} by a factor of 2.5. However, the disadvantages are the increasing demands on beam stabilization, higher IF bandwidths, a less miniaturized system, and a larger, absolute integration path for equal spatial resolution. Therefore, these parameters should be taken into account when designing the system.

Installation angle of the sensor

The optimal preset, fixed depression angle ϵ of the SAR sensor can be derived from Fig. 3.1a and knowledge of r_{max}. To keep the airplane at a predefined height h_z, in stripmap mode only the gravitational force $\vec{\mathbf{F}}_g = m \cdot \vec{\mathbf{g}}$ with m the platform's mass and $\vec{\mathbf{g}}$ the acceleration of gravity, has to be compensated by the forward velocity $\vec{\mathbf{v}}_s$ (uplift). The degree of the uplift caused by the forward velocity depends on the respective platform (wing loading).

While moving on a circular trajectory, in addition to the uplift $-\vec{\mathbf{F}}_g$, a centripetal force $\vec{\mathbf{F}}_z$ acting in the direction of the center of the circle works on the aircraft. By tilting the wings (rolling), the lift is divided into a vertical and a centripetal force yielding:

$$\tan(\phi) = \frac{m \cdot |\vec{\mathbf{a}}_z|}{m \cdot |\vec{\mathbf{g}}|} = \frac{|\vec{\mathbf{v}}_s|^2}{R_m \cdot |\vec{\mathbf{g}}|} = \frac{|\vec{\mathbf{v}}_s|^2}{r \cdot \cos(\theta) \cdot |\vec{\mathbf{g}}|} \Leftrightarrow \phi = \arctan\left(\frac{|\vec{\mathbf{v}}_s|^2}{r \cdot \cos(\theta) \cdot |\vec{\mathbf{g}}|}\right) \Rightarrow \epsilon = \theta - \phi \tag{3.7}$$

with $\vec{a}_z$ being the centripetal acceleration and ϕ the roll angle. Given specific sensor-, target- and aircraft specifications, an optimal CSAR flight geometry can be designed by the derived parameters. As an example, Fig. 3.1b indicates r_{max} (equation 3.6) and the swath width for two different antenna sizes L and the maximum available output power P_e as a function of φ_{az}. It is observable that with small φ_{az} the resolution increases rapidly, the cell size becomes smaller, and the range, therefore, decreases significantly. At larger φ_{az} this effect is partially compensated by the longer integration time since the resolution increases much more slowly. However, this always assumes a perfect coherent integration over a sizeable angular interval.

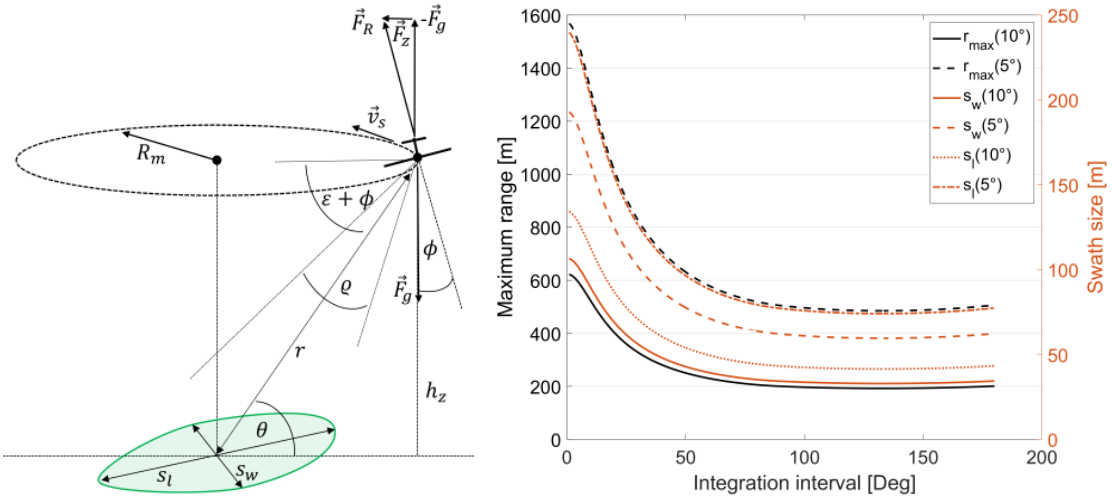

(a) (b)

Figure 3.1: Forces acting on the aircraft and achievable distances and swath sizes in CSAR mode. a) Force diagram of aircraft on circular flight path, b) range r_{max}, swath width s_w and swath length s_l as a function of antenna beam width (5° and 10°) and φ_{az}. Simulated for $P_e = 29dBm$, N=25, $\theta = 35°$, $B = 2\,\text{GHz}$, $|\vec{\mathbf{v}}_s| = 35\,\text{m/s}$, $\sigma_0 = -10dB$ and $\lambda = 3.2\,\text{mm}$.

Beam steering requirements

Experimental evaluations based on the derived parameters and shown by Palm et al. [2013]; Palm et al. [2015] carried out on an ultralight aircraft indicate that the standard deviations and thus the absolute variation of parameters such as roll angle, squint angle and velocity within the length of a synthetic aperture are 40% higher on circular than on linear flight paths. Besides very high requirements placed on the GPS/INS sensor, it turned out that full aspect coverage in Ka- or W-band on circular trajectories on small radii and light airplanes with sensors primarily developed for stripmap campaigns can hardly be achieved. Even when operating with antennas with significantly larger beam widths, the platform movement is typically too inaccurate to continuously illuminate a specific region in full aspect mode. It became apparent that slight deviations due to air turbulences or corrective movements of the pilot are sufficient to let the beam constantly drift out of the target region. Even if the deviations are only short-term, this leads to the spectrum of the corresponding synthetic apertures being only partially occupied, resulting in reduced resolution and reduced signal-to-noise ratios (low image contrast). To achieve optimal illumination of the target area, the evaluation of the experiments demonstrated that it typically would need a correction rate of approximately $\pm 12°$ for roll, $\pm 8°$ for pitch, and $\pm 10°$ for heading. The angular velocities to be compensated are about $\pm 3.0°/s$ for heading and pitch and $\pm 6.0°/s$ for roll.

Consequently, a W-band SAR system operating on circular flight path should rely on relatively large beamwidths and a real-time beam stabilizing procedure of either mechanical or electronic form to achieve consistently good measuring results regardless of the respective flight track. However, the operational use of a W-band phased array airborne SAR system is not known to the author from the literature. Recently, there has been increasing interest in designing phased array systems in this frequency band, especially from communications, see [Gu et al., 2015; Shi et al., 2015], but the generated output power is still far too low for airborne SAR imaging applications.

3.3 Required angular corrections for real-time beam alignment

A possible solution is designing a real-time, mechanical and automatic antenna beam steering procedure. The geometry for performing the beam alignment for such an interface is presented in Fig. 3.2. The flight trajectory and attitude of the platform are indicated by the red arrow and can be derived in real-time by actual GPS data, flight velocities, and angular orientation since these parameters are continuously recorded and evaluated by the on-board GPS/INS unit.

Assuming a flat plane model, the center of the currently illuminated area $\vec{\mathbf{P}}_0$ on the ground is derived by the actual's antenna position $\vec{\mathbf{x}}_s(nT)$ and the normalized line of sight vector (LoS vector) $\vec{\mathbf{r}}_0$ pointing in the direction of the antenna's main beam. $\vec{\mathbf{r}}_0$ is thus a function of the orientation angles $f_{(\psi,\phi,\gamma)}$. It follows

$$\vec{\mathbf{P}}_0(nT) = \vec{\mathbf{x}}_s(nT) + b(nT) \cdot \vec{\mathbf{r}}_0(nT) = \vec{\mathbf{x}}_s(nT) + b(nT) \cdot f_{(\psi,\phi,\gamma)}(nT) \cdot \vec{\mathbf{a}}_0, \tag{3.8}$$

in which $f_{(\psi,\phi,\gamma)}$ represents a rotational matrix and $\vec{\mathbf{a}}_0$ the initial LoS of the radar. The three angles determine the platform's heading angle ψ, the roll angle ϕ, and the pitch angle γ. The term nT describes the actual radar sweep at slow time T and $b \in \mathbb{R} > 0$ the length of the vector. In the side-looking SAR configuration, the antenna typically looks perpendicularly to the platform's heading vector ψ with a fixed, embedded depression angle ϵ. By banking or rolling the platform on circular trajectories, the total depression angle increases or decreases by the actual roll angle

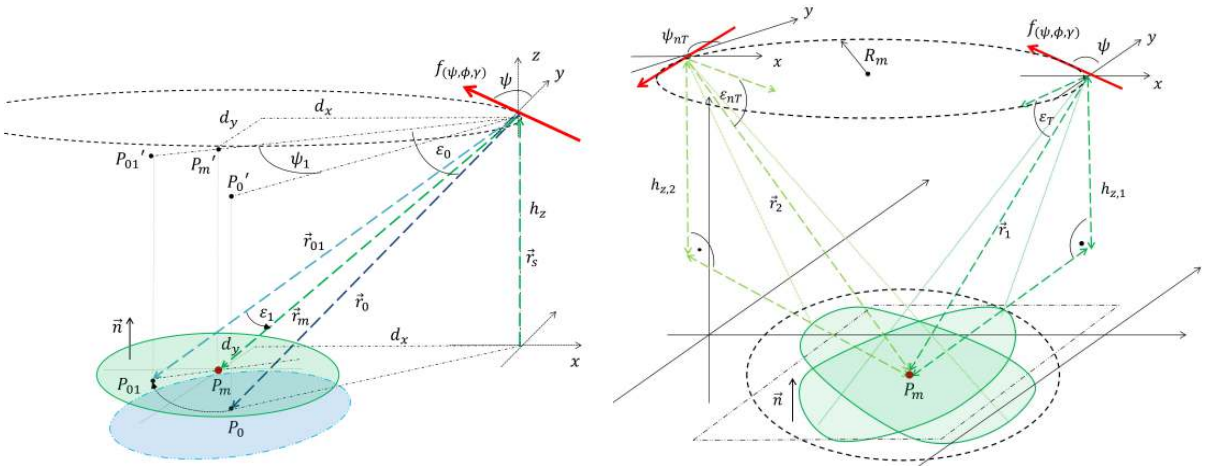

Figure 3.2: Geometrical representation of required beam steering corrections and optimal illumination. a) Required parameters to adjust the beam footprint from point $\vec{\mathbf{P}}_0$ (blue) to the ideal center position $\vec{\mathbf{P}}_m$ (green), b) visualization of two overlapping beams from different subapertures in the scene's center. Optimal illumination of target scene by continuous beam steering.

to $\epsilon_0 = \phi + \epsilon$. Based on equation 3.8 the first rotational matrix $f_{(\epsilon_0,\gamma)}$ in the Cartesian coordinate system can then be derived to

$$\mathbf{A} = \begin{pmatrix} cos(\gamma) & 0 & -sin(\gamma) \\ sin(\epsilon_0) \cdot \sin(\gamma) & cos(\epsilon_0) & sin(\epsilon_0) \cdot sin(\gamma) \\ cos(\epsilon_0) \cdot cos(\gamma) & -sin(\epsilon_0) & cos(\epsilon_0) \cdot cos(\gamma) \end{pmatrix}, \tag{3.9}$$

while $\mathbf{A}$ describes the rotation due to a change in pitch and depression angle. Next, the rotation in the third dimension, the heading angle ψ, can be performed. Depending on the installation of the SAR antenna - viewing direction to the right side ($+90°$) or left side ($-90°$) - for $\mathbf{B}$ it follows

$$\mathbf{B} = \begin{pmatrix} cos(\psi \pm \frac{\pi}{2}) & sin(\psi \pm \frac{\pi}{2}) & 0 \\ -sin(\psi \pm \frac{\pi}{2}) & cos(\psi \pm \frac{\pi}{2}) & 0 \\ 0 & 0 & 1 \end{pmatrix}. \tag{3.10}$$

This finally leads to a line of sight $\vec{\mathbf{r}}_0$ of

$$\vec{\mathbf{r}}_0 = \mathbf{B} \cdot (\mathbf{A} \cdot \vec{\mathbf{a}}_0). \tag{3.11}$$

The point $\vec{\mathbf{P}}_0$ as intersection between LoS vector $\vec{\mathbf{r}}_0$ and the imaging plane with normal vector $\vec{\mathbf{n}} = (0, 0, 1)'$ and support vector $\vec{\mathbf{r}}_p$ is then derived by

$$\vec{\mathbf{P}}_0 = \vec{\mathbf{x}}_s + \frac{\vec{\mathbf{n}}' \cdot (\vec{\mathbf{r}}_p - \vec{\mathbf{x}}_s)}{\vec{\mathbf{n}}' \cdot \vec{\mathbf{r}}_0} \cdot \vec{\mathbf{r}}_0 \tag{3.12}$$

In the case of a manually selected or predefined target coordinate $\vec{\mathbf{P}}_m$ (red point, see Fig. 3.2), usually placed in the center of the circular trajectory, the antenna's main lobe must continuously be adjusted. Many ambiguous solutions for obtaining the ideal vector $\vec{\mathbf{r}}_m$ exist, which optimally illuminates the region by means of different rotations of the three axes. We are interested in a solution with possibly small rotation angles on the condition that the maximum rotation rate of the system is restricted. For reducing complexity, it is intended to focus on the two most critical angles heading and roll. Therefore, an implemented routine shall keep the pitch angle constantly

at zero degrees, yielding $\gamma = 0$. The two still missing correction angles are determined in two steps. First, the required correction angle ψ_1 is calculated in heading, then the correction angle in depression ϵ_1 is derived. The former is determined as the angular difference of the two projection points $\vec{\mathbf{P}}'_0$ and $\vec{\mathbf{P}}'_m$ using the following relationship:

$$\psi_1 = \arctan 2(\frac{\vec{\mathbf{r}}_0 \cdot \vec{\mathbf{e}}_x}{\vec{\mathbf{r}}_0 \cdot \vec{\mathbf{e}}_y}) - \arctan 2(\frac{d_x}{d_y}). \tag{3.13}$$

By executing the rotation in heading direction with ψ_1, the main lobe is thus shifted to the point $\vec{\mathbf{P}}_{0,1}$. By knowing the distance from the sensor to the desired target $\vec{\mathbf{P}}_m$, the ideal correction angle ϵ_1 can then be derived by

$$\epsilon_1 = \epsilon_0 - \arcsin(\frac{h_z}{\|\vec{\mathbf{r}}_m\|}), \tag{3.14}$$

with h_z being the height of the sensor above ground level. Performing both rotations, the radar's main lobe is then shifted to the ideal center at the point $\vec{\mathbf{P}}_m$. In the case of targets with high elevation above the ground level, the variable h_z can be adjusted for even better focus. This can be useful in the case of challenging topography, where, for instance, specific objects on high buildings or high electricity pylons are observed.

3.4 Real-time beam steering realization

A mechanical mount was acquired that is able to achieve the derived specifications of Section 3.2 and can carry the designed radar front-end. Its specifications are presented in Chapter 7. The manufacturer designs the mount to operate airborne cameras to keep the carried sensor in the nadir direction on the flight line. For acquiring a circular SAR data set, a different functionality is required that can automatically align the footprint to a fixed, programmable GPS coordinate.

A solution to this problem is the implemented real-time beam steering framework that consists of a programmable interface between GPS/INS and mount, which was developed in this thesis. Continuously transmitting the flight attitude data in real-time via this interface allows calculating new control commands for the movement of the mount as derived in Section 3.3. When starting the real-time alignment in flight, the board computer opens two sockets to the GPS/INS and mount. On the first socket, the GPS/INS data packages (position, angle, speed) are continuously received with a typical data rate of 128-512 Hz. The calculated solution for the new angular rotation of the antenna is sent via the second data channel back to the mount. These new angular rotation instructions are then converted into control commands for the mount and executed. A new adjustment is calculated after recapturing the new geometrical position and angular orientation.

Being able to continuously detect the illuminated footprint of the ground, the framework can automatically adjust the antenna orientation by fast angular movements. To precisely measure the actual orientation of the mount, the inertial measuring unit (IMU) is positioned on top of the rotatable mount directly coupled to it, see Chapter 7. Any movement of the mount is then captured in real-time, which means that the whole sensor system represents a closed-loop as indicated in Fig. 3.3. By being restricted to specifications of the stabilized mount, the beam alignment can only be applied if the required angular corrections are within the parameters of the maximum steerable angles. Otherwise, the mount is instructed to rotate the antennas to the mechanical limit and hold the position until the region of limited conditions can be left again. Input parameters that are required to start the system's circular mode are the current target coordinate P_m and the update rate.

By applying the proposed framework, an entire aspect circular data acquisition as indicated in Fig. 3.2b becomes operable that is less affected by air turbulences or divergent flight movements.

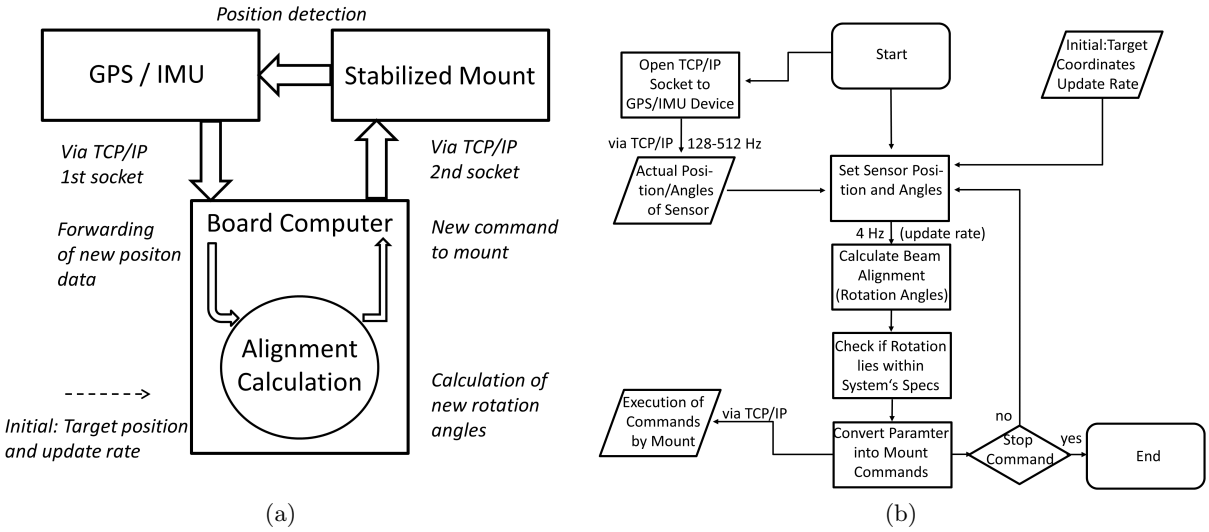

Figure 3.3: Interaction of required system components and the flow chart of real-time beam steering procedure. a) Representation of the real-time data flow within the components involved. The developed software interface communicating with GPS/INS and mechanical mount constantly calculates the optimal angular steering solution, b) flow chart of implemented software interface.

Effects caused by rotating the mount and antenna on the processing of the SAR data in this configuration are discussed in Section 8.1.

4 Processing, image registration and visualization of CSAR data

Evaluating the acquired SAR data requires a SAR signal processor chain capable of focusing the FMCW data in high resolution. The developed architecture must also be able to process non-linear flight and different focusing geometries. This Chapter describes the design of a SAR processor that meets these requirements, focusing on a very high-frequency FMCW radar. The image resolution that can be achieved in urban areas by not knowing the target heights of individual buildings on a circular data acquisition is analyzed. Further, the image registration of subaperture images acquired from different aspects is presented. Based on this, an adapted concept of Video-CSAR (ViCSAR) is introduced that is able to illustrate a high-resolution dynamic situation assessment of urban areas.

4.1 Processing circular SAR data

Based on the theoretically achievable point target response of a SAR sensor on a circular aperture, a SAR processor has to be optimized for the scope of work. Therefore, the impulse response function (IRF) for circular SAR shall be considered in the first step. Its derivation is based on [Ponce et al., 2014] with minor modifications and extensions. Henceforth, $\vec{\mathbf{x}}$ describes a 3d-vector in the Cartesian coordinate system while $\vec{x}$ describes a 2d-vector, typically the location on the image grid.

4.1.1 Theoretical considerations

Circular SAR geometry is defined by moving a radar sensor along a circular-shaped trajectory over a defined, spotlighted target region with coordinates $\vec{\mathbf{r}}(\varphi) = (R_m \cdot cos(\varphi), R_m \cdot sin(\varphi), h_z)$. R_m specifies the radius, h_z the height of the circle and $\varphi \in [0, 2\pi]$ the azimuth angular variation or aspect angle.

Signal model

The signal model of the collected radar echos in the spatial frequency domain $s(\vec{\mathbf{k}}, \varphi)$ can be described as

$$s(\vec{\mathbf{k}}, \varphi) = P_\omega(\omega) \int \alpha(\vec{\mathbf{r}}_g) \cdot e^{-j2\|\vec{\mathbf{k}}\| \cdot \|\vec{\mathbf{r}}_g - \vec{\mathbf{r}}(\varphi)\|} d\vec{\mathbf{r}} \tag{4.1}$$

with $\alpha(\vec{\mathbf{r}}_g)$ as the complex reflectivity of the imaging grid with $\vec{\mathbf{r}}_g = (r_x, r_y, r_z)$, P_w the transmitted chirp in the spatial frequency domain, $k = \|\vec{\mathbf{k}}\| = \frac{2\pi}{\lambda(\omega)}$ as the wavenumber with ω as the fast-time angular frequency and λ the radar wavelength. The components of the wavenumber $\vec{\mathbf{k}}$ are

$$k_x = 2k \cdot \cos(\theta) \cdot \cos(\varphi), k_y = 2k \cdot \cos(\theta) \cdot \sin(\varphi), k_z = 2k \cdot \sin(\theta) \tag{4.2}$$

where $0 \leq \theta < \frac{\pi}{2}$ is the elevation angle. For simplification, it is further assumed in the model that $P_\omega = 1$ and that the complex reflectivity of the scene is represented by a 3d Dirac delta function with a single potential scatterer at position $\vec{\mathbf{x}}_p$ with reflectivity $\alpha(\vec{\mathbf{x}}_p) = 1$.

Inverse operation

The unknown reflectivity $\alpha(\vec{\mathbf{r}}_g)$ of the imaging grid can then be derived by the inverse operation

$$\alpha(\vec{\mathbf{r}}_g) = \int s(\vec{\mathbf{k}}, \varphi) \cdot e^{j2\|\vec{\mathbf{k}}\| \cdot \|\vec{\mathbf{r}}_g - \vec{\mathbf{x}}_s(\varphi)\|} d\vec{\mathbf{k}}. \tag{4.3}$$

with $\vec{\mathbf{x}}_s(\varphi) = \vec{\mathbf{r}}(\varphi)$ as the sensor's current position. Assuming that the platform follows a circular trajectory on a given height h_z and knowing that $k_r = 2k \cdot \cos(\theta) = \sqrt{k_x^2 + k_y^2}$ and $2 \cdot \|\vec{\mathbf{k}}\| = 2k = \frac{k_r}{\cos(\theta)}$ the complex line integral from equation 4.3 can be transformed with the Jacobian

$$det\left(\frac{d(k_x, k_y)}{d(k_r, \varphi)}\right) = \begin{vmatrix} \cos\varphi & -k_r \sin\varphi \\ \sin\varphi & k_r \cos\varphi \end{vmatrix} = k_r \cdot (\cos^2(\varphi) + \sin^2(\varphi)) = k_r \tag{4.4}$$

and the model simplifications to a complex surface integral with

$$\alpha(\vec{\mathbf{r}}_g) = \int_{k_r} \int_{\varphi} k_r \cdot e^{-j\frac{k_r}{\cos(\theta)} \cdot \|\vec{\mathbf{x}}_p - \vec{\mathbf{x}}_s(\varphi)\|} \cdot e^{j\frac{k_r}{\cos(\theta)} \cdot \|\vec{\mathbf{r}}_g - \vec{\mathbf{x}}_s(\varphi)\|} d\varphi dk_r, \tag{4.5}$$

while $\vec{\mathbf{x}}_p$ denotes the actual 3d position of the potential scatterer. With $k_z = k_r \cdot \tan(\theta)$ and considering the Fourier analysis of the free-space Green's function $e^{j2k \cdot \|\vec{\mathbf{r}}_g - \vec{\mathbf{x}}_s(\varphi)\|}$, see [Soumekh, 1996; Ponce et al., 2014], the exponential terms in 4.5 can be separated according to their Cartesian components yielding

$$\begin{aligned} \alpha(\vec{\mathbf{r}}_g) = \int_{k_r} \int_{\varphi} & k_r \cdot e^{-jk_r \cdot \tan(\theta)(x_{p,z} - r_{g,z})} \\ & \cdot e^{-jk_r \cdot \|\vec{x}_{p,xy} - \vec{x}_{s,xy}(\varphi)\|} \cdot e^{jk_r \cdot \|\vec{r}_{g,xy} - \vec{x}_{s,xy}(\varphi)\|} d\varphi dk_r \end{aligned} \tag{4.6}$$

It should be noted that a mismatch of the height of the focusing plane $r_{g,z}$ compared to the object's actual height $x_{p,z}$ causes a further phase term in the expression. Considering an ideal trajectory and an ideal target in the circle's center, this phase term is constant. It corresponds to the projected distance between radar and object on the flat focusing plane, commonly referred to as foreshortening. However, real data sets will show a slight variation in platform altitude resulting in $\theta \to \theta(\varphi)$, and thus the foreshortening is not constant. In addition, most objects are not located in the center of the circle. This mismatch, on the one hand, limits the resolution capacity in urban scenarios, which is further investigated in Section 4.3. On the other hand, it allows 3d extraction, and a proposed method to evaluate this context is presented in Section 5.

If the target is further placed in the center of the coordinate system $\vec{\mathbf{x}}_p = (0, 0, 0)$, equation 4.6 can be simplified to

$$\alpha(\vec{\mathbf{r}}_g) = \int_{k_r} \int_{\varphi} k_r \cdot e^{jk_r \cdot r_{g,z} \cdot \tan(\theta)} \cdot e^{-jk_r \cdot (\|\vec{x}_{s,xy}(\varphi)\| - \|\vec{r}_{g,xy} - \vec{x}_{s,xy}(\varphi)\|)} d\varphi dk_r \tag{4.7}$$

Given an ideal circular trajectory, from Fig. 4.1 it then holds:

$$\|\vec{x}_{s,xy}(\varphi)\| - \|\vec{r}_{g,xy} - \vec{x}_{s,xy}(\varphi)\| = \vec{r}_{g,xy} \cdot \sin(\varphi) \tag{4.8}$$

Subsequently, the second exponential expression in equation 4.7 represents an integral notation of the Bessel function and by solving equation 4.7 with respect to φ we get

$$\alpha(\vec{\mathbf{r}}_g) = 2\pi \int_{k_{r_1}}^{k_{r_2}} k_r \cdot e^{jk_r \tan(\theta) \cdot r_{g,z}} \cdot J_0(k_r \cdot \vec{r}_{g,xy}) dk_r \tag{4.9}$$

with J_0 the Bessel function of the first kind and zeroth order [Watson, 1995].

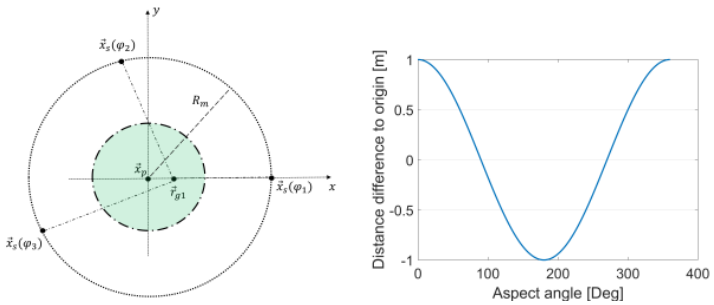

(a) (b)

Figure 4.1: Phase error in [m] at grid position $\vec{r}_{g1}$ at 1 m distance to the focus origin over full aspect interval. a) Graphical representation of distance at different sensor positions $\vec{\mathbf{x}}_s$, b) absolute distance difference of position $\vec{r}_{g1}$ to the focus origin.

Impulse response function

Given a scatterer placed in the center at $\vec{\mathbf{x}}_p = (0, 0, 0)$ and further assuming that the focus height and target height are in match ($r_{g,z} = x_{p,z}$), the integral of equation 4.9 can be solved from [Ponce et al., 2014] resulting in the IRF

$$\alpha(\vec{\mathbf{r}}_g) = 2\pi \cdot k_r \cdot J_0(k_r \cdot \vec{r}_{g,xy}) \tag{4.10}$$

for a signal with narrow bandwidth and

$$\alpha(\vec{\mathbf{r}}_g) = \frac{2\pi}{\vec{r}_{g,xy}}[k_{r_2} \cdot J_1(k_{r_2} \cdot \vec{r}_{g,xy}) - k_{r_1} \cdot J_1(k_{r_1} \cdot \vec{r}_{g,xy})] \tag{4.11}$$

for a signal with wide bandwidth whose IRF in W-band is indicated in Fig. 4.2b.

4.1.2 Resolution of targets at reference height

From equation 4.11, a full 360° coherent processing results in a completely symmetrical 3d-IRF, which means that using the terms azimuth and range resolution is no longer appropriate. Ideal targets placed in the circle center at focusing height show a resolution of $\frac{\lambda}{4}$ [Ishimaru et al., 1998]. Applied to W-band data, the spectral density function and the 3d-IRF for an ideal point target are illustrated in Fig. 4.2. Assuming an ideal target, a theoretical resolution of approx. 1 mm is feasible, see Fig. 4.2b. The high dependency of the IRF on precise knowledge of the object height is highlighted in Fig. 4.2c.

More manageable in this high-frequency domain is handling significantly smaller aspect integrations. The level of azimuth resolution δ_y can then be varied by choosing a suitable aspect angle interval $\varphi_{az} = \varphi_2 - \varphi_1$. From Fig. 4.3a and knowing equation 4.2, the resolution is derived by collecting the projected frequencies over φ_{az} in the k-space domain. By integrating over φ_{az} and with $\varphi \in [\varphi_1, \varphi_2]$, B the signal's total RF bandwidth, and $k_{max} = (2\pi \cdot (f_0 + B/2)/c_0)$ for the azimuth resolution it can be derived

$$\delta_y = \frac{\pi}{k_{max} \cdot [max(\sin(\varphi)) - min(\sin(\varphi))] \cdot \cos(\theta)} \tag{4.12}$$

where $max(\sin(\varphi))$ is the maximum and $min(\sin(\varphi))$ the minimum of the sinus function in the interval $0 \leq \varphi_1 < \varphi < \varphi_2 \leq 2\pi$. Analog, with $k_{min} = (2\pi \cdot (f_0 - B/2)/c_0)$ and $B_c = \frac{2\pi \cdot B}{c_0}$ the range resolution is derived by

$$\delta_x = \frac{\pi}{\cos(\theta)[B_c(1-\chi) + (B_c \cdot \chi + k_{min}) \cdot [1 - min(\cos(\varphi - \varphi_1))]]} \tag{4.13}$$

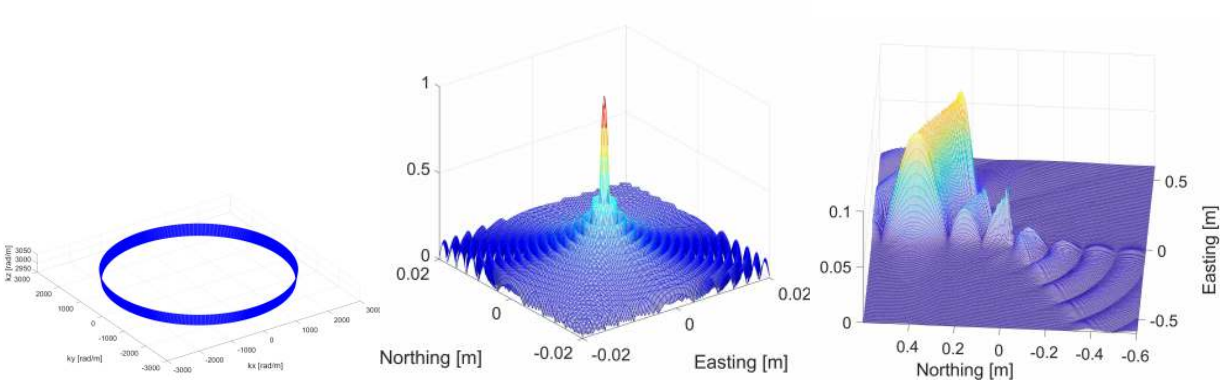

(a) (b) (c)

Figure 4.2: Simulated CSAR spectrum in K-space and processed point targets at 94 GHz. a) CSAR spectrum of a point target placed in the Cartesian origin in slant-range with an elevation angle of $\theta = 40°$ and a bandwidth of 1.5 GHz, b) 3d-IRF of full aspect 360° coherent processing at focus height, c) 3d-IRF of a target placed at 35 cm above focusing plane and 60° processing.

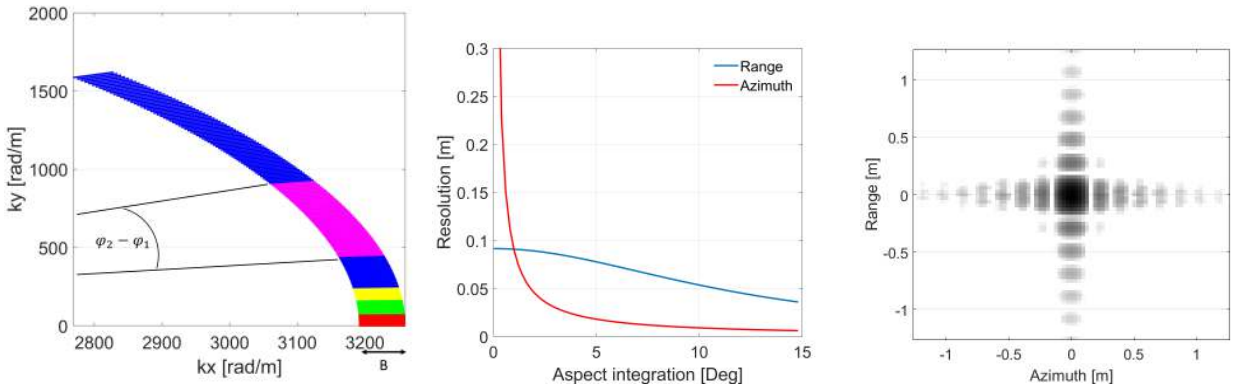

(a) (b) (c)

Figure 4.3: Projected K-space spectrum and resolution of objects in CSAR as a function of aspect integration in W-band. a) First 30° of the spectrum of an ideal target. Simulated RF bandwidth of 2 GHz and $\theta = 35°$. Individual colors specify processed subapertures of 1.5° (red, yellow, green) and 8° (magenta), b) range and azimuth resolution of the same target as a function of φ_{az}, c) point target processed with $\varphi_{az} = 1.5°$.

with

$$\chi = \begin{cases} 0 & 0 < \varphi < \frac{\pi}{2} \\ 1 & \varphi > \frac{\pi}{2}. \end{cases} \tag{4.14}$$

The height resolution [Ponce et al., 2014] is further derived by

$$\delta_z = \frac{2}{\sqrt{2\pi} \cdot \sin\theta} \cdot \frac{c_0}{B}, \tag{4.15}$$

if the angular persistence of the scatterer with respect to φ is adequate. From Fig. 4.3b, the range resolution is initially limited by the signal's bandwidth for small angles but rapidly improves for larger aspect intervals. Different resolution-based analysis for optimizing subaperture CSAR measurements of targets at reference heights are presented by Wu et al. [2018].

4.2 SAR processor design

To process both the SAR data acquired from the circular trajectories and the data from the mobile mapping experiments, the developed SAR processor shall be able to cope with large apertures, high carrier frequencies, and different flight and focusing geometries. Furthermore, it must be taken into account that the flight movement of the platform is rather turbulent.

For such highly non-linear trajectories, time domain backprojection routines are well suited as the matched filter operation for each image pixel can analytically be derived individually [Ulander et al., 2003; Frey et al., 2009]. In particular, the motion compensation process, which in frequency-based focusing algorithms is often approximated for entire distance areas, is improved by deriving the individual filter for each pixel. Further, the processing of arbitrary high bandwidths on different focusing geometries is feasible. As backprojection is commonly known, only adaptations concerning the sensor constellation and the focusing geometry are to be addressed here.

4.2.1 FMCW processing requirements at high carrier frequencies

Specific requirements that apply to very high-frequency FMCW SAR shall be addressed. With knowledge of equation 2.7 and 4.5, the unknown reflectivity $\alpha(\vec{\mathbf{r}}_g)$ of the imaging grid in time domain backprojection processing for FMCW SAR is derived by

$$\begin{aligned}\alpha(\vec{\mathbf{r}}_g) = \int_{\varphi}\int_{t} &\exp\left\{-j2\pi f_0 t_r(t,\varphi)\right\}\exp\left\{j\pi k_T (t_r(t,\varphi))^2\right\} \\ &\cdot \exp\left\{j2\pi t\left[k_T t_r(t,\varphi) - f_{R0}\right]\right\} dt d\varphi\end{aligned} \tag{4.16}$$

Again, $t_r(t,\varphi)$ is the two way time delay, $k_T = \frac{B}{T}$ the chirp rate, f_0 the carrier frequency and f_{R0} the mid-range frequency shift. In contrast to pulsed radar systems, the duration of the sweeps in FMCW systems is considerably longer, and the movement while simultaneously sending and receiving can not be neglected. Since the radar sends and receives continuously, the sensor's own movement causes a micro-Doppler, which should considered during processing. Thus, the two way time delay $t_r(t)$ in each phase term of equation 4.16 is fast-time-dependent. Ignoring this movement causes distance and phase errors, and applying the start-stop approximation, which is commonly used in pulsed SAR or FMCW SAR at low frequencies, is questionable. The Doppler frequency f_D within each chirp is defined by

$$f_D = 2\frac{|\vec{\mathbf{v}}_{\mathbf{x}}|}{\lambda} = 2\frac{\vec{\mathbf{v}}_s \cdot r(\vec{\mathbf{x}}_p, \vec{\mathbf{x}}_s)}{|r(\vec{\mathbf{x}}_p, \vec{\mathbf{x}}_s)| \cdot \lambda} \tag{4.17}$$

with $\vec{\mathbf{v}}_s \cdot r(\vec{\mathbf{x}}_p, \vec{\mathbf{x}}_s)$ the scalar product of platform velocity and distance vector between sensor and target and $\vec{\mathbf{v}}_{\mathbf{x}}$ the radial velocity towards the scatterer. Although the absolute velocity $|\vec{\mathbf{v}}_s|$ of the platform might be small, the applied carrier frequency f_0 in W-band is high. Since the frequency is proportional to the Doppler, this leads to a high coefficient $\frac{1}{\lambda} = \frac{f_0}{c_0}$.

The modified backprojection algorithm presented by Ribalta [2011] gives a computationally efficient solution by a first-order approximation of the first phase term in equation 4.16. The method takes advantage of the fact that the coefficients of $t_r(t)$ in the second and third term of the received IF signal of equation 4.16 are bounded by $k_T = \frac{B}{T}$, whereas in the first term by f_0, a factor several ten times larger than B in W-band. Thus, a first-order approximation of $t_r(t)$ is given by

$$t_r(t) = \frac{2r(\vec{\mathbf{x}}_p, \vec{\mathbf{x}}_s(t))}{c_0} \approx \frac{2r(\vec{\mathbf{x}}_p, \vec{\mathbf{x}}_s(t_0))}{c_0} + \frac{2v_{\mathbf{x}}t}{c_0} \tag{4.18}$$

with $v_{\mathbf{x}}$ the absolute radial velocity and being the derivative of $r(\vec{\mathbf{x}}_p, \vec{\mathbf{x}}_s(t))$ at time $t = 0$, assuming a linear and constant motion within each chirp. Applying equation 4.18 on the first phase term of equation 4.16 by knowing [Ribalta, 2011]

$$k_T \cdot \frac{2v_{\mathbf{x}}(\varphi) \cdot t}{c_0} = \frac{B}{T} \cdot \frac{2v_{\mathbf{x}}(\varphi) \cdot t}{c_0} \underbrace{<}_{t \to T} B \cdot \frac{2v_{\mathbf{x}}(\varphi)}{c_0} \ll f_0 \cdot \frac{2v_{\mathbf{x}}(\varphi)}{c_0}. \tag{4.19}$$

results in

$$\begin{aligned} \alpha(\vec{\mathbf{r}}_g) = \int_{\varphi} \int_{t} & \exp\left\{-j2\pi f_0 t_r(t_0, \varphi)\right\} \exp\left\{j\pi k_T (t_r(t_0, \varphi))^2\right\} \\ & \cdot \exp\left\{j2\pi t \left[k_T t_r(t_0, \varphi) + \frac{2f_0 v_{\mathbf{x}}(\varphi)}{c_0} - f_{R0}\right]\right\} dt d\varphi \end{aligned} \tag{4.20}$$

with $t_r(t_0)$ the two time delay at $t = 0$ (start-stop approximation). This leaves only the third phase term dependent on the fast time t.

4.2.2 Sensor trajectory reconstruction

The flight attitude data is acquired from a high precision fiber-optic gyroscope, and GPS/INS solution is provided. Since all further processing stages rely on high-quality inertial data, a dGPS postprocessing and a forward/backward solution is calculated. The navigational data of an entire circular trajectory are then interpolated with a cubic spline interpolation to meet the radar's PRF. By knowing the exact pulse duration T and $\vec{\mathbf{x}}_{s0}$ the start position, $\vec{\mathbf{x}}_s(nT)$ is derived by

$$\vec{\mathbf{x}}_s(nT) = \vec{\mathbf{x}}_{s0} + \int_0^{nT} \vec{\mathbf{v}}_s(t) dt \approx \vec{\mathbf{x}}_{s0} + \sum_{m=1}^{m=n} \vec{\mathbf{v}}_s(mT) \cdot T, m, n \in \mathbb{N} \tag{4.21}$$

Lever arm correction

In CSAR mode, the antenna is not fixed to the platform but instead in a constantly changing position due to the mount's movement. Capturing the movement is realized by the IMU that is at several ten centimeters distance directly coupled to the antennas. Since the antennas' phase center is not in the center of rotation, a lever arm correction must be included. Each angular antenna steering of the mount will cause an additional positioning shift $\vec{d}_m$ of the antenna's phase center and a minor Doppler frequency shift $f_{D,m}$ in the FMCW data that has to be compensated. The corresponding spatial positioning shift $\vec{d}_m$ can be derived by calculating the rotation matrix $\mathbf{A}_m$ of the mount and the lever arm $\vec{a}_m$ to $\vec{d}_m = \mathbf{A}_m \cdot \vec{a}_m$, while $\mathbf{A}_m$ is determined from the navigational data. The additional Doppler shift $f_{D,m}$ within each radar sweep while rotating the mount superimposes additively with the existing Doppler shift to the target. Both parameters can be considered in equation 4.20 by replacing the radial velocity $v_{\mathbf{x}}(\varphi)$ and $t_r(t_0, \varphi)$ by

$$\begin{aligned} v_{\mathbf{x}}(\varphi) &= v_{\mathbf{x}}(\varphi) + v_d(\varphi), \\ t_r(t_0, \varphi) &= \frac{2r(\vec{\mathbf{x}}_p, (\vec{\mathbf{x}}_s(t_0, \varphi) + \mathbf{A}_m \cdot \vec{a}_m))}{c_0} \end{aligned} \tag{4.22}$$

with $v_{\mathbf{d}}(\varphi)$ the radial rotational speed of the mount during a radar sweep.

Focusing function

From equation 4.20 and 4.22, the actual focusing is then achieved by an FFT pulse compression operation in fast time domain and coherent processing in slow time domain over the slowly changing aspect angle φ, leading to a discrete implementation of

$$\begin{aligned}\alpha(\vec{\mathbf{r}}_g) = \int_{\varphi} &\exp\left\{-j2\pi f_0 t_r(t_0,\varphi)\right\} \exp\left\{j\pi k_T (t_r(t_0,\varphi))^2\right\} \\ &\cdot S_m\left[k_T t_r(t_0,\varphi) + \frac{2f_0 v_{\mathbf{x}}(\varphi)}{c_0} - f_{R0}\right] d\varphi\end{aligned} \tag{4.23}$$

with S_m being the Fourier transform of the IF term. To further compensate for effects caused by range migration, a high zero-padding factor is applied to the sampled raw data. This ensures that applying the discrete sum of the phase information of the range-compressed complex samples in S_m over φ is feasible without significant phase shifts and thus much smoother.

Filtering corrupted samples in FMCW SAR

As described in equation 2.7, in FMCW systems, the received signal is typically mixed with the instantaneous transmit signal. For obtaining an uncorrupted beat signal $s_r(t)$, it is important that both signals (transmit and receive) are not affected by structural interferences of any kind. These can be caused by non-linearity of the RF components (low noise amplifier (LNA), filter, several multipliers ...) or due to reflections of the wave within the front-end (mixer). Often, these interferences are highly frequency dependent (stationary waves, harmonics, subharmonics...). If not recognized or suppressed, these interferences usually can corrupt a certain number of samples at fast time t_c within the received beat signal. This results in a loss of signal to noise power and RF bandwidth loss or can cause artifacts in the final SAR image. However, as the sensor is continuously transmitting coherent chirps $s_e(t)$ of the same length and bandwidth, such structural corruptions of the signal occur at the same position (same point of fast time t). They thus are coherent in the Doppler domain, too. The phase gradient in azimuth or slow time T of such a corrupted signal is constant, which leads to

$$\frac{d}{d\varphi} s_r(t = t_c, \varphi) = const, \varphi \in [0, \varphi_{max}] \tag{4.24}$$

The corrupted samples can be removed with a zero Doppler filter in the Doppler domain. All relevant targets in the echoed signal are not affected by this operation. Due to the movement of the sensor and the geometry of SAR and circular SAR, static objects on the ground do not result in a constant phase response within a synthetic aperture (except an ideal point target in the center of a circle assuming further a perfect trajectory). Using FFT operations in the Doppler domain, a realized implementation of the method in the framework's processing steps results in

$$s_r(t,\varphi) \xrightarrow{\mathcal{F}} \mathbf{S}(t, f_D) \rightarrow \mathbf{S}(t, f_D(0) = 0) \xrightarrow{\mathcal{F}^{-1}} s_r(t, \varphi; f_D(0) = 0). \tag{4.25}$$

Window functions

Urban scenes are characterized on the one side by very high backscattering responses caused by man-made objects. In contrast, on the other side, roof areas, streets, or vegetation typically show low responses. To preserve the fine resolution of small-scale objects and suppress secondary sidelobes from strong corner echoes a combination of two filter windows in the processing is implemented. A rectangular window that is highly frequency-selective with a PSLR of -13 dB is combined with a hamming window that is less selective with a PSLR of -41 dB, [Oppenheim et al., 1999]. The raw data are processed with both windows, and the minimum of both window

functions is selected. As a result, the frequency selectivity of the rectangular window dominates up to the area of the first sidelobe, while from this area, the hamming window dominates and suppresses secondary sidelobes. As a result, the PSLR of this window combination reaches a PSLR of -13.9 dB with all secondary sidelobes below -41 dB.

4.2.3 Efficient focusing of different image geometries

The focusing of different image geometries as indicated in Fig. 4.4 shall be feasible due to the various acquisition strategies. In CSAR, this is realized by adapting the flat image plane as indicated in Fig. 4.4a. If additional relative height information δh or absolute height information H_0 is available or has been extracted, in a first step, the location of this information $f(\delta h) \rightarrow f(\vec{\mathbf{x}}_p)$ on the georeferenced focusing plane is derived. The corresponding pixel at the derived position is then adapted by $\vec{\mathbf{x}}_p = \vec{\mathbf{x}}_p + (0, 0, \delta h)'$.

Focusing on vertical planes is realized as indicated in Fig. 4.4b. The target's center position $\mathbf{P}_m$ - e.g., in the form of a GPS coordinate - and the mean orientation ϑ_f of the object in space are required as input parameters. Each pixel with coordinates (x_g, y_g) on the specified 2d image grid $\vec{\mathbf{E}} = (\vec{\mathbf{x}} - \vec{\mathbf{P}}_m) \cdot \vec{\mathbf{n}} = 0$ with constant pixel spacing δ_p is then mapped to a potential scatterer position $\vec{\mathbf{x}}_p$ in the 3d Cartesian coordinate system by

$$\begin{aligned} x_p &= P_x + \sin(\vartheta_f) \cdot (x_g - \frac{x_{max}}{2}) \cdot \delta_p \\ y_p &= P_y + \cos(\vartheta_f) \cdot (x_g - \frac{x_{max}}{2}) \cdot \delta_p \\ z_p &= P_z + y_g \cdot \delta_p, \qquad y_g \cdot \delta_p \leq d_h \end{aligned} \tag{4.26}$$

with d_l the length, d_h the height of the defined focusing plane and x_{max} corresponds to $\frac{d_l}{\delta_p}$.

The very high-resolution SAR focusing of the data in backprojection mode using two different window functions for each pixel is too computationally expensive to be processed sequentially on a single CPU in a reasonable time. In particular, if considered that the same data might be focused at different reference heights or further scene-specific information is included.

To realize an efficient processing, the illuminated area on the surface for each subaperture is separated into equidistant areas $\mathbf{X}_{e1}(\theta_1), \mathbf{X}_{e2}(\theta_2)$... with respect to the elevation angle as indicated

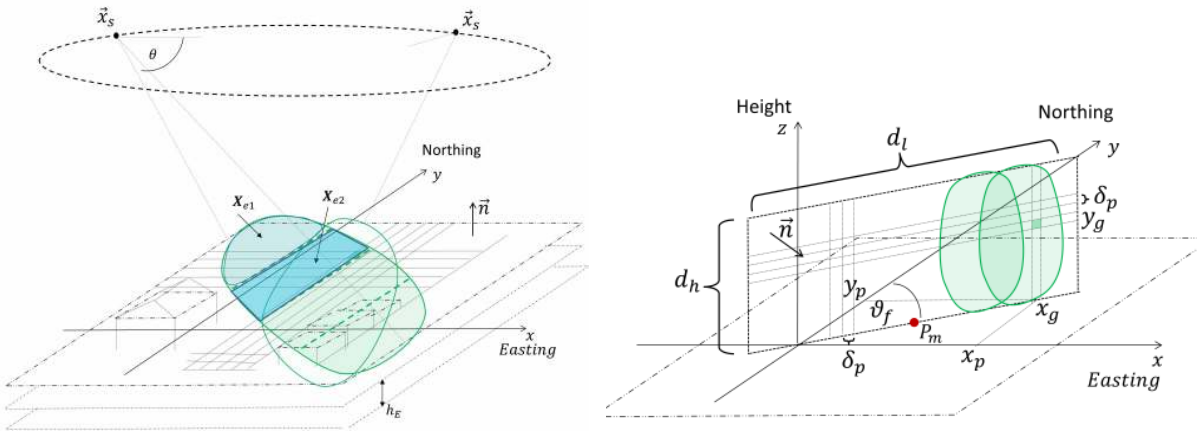

(a) (b)

Figure 4.4: Focusing of different image geometries. a) CSAR and street mapping geometry, b) vertical focusing geometry.

in Fig 4.4a. All pixel elements $\vec{\mathbf{x}}_p \in \mathbf{X}_{e,n}(\theta_n)$, n $\in \mathbb{N}$ are then stored in a n x 5 array $\mathbf{X}_{pA}$ that consists of the 3d coordinate $\vec{\mathbf{x}}_p$ and its corresponding image coordinate $\vec{x}_p$. With reference to the mean θ_n, a fixed aperture size φ_{az} is calculated for each sector that results in a fixed raw data matrix size of N x M, N,$M \in \mathbb{N}$. Thus, all elements of $\mathbf{X}_{pA}$ are processed in blocks with the same raw data matrix. This means that pixels at slightly different range distances are focused with slightly different angular intervals φ_{az}, but this effect is negligible. Range and azimuth focusing of $\mathbf{X}_{pA}$ are then performed highly parallel on multiple Graphic cards in CUDA, accelerating the processing by a factor of several hundred times.

4.3 Optimal coherent integration interval in urban scenes

This Section intends to answer the question of an optimal aspect integration interval for sub-aperture processing of urban scenes. Therefore, the maximum aspect interval shall be derived to allow coherent processing of high objects located above the flat plane image geometry and whose height is typically unknown in advance. This angular interval then also determines the spatial resolution of the image sequences.

4.3.1 Targets in the center of the circle

Considering the sensor is moved on an ideal trajectory, and the flight path can be measured accurately, then equation 4.1.2 specifies the obtained resolution of objects placed on the reference height. However, when using backprojection techniques, without using a dense digital surface model (DSM), the actual height of buildings, trees, or other objects in the scene is unknown. It can only be approximated by a digital elevation model (DEM) or a flat plane model. This brings in the question of an appropriate interval of $\varphi_{az} = \varphi_{max}$ for circular SAR data processing of urban areas, as even on perfect circular trajectories, the resolution of an isotropic scatterer will suffer due to the wrong height estimations.

Assuming a point target $\vec{\mathbf{x}}_p$ in Fig.4.5 at the center of the circle with a certain elevation dh above the image grid. In the easier case of linear platform motion, see Fig 4.5a, the 2d projection

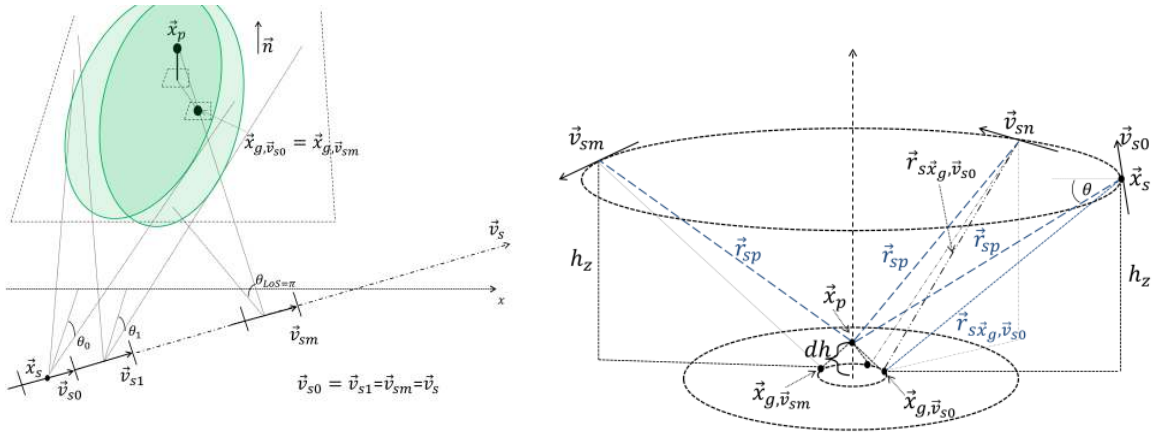

(a) (b)

Figure 4.5: Scatterer projection on the image grid in linear and circular SAR. Flight path and the actual direction of the sensor's motion is indicated with $\vec{\mathbf{v}}_s$. a) Stripmap or spotlight SAR geometry. Due to the linear motion, the projection on the image grid is fixed allowing a wide angular coherent integration of the target, b) CSAR geometry. Due to the non linear motion, the projection constantly changes which limits the coherent angular integration interval depending on the object's height and sensor's elevation angle.

$\vec{x}_g = \vec{x}_{grid}$ of this point on the image grid can be calculated by

$$\vec{x}_g = \begin{pmatrix} \vec{\mathbf{x}}_p \cdot \vec{e}_x \\ \vec{\mathbf{x}}_p \cdot \vec{e}_y \end{pmatrix} + \underbrace{dh \cdot \tan(\theta_{LoS=\pi}) \cdot \vec{u}}_{\vec{x}_{g,D}} \tag{4.27}$$

with $dh = \vec{\mathbf{x}}_p \cdot \vec{e}_z$, $\vec{u} = [cos(\varphi_v), sin(\varphi_v)]'$ and $\theta_{LoS=\pi}$ the elevation angle from sensor to the target at closest distance, which corresponds to a line of sight (LoS) angle of π. φ_v describes the angle of the platform's velocity vector $\angle(\vec{\mathbf{v}}_s)$. $\vec{x}_{g,D}$ is the displacement of the point target on the image grid referred to as foreshortening. The actual line of sight angle Ω_{LOS} is thereby defined by

$$\Omega_{LoS} = \arccos\left(\frac{\vec{\mathbf{v}}_s' \cdot \vec{\mathbf{r}}_{sp}}{|\vec{\mathbf{v}}_s| \cdot |\vec{\mathbf{r}}_{sp}|}\right) \tag{4.28}$$

with $\vec{\mathbf{r}}_{sp}$ the range vector from sensor to the target. Using backprojection techniques, the point $\vec{x}_g$ then perfectly satisfies the condition of expected slant range history and is well focused.
In the case of subaperture processing with $\vec{\mathbf{v}}_{s0} = \vec{\mathbf{v}}_{s1} = ... = \vec{\mathbf{v}}_{sm}$, the focused point at grid position $\vec{x}_{g,\vec{v}_s}$ will not vary or move on the image grid.

On non-linear or circular trajectories, equation 4.27 also holds for small angular integrations. However, φ_v is not constant and thus the phase error of the equivalent projection $\vec{\mathbf{x}}_{g,\vec{v}_{s0}}$ will steadily increase. Assuming a trajectory at constant height, the distance $\vec{\mathbf{r}}_{sp}$ from sensor $\vec{\mathbf{x}}_s$ to $\vec{\mathbf{x}}_p$ is constant. For defining an optimal φ_{max}, the distance error between target $\vec{\mathbf{x}}_p$ and its projection $\vec{\mathbf{x}}_{g,\vec{v}_{s0}}$ has to be evaluated with respect to the flight path. For achieving coherent processing of the data, phase errors should not exceed a predefined limit of $\lambda_x = \frac{\lambda}{10}$ m which results in the following equation:

$$2 \cdot \left| d_\varphi(\vec{\mathbf{r}}_{sp}) - d_\varphi(\vec{\mathbf{r}}_{sx_g,\vec{\mathbf{v}}_s}) \right| <= \lambda_x \tag{4.29}$$

where $d_\varphi(\vec{\mathbf{r}}_{sp})$ describes the length of the vector from sensor to $\vec{\mathbf{x}}_p$ at aspect angle φ, and $d_\varphi(\vec{\mathbf{r}}_{sx_g,\vec{\mathbf{v}}_s})$ the length of the vector from sensor to the projected point target with the subaperture's mean velocity vector $\vec{\mathbf{v}}_s$. As symmetry applies, we define the point $\vec{x}_{g,\vec{\mathbf{v}}_{s0}}$ at position $(x_{pg}, y_{pg}, 0)'$. At $\varphi_0 = 0$, this point has the same distance to the sensor as $d_\varphi(\vec{\mathbf{r}}_{sp}) = const.$ In the Cartesian coordinate system with flight radius R_m it can be derived

$$\begin{aligned} 2 \cdot \Big| &\sqrt{(R_m cos\varphi - x_{pg})^2 + (R_m sin\varphi - y_{pg})^2 + h_z^2} - \\ &\sqrt{(R_m cos\varphi_0 - x_{grid,\vec{v}_{s0}})^2 + (R_m sin\varphi_0 - y_{grid,\vec{v}_{s0}})^2 + h_z^2} \Big| <= \lambda_x, \varphi \in [0, \varphi_{lim}]. \end{aligned} \tag{4.30}$$

If we place the center of the coordinate system at the center of the circle we get $y_{pg} = 0$ and $\varphi_0 = 0$, yielding:

$$\begin{aligned} \Big| \sqrt{(R_m cos\varphi - x_{pg})^2 + (R_m sin\varphi)^2 + h_z^2} - \sqrt{(R_m - x_{pg})^2 + h_z^2} \Big| \\ <= \frac{1}{2}\lambda_x, \varphi \in [0, \varphi_{lim}]. \end{aligned} \tag{4.31}$$

As the second term is always smaller or equal to the first term, we can change the equation to:

$$\underbrace{\sqrt{(R_m cos\varphi - x_{pg})^2 + (R_m sin\varphi)^2 + h_z^2}}_{>0} <= \frac{1}{2}\underbrace{\lambda_x}_{>0} + \underbrace{\sqrt{(R_m - x_{pg})^2 + h_z^2}}_{>0} \tag{4.32}$$

and

$$R_m^2 + x_{pg}^2 - 2x_{pg}R_m cos(\varphi) <= \frac{1}{4}\lambda_x^2 + \lambda_x \cdot \sqrt{(R_m - x_{pg})^2 + h_z^2} + (R_m - x_{pg})^2. \tag{4.33}$$

The maximum angular integration intervall φ_{lim} can then be defined by

$$\varphi_{lim} = acos\left(1 - \frac{\frac{1}{4}\lambda_x^2 + \lambda_x \cdot \sqrt{(R_m - x_{pg})^2 + h_z^2}}{2R_m x_{pg}}\right). \tag{4.34}$$

Assuming a plane wavefront, x_{pg} can be replaced by θ and the target's elevation dh to

$$\varphi_{lim} = acos\left(1 - \frac{\frac{1}{4}\lambda_x^2 + \lambda_x \cdot \sqrt{(R_m - tan(\theta)dh)^2 + h_z^2}}{2R_m \cdot tan(\theta)dh}\right). \tag{4.35}$$

As symmetry applies, we finally end up with

$$\varphi_{max} = 2 \cdot \varphi_{lim}. \tag{4.36}$$

In contrast to Fig. 4.3, for high targets, the resolution is only improved up to φ_{max}, higher integration rapidly worsens it. Using typical CSAR geometries, Fig. 4.6 provides an overview of optimal integration intervals and the resulting maximum azimuth resolution for objects above/beneath the DEM or flat plane model at W-band. This roughly corresponds to a maximum resolution of about 12 cm, if we want to take into account that structures up to 10 m above the focusing plane, such as roofs or trees, should all be imaged without blurring or peak signal loss.

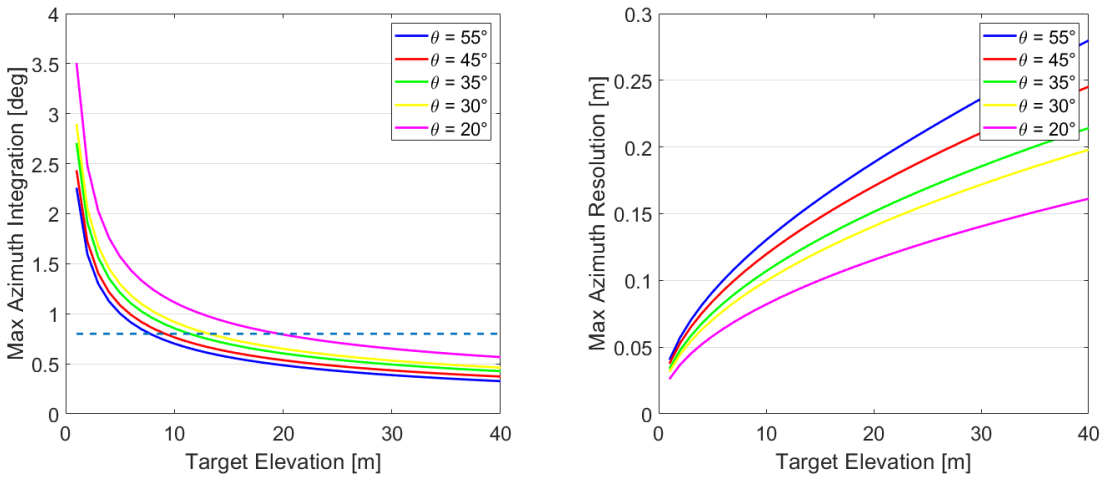

(a) (b)

Figure 4.6: Maximum coherent integration interval in CSAR as a function of object height and elevation angle in W-band. a) Comparison of true height of objects and maximum coherent azimuth integration interval for typical elevation angles. The aspect integration level of 0.8° for ViCSAR processing is marked with the dashed line, b) potential maximum achievable resolution of high objects without peak signal loss.

4.3.2 Targets outside the center of the circle

Considering the whole illuminated surface, the azimuth resolution of objects not placed in the geometrical center differs due to a constantly changing elevation angle and the object's distance to the circle center. With a constant angular processing interval, objects on the circle's border might be blurred more or less depending on the sensor's position. This effect is illustrated in Fig. 4.7, where the coherent azimuth integration intervals of high objects at $dh = 10$ m on different positions on the illuminated area are compared.

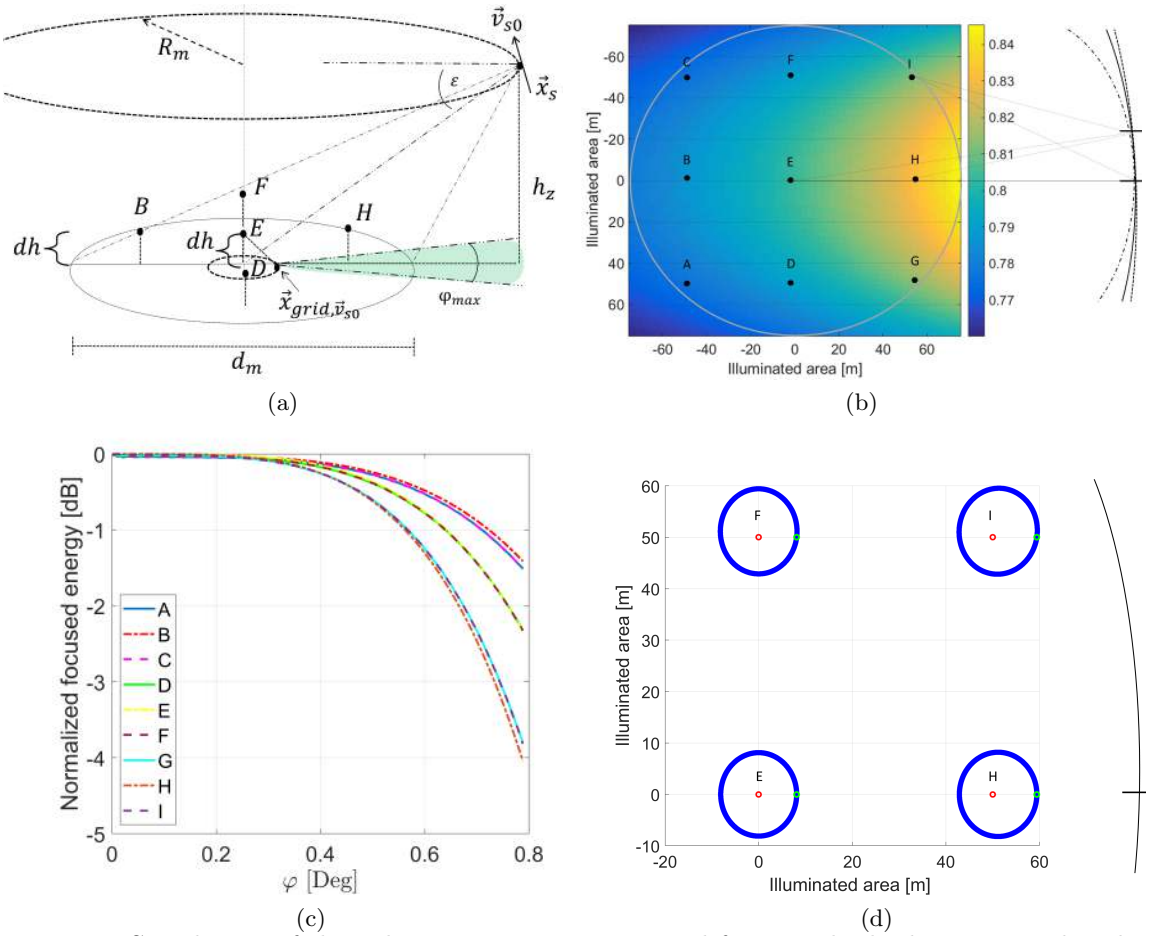

Figure 4.7: Simulation of the coherent processing interval for 10 m high objects not placed in the circle center. a) Data acquisition geometry with position of selected targets at 10 m height. d_m the diameter of the 360° illuminable area, b) heatmap [in Deg] of simulated integration interval φ_{max} for $dh = 10$ m high targets. Parameters are $\theta = 40°$, $h_z = 300$ m, $R_m = 360$ m and $\lambda = 3.2$ mm, c) normalized focused energy of targets A-I as a function of aspect integration. At $\varphi_{lim} = 0.4°$, coherency starts to degrade, d) 360° flat plane projection of targets E,F,I,H. In red, the true position of the target, in blue, its projection in form of ellipses. Green marks the first projection with start $\vec{\mathbf{x}}_s$. Only point E projects as a circle with the platform's angular velocity.

In a typical scenario, the heatmap in Fig. 4.7b indicates that the interval φ_{max} for all objects will vary by approximately 10% which is tolerable. While Fig. 4.6 indicates a higher integration at lower elevation angles, Fig. 4.7b reveals that this effect can be offset in areas at closer range to the moving sensor. This is due to the fact that the projection of high objects not placed in the center will have the form of ellipses as simulated in Fig. 4.7d for the points 'E,F,H,I'. Compared to the center position, the actual circular path of the platform is too large for these objects; the movement in the same angular interval becomes more linear, which improves the coherent integration interval. The projection in the type of ellipses also means that the angular velocity of the scatterers' movement on the image plane is different for all scatterers. The closer the object is to the sensor on the circular path, the faster its angular velocity.

To what extent a larger angular integration $> \varphi_{max}$ effects the normalized focused energy of a target is simulated in Fig. 4.7c. Observable is that the coherency starts to degrade at $\varphi_{lim} = \frac{\varphi_{max}}{2} \approx 0.4°$ and the peak energy will drop from -0.15 dB at φ_{lim} to -2.5 dB or -4 dB at $2 \cdot \varphi_{max}$.

4.4 Registration of subaperture CSAR images to the georeferenced image stack

A joint representation of the individual subaperture images processed from different aspects requires a form of image registration. This is also essential for extracting aspect dependent information in a further processing step, see Chapter 5.

By assuming an exact trajectory reconstruction, image registration can be realized straightforward in backprojection processing as the focusing is performed in the desired image geometry. Considering a flat plane with $E = (\vec{\mathbf{x}} - (0,0,H_0)') \cdot \vec{\mathbf{n}}$ with $\vec{\mathbf{n}} = (0,0,1)'$ and H_0 the reference height. As the continuous calculation of the sensor's trajectory $\vec{\mathbf{x}}_s$ with start position $\vec{\mathbf{x}}_{s0} = (0,0,h_z(T=0))$ is also carried out in the same geometry, a GPS coordinate can be assigned to each image pixel $\vec{\mathbf{x}}_p$. This allows the scene to be imaged in the the aircraft's GPS/INS reference system, which is WGS84.

In ViCSAR mode, the whole trajectory is processed in equidistant steps defined by choice of φ_{az}. With $n, m \in \mathbb{N}$, the individual subapertures at the platform's center position $\vec{\mathbf{x}}_s(T)$ are marked in colors, the aspect integration interval is indicated with φ_{max}. For registering the consecutive images, the first subaperture image as a reference image is focused in the flat plane geometry with a fixed pixel spacing δ_p as indicated in Fig 4.8. The image is then defined as the 'master image' and is used as a reference for the following images. Since the sensor also moves continuously in the initial geometry, all subsequent images are focused on the same geometry. The size of the image plane ranging from $(x_{min}, ..., x_{max}; y_{min}, ..., y_{max})$ is continuously adapted to match for every type of flight trajectory and illumination. Enlarging the plane in integer multiplies of $u \cdot \delta_p$, $u \in \mathbb{N}$, depending on the subapertures' illumination, guarantees that no interpolation is needed when fusing the single images to a 3d image stack as indicated in Fig. 4.8b. The procedure can thus support circular SAR, stripmap, or spotlight SAR geometries. Geocoding the image sequence defines the 3d image stack in dimensions of easting, northing, and aspect angle.

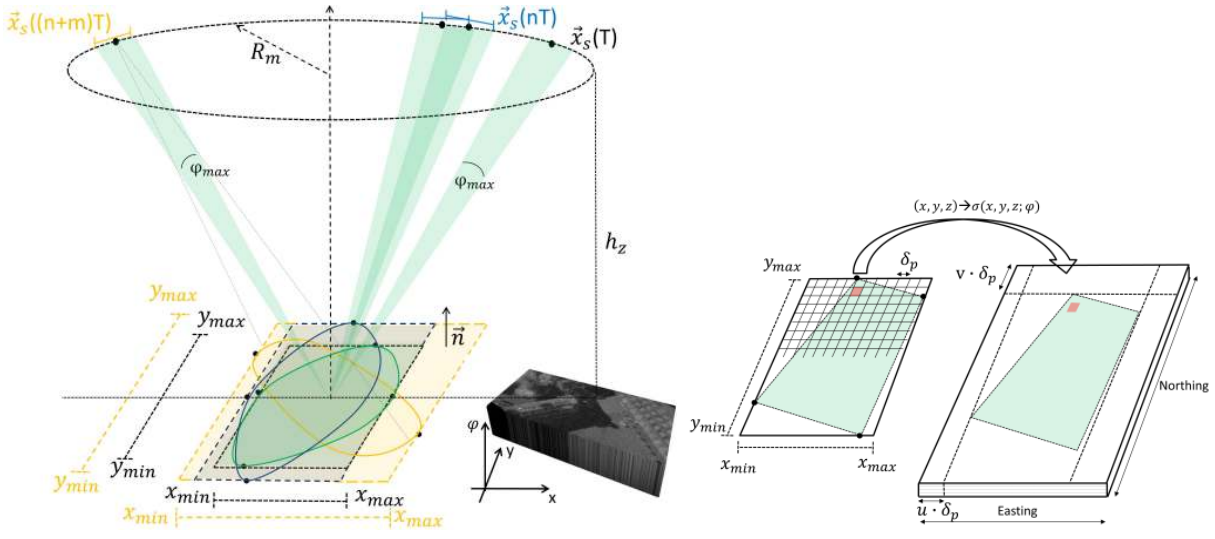

Figure 4.8: Visualization of the CSAR image stack generation. a) Subaperture images of different aspects are focused in the same image geometry. The size of the focusing plane is continuously adapted to the illuminated spot, b) registration of images in a 3d Cartesian image stack. The final image sequence reveals the scene in equidistant aspect angle spacing.

Given an object placed at focusing height at $\vec{\mathbf{x}}_p$, its complete aspect dependent backscattering σ and phase information ϕ is mapped into one column of the created 3d image stack. It holds:

$$\begin{aligned} &\vec{\mathbf{x}}_p \rightarrow (\vec{x}_p, \sigma_{1,\ldots,n}, \phi_{1,\ldots,n}, \varphi_{1,\ldots,n}), \text{ for CSAR mode and} \\ &\vec{\mathbf{x}}_p \rightarrow (\vec{x}_p, \sigma_1, \phi_1, \varphi_1), \text{ for linear SAR mode.} \end{aligned} \tag{4.37}$$

4.4.1 ViCSAR subaperture processing

The generated, geocoded subaperture image sequences can be visualized in a continuous image stream in a concept closely related to Video-Stripmap SAR (ViSAR). Generating a dynamic situation assessment of an urban scene shall, on one side, provide high resolution but also a short illumination time. The shorter the illumination time for each subaperture, the higher the possibility of detecting dynamic events in the otherwise smeared scene. Gaining an optimal insight into challenging urban areas such as narrow streets between street canyons is also related. A good trade-off of these partially contradicting requirements shall be derived.

The illumination time $T_{\varphi_{az}}$ of each subaperture is defined by $T_{\varphi_{az}} = \frac{\varphi_{az} \cdot R_m}{|\vec{\mathbf{v}}_s|}$. Applying φ_{max} as the angular size of the aperture and knowing Section 3.2, this corresponds to $T_{\varphi_{az}} < 0.25\,\text{s}$. This provides a resolution of the images in the order of 12 cm at a short illumination time and should therefore serve as a good compromise.

Choice of the aperture overlap factor

A further increase of the potential frame rate can be achieved by processing the subapertures with a high overlap factor. This means that the spectral information of the n-th subaperture comprises a high degree of the spectral information from the (n-1)-th aperture as indicated in Fig. 4.9. This technique is intended to prevent targets above the reference plane from moving too

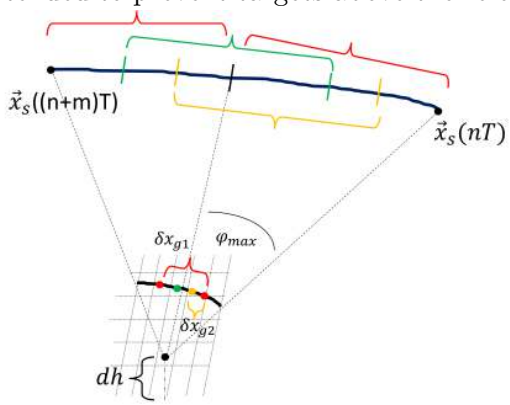

Figure 4.9: Influence of scatterer projection by subaperture processing with a high overlap factor. Subsequently the red, orange and green aperture is processed with constant φ_{az}. δx_{g2} is then in a subpixel order.

quickly on the imaging plane, which gives a rather disturbing impression. From Section 4.3, the projection of a high roof scatterer at height dh will follow an arc-like course on the image plane. The distance δx_{g1} of the projection between two subapertures can be derived to

$$\delta x_g = \varphi_{max} \cdot \tan\theta \cdot dh \tag{4.38}$$

that is indicated by the red points in Fig. 4.9. If δx_{g1} is larger than the pixel size, the CSAR video seems unsteady, the scatterer's projection 'jumps' from pixel to pixel in the sequence. Applying a high overlap factor of 60-80% ensures that δx_{g2} decreases. The movement of high scatterers on the image plane becomes feasible on a subpixel scale that results in a more smooth visualization. Further, dynamic events are better observable and evaluable in later processing steps.

5 Extraction of 3d point clouds in urban areas

This Chapter presents a new framework to extract 3d information from the single-pass and single-channel CSAR data. The focus is both on the precise 3d evaluation of very small, detached objects and more prominent buildings in urban areas. In Section 5.1, a method to extract 3d scene information of individual objects by non-coherently evaluating CSAR amplitude image sequences is presented. An answer is given to the question of how accurate the movement of objects above the focusing plane and its energy flow in CSAR amplitude image sequences can be evaluated in terms of 3d extraction. The main focus is on the proposed methods in Section 5.2 that generate a global 3d point cloud by extracting 3d information over larger coherent apertures and subsequent fusion, thereby revealing the urban scene from 360°. The generated 3d scene information is exploited in a final iteration to propose a processing chain that optimizes the CSAR focusing process to a specific scene. It allows the fusion of different views in a single SAR image in Section 5.3.

5.1 3d target estimation based on single object tracking

The deterministic projection of scatterers on the flat image plane shall be exploited to extract height information. Since the aspect visibility or the angular persistence of objects in urban scenes is relatively small, 3d extraction has to be realized in a finite aspect interval.

5.1.1 Strategy and signal model

Considering a dominant scatterer model and let $g \in \mathbb{C}^{M\times N}$ be the processed CSAR subaperture image with a number of isolated scatterers $P \in \mathbb{N} > 0$, an image sequence $g_v[m,n], v \in \mathbb{N} > 0$ consisting of objects at arbitrary height can be modeled as

$$\begin{aligned} g_v[m,n] = \sum_{p=1}^{P} \int_{\frac{(v-1)}{u}\varphi_{max}}^{(1+\frac{v-1}{u})\varphi_{max}} \alpha_p(\varphi)\cdot e^{j2kr_p(\varphi)}d\varphi \\ \cdot \delta[m - m_p + x_{g,D}\cos(\varphi_m), n - n_p + x_{g,D}\sin(\varphi_m)], \end{aligned} \tag{5.1}$$

if we further apply the constraints of equation 4.36 with $\varphi_{max} \in [-\varphi_{lim}, \varphi_{lim}]$. $\alpha_p(\varphi)$ is the object's reflectivity, k the wavenumber, $r_p(\varphi) = |\vec{\mathbf{x}}_p - \vec{\mathbf{x}}_s(\varphi)|$ and $\delta(m,n)$ the discrete unit impulse signal at image location $[m_p, n_p]$. Further, $u \in \mathbb{N} > 0$ indicates the overlap factor of the subapertures, $x_{g,D}$ the object's displacement on the image grid $[m,n]$, and φ_m the mean aspect angle of the synthetic subaperture. Applying a high overlap factor in W-band, the displacement change in the image sequence can be chosen to be in a subpixel order of magnitude.

In contrast to typical radargrammetric methods, which try to exploit measurements from different viewing positions by cross-correlating image patterns and find stereo matches [Palm

et al., 2012; Schmitt & Stilla, 2014b; Zhang et al., 2018], the proposed method shall locally track the scatterers' backscattering energy over the visible angular section. The tracking is relatively robust to the anisotropic behavior of objects since the intensity I(x,y) of the pixels may vary, but the relative intensity maximum in each frame will be located at the actual projected position $f(\vec{\mathbf{x}}_p)$. Depending on the pixel spacing and the tracking window size, the Dirac or better sinc sequence from equation 5.1 may then be interpreted as a continuous energy stream of individual isolated scatterers, or can be considered as an accumulation of point targets that belong to a respective object like volume scatterers such as trees. These characteristics are similar to the optical flow concept that describes a vector field that represents the direction and distance of movement between corresponding gray values of an image sequence. Each vector can be interpreted as the length of the path covered by a pixel $\vec{x}$ during a specific time interval. Knowing both the pixel distance covered and the observer's own movement allows 3d extraction given specific model restrictions. Algorithms based on optical flow are, however, based on the brightness constancy equation that requires constant pixel intensity and constant illumination over subsequent frames [Barron et al., 1994]. Both assumptions are problematic concerning SAR images.

However, the movement of isolated scatterers or whole objects with moderate signal to clutter ratio (SCR) can still be detected and tracked in subaperture CSAR image sequences. Given the model equation 5.1 and assuming the local intensity center $\vec{x}_{sf}(\varphi)$ at location $[m_p, n_p]$ is associated with the projected position of a valid scatterer, by knowing the imaging geometry and assuming that the object's real position is static, we can derive its 3d location $\vec{\mathbf{x}}_p = f(\vec{x}_{sf}(\varphi_s))$ by a radargrammetric function f over the tracked aspect interval $\varphi_s \in (\varphi_{start}, \varphi_{end})$. 3d extraction shall then be based on evaluating the tracked energy flow compared to the theoretically expected movement, which is derived from seed point hypotheses as indicated in Fig. 5.1.

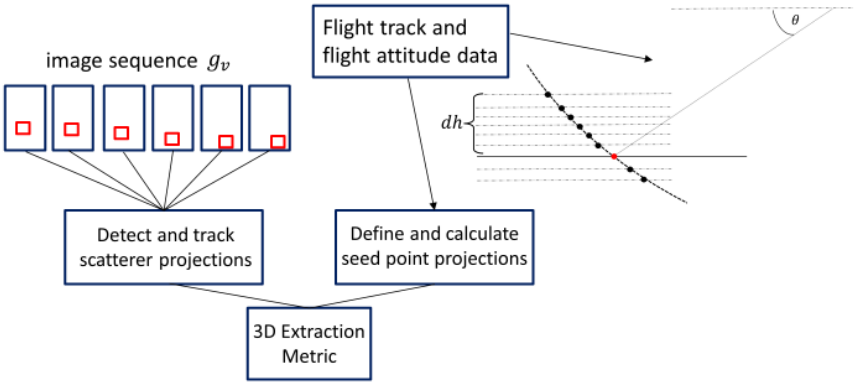

Figure 5.1: Synoptic of the non-coherent 3d extraction.

5.1.2 Deriving the precise projection of the scatterer

Obtaining 3d information from the tracked projections requires an exact derivation of the projection geometry. In Chapter 4.3, the projection $\vec{x}_g$ of a valid scatterer $\vec{\mathbf{x}}_p$ assuming an ideal circular trajectory on a constant height h_z is derived by

$$\vec{x}_g = \begin{pmatrix} \vec{\mathbf{x}}_p \cdot \vec{e}_x \\ \vec{\mathbf{x}}_p \cdot \vec{e}_y \end{pmatrix} + \underbrace{dh \cdot \tan(\theta_{LoS=\pi}) \cdot \vec{u}}_{\vec{x}_{g,D}}. \tag{5.2}$$

Due to platform drift or antenna squinting, the sensor might not pass the target perpendicularly while forming a synthetic aperture. Estimating $\vec{x}_g$ with the mean elevation angle θ is indeed too

inaccurate at very high resolution. Knowing that the angular integration φ_{az} in CSAR mode is small, the elevation angle $\theta_{LoS=\pi} = \theta_\pi$ can be derived by the smallest distance from the target to the projected velocity vector $\vec{\mathbf{v}}_s$ which yields

$$\vec{x}_g = \begin{pmatrix} \vec{\mathbf{x}}_p \cdot \vec{\mathbf{e}}_x \\ \vec{\mathbf{x}}_p \cdot \vec{\mathbf{e}}_y \end{pmatrix} + dh \cdot \tan(\arcsin\left(\frac{(h_z - dh) \cdot \|\vec{\mathbf{v}}_s\|}{\|\vec{\mathbf{v}}_s \times (\vec{\mathbf{x}}_p - \vec{\mathbf{x}}_s)\|}\right)) \cdot \vec{u} \tag{5.3}$$

with $dh = \vec{\mathbf{x}}_p \cdot \vec{\mathbf{e}}_z$. This assumes a planar wavefront at the target, resulting in projections that are several centimeters or a few ten centimeters too short. A better derivation of θ_π for very high-resolution data is to use the mean of the calculated elevation angles between target and reference height by

$$\theta_\pi = \frac{1}{2}\left(\arcsin\left(\frac{(h_z - dh) \cdot \|\vec{\mathbf{v}}_s\|}{\|\vec{\mathbf{v}}_s \times (\vec{\mathbf{x}}_p - \vec{\mathbf{x}}_s)\|}\right) + \arcsin\left(\frac{h_z \cdot \|\vec{\mathbf{v}}_s\|}{\|\vec{\mathbf{v}}_s \times (\vec{\mathbf{x}}_p - \vec{\mathbf{x}}_s)\|}\right)\right). \tag{5.4}$$

For sufficiently small subapertures in CSAR processing, the platform's velocity vector $\vec{\mathbf{v}}_s(t)$ can be approximated to be linear ($\vec{\mathbf{v}}_s \approx \text{mean}(\vec{\mathbf{v}}_s(t))$) and thus equation 5.3 holds. However, more critical is the assumption that the platform moves at constant height h_z when considering the unstable flight platform and the circular trajectory, see Fig. 5.2. To account for a platform's upward or downward component with $\vec{\mathbf{v}}_s \cdot \vec{\mathbf{e}}_z \neq 0$ the additional displacement of the object's projection has to be compensated when it comes to high-resolution imaging. By deriving the angle of intersection Φ between $\vec{\mathbf{v}}_s$ and the flat plane's normal vector $\vec{\mathbf{n}}$ with

$$\Phi = \arcsin\left(\frac{\vec{\mathbf{n}} \cdot \vec{\mathbf{v}}_s}{|\vec{\mathbf{n}}| \cdot |\vec{\mathbf{v}}_s|}\right) \tag{5.5}$$

the additional displacement shift $\vec{x}_{g,d}$ can be approximated by

$$\vec{x}_{g,d} = dh \cdot \tan(\Phi) \cdot \vec{w} \tag{5.6}$$

with $\vec{w} = [\sin(\varphi), \cos(\varphi)]'$. The absolute position of the point target $\vec{\mathbf{x}}_p$ projected on the flat plane image grid at each subaperture is then derived by

$$\vec{x}_g = \begin{pmatrix} \vec{\mathbf{x}}_p \cdot \vec{\mathbf{e}}_x \\ \vec{\mathbf{x}}_p \cdot \vec{\mathbf{e}}_y \end{pmatrix} + dh \cdot \tan(\theta_\pi) \cdot \vec{u} + dh \cdot \tan(\Phi) \cdot \vec{w}. \tag{5.7}$$

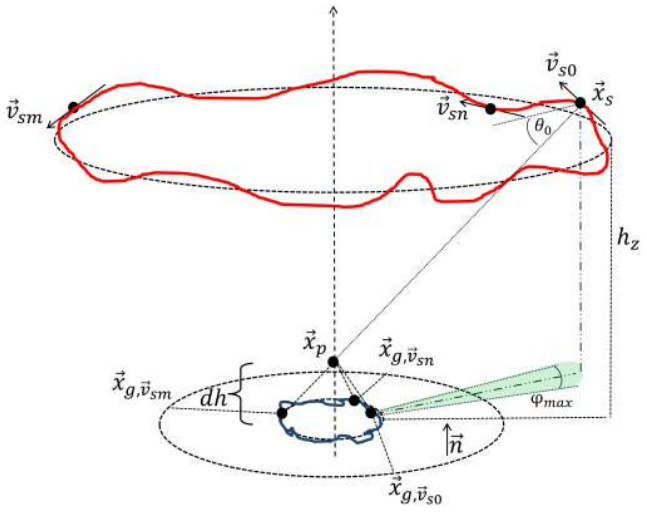

Figure 5.2: Projection of objects on flat plane geometry in real CSAR flight tracks. The sensor's trajectory is marked red. Depending on $\theta(\varphi)$ and $\vec{\mathbf{v}}_s(\varphi)$, the projection (blue) varies for each subaperture. At constant height, the projection follows the circular path of the moving sensor in the form of a circle (center) or ellipse. With up- or downward velocity components, the projection partially runs faster or even counterclockwise to the sensor's rotation.

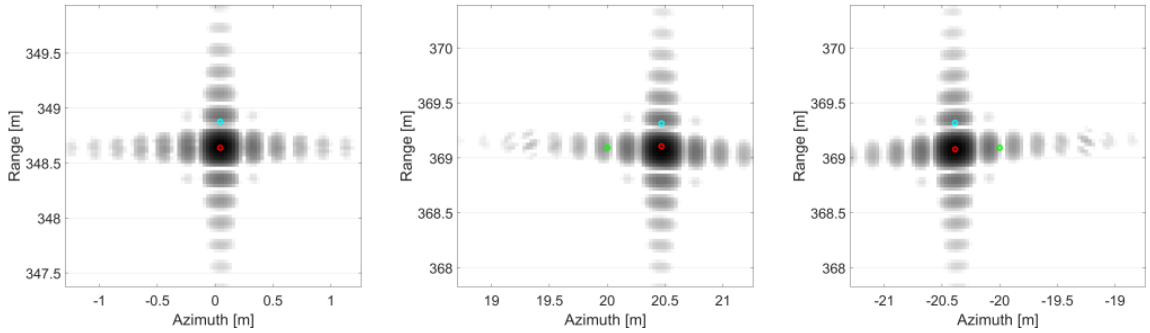

(a) (b) (c)

Figure 5.3: Focused scatterer in CSAR geometry with parameters $R_m = 357$m, $h_z = 300$m, $dh = 10$m, $B = 1$ GHz, $\varphi_{az} = 0.8°$ and $\vec{\mathbf{x}}_s$ at $(0, 0, h_z)$. Calculated projections in different colors. Green neglects up/downward components, cyan is planar wavefront assumption and red is proposed calculation of projection. a) $\vec{\mathbf{x}}_p$ in the center at $(0, R_m, dh)'$, $\vec{\mathbf{v}}_s\vec{\mathbf{e}}_z = 0\ \frac{m}{s}$, b) $\vec{\mathbf{x}}_p = (20, R_m + 20, dh)'$, $\vec{\mathbf{v}}_s\vec{\mathbf{e}}_z = 1.5\ \frac{m}{s}$, c) $\vec{\mathbf{x}}_p = (-20, R_m + 20, dh)'$, $\vec{\mathbf{v}}_s\vec{\mathbf{e}}_z = -1.5\ \frac{m}{s}$.

For larger integration intervals $> \varphi_{max}$, the projection $\vec{x}_g$ will no longer be a fixed point but can be modeled as a set of smeared points on the image grid, which is further addressed in Chapter 5.2. The extension of the displacement calculation with $\vec{\mathbf{v}}_s \cdot \vec{\mathbf{e}}_z$ is crucial when evaluating very high-resolution data as the upward or downward component especially on circular trajectories is present, see Fig. 5.3. With $\vec{\mathbf{v}}_s \cdot \vec{\mathbf{e}}_z = 0$, the projection of objects above the reference height in the center of the circle moves at the same angular velocity ω on a circular path as the moving platform. With fast sink rates ($\vec{\mathbf{v}}_s \cdot \vec{\mathbf{e}}_z < 0$), the projection can run partially counterclockwise to the direction of the moving platform, see Fig. 4.5, while with climb rates, the projection moves with higher angular velocity. Objects not placed in the center of the circle will move on ellipses with varying ω dependent on their positions and the current sensor position, see Fig. 4.7d.

5.1.3 Non-coherent energy tracking and height decision process

The method of non-coherent tracking of backscattering energy requires valid scatterers that can be tracked over a sufficiently large aspect interval. Therefore, only potential scatterers of interest that pass a radiometric criterion are evaluated. With a m x m pixel search matrix, the local mean intensity I_m is compared to a threshold η that is derived by the image's mean noise level. Objects that pass the threshold are handled as potential valid scatterer positions with $w = 1$. The decision criterion is derived by

$$w(I_m(\varphi_{start})) = \frac{1}{m^2} \sum_{x-\frac{m}{2}}^{x+\frac{m}{2}} \sum_{y-\frac{m}{2}}^{y+\frac{m}{2}} I(\varphi_{start}; x, y) \begin{cases} 0 & w \leq \eta \\ 1 & \text{else.} \end{cases} \tag{5.8}$$

For each valid scatterer position $\vec{x}_g$, a set of possible absolute 3d positions $\vec{\mathbf{x}}_p(dh)$ with step size Δh are derived that are referred to as seed points, see Fig. 5.1. Given the flight path of the actual subaperture, these seed points all project into the same image coordinate $\vec{x}_g$. From equation 5.7, it holds

$$\begin{aligned} \vec{x}_p(dh) &= \vec{x}_g \cdot \vec{e}_{xy} - dh \cdot \tan(\theta_\pi) \cdot \vec{u} - dh \cdot \tan(\Phi) \cdot \vec{w}, \qquad dh \in [0, h_{max}] \\ \Rightarrow \vec{\mathbf{x}}_p(dh) &= [\vec{x}_p(dh) \cdot \vec{e}_x, \vec{x}_p(dh) \cdot \vec{e}_y, 0]' + dh \cdot \vec{\mathbf{e}}_z. \end{aligned} \tag{5.9}$$

Prior knowledge about the potential maximum height h_{max} of scatterers in the scene is beneficial to minimize the number of seed points. Tracking of the scatterer's displacement in the interval

$\varphi_s \in [\varphi_{start}, \varphi_{end}]$ is evaluated by the movement of the backscattering energy intensity in the image sequence g_v. The energy or intensity center $\vec{x}_{sf}(\varphi)$ of each frame in the local search matrix is derived by

$$x_{sf}(\varphi) = \frac{\sum_x \sum_y (x \cdot I(\varphi; x, y))}{\sum_{x,y} I(\varphi; x, y)}, \quad y_{sf}(\varphi) = \frac{\sum_x \sum_y (y \cdot I(\varphi; x, y))}{\sum_{x,y} I(\varphi; x, y)} \tag{5.10}$$

that specifies the geometric center of the intensity distribution, and allows to measure a shift in the subpixel order. In particular, the initial absolute position $\vec{x}_{sf}(\varphi_0)$ on the image grid has to be calibrated in a subpixel order.

The tracked intensity displacement history $\vec{x}_{sf}(\varphi_1, ..., \varphi_n)$ over the entire sequence g_v with $dh \in [0, h_{max}]$ is then matched with the computed ideal displacement history of the various seed points from equation 5.9 by a L1 norm minimization with

$$H_{\vec{\mathbf{x}}_p} = arg\left[\min_{dh}\left(\sum_{\varphi_s}\left|x_{sf}(\varphi) - f(\vec{\mathbf{x}}_p(\varphi, dh)) \cdot \vec{e}_x\right| + \left|y_{sf}(\varphi) - f(\vec{\mathbf{x}}_p(\varphi, dh)) \cdot \vec{e}_y\right|\right)\right] < \lambda_{xy}. \tag{5.11}$$

Again, $f(\vec{\mathbf{x}}_p(\varphi, dh)) = \vec{x}_g(\varphi, dh)$ describes the position of each potential 3d seed point at aspect view φ on the image grid by applying equation 5.7. $H_{\vec{\mathbf{x}}_p}$ then selects the seed point position $\vec{\mathbf{x}}_p(dh)$ with the most similar calculated displacement trajectory (minimum displacement distance) to the tracked intensity function by a L1 norm. The term λ_{xy} guarantees the selection of objects only below a defined threshold if, for any reason, the subsequent SAR images are considerably blurred. Objects whose tracking history does not match those of the seed points by a more considerable distance than λ_{xy} are also filtered by the threshold.
To further avoid false target estimations, the criterion can be modified by separating both terms within the sum. It follows

$$\begin{aligned} H_{\vec{\mathbf{x}}_p,1} &= arg\left[\min_{dh}\left(\sum_{\varphi_s}\left|x_{sf}(\varphi) - f(\vec{\mathbf{x}}_p(\varphi, dh)) \cdot \vec{e}_x\right|\right)\right] < \lambda_{xx} \\ H_{\vec{\mathbf{x}}_p,2} &= arg\left[\min_{dh}\left(\sum_{\varphi_s}\left|y_{sf}(\varphi) - f(\vec{\mathbf{x}}_p(\varphi, dh)) \cdot \vec{e}_y\right|\right)\right] < \lambda_{yy} \\ \left|H_{\vec{\mathbf{x}}_p,1} - H_{\vec{\mathbf{x}}_p,2}\right| &< \epsilon \begin{cases} \text{valid} \\ \text{else} \end{cases} \end{aligned} \tag{5.12}$$

with $\epsilon = l \cdot dh$, $l \in \mathbb{N}$, l small and $\lambda_{xx}, \lambda_{yy}$ as threshold. This criterion is stricter as both the x-axis, and y-axis displacement movements are analyzed separately. The extracted 3d positions $\vec{\mathbf{x}}_p(H_{\vec{\mathbf{x}}_p})$ from each sequence can then be fused to a georeferenced point cloud alongside with the information from which aspect angle interval the object was visible.

5.1.4 Deriving the minimum aspect interval for the required height accuracy

To evaluate an optimal tracking aspect interval φ_s in terms of height accuracy, the response of $H_{\vec{\mathbf{x}}_p}(\varphi)$ is analyzed. At the start of the tracking at $\varphi_{start} = \varphi_0 = 0$, all potential 3d seed points $(\vec{\mathbf{x}}_{p0}, ..., \vec{\mathbf{x}}_{pn})$ project into the same 2d imaging grid position $\vec{x}_{g,\vec{v}_{s0}}$, see Fig. 5.4. With increasing aspect variation, the backscattering energy will slowly move through adjacent pixels as indicated in Fig. 5.4b, while the main energy of an object at focus height will be fixed at the initial pixel position, see Fig. 5.4c. Thus, the minimum size of the aspect angle interval causing a measurable tracking difference between two potential seed points that leads to a height resolution of δh is of interest. Considering an ideal circular flight at constant height h_z and let $E = f\left(H_{\vec{\mathbf{x}}_p}\right)$ be the tracking error filter response before minimization, see equation 5.11. With $\varphi < \varphi_{end} = \varphi_e < 90°$,

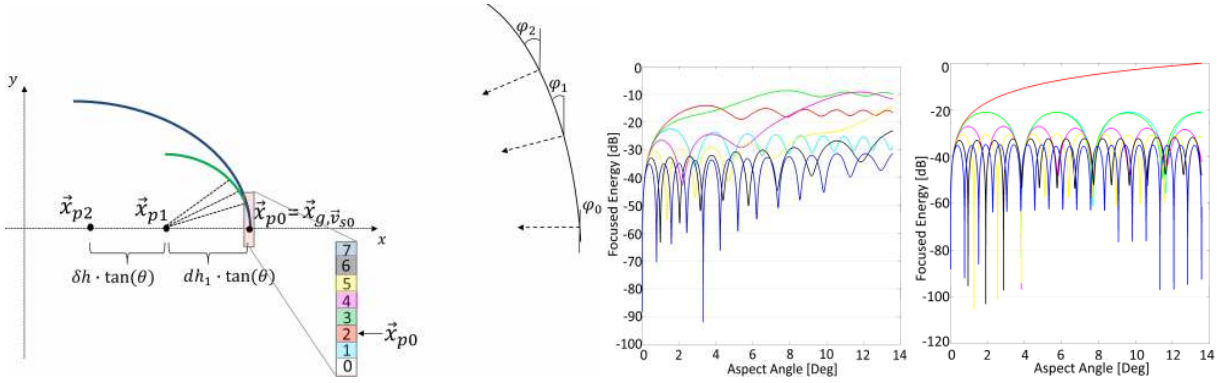

(a) (b) (c)

Figure 5.4: Projection and energy distribution of different seed points on adjacent image pixels in CSAR geometry. a) Top view of 3 potential seed points ($\vec{\mathbf{x}}_{p0}, ..., \vec{\mathbf{x}}_{p2}$) and their projection $\vec{x}_{g,\vec{v}_{s0}}$ at $\varphi = 0$. Different projection courses for $\vec{x}_{p2}$ in blue and $\vec{x}_{p1}$ in green. Red column indicates neighboring pixels on the image grid with $\vec{x}_{p0}$ centered at position 2 (red), b) simulated focused energy distribution of the pixels 1-7 of a) as a function of aspect integration in corresponding colors. Data corresponds to $\vec{x}_{p1}$ at a height of 0.5 m above the reference plane with its projection at φ_0 starting in pixel 2. $\delta_p = 3\,\text{cm}$, $\theta = 40°$, $f_0 = 94\,\text{GHz}$ and $B = 1\,\text{GHz}$. The energy flow through the different pixels and the appearance of high azimuth sidelobes can be observed. The center of energy moves upwards (from pixel 2 to 6) while increasing the aspect integration, c) comparison with an object at position $\vec{x}_{p0}$ placed at the reference height. The energy center is fixed and concentrated at pixel position 2 (red).

the tracking distance difference for two adjacent seed points $\vec{\mathbf{x}}_{p1}, \vec{\mathbf{x}}_{p2}$ with altimetric difference $\delta h = dh_2 - dh_1 > 0$ can be derived by

$$\begin{aligned}
\Delta E(\delta h) &= \sum_{\varphi=\varphi_0}^{\varphi_e} \Big|\tan(\theta)\cdot(dh_1\cos(\varphi) - dh_2\cos(\varphi) + \delta h)\Big| + \Big|\tan(\theta)\cdot(dh_1\sin(\varphi) - dh_2\sin(\varphi))\Big| \\
&= \sum_{\varphi=\varphi_0}^{\varphi_e} \Big|\tan(\theta)\cdot\underbrace{(-\delta h\cdot\cos(\varphi) + \delta h)}_{\geq 0}\Big| + \Big|\tan(\theta)\cdot\underbrace{(-\delta h\cdot\sin(\varphi))}_{\leq 0}\Big| \\
&= \sum_{\varphi=\varphi_0}^{\varphi_e} \delta h\cdot\tan(\theta)(\sin(\varphi) - \cos(\varphi) + 1) = \sum_{\varphi=\varphi_0}^{\varphi_e} \delta h\cdot\tan(\theta)(1 + \sqrt{2}\sin(\varphi - \frac{\pi}{4})).
\end{aligned} \tag{5.13}$$

The tracking difference increases nearly linearly for each angular aspect step that leads to a filter response with quadratic gradient for small φ_s, see equation 5.14. Wide angular tracking is therefore essential to achieve fine height resolution. For arbitrarily selectable angular step sizes $\frac{\varphi'}{n}$, $(n, \varphi' \in \mathbb{N})$, and small φ_s, we can approximate $\Delta E(\delta h)$ as

$$\Delta E(\delta h) \approx \frac{1}{n}\cdot\delta h\cdot\tan(\theta)\cdot\frac{\pi}{180}\cdot\frac{n\varphi_e(n\varphi_e+1)}{2}. \tag{5.14}$$

In practice, neither the angular step size can be chosen arbitrarily small, nor the exact location of the scatterer's main energy on the image grid (subpixel accuracy, resolution, and noise effects) can be measured. Thus, even the filter response of the tracked energy of a scatterer placed precisely on the focusing height will show slight position drifts resulting in $\Delta E \neq 0$. For determining a suitable aspect interval φ_s, the measuring accuracy of objects in subaperture images has to be

further estimated. From Bamler & Eineder [2005], we know that the differential shift error σ_s or the measuring accuracy in units of resolution elements for a point scatterer in incoherent clutter is a function of the SCR with

$$\sigma_s = \frac{\sqrt{3}}{\pi} \cdot \frac{1}{\sqrt{SCR}}. \tag{5.15}$$

As σ_s is derived by a correlation of a complex image, the equation is modified by a factor of $\sqrt{2}$ to account for the fact that amplitude images are used. From equation 5.13, the minimum aspect interval φ_e can then be determined that is theoretically needed to retrieve height information. Filter responses from aspects $> \varphi_e$ will significantly contribute to the height resolution. With δ_{xy} as the processed ground resolution, it follows

$$\begin{aligned} &\delta h \cdot \tan(\theta)(1 + \sqrt{2}\sin(\varphi_e - \frac{\pi}{4})) \geq \sqrt{2} \cdot \sigma_s \cdot \delta_{xy} \\ \Leftrightarrow\ &\varphi_e \geq \arcsin\left(\frac{\frac{\sqrt{3}}{\pi} \cdot \frac{1}{\sqrt{SCR}} \cdot \delta_{xy}}{\delta h \cdot \tan(\theta)} - \frac{1}{\sqrt{2}}\right) + \frac{\pi}{4}. \end{aligned} \tag{5.16}$$

In Fig. 5.5, the minimum aspect interval φ_e for an isolated scatterer is plotted as a function of the SCR for typical elevation angles and image resolutions. Notice, that the measuring accuracy for high SCR significantly improves, but still φ_e is limited by a lower bound. This is due to the fact that a certain amount of aspect information has to be collected to process at least two images in the required ground resolution δ_{xy}. For putting this into perspective, in the processed data, a mean SCR of 7 dB and 17 dB for two types of smaller corner reflectors in the scene was measured with $\theta \approx 40°$ and $\delta_{xy} = 10$ cm, corresponding to an aspect integration of $\varphi_{az} = 1.4°$. Achieving a height resolution of δh =0.1 m would then result in a minimum tracking aspect interval of $\varphi_e = 19°$ and $\varphi_e = 8°$, respectively. However, from Fig. 5.5, it is also apparent that height extraction of ground clutter or of volume scatterers such as trees is problematic since the SCR in these areas is very low, which theoretically requires a very large φ_e.

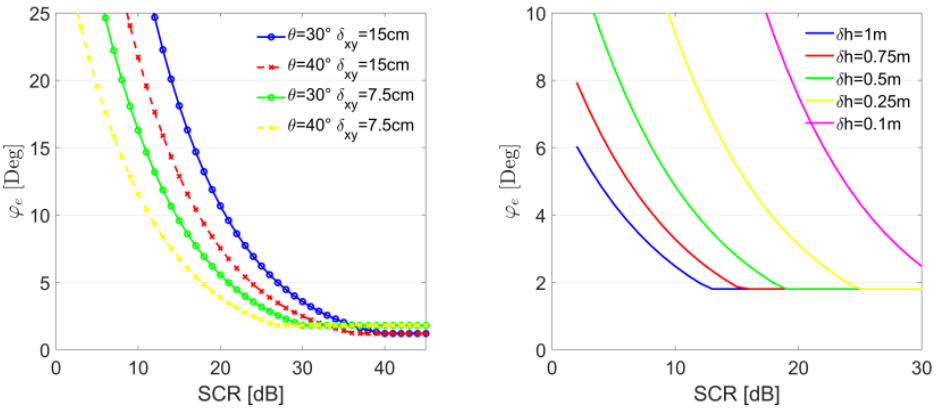

Figure 5.5: Minimum aspect interval φ_e for an isolated scatterer in clutter as a function of the SCR (in decibel). a) φ_e with fixed $\delta h = 0.1$ m and varying resolution δ_{xy} and elevation angles θ, b) φ_e with fixed $\theta = 40°$, $\delta_{xy} = 0.15$ m and varying δh.

5.2 3d point cloud generation of an urban scene

This Section proposes a strategy to extract a global 3d point cloud from a fusion of multiple stacks of CSAR amplitude images acquired from different aspects. The approach is motivated by

the natural object's low SCR and often short angular persistence. Therefore, coherent integration of considerably larger aspect intervals seems promising to enhance the SCR and the resolution of objects. However, this assumption is only valid if the object's correct height can be estimated.

5.2.1 Signal model

By focusing the data in a stack of different heights, the actual SAR process can be regarded as estimating the best height hypothesis allowing for the most extended coherent energy integration or tracking, analog to Chapter 5.1.3 and Fig. 5.4. Focusing objects at wrong heights instead can be interpreted as adding a further transfer function $h(m,n)$ to the signal model in equation 5.1 with $g_s[m,n] = g[m,n] * h(m,n)$. $h(m,n)$ in particular lowers the amplitude and spreads or smears the reflected impulse response signal over neighboring pixels in flight path direction, similar to a low pass behavior and observable in Fig. 4.2c. Analog to equation 5.1, the focused subaperture SAR image $g_s[m,n]$ for larger aspect intervals $\varphi_{az} \gg \varphi_{max}$ can be modeled as

$$\begin{aligned} g_s[m,n] &= g[m,n] * h[m,n] \\ &= \sum_{p=1}^{P} \sum_{q=1}^{Q} \int_{(q-1)\varphi_{max}(p)}^{q\varphi_{max}(p)} \alpha_p(\varphi) \cdot e^{j2kr_p(\varphi)} d\varphi \\ &\cdot \delta[m - m_p + x_D(p)\cos(\varphi_{m,q}), n - n_p + x_D(p)\sin(\varphi_{m,q})], \quad Q \in \mathbb{N} > 0 \end{aligned} \tag{5.17}$$

with

$$Q = \lfloor \frac{\varphi_{az} \cdot x_D(p)}{\delta_p} \rfloor + 1, \tag{5.18}$$

$x_D(p)$ the displacement, and δ_p the pixel spacing that is assumed to be in the scale of the ground resolution. The variable Q specifies the number of pixels passed through by the scatterer. Again, φ_{max} specifies the maximum aspect interval the object $\vec{\mathbf{x}}_p$ can be coherently focused as a function of its height. Only the backscattering energy E_p over φ_{max} will be collected in one image pixel and gets more significant the closer the focusing plane height is at the object's actual height, see Fig.5.6a. If the object is at zero elevation, then $x_D(p)$ equals zero, Q equals one, and the whole energy of the scatterer is collected in one pixel as indicated in Fig. 5.6.

Which pattern or energy distribution the object forms in the image is aside from its height and θ dependent on $\alpha_p(\varphi)$. Natural objects can show any form of reflectivity distribution, which is unknown in advance, see Fig. 5.6a. In the case of high angular persistence, the energy of a single object can be very unevenly distributed, pretending multiple objects. Given an ideal isotropic scatterer, the total energy will be evenly distributed over Q pixels at the derived positions, which is shown in simplified form in Fig. 5.6b. Objects at correct height will show maximum peak sidelobe ratio (PSLR) while it's energy is concentrated at position $[m_p, n_p]$. If the angular persistence is smaller than φ_{max}, the height can not be evaluated.

5.2.2 Strategy

For extracting height information, the proposed method shall be able to evaluate the energy flow from random scatterers on all possible projection paths in a local area at equidistant height intervals. For this purpose, the focused urban scene is scanned by a search matrix in equidistant steps, and the CSAR amplitude image information is evaluated with respect to its potential 3d information. Therefore, the related image content at different height levels shall precisely be determined and assessed what is indicated in Fig. 5.7. The locally extracted height information from multiple angular aspect angles φ_m shall then be fused to a global 3d point cloud.

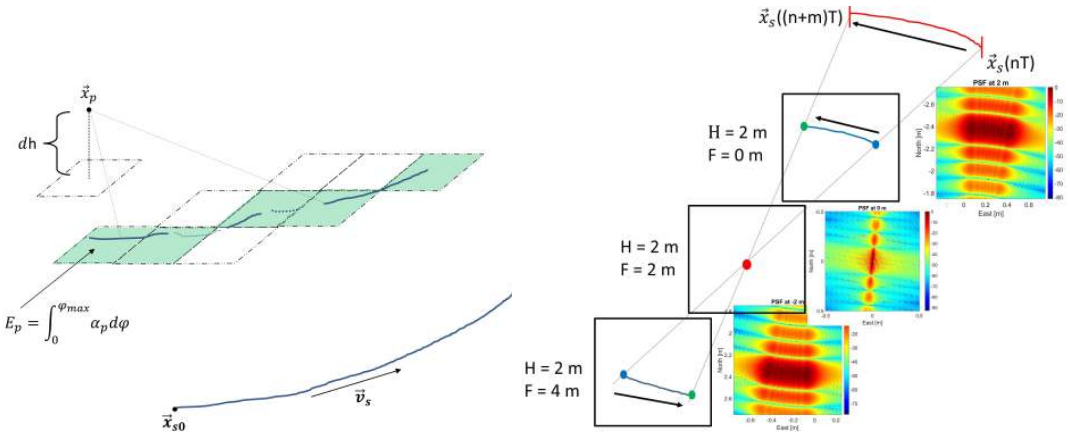

(a) (b)

Figure 5.6: Projected energy flow of a scatterer focused at different heights. a) Focused at wrong height, each pixel collects the maximum energy E_p. α_p can cause different energy centers, b) projected energy flow of isotropic scatterer placed at height H=2 m and corresponding reference height F. In optimal case the energy flow can be evaluated in a single local search matrix.

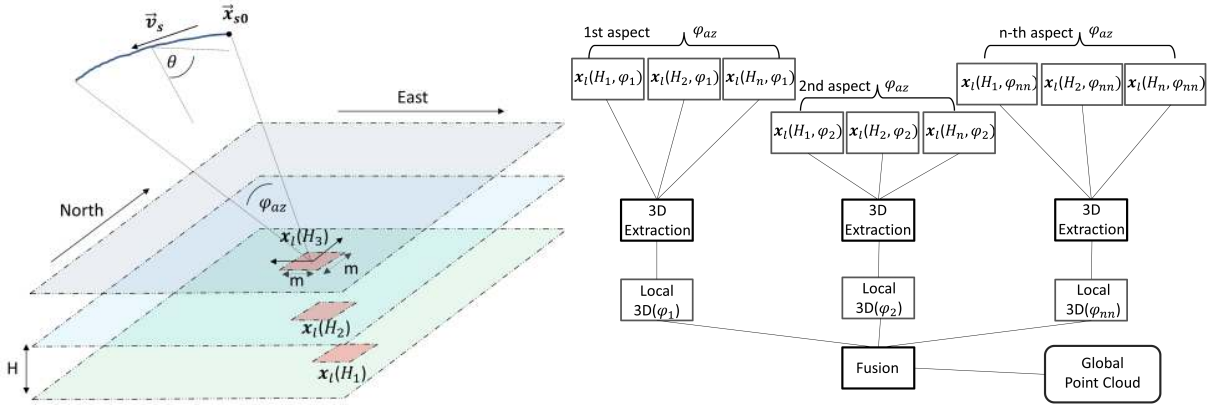

(a) (b)

Figure 5.7: Strategy of generating a 3d point cloud. a) Local 3d extraction by scanning the amplitude image area and evaluating the corresponding areas at different heights, b) synoptic of local 3d extraction and fusion of a global 3d point cloud.

Preprocessing and data alignment

The whole 360° circular data set is divided into equidistant circular arcs each illuminating the scene in angular intervals of $\varphi_{az} \gg \varphi_{max}$. Assuming that the height of the buildings in the urban scene does not exceed the height h_{max}, each circular arc is focused in ΔH m height steps $H \in [0, h_{max}]$ forming an image stack in the dimension (north,east,H)' as indicated in Fig. 5.7a. Due to the computational complexity, for larger urban scenes, ΔH typically is 1 m while δ_p is 3 cm.

Identifying very strong reflections that typically occur from building edges is realized by a radiometric criterion. These overexposed areas are widely filtered since they do not contain information for further processing and distort the neighboring pixels.

As modeled in equation 5.17, the energy flow of potential scatterers in the local search matrix area x_l with size m x m will typically show an arc-like projection as indicated in Fig. 5.6 and

Fig. 5.8. Notice that if the potential object is above/below the focusing plane, the arc-like projection is mirrored or instead rotated by 180°, see Fig. 5.6b. Its radius and center are unknown in the scene and are visualized in Fig. 5.8 as green, black and blue for a full circle. However, for a small circular flight path of size φ_{az}, arbitrary scatterers P in the red search matrix will project almost in a linear form. Yet, depending on the aperture's mean aspect angle φ_m, they will project through different image columns, similar to the range cell migration of range compressed SAR data. For aligning the energy flow of all objects, the search matrix $x_l(H)$ is therefore rotated in the direction of φ_m by

$$x_l^{'}(H) = Rot(\varphi_m) \cdot x_l(H). \tag{5.19}$$

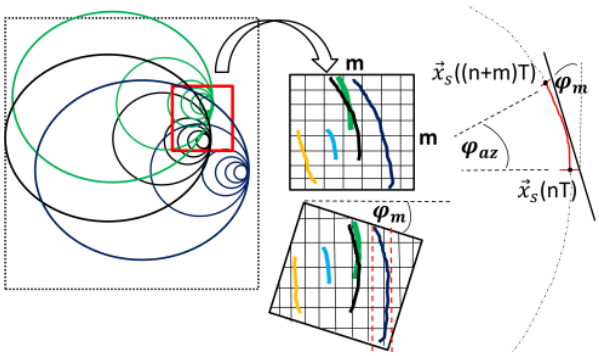

Figure 5.8: Aligning the projected energy flow of arbitrary objects in the search matrix. Yellow projection is object below focusing plane (convex course), others are from high objects (concave).

In a second step, the image columns of $x_l'(H)$ are resampled. The most unfavorable object that projects into most columns would be a high scatterer, whose projection starts at the border of the search matrix (indicated in blue). Due to the already carried out rotation, the maximum displacement d_{rp} in 'range dimension' can be derived by

$$d_{rp} = h_{max} \cdot \tan(\theta) \cdot \left(1 - \cos\left(\frac{\varphi_{az}}{2}\right)\right). \tag{5.20}$$

The resampled width of the columns of $x_l'(H)$ is thus adapted to $2 \cdot d_{rp}$.

Matching the search matrix area $x_l^{'}(H)$ to the corresponding height hypotheses areas $(x_l^{'}(H+1), ..., x_l^{'}(h_{max}))$ is achieved by computing the local displacement vector from the matrix center coordinate $\vec{x}_{lm}^{'}(H) \rightarrow \vec{x}_{lm}^{'}(H+1)$ to the different heights, given by equation 5.7 and the seedpoint equation 5.9. The content of both matrices then represent the same scene focused at different height and aligned in orientation.

5.2.3 Height extraction process

Several metrics can be considered to evaluate the level of target energy flow or azimuth spreading. Two different approaches are proposed in this Section.

(a) Kurtosis operator

One solution is the kurtosis operator, which is a high order statistic sensitive to outliers of the distribution, see [Westfall, 2014]. A considerable value indicates a more severe outlier issue; a small value indicates a distribution with generally fewer outliers. This behavior corresponds to sharp peaks with high PSLR at focus and a distributed energy flow in along-track at the wrong

height. The level of local energy flow at each corresponding height is then evaluated by the designed vector $\vec{s}(H)$ with

$$\vec{s}(H) = \frac{1}{m}\sum_{j=1}^{m}\Bigg(\underbrace{\sum_{i=1}^{m}\Big(\frac{x'_{l;i,j}(H)\cdot w_i - \mu_{i,j}(H)}{\sigma_{i,j}(H)}\Big)^4}_{Kurt(x'_{l;j})}\cdot \left|(x'_{l;j})(H)\right|_{max}\Bigg). \tag{5.21}$$

The metric measures the mean kurtosis moment of the investigated area in the rotated and resampled along-track direction. The first sum over i is along the rotated azimuth direction, the second sum over j collects the derived kurtosis moments for each height. $\mu_{i,j}(H)$ is the mean, $\sigma_{i,j}(H)$ the standard deviation of the distribution and $\left|(x'_{l;j})(H)\right|_{max}$ the maximum value of each along-track column. This allows an additional weighting of the individual columns by their highest pixel intensity, since the statistic is otherwise too much falsified by scene clutter.

Suppressing smearing peaks or sidelobes from more substantial objects at wrong focusing heights in the vicinity of the search matrix is realized by a hamming filter w in the along-track dimension. This filtering significantly reduces the noise sensitivity of the estimator. The 3d position $\vec{\mathbf{x}}_p$ of the search area x_l is then determined by the operator's maximum with

$$\vec{\mathbf{x}}_p = g\left(arg\Big[\max_{H}\left(\vec{s}(H)\right)\Big]\right) \tag{5.22}$$

that describes the metric of height estimation. Again, the function g is the transformation from the 2d matrix center pixel $\vec{x}_{lm}(H)$ to 3d coordinates, see equation 5.9. For achieving a finer height step size, the vector $\vec{s}(H)$ should further be interpolated in step sizes of typically $\Delta H = 0.1$ m.

(b) Image spectrum operator

A second operator shall detect the potential energy flow in the image spectrum of the search matrix. Based on the model equation 5.17, we expect the reflectivity of objects to be imaged in accordance to a small rect or even a Dirac function at the correct height. Conversely, objects are smeared at wrong focusing heights and appear more similar to a low-pass filtered broader rect function. In the image frequency domain, this yields

$$rect(\frac{m_j}{N\cdot\delta_p}) \xrightarrow{\mathcal{F}} \frac{1}{\sqrt{2\pi}}\cdot N\cdot\delta_p\cdot si(\pi\cdot f_i\cdot N\cdot\delta_p) \tag{5.23}$$

where m_j are the image elements, $N\cdot\delta_p$ the width of the rect function that corresponds to the width of the projected object in azimuth direction, and f_i the image frequencies. An object at the correct height will show more significant image frequency coefficients at medium and higher frequencies, whereas this is less pronounced at lower frequencies. Therefore, the operator shall evaluate the band-pass filtered image frequencies in the spatial frequency domain.

Let $\mathbf{X}'_l(H) = \left|\mathcal{F}((x'_l(H))^3\cdot w_i)\right|$ be the magnitude of the Fourier transform along the rotated along-track orientation of $(x'_l(H))^3$ weighted by the hamming window. The level of local energy flow for this operator is then evaluated by $\vec{s}(H)$ with

$$\vec{s}(H) = \sum_{i=1}^{m}\left(\sum_{j=1}^{m}\left(\mathbf{X}'_{l;i,j}(H)\cdot\left|(x'_{l;j}(H))\right|_{max}\right)\right)\cdot\hat{w}_i \tag{5.24}$$

whereby $\hat{w}_i$ is a further window function that selects specific frequency coefficients. It is defined by

$$\hat{w}_i = \begin{cases} 1 & \frac{1}{8\cdot\delta_p} < \hat{w}_i < \frac{1}{2.5\cdot\delta_p} \\ 0 & \text{else.} \end{cases} \tag{5.25}$$

$\frac{1}{8 \cdot \delta_p}$ is the first zero crossing of the si-function of an object that shows a width of $8 \cdot \delta_p$. Thus, we expect valid objects in urban scenes to be imaged in the order of 1-8 pixels, but this parameter can, of course, be adapted. Also, the highest frequency components of f_i shall be filtered.

The first sum over j of equation 5.24 collects the spectral frequency coefficients along range dimension and the second sum over i collects the weighted spectral information for each height. The metric is then designed to measure the band limited and weighted mean spectral power density along the rotated direction. To further suppress noise and to account for the fact that a reliable height estimation will also result in reasonable estimates at the close vicinity of the optimum, $\vec{s}(H)$ is further low pass filtered, which yields

$$\vec{s}_n(H) = \frac{1}{3}\left(\vec{s}((H-1)) + \vec{s}(H) + \vec{s}((H+1))\right). \tag{5.26}$$

The 3d position $\vec{\mathbf{x}}_p$ of the search area x_l is then determined by the operator's maximum of the normalized vector with

$$\vec{\mathbf{x}}_p = g\left(arg\left[\max_H\left(\frac{\vec{s}_n(H)}{\sum \vec{s}_n(H)}\right)\right]\right). \tag{5.27}$$

Both metrics assume that objects in the immediate neighborhood are ideally at a similar height, therefore a constraint.

Aligning the search matrix to the scene

Fig. 5.9 discusses the effect that the focused local scene content of $x_l(H)$ may vary significantly depending on the selected reference height H and potential multiple scatterers of different reflectivity in close vicinity or at the edge of the local scene. This problem is associated with analyzing a small image section of an urban area in equidistant step sizes. The image pixels of the search matrix $x_l(H)$ can be located in between buildings or their edges, contain shadow areas mixed with clutter information, or show several nearby scatterers combined with volume scattering. When processed at different heights, each object starts to spread, and also, the shadow area moves on the image plane due to the various projections on the focusing plane. Scatterers located in the vicinity of the search matrix that have not been included in $x_l(H = 0)$ may enter the matrix e.g.,

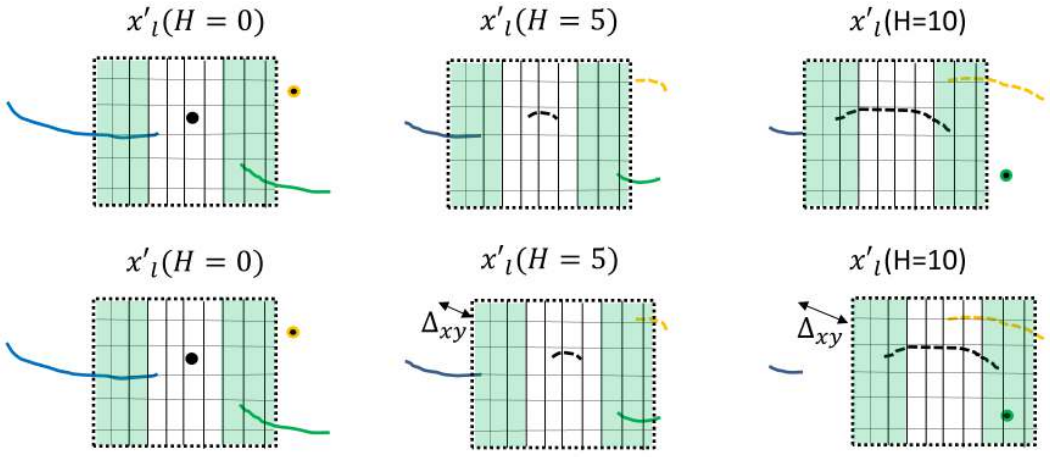

Figure 5.9: Interference by spreading of adjacent scatterers into the search area. Objects at 0 m, 10 m and 12 m height. Impact of the hamming window is indicated in green. (1st line) Evaluation of the central black object is falsified by adjacent objects that move into $x_l(H)$. (2nd line) Adapting matrix to the scene. If the green object is dominant, the search matrix can continuously be aligned to it.

at $x_l(H = 5)$ due to their spreading or defocusing. Other scatterers may already be vanished in $x_l(H = 5)$, if their correct reference height is chosen, and their true location is in the vicinity of the local scene. Applying the hamming window reduces this effect but does not prevent it. This raises the question of which image information is then actually investigated by the operators, since the local scene may contain different objects at different reference heights. Obviously, if the green scatterer in Fig.5.9 is dominant, information for higher regions is missing, since the projection of the scatterer is no longer visible in $x_l(H = 10)$.

For addressing this problem, the mean intensity shift from $(x_l(H)) \rightarrow (x_l(H+1))$ by capturing the shift $\Delta_{x,y}$ of the geometric intensity center of both local image regions is calculated as derived from equation 5.10. Selecting the corresponding $(x_l(H + 1))$ is then a function of the derived seedpoints by equation 5.9 and the calculated geometric shift $\Delta_{x,y}$ which results in

$$x_{lm}(H + 1) = x_{lm}(H) - dh \cdot \tan(\theta_\pi) \cdot \vec{u} - dh \cdot \tan(\Phi) \cdot \vec{w} + \Delta_{x,y}. \tag{5.28}$$

This calculation guarantees that the method better follows the energy flow of more significant scatterers in the scene. However, suppose the intensity shift is too high, or the geometric center is located at the border of the search matrix. In that case, the model is falsified, and the data is filtered and not evaluated.

Choice of a search window size

The search matrix has to be small to achieve a dense point cloud and a good spatial resolution. On the other side, both operators need a statistical data set of an appropriate size. In addition, the energy flow of high objects can easily reach a few meters in along-track direction. From equation 5.18, Q_{max} is derived by $Q_{max} = \frac{\varphi_{az} \cdot h_{max} \tan(\theta)}{\delta_p}$. Therefore, a good approximation is a matrix size between 1 m and $(Q_{max} \cdot \delta_p)$ m for medium heights.

Thresholding

As the SAR images are not radiometrically calibrated and the 3 dB footprint is relatively small, the contrast in the images varies. At first, an absolute threshold value is set to cancel shadowed areas and clutter regions with low SCR. Normalized to a shadowed area, $\vec{s}(H)$ is differentiated in high and low contrast areas. For the kurtosis operator, two different absolute threshold levels $\lambda_{lc} = v \cdot \lambda_{hc}$ with $v = 1.5$ in low contrast areas (λ_{lc}) and high contrast areas (λ_{hc}), respectively, are applied to the operator's estimation. For the spectrum operator, two different relative threshold levels $\lambda_{lc}, \lambda_{hc}$ are applied as the normalized $\vec{s}(H)$ is analyzed.

Point cloud fusion

The extracted 3d point clouds of each aspect angle are computed independently. Then, they are transferred to a three-dimensional Cartesian coordinate system which is derived from the respective flight trajectory in the WGS84 format, see Section 4.4. For fusing the individual point clouds PC to a global point cloud PC_g, a new global coordinate system is set up based on the first selected point cloud PC_m, which then serves as 'master view'. Knowing the coordinates of each local cloud, the displacement vector to the 'master view' is derived as a function of both WGS84 coordinates, and the global cloud is then successively filled with information from all aspect views N by adding the 3d points with

$$PC_g(\vec{\mathbf{x}}) = PC_m(\vec{\mathbf{x}}) + \sum_{n=1}^{N} g(PC_n(\vec{\mathbf{x}}) \rightarrow PC_m(\vec{\mathbf{x}})), \tag{5.29}$$

where g describes the shift by the displacement vector to the 'master view'.

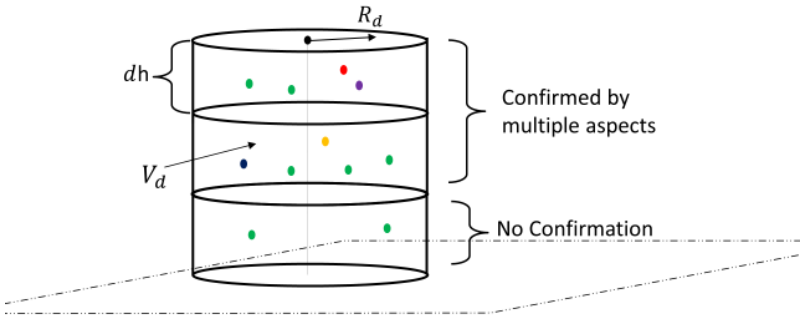

Figure 5.10: Point cloud filtering visualization. At each volume element, a confirmation number N is derived. Scatterers from different aspects are color coded.

Point cloud filtering

To further reduce the noise level of the global point cloud, two filtering operations are designed. At very high and very low height estimations, the most errors are assumed due to the search matrix alignment, see Section 5.2.3. Therefore, for each point at $H > H_1$ and $H < H_2$, the number of points in a certain volume $V_d = \pi \cdot {R_d}^2 \cdot \delta h$ with R_d the radius is compared to a minimal number M in the local point cloud. In the experiments, H_1 was set to 10.5 m and H_2 to 1.5 m, R_d=3 m and $M = 5$.

In a second step, it is assumed that all points $\vec{\mathbf{x}}_p$ in the global cloud shall at least show a minimum number of confirmations N from different aspects as indicated in Fig. 5.10. For $\vec{\mathbf{x}}_p$ in the volume V_d at each corresponding height it holds

$$\vec{\mathbf{x}}_p = \begin{cases} \text{filtered if} & \sum_k \left(k_i \cdot (1 + \sin(\frac{\Delta\varphi}{2})) \right) < N, k_i \in V_d \\ \text{else} \end{cases} \tag{5.30}$$

with k the number of different scatterers in V_d, k_i the individual point and $\Delta\varphi$ the angular difference of their visibility. Points that are confirmed from different aspects are higher weighted. In the experiments, the values were set to R_d=2 m, δh= 2 m and N=4.

5.2.4 3d extraction derived from the entire circular aperture

By now, in Section 5.2.2, 3d information was estimated from different aspect views and then fused to a global point cloud. Therefore, each valid pixel area $x_l(\varphi)$ resulted in a projection line $g(\vec{s}(H))$ that was maximized to extract the 3d position with the highest probability.

In this new approach, the 3d information shall not be derived based only on information from a single aspect interval φ_{az}. Instead, the entire circular trajectory's acquired information shall be exploited to derive a global point cloud. The basic strategy behind this approach is that the same object is recognized from different aspects, and combining this information can increase the accuracy of the 3d estimation. In addition, false detections are to be reduced, and the detection threshold for those difficult to locate objects are to be raised.

Strategy

Let's assume that the area of the search matrix $x_l(\varphi_0)$ from a single aspect view is projected in the volume element V_B located around $\vec{\mathbf{x}}_p$ with a probability of $P(\vec{\mathbf{x}}_p(\varphi))$ as indicated in Fig. 5.11. V_B shall have the dimensions (b_x, b_y, b_z). We are now looking for different aspect views that may confirm or negate this estimation, or indicate that another volume element along the projection line may be more likely. Therefore, all relevant aspect views $\varphi_n \neg \varphi_0$ are evaluated that contain

valid image areas that are also projected in V_B with a probability $P(\vec{\mathbf{x}}_p(\varphi_n))$. This allows the derivation of a new weighting factor along the original projection line $g(\vec{s}(H, \varphi_0))$.

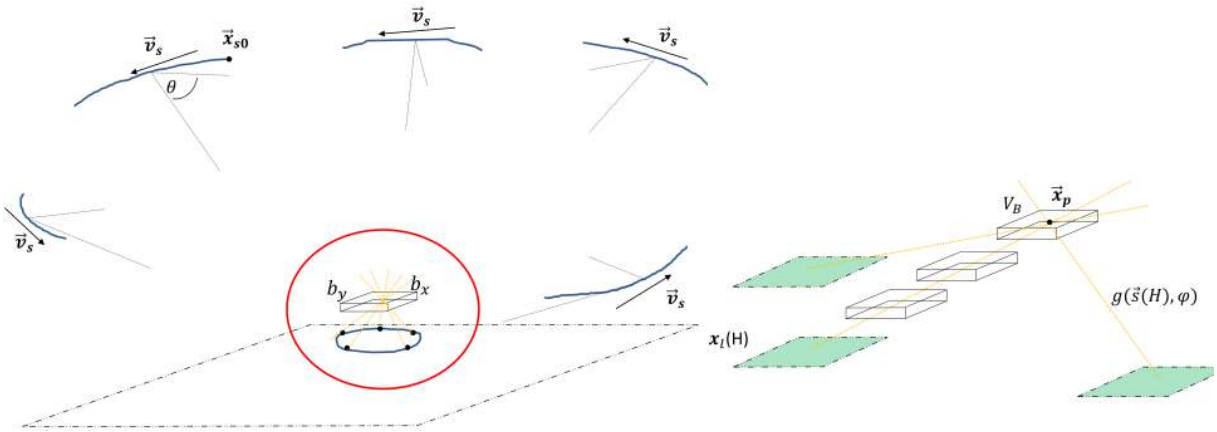

(a)

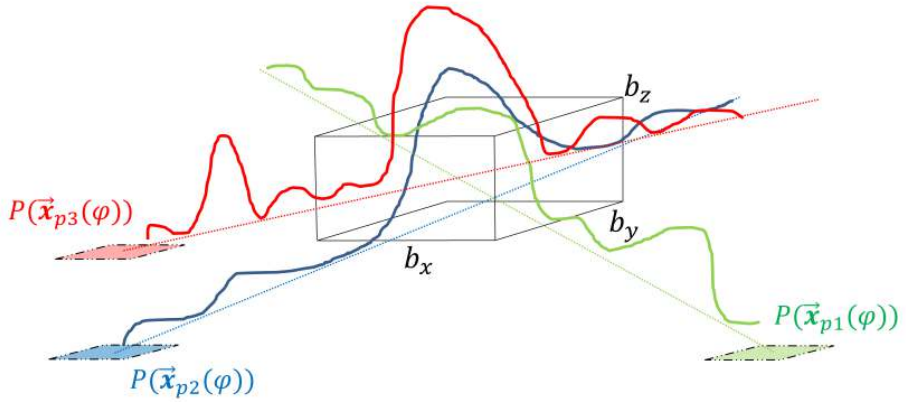

(b)

Figure 5.11: Visualization of 3d extraction based on information acquired from multiple aspect views. a) Left side: A potential target is seen from multiple aspects. The derived projection lines from all aspects intersect at the same volume element V_B. Right sight: Enlargement of area in the red circle. Target $\vec{\mathbf{x}}_p$ is seen from 3 aspects, b) zoom on one volume element that may contain a dominant target that is seen from 3 aspects. The derived probability density functions (PDFs) from each view (red,green,blue) will show their maximum probability in the area of V_B.

New weighting factor

Let M be the number of projection lines from all aspect views except φ_0 that cross the element V_B located at g(H). For each volume element $V_B(H)$ along the original projection line, a new weighting factor is derived by

$$f(H) = \frac{1}{M+1} \cdot \left(P\left[\vec{\mathbf{x}}_p(\varphi_0) = g(H)\right] + \sum_n P\left[\vec{\mathbf{x}}_p(\varphi_n) = g(H)\right] \right) \tag{5.31}$$

with n as the different aspect views collected within the entire circular trajectory. In this way, all aspects are equally weighted along the possible projection line. Volume elements in which several aspects show a high probability of estimating a target are assigned a high weighting factor $f(H)$ which is indicated in Fig. 5.11b.

(c) Weighted mean operator

Analog to Section 5.2.2 the vector $\vec{s}(H, \varphi)$ for each valid search area $x_l(\varphi)$ and all valid aspect views φ is derived using either (a) the kurtosis operator or (b) the image spectrum operator. $\vec{s}(H, \varphi)$ is further normalized and interpolated in steps of $\Delta H = 0.1\,\mathrm{m}$ to obtain a probability density function (PDF) $P(\vec{\mathbf{x}}_p(\varphi))$ of 3d points that are positioned along the projection line. A fusion of all extracted PDFs in one 3d Cartesian coordinate system is again implemented by shifting the geocoded information from WGS84 to a reference system as described in equation 5.29.

Subsequently, all possible projection lines are evaluated and new weighting factors $f(H)$ are derived for each height, see equation 5.31. The size of the volume elements V_B from Fig. 5.11 centered along the original projection line shall be small to evaluate only valid different views. On the other hand, the data is focused in equidistant height steps of $\Delta H = 1\,\mathrm{m}$. Therefore, a practical implementation for the size of V_B is $b_x = b_y = \Delta H/2$ and $b_z = 0.05 \cdot \Delta H$. Extracting the 3d position $\vec{\mathbf{x}}_p$ is finally derived by

$$\vec{\mathbf{x}}_p = g\left(arg\left[\underset{H}{max}\left(f(H)\right)\right]\right). \tag{5.32}$$

No further fusion of 3d points is required, as the 3d extraction has already been conducted in the geocoded, global reference system.

5.3 Optimizing the focusing process to a specific scene

Knowing the absolute height of a scene allows the fusion of different aspect views in the same image geometry. Therefore, the more precise the height information and the more accurate the measured track is, the less the effect that objects project from different views into different pixels. Areas covered with shadow from a single aspect can further be filled with information from a different aspect view. In this context, each pixel intensity I(x,y) in the final image may not only be dependent on the aspect view φ but is also a function of the observing time I(x,y;$\varphi(T)$) since the scene is not static. For recognizing these temporal changes, one strategy is a superposition of different views where a different color indicates each view. However, this will still cause shadowing, and high objects will still project in the corresponding view, making this strategy only well suitable in planar areas. A strategy for the fusion of different views eventually depends on the individual application and the scene's context.

Fusion strategy

As this work is focused on urban mapping, a method is proposed to focus the radar data and map buildings from multiple aspect views allowing a shadow reduced view and a reduction of the potential overlay. The processed image shall reveal the areas next to the facade from all sides since these areas are typically shadowed or show overlay characteristics. Simultaneously, the entire roof area shall be imaged in a single high-resolution SAR image. To avoid that shadowed areas are filled with information from overlayed areas, an optimal viewing angle φ_{vm} to focus each pixel has to be defined. The required context for this approach is provided by the generated 3d point cloud in Section 5.2.

Knowing the buildings' 3d dimensions and location, the evaluation strategy is indicated in Fig. 5.12. The green pixels visualize the area affected by shadowing or overlaying based on the dimensions of the building. The arrows illustrate the incident radar waves. While the red arrows would result in a shadowed or overlayed pixel, the blue arrows in interval φ_v indicate a line of sight that is unproblematic. When considering a higher pitch of the roof, its area can only be

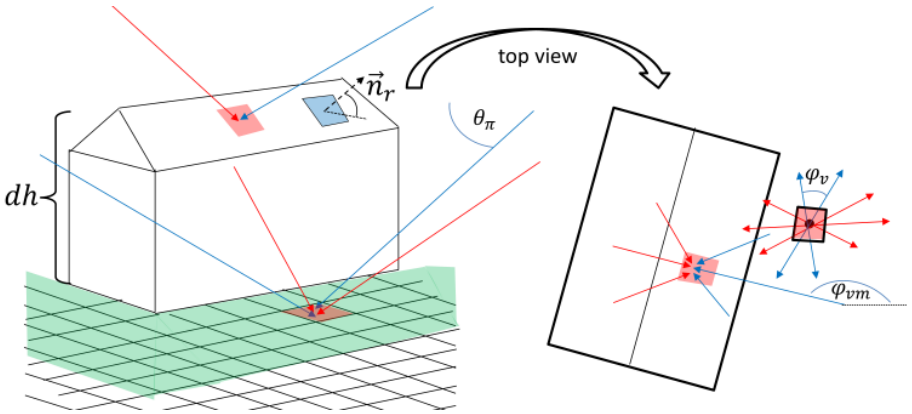

Figure 5.12: Visualization of a building and the adjacent green area that is affected by shadowing and overlaying. Blue arrows mark line of side of radar that is optimal for shadow-free view on the target. $\vec{\mathbf{n}}_r$ indicates the orientation of the roof area.

illuminated from one main direction, while the ground can be mapped from views offset by 180°. Based on the knowledge of the height of the roof area, the CSAR data shall be refocused in the new image geometry allowing an increased and uniform spatial resolution that is otherwise not possible due to the height constraints. For this purpose, a surface model with a fixed pixel spacing shall be derived from the generated point cloud, similar to a DSM.

Implementation

For optimizing the focusing process to a specific scene, the following processing chain is applied:
(1) Deriving a surface model H(x,y) from the generated 3d point cloud: In a m_1 x m_1 raster step size, the mean point cloud height within the raster is derived and selected as the surface height H(x,y). The surface model is further low-pass filtered to create a roof level that is preferably smooth and does not cause image distortions in the process of refocusing.
(2) Calculation of the optimal viewing angle to the target region: The derived surface map is thresholded by the parameter η_r to

$$H(x,y) = \begin{cases} 0 & H(x,y) \leq \eta_r \\ H(x,y) & \text{else.} \end{cases} \tag{5.33}$$

This approach defines a unique roof area with $H(x,y) > \eta_r$ and ground areas below the threshold. It further ensures steeper facade shapes, otherwise smeared by the low-pass filtering. In roof areas, with a m_2 x m_2 raster step size, the normal vector $\vec{\mathbf{n}}_r$, see Fig. 5.12, is computed by a plane that best fits the sampled points by the least square of the normal distance to the approximated plane. The mean orientation φ_{vm} of the roof area relevant for the data fusion is then derived by

$$\varphi_{vm}(H(x,y) > 0) = \angle(n_{r,2} + j \cdot n_{r,1}). \tag{5.34}$$

For each pixel position $\vec{x}_p$ on the ground with $H(x,y) = 0$, the radar wave's direction is validated to check whether high objects in the vicinity potentially cause shadow or overlay effects. With dh_{max} the highest roof element and θ_m the mean elevation angle, a set of n aspect angles φ_r that will cause shadow or overlay is derived by

$$\varphi_{r1,\ldots,rn} = \begin{cases} 1 & \text{if } H\left(\vec{x}_p + dh_{max} \cdot \tan(\theta_m) \cdot (\cos(\varphi_r), \sin(\varphi_r))'\right) > 0 \\ 0 & \text{else.} \end{cases} \tag{5.35}$$

The optimal viewing angle φ_{vm} for ground pixels is then calculated by

$$\varphi_{vm}(H(x,y) = 0) = \begin{cases} \angle\left(\sum_n e^{j \cdot \varphi_{rn}}\right) + \frac{\pi}{2}, & \text{if n} > 0 \\ [0, 2\pi], & \text{else.} \end{cases} \tag{5.36}$$

It can be derived from the size of n if there exists an optimal viewing angle at all or whether all views are problematic. This may happen, for example, if two perpendicular facades surround the ground position.
(3) Refocus of the CSAR data set on the derived surface model H(x,y) by selecting the optimal viewing angle for each pixel and each subaperture from φ_{vm}(H(x,y)). This task is realized by the designed SAR processor and knowledge of Section 4.2.3.

At last, an overview on the derived and implemented functionalities with respect to urban scene mapping and monitoring is presented in Fig. 5.13.

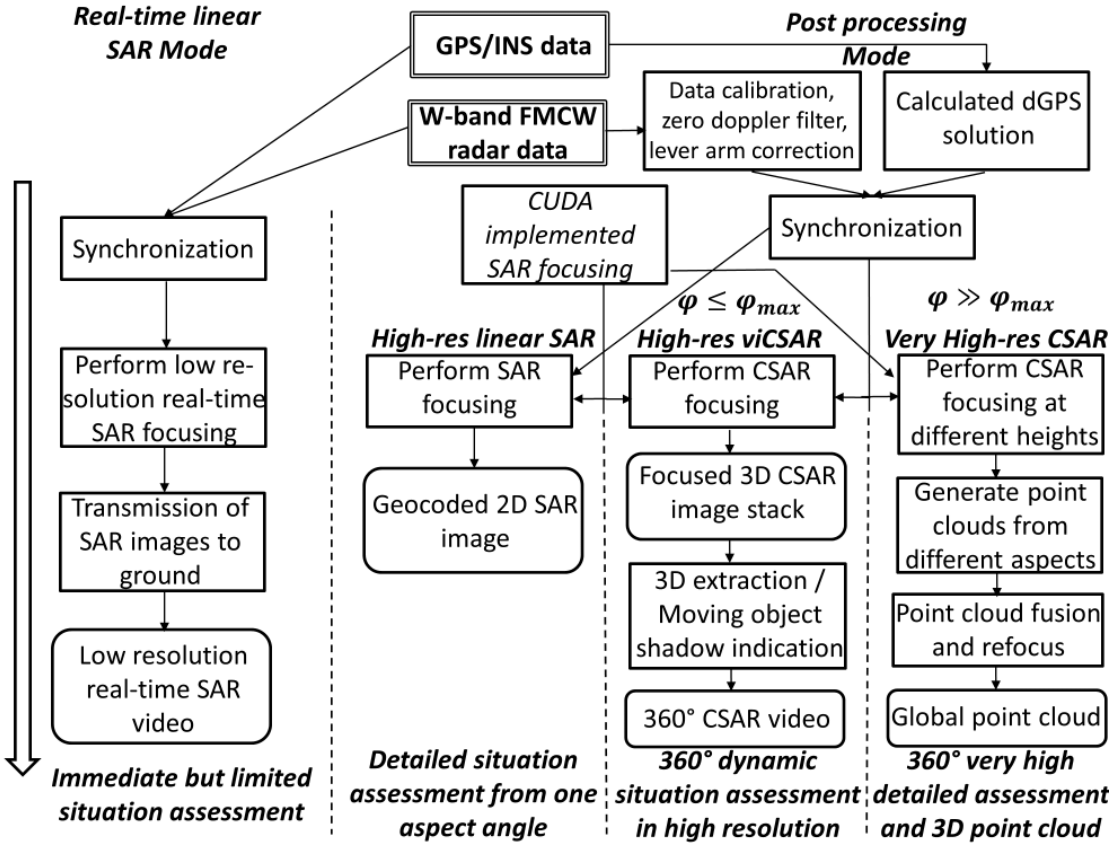

Figure 5.13: Overview of the developed and implemented functionalities and their specific capabilities in terms of urban scene mapping and monitoring. Indicated are implemented functions (single line rectangle), raw input data (double line rectangle) and output data (rounded rectangle).

6 Mobile radar mapping - close range urban imaging in subcentimeter resolution

This Chapter presents a method to adapt the focusing geometry for ultra-high-resolution carborne close range street mapping in Section 6.1. Challenges that arise from applying the lower terahertz frequency domain in mobile mapping scenarios are addressed. A further adaptation to focus and map facades in close vicinity of streets is shown in Section 6.2. The geometry of the vertical focusing plane can be further optimized by including 'a priori' or extracted information from the SAR images.

6.1 Street mapping

From the geometrical perspective of a side-looking SAR sensor, street mapping offers optimal conditions since streets are typically flat in cross-track, and there are no high objects that lead to shadowed areas. In order to obtain ultra-high resolution imaging and, at the same time, the ability to measure the objects mapped in the SAR images precisely, it is essential to determine a suitable 'a priori knowledge' of the illuminated scene. As detailed in Chapter 4.3, due to the analytically derived matched filter for each pixel, backprojection then provides very good results even on non-linear trajectories. From equation 4.18 and 4.23, a reliable height approximation of the currently illuminated region will ensure a good approximation of the term $2r(\vec{\mathbf{x}}_p, \vec{\mathbf{x}}_s(t))$. In contrast to airborne missions where a flat plane model of several hundred square meters with constant height can already be a good approximation of the scene, this gets more challenging in close-range mobile mapping scenarios at ultra-high resolution.

Since the sensor is moved only several decimeters up to a few meters above the street, the distance to the target scene is much smaller. Therefore, the focusing geometry is much more sensitive to height deviations. Applied to subcentimeter street mapping, the following problems arise with flat plane backprojection focusing:

a) Blurring and image distortions due to profile and slope of roads.

b) Influence of the non-linear movement of the sensor platform on SAR processing.

c) Path measurement requirements due to the use of extremely small radar wavelengths.

Moving the sensor along a road is different from carrying it on a platform in the air. Roads may be curvy and sloped downwards or upwards. A flat plane model at constant height is then insufficient, as the sensor is only attached at a comparatively small height h_0 above the imaging plane. While moving several hundred meters on a slightly sloping road, the focusing geometry

would end up with the sensor being several meters above/below the focusing plane. Depending on the slope of the road, the minimum distance from the sensor to the illuminated region would at least be subject to frequent fluctuations.

In the best-case scenario of a perfectly linear movement, slight height deviations will cause image distortions indicated in Fig. 6.1c but the focusing will not suffer. However, in the case of non-linear sensor movement that typically occurs in carborne applications, the focusing deteriorates similar to the effects indicated on circular trajectories, see Chapter 4.3 and Fig. 6.1b. The Figure indicates that while the car is on a curved road, objects above the reference height at a certain height dh (for instance curbs or side walk) can only be evaluated coherently over a limited aperture. Further, due to the small wavelength, already small accelerations in the order of 0.2 $\frac{m}{s^2}$ down/upwards or in cross-track result in considerable blurring [Palm et al., 2018]. More effects on the focusing quality by using erroneous digital elevation maps applied to linear SAR have been investigated by Duersch & Long [2015].

The last problem is due to the application of extremely high radar frequencies that in turn raise the requirements on the measured track accuracy by a further factor of larger than three compared to the already high standards of the W-band. This is definitely at the limit of current state high precision GPS/INS systems. At a given wavelength of 1 mm, building up a coherent trajectory with a stability of $\frac{\lambda}{10}$ m is very challenging even for small φ_{az}. With an azimuth beamwidth of 20° corresponding to a possible azimuth bandwidth of approx. 100 GHz, a coherent processing of such apertures without autofocus routines is at least questionable. Since the asphalt surface with its clutter behavior hardly provides strong reflections that can be evaluated for autofocus algorithms, currently, the best option is to use very high precision GPS/INS sensors and subsequent dGPS post-processing.

Since small aspect intervals at this wavelength are already sufficient to generate high azimuth bandwidths, this characteristic is again used to work with overlapping subapertures which brings in the technique of multilook processing. In the street mapping application, this offers two advantages: First, the build-up of smaller but with higher probability coherent subapertures, for example, with $\varphi_{az} = 6°$ generating 5 mm azimuth resolution. And second, it reduces the

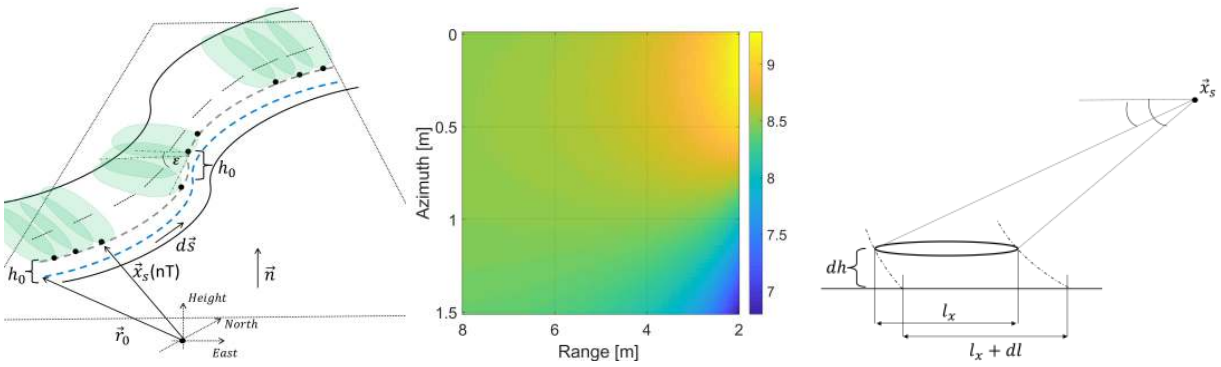

(a) (b) (c)

Figure 6.1: Top view of the street mapping geometry and possible image distortions due to height deviations. a) Stripmap street mapping visualization on a curved street. The trajectory of the platform is indicated in blue, b) heatmap [in Deg] of simulated integration interval φ_{max} for $dh = 30$ cm high targets on a curved trajectory with 30 m radius at 300 GHz, c) profile view of possible image distortions in street mapping geometry due to wrong height estimations. The length l_x of the object is enlarged by dl.

speckle noise of the street surface and its clutter behavior. This effect is increased by the natural averaging caused by the diffuse scattering of the rough surface as mentioned in Chapter 2.2.

Although the height deviation defocusing effects are also reduced by smaller subapertures, targets assumed at wrong elevation will still be displaced to different positions in the consecutive subaperture images and then non-coherently summed up at wrong pixel positions in the multilook process. To reduce these effects, the following focusing methodology is proposed that uses the fact that in carborne street mapping applications, the SAR sensor itself continuously evaluates the scene's actual surface height.

In street mapping geometry, the sensor is mounted at a height h_0 on the car, illuminating the street in stripmap, side-looking SAR geometry. Fig. 6.1a shows the corresponding geometry, where the sensor moves along the blue dashed line on the right side of a street. A profile of the slope of the trajectory is indicated in Fig. 6.2 with the actual height marked as $h(T_n)$ with T being a multiply of the radar's slow time. Starting with a flat plane model $E = (\vec{\mathbf{x}} - (0, 0, h_{T1})') \cdot \vec{\mathbf{n}}$, the

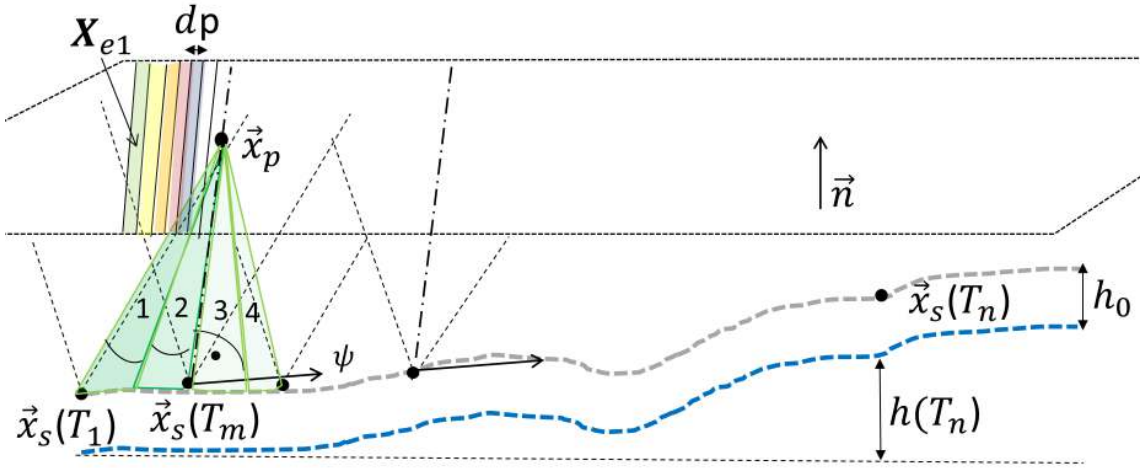

Figure 6.2: Profile of the street mapping geometry indicating the strategy of adapted planes.

imaging grid is then rastered in equidistant steps dp rectangular to the actual heading direction ψ of the car. The height of the areas $\mathbf{X}_e$ with width dp are then assigned to the current street level $h(T)$. Thus, the height of the potential scatterer at position $\vec{\mathbf{x}}_p$ is adapted to the actual street surface height $h(T_m)$ at the sensor position $\vec{\mathbf{x}}_s(T_m)$. This assumes that the surface height of the street in a narrow width dp in cross-track direction is nearly constant, which is a good approximation for streets. For a real-time implementation this would correspond to being able to focus the first 2 subapertures (out of 4 indicated in Fig. 6.2) of the pixel at position $\vec{\mathbf{x}}_p$ by reaching $\vec{\mathbf{x}}_s(T_m)$. Focusing on these 'height adapted plains' $\mathbf{X}_e$ is then similar to focusing on a dense and very high-resolution DEM, which, however, is generated instantaneously. In contrast to a flat plane model with support vector $x_0 = (0, 0, h(T_1))'$, the projection $\vec{x}_{pg}$ of the potential scatterer $\vec{\mathbf{x}}_p$ is shifted closer to its real 3d position resulting in a better approximation of

$$r(\vec{\mathbf{x}}_p, \vec{\mathbf{x}}_s) = \left|\left| \begin{pmatrix} x_s(T) \\ y_s(T) \\ z_s(T) \end{pmatrix} - \begin{pmatrix} x_{pg} + (h(T) - h(T_1)) \tan(\theta_\pi) \cdot \cos(\psi) \\ y_{pg} + (h(T) - h(T_1)) \tan(\theta_\pi) \cdot \sin(\psi) \\ z_{pg} + (h(T) - h(T_1)) \end{pmatrix} \right|\right|, \tag{6.1}$$

with θ_π the elevation angle at closest distance. The actual focusing is then carried out by the described time domain SAR processor in Chapter 4.2.

6.2 Facade mapping

By modifying the sensor's antenna look direction, the mapping of vertical structures such as housing facades or trees becomes feasible in carborne SAR applications at ultra-high resolution. Therefore, the depression angle was adapted by $\approx 60° - 70°$ resulting in an upward antenna look direction with an elevation angle of $\theta_1 \approx 30° - 40°$. This allows the illumination of vertical structures at relatively close distances by driving the sensor platform on conventional roads in side-looking geometry. In the absence of GiS or DSM information, the problems associated with a lack of good 'a priori knowledge' are similar to those described in Chapter 6.1. However, in contrast to the street mapping geometry, the distance to facades is challenging to predict and may be subject to frequent fluctuations while moving the sensor on the road.

Focusing strategy

Fig. 6.3a indicates the geometry of facade mapping for a typical urban scenario where the use of a flat, vertical image plane is proposed to focus the radar data in backprojection mode. Its mean

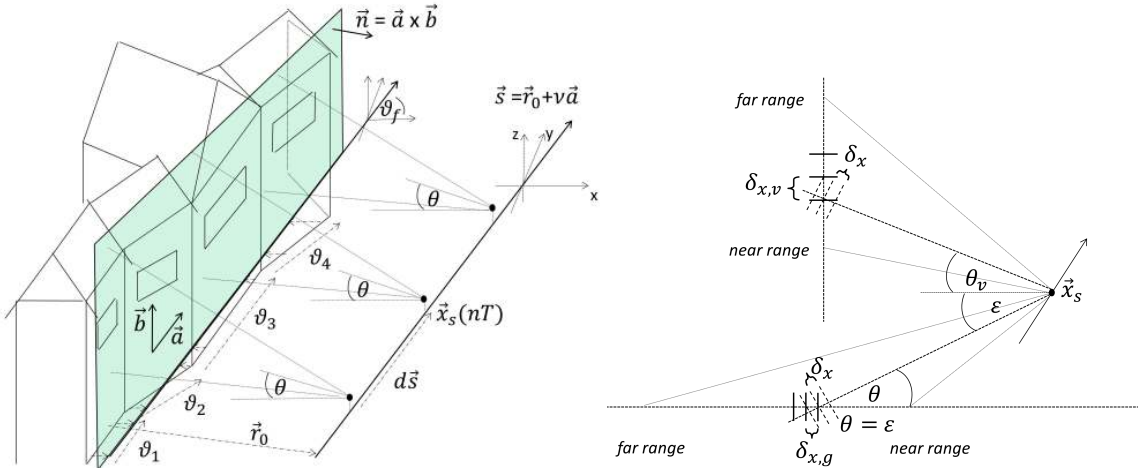

(a) (b)

Figure 6.3: Facade mapping geometry and its projected resolution. a) Design of a facade imaging plane in carborne upward looking SAR. The focusing plane is indicated green, b) comparison of down looking and 90° rotated upward looking SAR geometry with respect to projected resolution.

orientation angle $\vartheta_f \approx \frac{\sum_{i=1}^{k} \vartheta_i}{k}$, $i, k \in \mathbb{N}$, is estimated to be parallel to the street and thus parallel to the trajectory $\vec{\mathbf{s}}$ of the sensor indicated as $\vec{\mathbf{s}} = \vec{\mathbf{r}}_0 + \nu\vec{\mathbf{a}}$ with $\vec{\mathbf{r}}_0$ the start of the sensor's trajectory, $\vec{\mathbf{a}}$ the mean directional vector of the sensor's trajectory $\vec{\mathbf{s}}$, and $\nu \in \mathbb{R} > 0$. The assumption of a mean orientation of the facades is reasonable since houses are often aligned to the street direction. The focusing plane can then be described by a normal vector $\vec{\mathbf{n}}$ perpendicular to the trajectory. In contrast to the flat plane model in the airborne case, the facade plane can be defined arbitrarily in space, depending on the sensor's trajectory and the estimated orientation of the facade. The focusing plane in the Cartesian coordinate system then becomes

$$\vec{\mathbf{E}} = \vec{\mathbf{x}}_0 + \mu_1\vec{\mathbf{a}} + \mu_2\vec{\mathbf{b}}, \mu_i \in \mathbb{R} \tag{6.2}$$

with $\vec{\mathbf{x}}_0 = 0$, corresponding to a zero crossing of the plane to the coordinate system and $\vec{\mathbf{b}} = (0, 0, 1)'$, assuming a vertical facade structure that is reasonable for most man-made buildings. With the derivation of the normal vector $\vec{\mathbf{n}}$ of the image plane as $\vec{\mathbf{n}} = \vec{\mathbf{a}} \times \vec{\mathbf{b}}$, we end up in a

right-handed trihedron. From Chapter 4.2.3, the design of the imaging grid can be easily adapted to the SAR processor.

Concerning resolution aspects, the entire focusing geometry is rotated by 90° as indicated in Fig. 6.3b. While the azimuth resolution δ_y is not affected with $\delta_y = \frac{\lambda}{4\tan(\frac{\varphi}{2})}$, for the range resolution $\delta_{x,v}$ it holds $\delta_{x,v} = \frac{c_0}{2B \cdot \sin(\theta_\nu)}$ where B is the bandwidth, φ the main lobe coherent aspect integration angle and $0 < \theta_\nu < \frac{\pi}{2}$ the elevation angle. $\delta_{x,v}$ in this geometry becomes the 'range' resolution projected on the vertical axis, which corresponds to height. Depending on the height of the building and distance to the street, the elevation angle θ_ν must be adapted continuously. In typical vertical mobile mapping scenarios, θ_ν will be relatively flat that results in a slightly reduced resolution in vertical height compared to ground resolution $\delta_{x,g}$. Upwards, the resolution improves. With r_c as the smallest, perpendicular distance from the start of the sensor's trajectory to the facade, the start position $\vec{\mathbf{r}}_0$ of the trajectory can be selected to $\vec{\mathbf{r}}_0 = 0 \pm \vec{\mathbf{n}} \cdot r_c$, depending on which side the sensor looks.

The determination of the smallest distance r_c from the sensor to the facade at the start of the trajectory is problematic and has effects similar to the height deviation defocusing in street mapping. If no prior information is at hand, r_c can be estimated based on the first stronger echoes of the radar adjusted by the elevation angle θ_ν, but this selection is unambiguous, however. A second option to estimate r_c and the average facade orientation ϑ_f of single houses or a whole row of houses is the use of GiS data. Particularly suitable are georeferenced aerial or satellite images (orthophotos) where individual facade orientations can immediately be extracted. The extracted GiS information can improve the accuracy of the focusing plane and thereby reduce possible distortions in the focused SAR image due to wrong r_c and/or ϑ_f.

At longer trajectories, however, the orientation of the individual facades ϑ_i will not be consistent with the derived plane's orientation ϑ_f. If the angular difference $d\vartheta_i = \vartheta_f - \vartheta_i$ is small, the SAR focusing process will still generate sharply focused details, but the facades will be displayed visually slightly distorted. Similar to an optical image, with $d\vartheta \neq 0$, the facades and windows will either be displayed to come out of the image plane or move into it. The following applies: For $d\vartheta_i < 0$, the facade moves away from the sensor, for $d\vartheta_i > 0$, the facade moves towards the sensor. With additional object information, this effect can be further exploited to redesign a more suitable ϑ_f in a second iteration.

Adapting the image plane orientation

Housing facades are usually characterized by different surface structures such as bricks, concrete, timber, or plaster. These materials have various backscattering characteristics and geometries and are therefore not uniform. However, windows are typically aligned to the facade orientation. Their geometry is easy to determine in mmW SAR images as they have weak backscatter characteristics (mirror effect) and appear dark. Their geometry is usually consistent as they are built rectangular while orientated in the perpendicular. Based on a window mapped in the facade, Fig. 6.4 shows the geometry and parameters needed to recalculate an optimal facade orientation.

Assuming that a good approximation of the height of a specific window h_{BA} is known or can be estimated, this fact can be used to calculate its proper 3d position from the SAR image and thus design the optimal facade orientation for this specific building. Without the knowledge of h_{BA}, it is not possible as there might exist numerous imaged projections of the actual window's 3d location, see Fig. 6.4b.

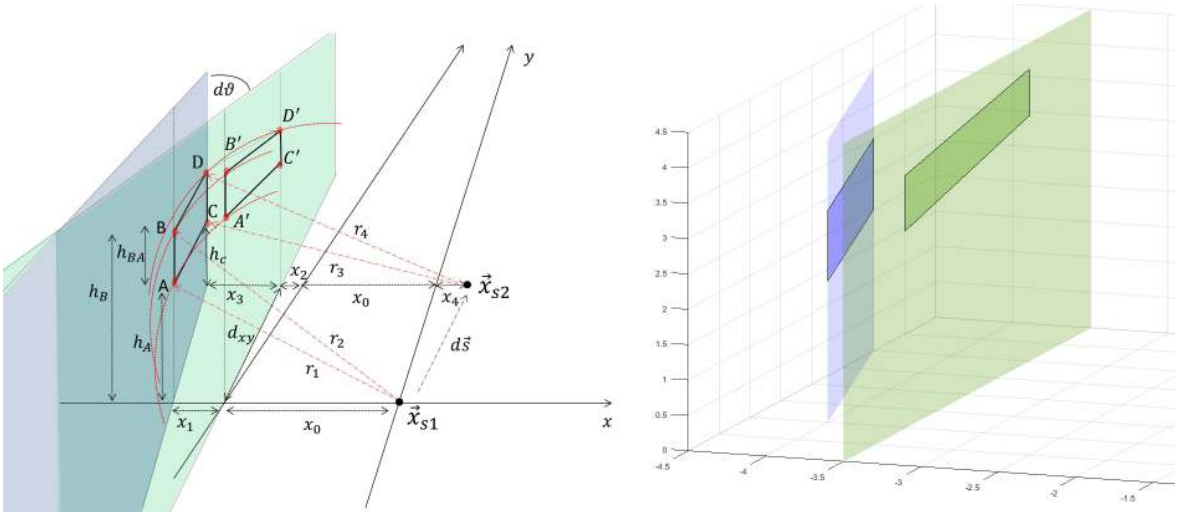

(a) (b)

Figure 6.4: Visualization of required parameters to adapt the facade's imaging plane. a) Mapping of a window on green focusing plane while its true position is aligned to blue facade, b) simulated window position on green focusing facade and true position on real facade in blue. Axes in meters. Optical distortion due to wrong estimation of ϑ_f and r_c.

With $d_1 = x_0 + x_1$ and $d_2 = x_0 + x_2 + x_3 + x_4$ as the perpendicular distance to the true facade and knowing h_{BA}, the absolute height of Point A can be derived by

$$h_A^2 = h_B^2 - r_2^2 + r_1^2 = (h_A + h_{BA})^2 - r_2^2 + r_1^2 \Leftrightarrow h_A = \frac{r_2^2 - r_1^2 - h_{BA}^2}{2 \cdot h_{BA}} \tag{6.3}$$

and points B to D likewise. Further d_1 analog to $d_2, ...$ can be derived by

$$d_1 = \sqrt{r_1^2 - h_A^2} = \sqrt{r_1^2 - (\frac{r_2^2 - r_1^2 - h_{BA}^2}{2h_{BA}})^2}. \tag{6.4}$$

By manually identifying the point A' at image position $(x_{A'}, y_{A'})$ the radial vector $\vec{\mathbf{r}}_1$ at the sensor's position $\vec{\mathbf{x}}_{s1}$ follows to

$$\vec{\mathbf{r}}_1 = x_{A'} \cdot \vec{\mathbf{a}} \cdot \delta_p + y_{A'} \cdot \vec{\mathbf{b}} \cdot \delta_p - \vec{\mathbf{x}}_{s1} \tag{6.5}$$

with δ_p the image pixel spacing. By determining the real 3d position of point A with $\vec{\mathbf{A}} = (\vec{\mathbf{x}}_{s1} + (d_1 \cos(\vartheta_f), d_1 \sin(\vartheta_f), h_A)')$ and point B to D analog, the angular difference $d\vartheta$ can finally be derived by

$$d\vartheta = \arctan\left(\frac{x_3 - x_1}{d_{xy}}\right). \tag{6.6}$$

By choosing vector $\vec{\mathbf{A}}$ as a new support vector, the design of an adapted focusing plane shifted by $d\vartheta$ in a next iteration step can lead to better focusing performance and fewer image distortions.

7 Experimental setup

This Chapter comprises the experimental setups, sensor and processing specifications, and the carrier platforms for airborne CSAR and carborne mobile radar mapping (MRM) campaigns. It further presents the flight campaigns with the small aircraft that have been carried out to acquire the data sets and shows the carborne experiments that have been investigated.

7.1 CSAR measurement campaigns with a W-band sensor

The airborne measurement campaigns were conducted with the ultralight aircraft DELPHIN, a single-engine aircraft owned and operated by the Fraunhofer Institute for High Frequency Physics and Radar Techniques FHR. The highly flexible carrier platform is well suited for measurement campaigns at comparatively low altitudes and can handle non-linear or circular trajectories even at smaller radii. These characteristics are meaningful for the described sensor application as due to the comparatively low output power in W-band, only limited flight altitudes can be handled. Typical flight velocities are usually in the range of 30 $\frac{m}{s}$ to 40 $\frac{m}{s}$ resulting in PRF cycles up to 10 kHz when using antennas with larger azimuth beam widths. Flight heights over urban areas were carried out just above the prescribed minimum flight altitude of 300 m. Due to the aircraft's small size and low weight, it is significantly more sensitive to thermal lift, wind, or gusts of wind. The requirements on the GPS/INS are correspondingly very high, especially concerning the use of the very high carrier frequency of the SAR sensor. To put this into perspective, at W-band with $\lambda = 3.2$ mm, the flight path measurement error along the length of a synthetic aperture needs to be less than 0.3 mm, which is very challenging to be achieved with state of the art GPS/INS systems. The carrier platform and the installed W-band sensor below the wing with a total weight of 25 kg are shown in Fig. 7.1.

7.1.1 SAR sensor setup

The W-band radar sensor which was investigated for collecting the data sets is called Millimeter Radar using Analog and Digital Approach (MIRANDA-94). It is a compact and lightweight FMCW airborne SAR sensor operating at 94 GHz with up to 10 GHz RF bandwidth designed and operated at Fraunhofer FHR. Essential active components of the radar like the frequency multiplier from 8 GHz to 94 GHz, the frequency mixer, LNA, and the RF HPA based on gallium arsenide technology are designed at Fraunhofer IAF [Ture et al., 2017; Quay et al., 2017]. With these new components, the sensor is a further development of the experimental W-band airborne sensor based on Stanko et al. [2011]. A direct digital synthesizer (DDS) generates the highly linear chirp signal from 1.1 GHz to 2 GHz resulting in a multiplied maximal RF bandwidth of 10 GHz. As described in Chapter 3, the sensor's front-end is embedded in a stabilized mechanical mount, a CSM 130 designed from Somag. Based on the developed beam steering methodology presented in Chapter 3, this allows a real-time and autonomous beam-steering mode specially designed for circular trajectories. In this mode, the antennas are continuously aligned in the direction of the

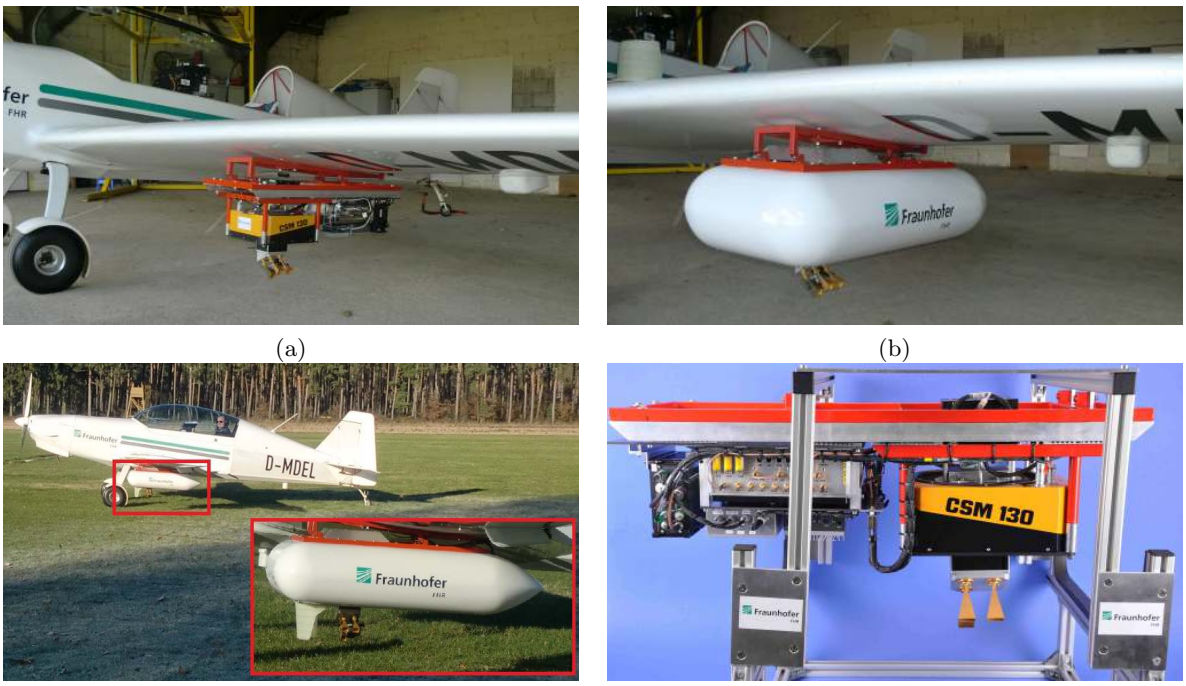

Figure 7.1: Beam-stabilized W-band FMCW MIRANDA-94 SAR on the platform wing of ultralight aircraft. a) Open sensor unit. Right side is board computer and data recording. Left side stores the radar front-end integrated in the stabilized mount (Somag CSM 130) with GPS/INS sensor on top of mount, b) sensor ready for flight. Only sending and receiving antennas stay maneuverable. System's total weight is 25 kg, c) UL with SAR sensor before start, d) complete sensor in the lab. Front-end right, back-end left side. Transmitting antenna on the right, two receiving antennas on the left, which can be installed in semi-polarimetric or interferometric mode.

target coordinate set by the operator. Moreover, this GPS coordinate can be modified during the flight from the ground station, making the system very flexible.

Transmitting and receiving antennas are 10° standard gain horn antennas, see the antenna pattern in Fig. 7.2. Experiments conducted by Palm et al. [2013]; Palm et al. [2015, 2016c] with slotted antennas with 1.3 to 3° azimuth beam width indicated that the footprint of these antennas was far too small to collect a 360° circular data set of a reasonable area on the ground. The antenna gain is considerably reduced by applying the more comprehensive horn antennas, which limits the flight height. Still, the advantages are a significantly wider footprint and considerably higher RF bandwidths. Applying the horn antennas and flying the sensor at the height of 300-350 m above ground level results in a 360° illuminated area on the ground of 100-150 m in diameter. A further advantage is that the requirements for the accuracy of the beam stabilization are less stringent with a broader beam, which is beneficial considering the platform's more turbulent flight patterns on circular trajectories.

The decoupling between both antennas is 65 dB. An 800 kHz high-pass filter (−20 dB) is further used to suppress strong targets at close range. At last, the applied GPS/INS device is a highly sensitive fiber optic gyro GPS/INS unit from IGI. Sensor and GPS/INS specs are further specified and summarized in Table 7.1. The whole sensor system is operated by remote control from a ground station with usually two people and two laptops. A remote data link from the ground station to the aircraft can operate in ranges up to 40 km. It is used to monitor the radar system, set new parameters, or to start/stop the data recording. In addition, a real-time stripmap

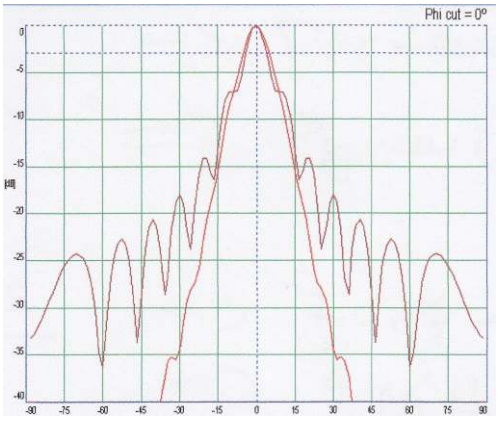

Figure 7.2: Antenna pattern (E-plane and H-plane) of standard gain horn antennas which are used as transmitting and receiving antennas.

Parameter	*Description*
Transmission mode	FMCW
Transmit power	800 mW / 29 dBm
Center frequency	94 GHz
RF bandwidth	1 and 2 GHz
Range resolution	15 or 7.5 cm
Azimuth resolution ViCSAR	15 or 7 cm
Azimuth high-resolution mode	< 3 cm
Sweep repetition frequency	10 kHz
Chirp duration	96.80 μs
Sampling frequency	100 MHz
Antenna dimension	27 x 23 mm
Weight front-end	2.4 kg
Total sensor weight	25 kg
Polarization	VV
Fiber optic GPS/INS	IGI AeroControl (2.4 kg)
Mount (gimbal)	Somag CSM130 (7 kg)
Mount angular steering rate	15° / sec
Mount alignment accuracy	$< 0.1°$ rms
Mount maximum steerable angle	Roll/Pitch ±15°, Heading ±25°
Alignment update rate	4 Hz
GPS/INS accuracy real-time	Roll/Pitch $< 0.025°$ rms, Heading $< 0.05°$ rms
GPS/INS accuracy postprocessed	Roll/Pitch $< 0.003°$ rms, Heading $< 0.007°$ rms
GPS/INS accuracy position	< 0.022 m

Table 7.1: Basic system parameters of MIRANDA-94 CSAR.

SAR processing with reduced resolution computed on-board the aircraft is also transmitted via the same data link and can be evaluated on the ground. This specific processing architecture is described in more detail in [Palm et al., 2014]. In a last but very critical step, the data from the GPS/INS is further post-processed, and a differential GPS (dGPS) solution for the trajectory is computed.

7.1.2 CSAR flight campaigns

As analyzed in Chapter 3.2, selecting suitable flight parameters is a trade-off between the size of the illuminated spot, flight radius, output power, and desired objects to be resolved. Therefore, optimal flight parameters for the CSAR mode have been evaluated in multiple trials. The campaign to evaluate the beam alignment is presented in Fig. 7.3, where the TIRA radom at the Fraunhofer FHR's Institute area was selected as the target. A flight height of 300 m was chosen corresponding to a flight radius of 360 m. Further flight and processing parameters of the circular SAR campaigns can be found in Table 7.2.

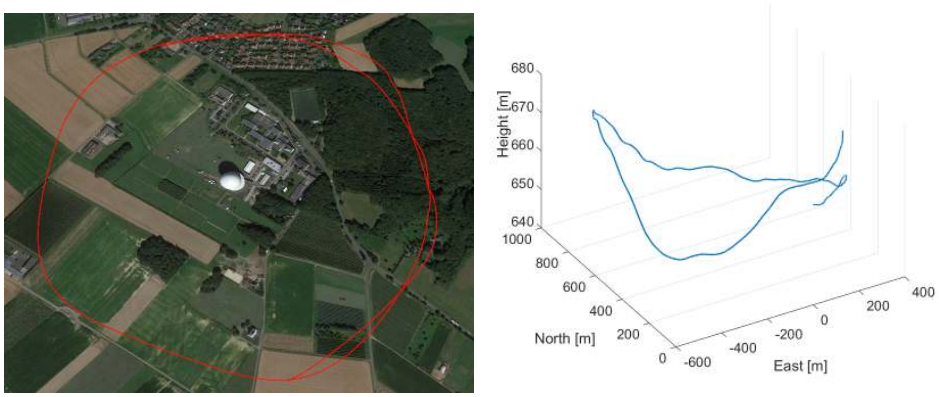

(a) (b)

Figure 7.3: Experimental CSAR campaign to validate the beam-stabilizing mode. Data set was collected at the FHR with the TIRA radom as the target center. a) Aerial photo [Google] with circular flight path (red), b) 3d flight trajectory which indicates the turbulent flight path. Flight height corresponds to approx. 300 m above ground level (AGL).

Parameter	*Description*
Flight height	300 m AGL
Flight radius	360 m
Flight velocity	$\approx 35\ \frac{m}{s}$
Mean roll angle	$\approx 8°$
Antenna beam width	10° x 10°
Processed aspect angle (ViCSAR)	0.8° - 1.2°
Processed aspect angle (HighRes)	8.5°
Subaperture overlap factor	80 %
Pixel spacing	12 or 3 cm
Full aspect illuminated area on ground	120 x 120 m
Mean target range	470 m
Installed depression angle	30°

Table 7.2: Geometry and processing parameters for the CSAR campaigns.

The primary campaign to reconstruct the urban scenario is shown in Fig. 7.4. The Figure shows three corresponding flight trajectories and the illuminated region of each flight, while the track profile of the urban trajectory is presented in Fig. 7.5 in red. An almost identical flight campaign over this scene was done in advance with slightly modified sensor parameters (1 GHz RF bandwidth). These data are also evaluated in Chapter 8.2.

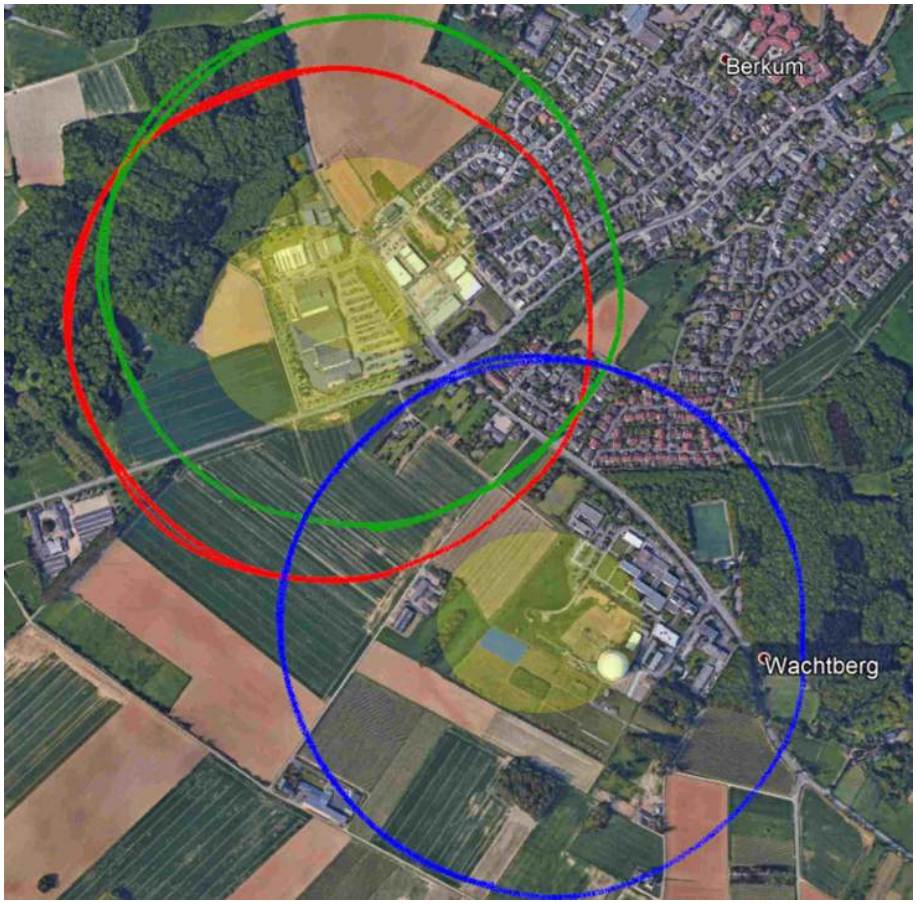

(a)

Figure 7.4: CSAR flight campaign over two target scenes. The northern trajectory (red) collected a data set over urban area with large buildings in Wachtberg. The southern trajectory (blue) shows data set collection over the Fraunhofer Institute where several corner reflectors were placed at different heights on a nearby heliport. The green trajectory indicates data set collection over a round about traffic to investigate moving cars. The illuminated spot of each campaign is highlighted with the yellow circles.

The northern trajectory (red) in Fig. 7.5a shows the campaign in a flight height of 320 m above a commercial shopping area with several large buildings built next to each other. In addition, there is a parking space in front of the buildings, several trees, a gas station, greenhouses, several street lamps, and a 12 m high advertising tower. The height of the objects and the roofs are determined by using an airborne laser scanning (ALS) data set*. Two corner reflectors ($10\,\mathrm{x}\,10\,cm^2$) are placed in the scene to assess the backscattering behavior over the entire aspect interval, but these reflectors are not used for autofocus routines.

The southern trajectory (blue) of Fig. 7.5a shows the flight over the FHR in Wachtberg. Several small corner reflectors of different sizes and heights were placed in the area of an adjacent heliport to validate the proposed methods of 3d extraction. Parts of this setup are presented in Fig. 7.6. The complete scene consisted of 11 square trihedral and triangular trihedral corner reflectors. The square trihedrals had an edge length of 4 cm corresponding to 8 dBsm. Five of the targets were placed on the ground, and the other six reflectors were placed at different heights ranging from 0.75 m to 4 m. The ground distance between the corners was a few decimeters up to

*Source: Land NRW 2020 - Data licence Germany - Version 2.0

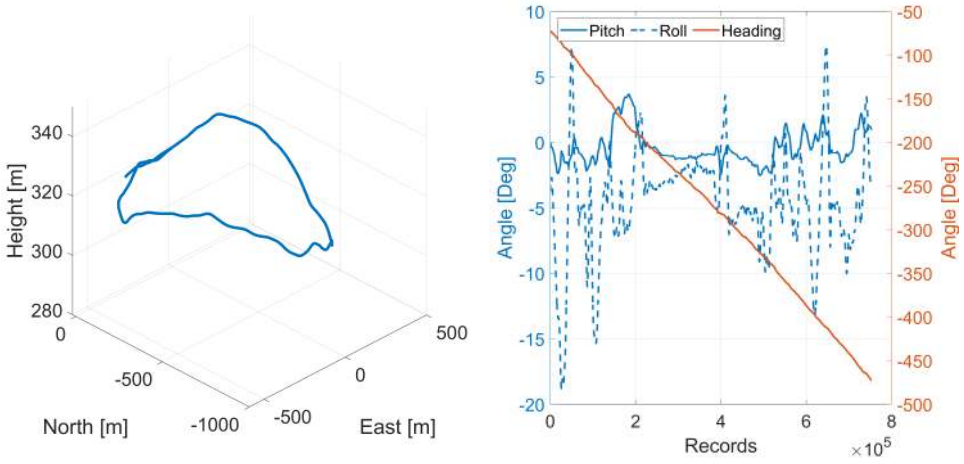

(a) (b)

Figure 7.5: Track profile and angular orientation of the urban trajectory from Fig. 7.4 (red). a) 3d trajectory profile, b) variation of pitch, roll and heading during flight.

several meters. Three triangular trihedrals had an edge length of 3 cm (-5 dBsm) to validate the system's and proposed method's ability to measure the exact 3d location of tiny targets. The exact distances of the corners and their heights were measured with a laser rangefinder device. A second experiment was carried out 50 m south of the corner reflectors in a meadow (blue rectangle). In a $30 \times 50\, m^2$ square, eight people moved at walking pace in different directions and thus served as small targets for evaluating the method's ability to detect small ground moving targets (GMTs).

The second northern trajectory of Fig. 7.5a was intended to collect data for an indication of larger GMTs, especially cars. Located right next to the commercial shopping area is a roundabout. In addition, some objects like street lamps or trees were also selected for 3d estimation. The mean depression angle during the flight is about 35° with an ideal roll angle of the plane of about 5° - 8°. Due to the influence of the wind and the thermals, the rolling movements of the aircraft during the measurement are temporarily much more substantial, see Fig. 7.5. The update rate for the mount's alignment was set to 4 Hz. In previous flight tests, it turned out that this is sufficient for a smooth illumination of the target region. If the correction rate is too slow, the beam tends to run out of the target, and the alignment is too volatile. An even higher rate would lead to excessive and unnecessary correction steps.

7.2 Mobile radar mapping measurement campaigns

The radar sensor investigated for the carborne mobile mapping applications is an experimental, compact FMCW sensor operating at a center frequency of 300 GHz with up to 50 GHz bandwidth called MIRANDA-300. Similar to the W-band sensor, it has been designed and is operated by Fraunhofer FHR whereby several critical components like the heterodyne receiver module, frequency multiplier, and HPA are developed at Fraunhofer IAF [Tessmann et al., 2014; Weber et al., 2011; Tessmann et al., 2011]. Currently, the output power of 5 dBm limits the system to relatively short-range applications.

The radar front-end and back-end, including GPS antenna, is installed in a van which can be used to drive on conventional roads, see Fig. 7.7. Data-recording and GPS/INS devices are

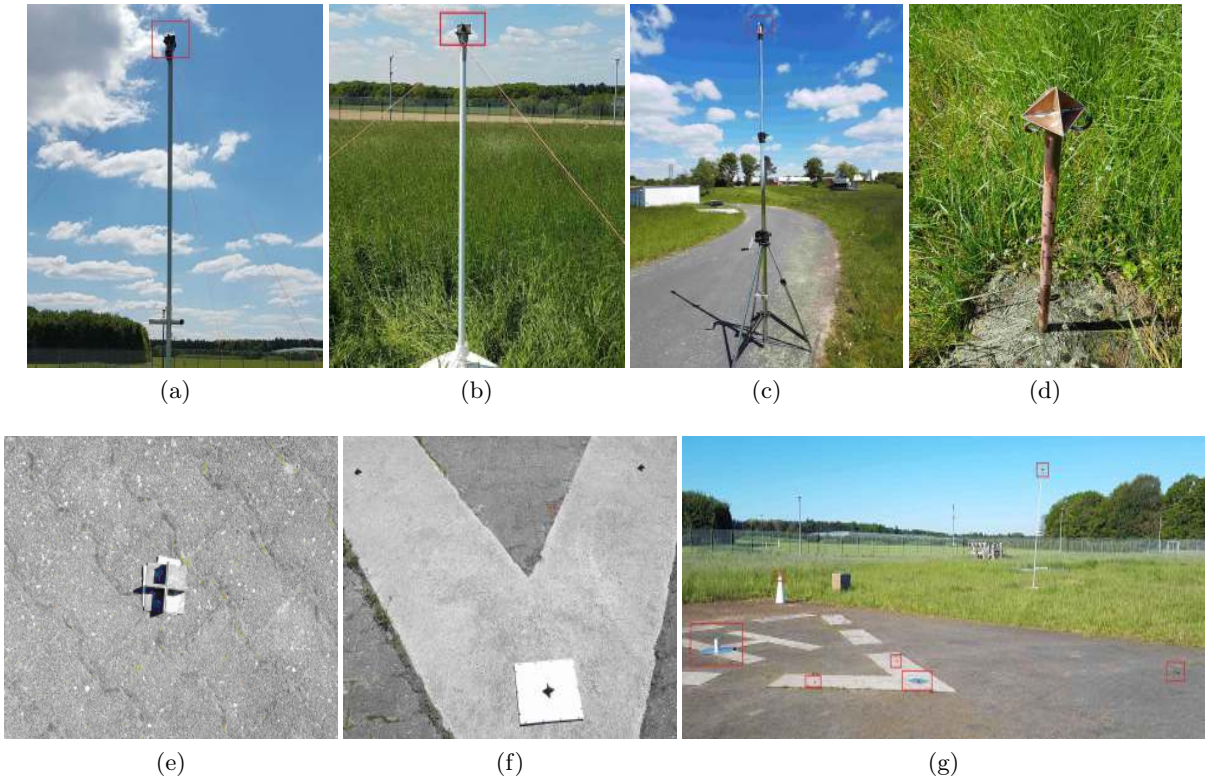

Figure 7.6: Photos of selected corner reflectors. Small sized reflectors are placed on a heliport at different heights dh to validate height extraction. a) 4 cm edge length square trihedral at dh=4 m, b) square trihedral at dh=2.10 m, c) square trihedral on a tripod at dh=3.75 m, d) triangular trihedral at dh=1.10 m, e) square trihedral placed on the ground at dh=0 m, f) 3 tiny trihedrals with 3 cm edge length at dh=0 m, g) view of the scene center with reflectors.

identical to the described W-band sensor. Further system parameters are listed in Table 7.3. In terms of its pure dimensions, the system could, of course, also be installed in a standard small car. Transmit and receive antennas are positioned behind the open window of the van at a height of 2 m in side-looking configuration (downwards for street mapping, upwards for facade mapping), see Fig. 7.7c. The depression angle can be modified manually depending on the data collection geometry. The GPS antenna is placed on top of the van while the sensor's back-end and the GPS/INS is installed in the interior. Several experimental campaigns on conventional roads in a small town illuminating the facades of a row of houses with a typical elevation angle of 30° - 35° were conducted. While collecting the data, the typical length of a trajectory was 50 m up to a few hundred meters, the distance to the facades was between 5 to 15 m, see Fig. 7.7d. The SRF is 5.2 kHz, and the platform's velocity in data acquisition mode can reach up to 40 km/h. Of course, platform velocity can be increased in exchange for reduced resolution. The parameters of the sensor and the geometry for processing are further specified in Table 7.3. The orientation of the facade of a row of illuminated houses as input parameter can be extracted from Google Earth.

Similar experiments were conducted in street mapping mode driving on conventional roads illuminating the opposite roadway, parking lane, and nearby infrastructure. The trajectories thereby have a length of a few ten meters up to some kilometers. With this side-looking geometry, a strip width of typically up to $\sim$ 6 m beneath the platform can be illuminated. The geometry and the processing parameters of the experiments are listed in Table 7.3. Again, a significant improvement of the path data is obtained by a further dGPS processing of the track.

(a) (b)

(c) (d)

Figure 7.7: Carborne MRM experiments. a) Antennas behind the window in street mapping mode. The window is opened while operating, b) distances of an experimental setup in street mapping mode, c) antennas and front-end behind open window in facade mapping mode, d) geometry and distances in facade mapping mode.

Table 7.3: Carborne sensor and processing parameters.

Transmission mode	FMCW
Transmit power	5 dBm
Center frequency	300 GHz
RF bandwidth	30 − 50 GHz
Sweep repetition frequency	5.2 kHz
Sensor dimensions	20 x 10 x 10 cm
Weight SAR system	5 kg
Power consumption	5 V / 3 W
GPS/INS system	IGI AEROControl
Sensor height above ground	2 m
Maximum measuring distance	25 m
Measuring depth	5 - 12 m
Velocity of van	up to 40 km/h
Processed bandwidth	30 GHz
Processed resolution	5 mm
Pixel spacing	2 mm

8 Experimental results and discussion

This Chapter presents the results of the carried out experiments and discusses the outcome. In Section 8.1, the evaluation of the beam steering mode on the CSAR processing is presented. In Section 8.2, the results of the urban mapping in very high resolution and ViCSAR mode are shown. In Section 8.3, the results on the measurement to derive the spatial resolution are presented. In Section 8.4, the extraction of 3d urban scene information and the generation of a global point cloud of the urban scene is demonstrated. In Section 8.5, the generation of a shadow-reduced view of the urban scene and the fusion of information acquired from different aspects in a single SAR image in high resolution is presented. Finally, in Section 8.6, the results of the urban mobile mapping experiments are demonstrated.

8.1 Real-time beam alignment

To analyze the quality of the implemented beam stabilization method from Chapter 3, the results are demonstrated in Fig. 8.1. A SAR image of the Fraunhofer TIRA (see Fig.7.3) that served as a target for this experiment is presented in Fig. 8.1a. The SAR image is composed of a non-coherent sum of all subaperture images geocoded in the same image domain and was one of the first images processed from the sensor. Each pixel indicates the mean backscattering from the entire collected 360° data set. A heatmap of the illuminated spotlight area is presented in Fig. 8.1b that indicates for each pixel how often it is located within the area of the 3 dB main lobe of each subaperture. More than 2000 overlapping subapertures were processed. A composite image of

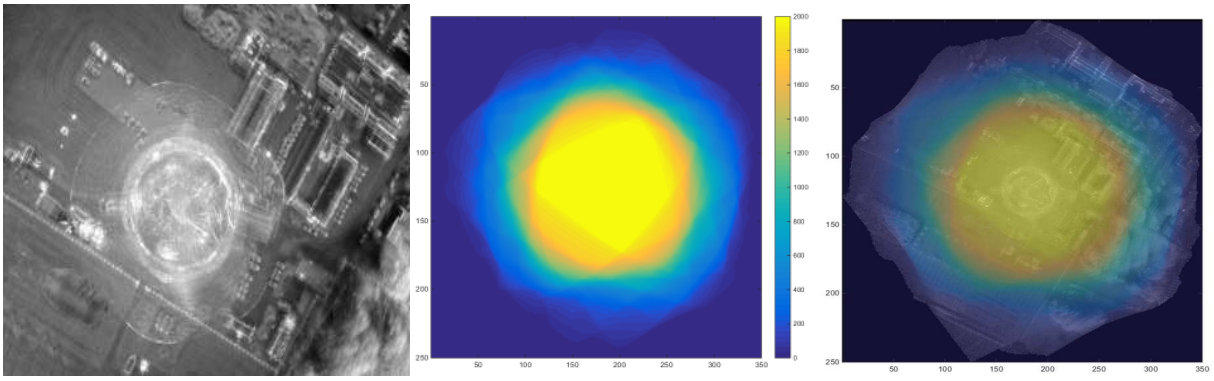

(a) (b) (c)

Figure 8.1: Heatmap of the beam-stabilized illuminated area. Axes in [m]. a) Full aspect CSAR multilook image of illuminated spot, b) heatmap of illuminated spot. Each pixel represents the number of subapertures in which it is located within the 3 dB lobe. Despite the challenging flight path, the center is constantly illuminated, c) multilook CSAR and superimposed heatmap.

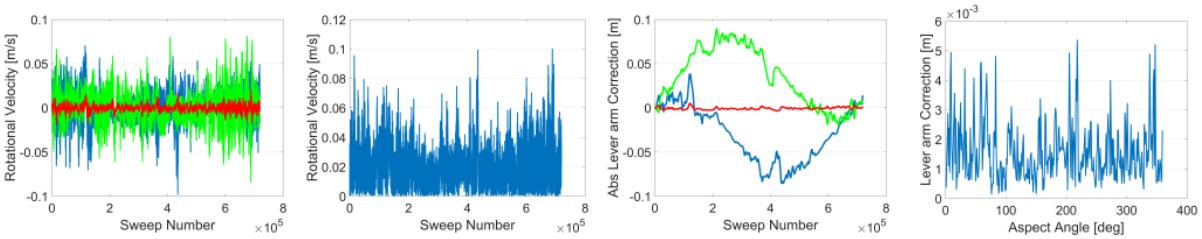

(a) (b) (c) (d)

Figure 8.2: Effects of the lever arm and the mechanical beam steering on CSAR processing. a) Rotational velocity for each radar sweep separated according to orientation: north (blue), east (green), down (red), b) absolute rotational velocity per sweep, c) absolute lever arm displacement during circular aperture, d) mean absolute position shift within a single coherent synthetic aperture of $\varphi_{az} = 0.8°$. Rotations in these short periods already cause positioning drifts up to 5 mm. In W-band, this corresponds to more than one wavelength that needs to be corrected.

the multilook SAR and the superimposed heatmap is presented in Fig. 8.1c. It is observable that the beam remains clearly fixed on the target center, whereby the TIRA is constantly illuminated despite the challenging flight geometry, see Fig. 7.3. Further, the dimensions indicate that the 360° illuminated spot on the ground has a diameter of approximately 120-140 m in the current geometry with a 300 m flight height.

The influence of the rotational velocity $\vec{\mathbf{v}}_r$ of the mount for each radar sweep during a full circular trajectory of about 80 s is demonstrated in Fig. 8.2. The different colors correspond to the rotational speed in northing (blue), easting (green) and down direction (red). The maximum value of $|\vec{\mathbf{v}}_r|$ remains below $0.08\frac{m}{s}$, which is considerably below the platform velocity of $v_s = 35\frac{m}{s}$, but with a different angle to the scene. The lever arm displacement of the antenna's phase center during a complete circular path is illustrated in Fig. 8.2c. In contrast, Fig. 8.2d indicates the calculated mean absolute position shift within a single synthetic aperture of an angular integration of 0.8°.

8.1.1 Discussion

The experiments indicate that the presented combination of compact SAR sensor on small aircraft and real-time controlled beam alignment allows the acquisition of full aspect airborne circular SAR data sets even on small radii. Both the update rate of the implemented beam alignment and the maximum angular steering rate of the mount system are adequate. The footprint is sufficient to map a small urban area.

Evaluating the collected data set with respect to the rotational velocity indicates that the effect of the additional fast time Doppler shift caused by the mount's movement during a single radar sweep is minimal. With $\lambda = 3.2$ mm, this results in a theoretical maximum Doppler shift of $f_d = 50$ Hz during a sweep. Compared to an assumed platform drift angle of 5°, the mean Doppler shift caused by $\vec{\mathbf{v}}_s$ is 1900 Hz and therefore significantly larger.

The absolute displacement of the phase center due to the mount's rotation adds up to several centimeters that would result in dislocations and shiftings in the consecutive subaperture images. However, more important are the findings of Fig. 8.2d. Within a synthetic aperture of only $\varphi_{az} = 0.8°$, it indicates position shifts up to 3-5 mm that is in the order of magnitude of one full wavelength. To achieve coherent SAR processing, it is, therefore, necessary to correct both the fast time Doppler and, in particular, the absolute displacement errors that are caused by the mechanical steering as indicated by equation 4.22.

With a higher output power of a possible next-generation system, the platform may fly higher while enlarging the footprint. Thus, a 360° data acquisition of considerably larger scenes becomes realistic. Recently, this stabilized configuration has also been successfully applied in an E-band communication experiment where a highly accurate beam alignment of an airborne antenna to an arbitrary ground station was required [Kallfass et al., 2019].

8.2 Urban mapping and monitoring

Very high-resolution stripmap SAR

The quality of the processed subaperture CSAR images shall be compared to the results of the designed processor that can be achieved on a linear trajectory of the sensor. Since the linear trajectory is less ambitious, it shall give a ground truth of what can be expected from a W-band high-resolution sensor combined with the designed, optimized SAR processor. Fig. 8.3 presents a SAR image processed with 2.5 cm resolution (6 GHz RF bandwidth) in both azimuth and range showing the TIRA and parts of the FHR's Institute area. The TIRA is located at the center of the image, smaller buildings and parked cars on the right and left side of the radom, a fence with fence posts (A) and street lamps (E) at the lower part, and several trees (B) on the right side. In addition, smaller objects like gully covers (C) on the right side of the TIRA or shadows of 2 standing persons (D) on the left side can also be observed.

Very high-resolution subaperture CSAR of an urban area

A 360° SAR image of the urban scene is presented in Fig. 8.4 and the 3d extraction of this scene in Section 8.4. The SAR image is built up by the 360° non-coherent fusion of all subaperture

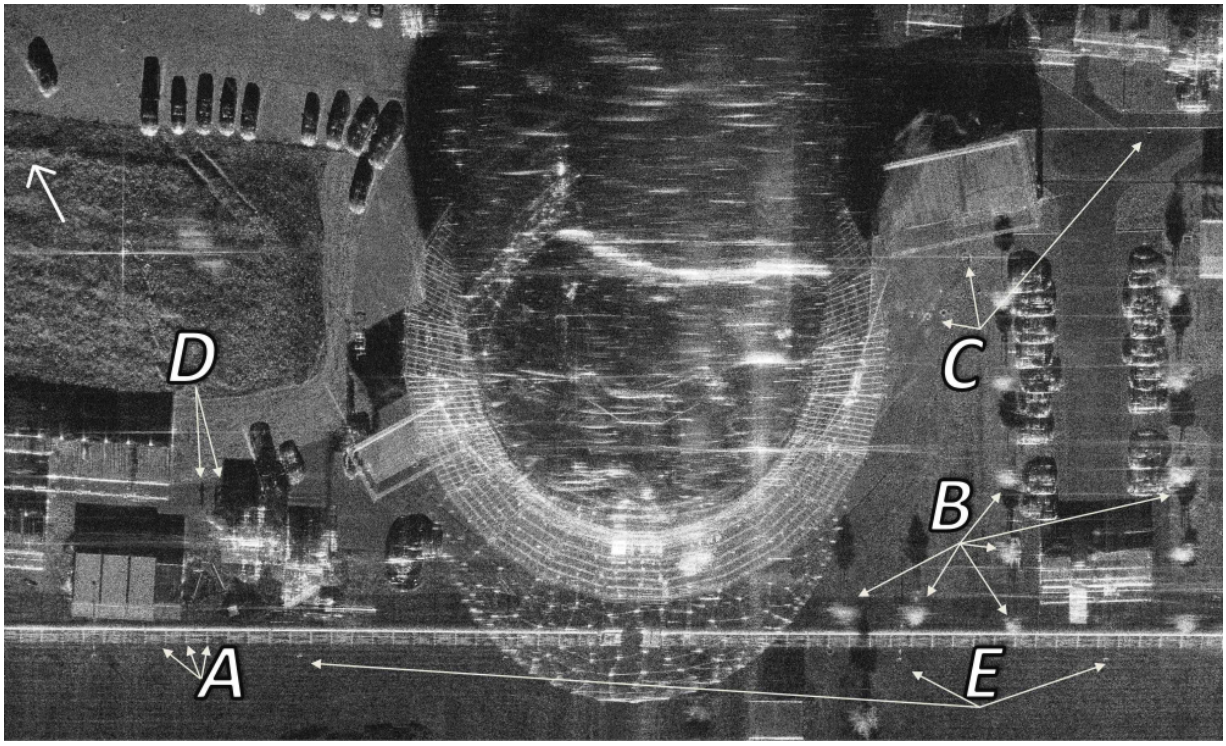

Figure 8.3: 2.5 cm resolution W-band stripmap SAR image. Ground truth image to validate the designed and optimized SAR processor with data acquired on linear trajectory. The image shows the TIRA and adjacent buildings and parking areas. The white arrow on the left indicates north.

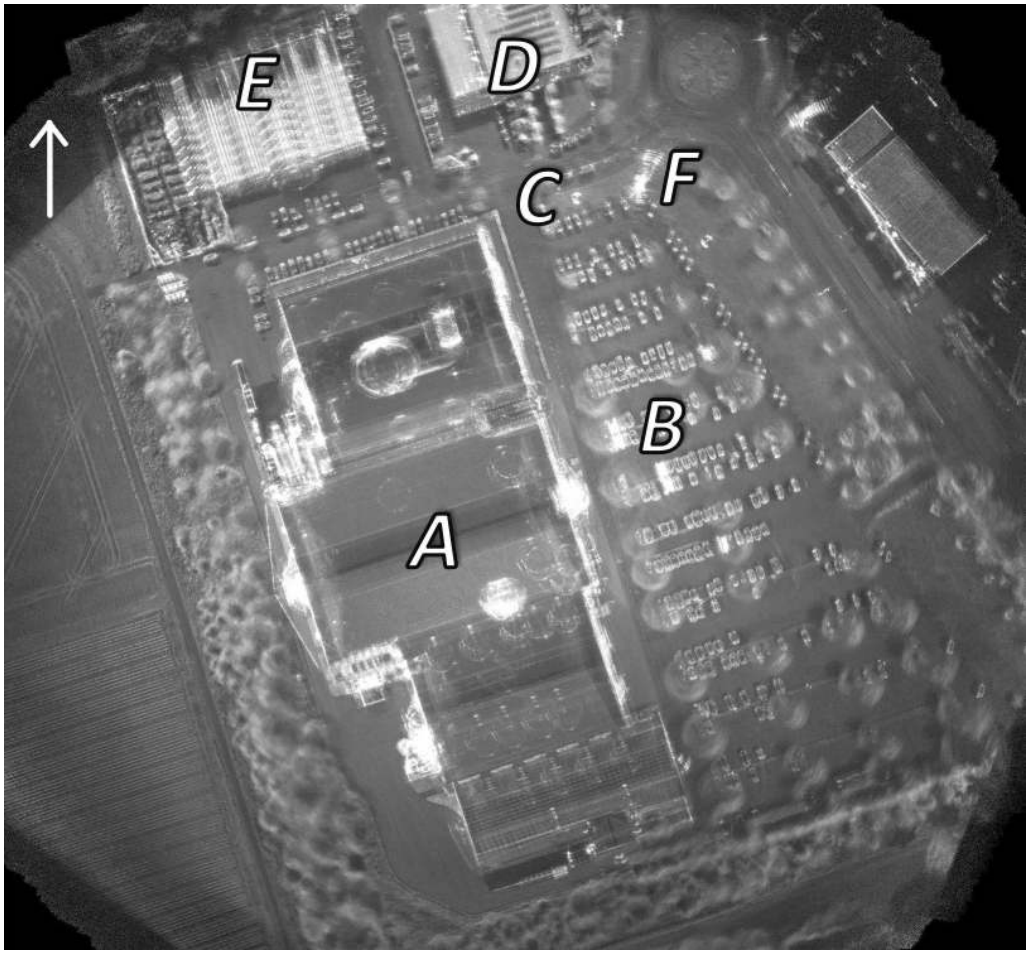

Figure 8.4: 360° multilook SAR image of an urban scene orientated to the north. Non-coherent sum of all aspects. The image shows buildings, a parking area, a gas station and greenhouses.

images processed at 7.5 cm spatial resolution in both dimensions. The outer edges of the image are not acquired from all aspects, which is indicated by fewer projections that typically show a circular pattern. Information from the main building in the center (A) and, to a large extent, from two adjacent buildings and the parking space (B) are acquired from 360°. There, the typical circular projections of strong scatterers are observable that can also be found in areas where trees are standing. Notice, although the circular blurred projections of the treetops are visible, it is possible to observe the ground below the treetops. This feature allows the observation of parked cars below the foliage as the car's backscattering from multiple aspects is significantly higher.

A corner reflector (C) can be seen at the northern end of the parking area that does not project to a full circle. The projection indicates that the corner was not located at reference height. This reflector has been used to evaluate the spatial resolution capacity in Section 8.3. Further north, a gas station (D) and on the western side of it, greenhouses (E) are located. Close to the corner and between the parking area and roundabout traffic in the northeast, a 12 m high metallic advertising tower (F) is situated. Multiple different street lamps are located in the parking area and around the building complex, but they are difficult to observe in the SAR image due to the multilook process. However, at some locations, the street lamp bases are visible, and their positions can be compared to the findings in Fig. 8.30.

Results for individual subapertures of the same scene processed at very high resolution are presented in Fig. 8.5. The radar's line of sight is east in Fig. 8.5a, while northeast in Fig. 8.5b.

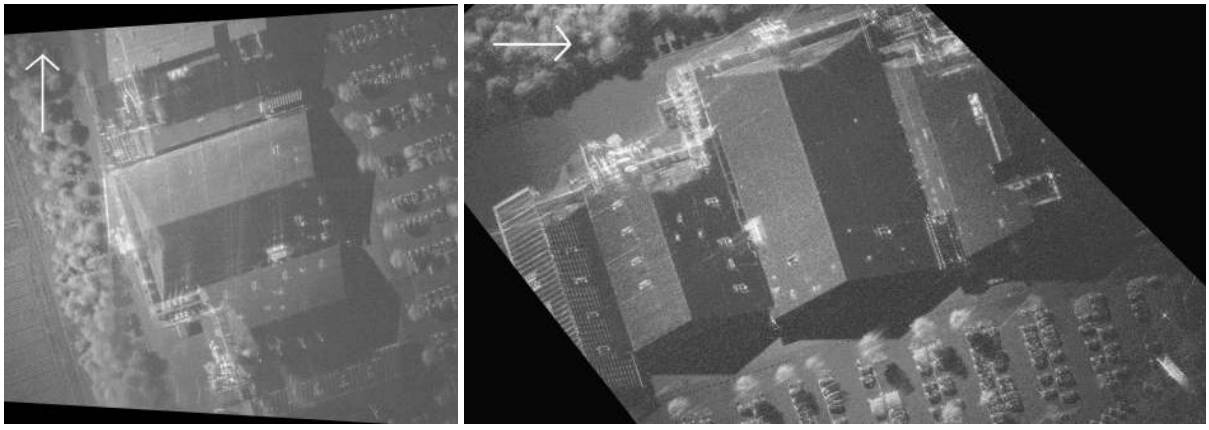

(a) (b)

Figure 8.5: Very high-resolution subaperture SAR image of an urban scene. Images are focused at ground level, white arrow indicates north. Zoom on buildings. a) Radar looking direction east, b) radar looking direction northeast. Image rotated by 90°.

It shows two aspects of the scene focused at ground level with $\varphi_{az} = 8.5°$. Since $\varphi_{az} >> \varphi_{max}$, scatterers above the focusing plane start to defocus. Based on these high-resolution SAR images from multiple aspects, the 3d extraction methods are evaluated in Section 8.4.

ViCSAR results of urban scenes

The W-band ViCSAR results of the urban scene of Fig. 7.4 with $\delta_x = 15\,\text{cm}$ and $\delta_y = 11\,\text{cm}$ are presented in Fig. 8.6. Eight subaperture images are selected that already reveal the scene dynamics. The center of this circular trajectory was located around the corner at the northern part of the parking area, and the sensor's RF bandwidth for this data set was only 1 GHz. The shadows of moving cars on the roads are marked in red. Two corner reflectors were also placed beside the road and marked in yellow. The left reflector was used for a more detailed quantified analysis of the aspect integration interval concerning the applied focusing height in Fig. 8.11. Since $\varphi_{max} = 0.8°$, high objects are well focused in the scene and show only very low peak signal loss. This can be recognized while investigating high objects like the building's roof or the high advertisement panel. These objects are sharply imaged; both the structure of the roof and small installations on it can be observed. Even the elements of an approx. 9 m high street lamp are imaged as a sharp point target (blue rectangle). These tiny but high targets are more noticeable by watching the CSAR video due to the constant movement of their projections (varying foreshortening, frequent flashing).

The anisotropic behavior in urban scenes especially regarding the roof area, is evident by comparing the different aspects. Substantial variation was examined at the roof by only slightly changing the aspect angle. In Fig. 8.6a and 8.6b, the aspect change is only 2°, while in Fig. 8.6e and 8.6f, only 1°. Despite the small aspect change, the reflection is considerably different. In Fig. 8.6g, the 1° difference is color-coded for even better visualization. This differs from volume scatterers such as trees, e.g., that provide homogeneous backscatter behavior for large aspects. Fig. 8.6a further indicates a courtyard with only minimal aspect visibility. It shows the interior of the northern building (green rectangle). Four windows, a door, facade and roof gable are projected in the image and can be observed. This characteristic of imaging objects with small aspect visibility is more investigated in [Palm et al., 2016c] with Ka-band data.

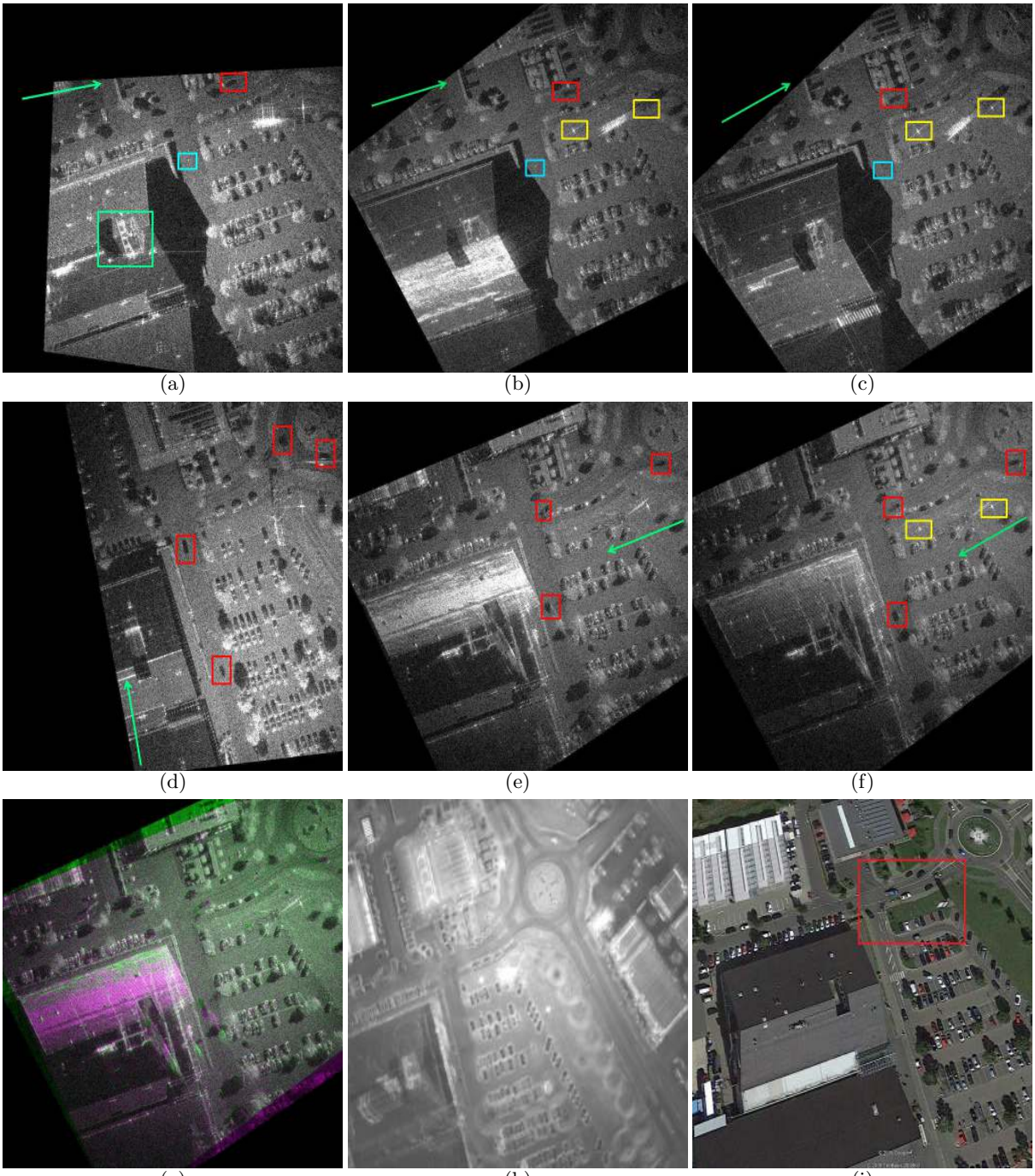

Figure 8.6: ViCSAR results of an urban scene. Zoom of selected images from the generated image stack with a 15 cm x 11 cm resolution. The line of sight is indicated by the green arrow. Strong anisotropic behavior of the scatterer can be evaluated. Observation of areas which are difficult to access (inner yard of the building) are feasible. Corners marked with yellow, moving cars with red and the top of a street lamp with blue rectangles. Aspects for each image are: a) $\varphi = 75°$, b) $\varphi = 73°$, c) $\varphi = 71°$, d) $\varphi = 348°$, e) $\varphi = 255°$, f) $\varphi = 254°$, g) composite image of two aspect views with 1° aspect difference (Fig. 8.6e and Fig. 8.6f) to indicate the anisotropic backscattering behavior of the roof area, h) non-coherent sum of all processed subapertures of scene, i) aerial photo (Google).

(a) (b) (c) (d)

Figure 8.7: Zoom of houses in an urban scene at different aspect angles with 7.5 cm resolution. Sequence shows the homogenous and relatively stable backscattering of flat roofs while gable roofs have a very anisotropic appearance. The roof of the red house is covered with tiles and can be divided into three different angles of inclination. Sectors with equal slope show similar scattering. a) $\varphi = 170°$, flash of northern roof area, b) $\varphi = 158°$, flash of top southern area with dormer windows, c) $\varphi = 124°$, flash of steep southern roof part, e) aerial photo (Google).

The aspect sensitivity of backscattering from different roof areas is further outlined in Fig. 8.7 that shows the flashing parts of a smaller roof at different viewing angles from a data set in a nearby village [Photogrammetry and Remote Sensing - TUM, 2020]. Flat roofs that are typically not covered with roof tiles tend to show a more homogeneous scattering behavior with only a few dominant scatterers that can be used for radargrammetric evaluation. Similar to Fig. 8.6, gabled roofs covered with roof tiles typically show fragile backscattering behavior for large aspects but tend to flash temporarily depending on the roof's pitch and the radar's viewing angle. The temporal distance of the flashing in the sequence of Fig. 8.7 is due to the fact that parts of the roof have a different slope. Sectors with equal tilt angles show similar backscattering.

Moving shadow tracking

The possibility of a dynamic scene evaluation by the subsequent representation of the data in W-band ViCSAR mode is demonstrated in Fig. 8.8 and Fig. 8.9. The results indicate the ability to detect and track multiple moving shadows in consecutive image frames. Both Figures show multiple moving cars at a moderate speed driving in the area of the parking space and the roundabout traffic.

In Fig. 8.8, eight subaperture ViCSAR images from the processed video sequence are selected while a section of the whole video can be watched following the link in [Photogrammetry and Remote Sensing - TUM, 2020]. The images are chosen in consecutive order in a slightly varying time interval t to represent the scene's dynamics better. In total, a section of the scene comprising a time interval of 6.3 s while covering 28° aspect change is illustrated. Each CSAR image has an approximate illumination time of 0.2 s corresponding to 0.8° aspect change. Some vehicles are marked with different colors to recognize them in the image sequence better. The radar's looking direction is from the north. It can be seen when and where cars approach the roundabout, when they enter, and at which exit they leave it again. Since a small tree is at one road's entrance, cars are partially covered depending on the radar's viewing angle.

At last, Fig. 8.9 shows very nicely in a timeline of 30 s the dynamics of the scene while the process of parking a car is captured. In the first six images ((a) - (f)), the car maneuvers into the parking lot, and while it is moving slowly front- and backward, the car's signature constantly changes direction due to the varying radial velocity. In (c), the signature of the parking car

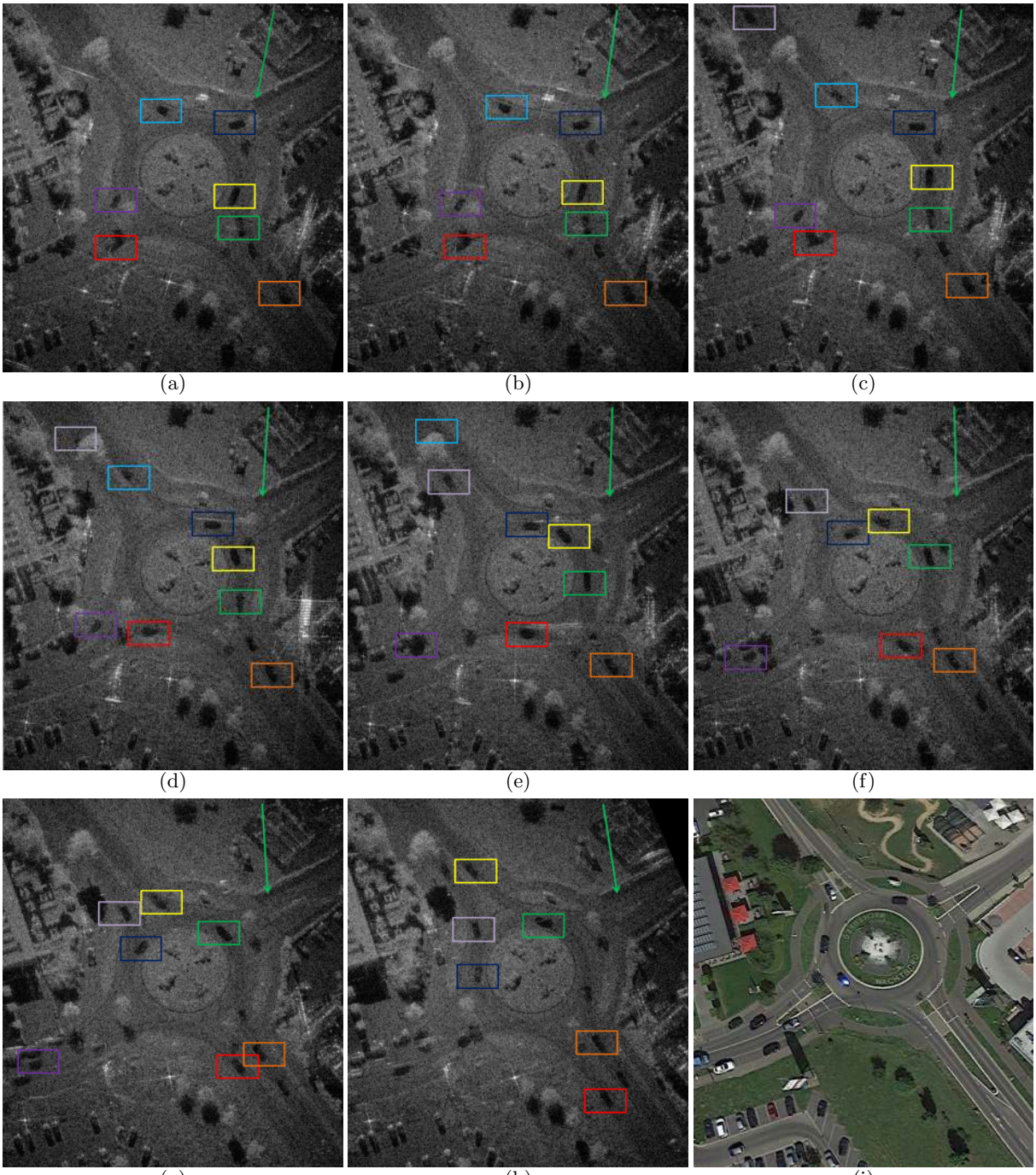

Figure 8.8: ViCSAR results and visualization of moving cars in the monitored urban scene with 15 cm x 11 cm resolution. Images are chosen in consecutive order but in a non linear temporal interval time t to better visualize the dynamic scene. The aspect is indicated with the green arrow. Multiple moving cars in the roundabout traffic can be tracked by their shadows and are displayed with different colors. It can be determined where and when a vehicle enters the roundabout and where it leaves it. Illumination time is 0.2 s, which assures that the shadows of the moving vehicles at moderate speed are only marginally smeared during their motion. a) t = 0 s, $\varphi = 195°$, b) t = 0.2 s, $\varphi = 194°$, c) t = 0.8 s, $\varphi = 192°$, d) t = 1.6 s, $\varphi = 188°$, e) t = 2.8 s, $\varphi = 183°$, f) t = 4 s, $\varphi = 177°$, g) t = 5.2 s, $\varphi = 172°$, h) t = 6.4 s, $\varphi = 167°$, i) aerial photo (Google).

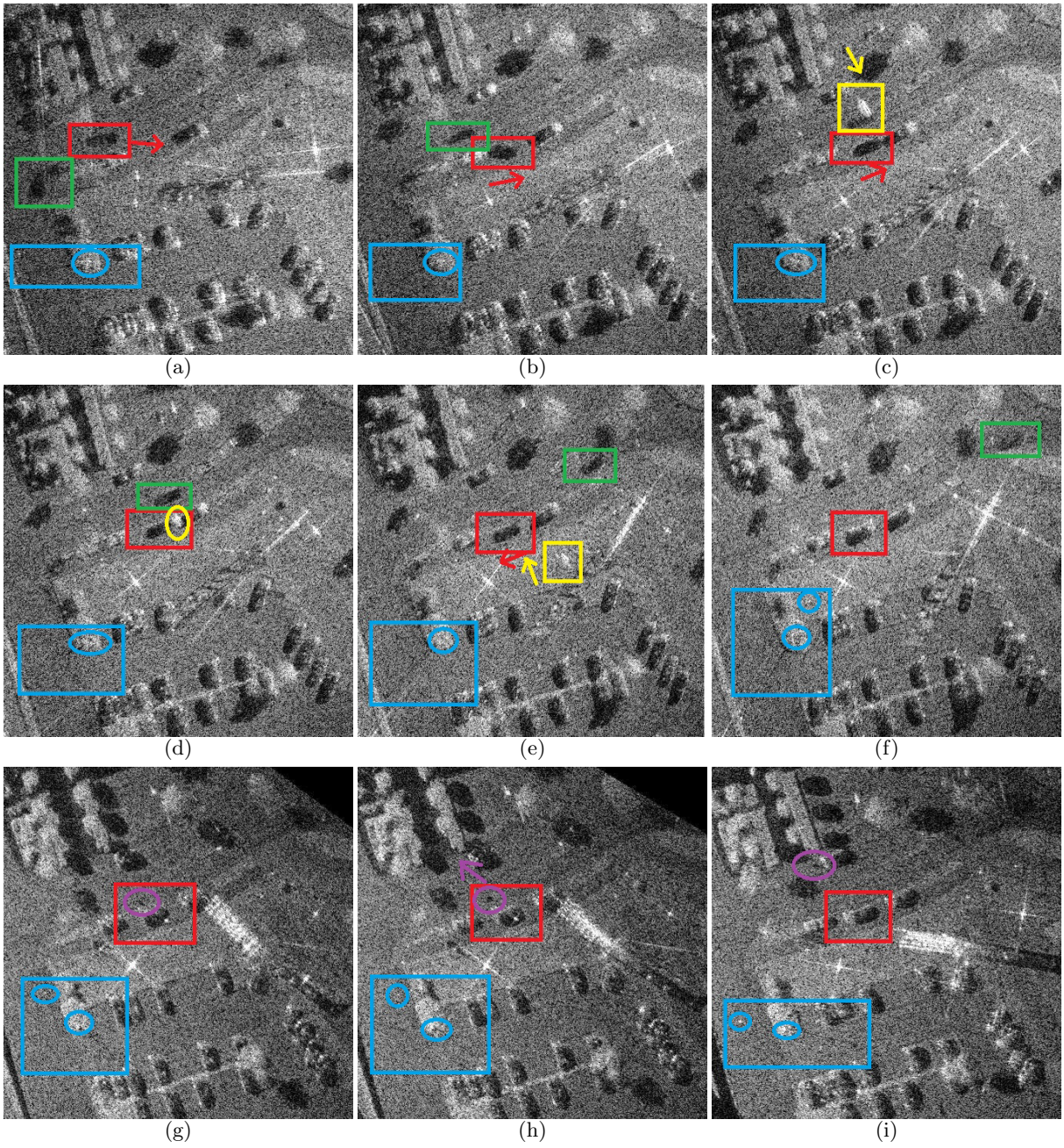

Figure 8.9: $50\,m^2$ zoom of ViCSAR results of scene dynamics with a parking car and a person leaving it in a 30 s time period. Due to the changing radial velocity, the car's signature can be tracked temporarily. Parking car in red, second car green. A street lamp and its shadow in blue. a) t = 0 s, car drives forward into the parking space, b) t = 3.36 s, car inside the parking space, still driving forward, c) t = 4.84 s, car reaches front vehicle and brakes. Signature (positive Doppler) in yellow interferes temporary with second car's shadow, d) t = 5.28 s, car stops. Signature coincides with position, e) t = 7.56 s, car moves slowly backwards. Signature now has negative Doppler and is offset in opposite direction, f) t = 9.44 s, car stops, g) t = 23.6 s, after 13 s a person leaves the car (shadow in purple circle), h) t = 24.56 s, person crosses the street, i) t = 28.84 s, after 5 s, the person has reached the opposite sidewalk. Street lamp base (blue circle) and signature of street lamp is mainly hidden in clutter but observable over asphalt background (blue rectangle).

interferes temporarily (≈ 8 frames) with the moving shadow of a second car driving past. After the car has parked, after 13 seconds, it can be seen that a small moving shadow is leaving the vehicle, crossing the street, and moving towards the gas station. This moving shadow will most likely have been a passenger or the driver of the parked car. More moving shadows of individual persons can be observed in [Photogrammetry and Remote Sensing - TUM, 2020] next to a church.

8.2.1 Discussion

Both the data acquired from linear and circular trajectories could be processed with very high resolution and sharp imaging quality. High detail levels from a specific aspect can be observed from individual subapertures while other regions are shadowed. A more or less shadow-free and comprehensive view of the urban area that even allows observing objects hidden by trees can be obtained by a non-coherent fusion of all aspects. However, the detail level is then reduced due to the multilook process and varying foreshortening behavior.

An effect that considerably complicates radargrammetric methods remains the very strong anisotropic behavior of objects in CSAR mode. In the context of urban scenes, this is particularly evident in the backscattering behavior of sloping roofs. However, from the perspective of the radar, roofs cover a large portion of the illuminated area in urban scenes. Therefore, the correct height estimation of buildings is highly dependent on the accurate 3d assessment of their roofs. Methods based on tracking movement of scatterers in ViCSAR image sequences in flat roof areas should therefore focus on the roof's border or edges. On the other hand, it requires a form of image segmentation in advance. In gabled roof areas covered with tiles it seems promising to ignore aspect views that cause the flashing of the roof but to focus on areas that are more favorable in revealing the individual tiles as a cluster of point scatterers. However, matching roof areas from different aspects with correlation-based methods to extract 3d seems challenging.

Further, in the urban scene, the parking space has only one entrance which also serves as an exit. Assuming that all vehicles had to enter or leave this area, it can be determined during the scene's illumination how many cars are leaving or entering the parking place, where they park, and which direction they go. If there is also a favorable clutter background, even smaller objects such as moving persons leaving or entering the car can be visualized. Also, which building the person enters may then be observed. Considering then multiple circular trajectories over a more extended period, the great potential in urban monitoring becomes obvious that may open a variety of new applications, such as disaster management or security applications. Due to the small aperture length in W-band, it is interesting to note that a potential observer may usually find an optimal viewing angle for smaller targets with low angular visibility that are generally more difficult to reveal.

Besides the short subapertures in length, the benefit also comes from a second feature in W-band. In X- or L-band data, roads usually appear relatively dark in the SAR images since the wavelength in these bands is too large compared to the surface roughness of asphalt. In W-band, the surface is rougher showing diffuse scattering and a potential shadow of a car on the road shows significantly more contrast. Of course, the shadow of moving objects off-road on different backgrounds like grass should even show more contrast level.

Further, the very short integration time per image causes the shadows of the moving vehicles - the shadowed region projected and the footprint of the object itself - in the presented data set to be only marginally smeared. Thus, they show a clear contrast compared to the ground clutter. This effect might be different when observing areas like highways where cars tend to move much faster or when the radius of the circular trajectory with constant sensor velocity becomes larger (longer illumination time). Then, a further reduction of aspect integration is necessary as the car

otherwise travels too far, which causes the shadow to smear. While the car is moving, parts of the area that were covered with shadow at the beginning of the subaperture will be uncovered at the end of the subaperture and vice versa. Assuming a car has four times the speed on a highway (120 km/h instead of 30 km/h), this would result in a reduction of the illumination time to 0.05 s, still generating an azimuth resolution of 50 cm that is still acceptable.

The shadow footprint of a car thereby differs in particular from the shadow footprint of a static object like a tree since it is independent of the radar's illumination geometry. A strategy to even enhance the detection of moving cars might include focusing only on the detection of moving shadows in the vicinity of mapped roads, but this shall not be part of this work. Further, processing the consecutive, geocoded CSAR images allows determining the speed, the actual position, the object's shadow size, and the direction of multiple moving objects in the scene. It might also be examined whether refocusing the vehicle's signature from the estimated motion parameters is possible. Thus, a W-band ViCSAR sequence may allow constantly monitoring the dynamics of an urban scene, and it should be investigated on which detail level a real-time change detection in subsequent processing steps is feasible.

Nevertheless, it could be observed that the contrast of the moving shadows varies partially. This is due to the superposition of moving shadows and signatures or sidelobes of different moving cars, or sidelobes from strong ground clutter in the vicinity. For example, the contrast variation of the shadow of the car in the green box from Fig. 8.8 (a) - (h) is due to the smeared signature of a different moving car at the beginning (b) - (c) and the strong sidelobes of the flashing object (d) right beside the street. From (e) - (h), the shadow shows again more contrast as there is no further superposition. This effect can happen if multiple moving targets are in the scene or strong ground clutter beside the road. Since the aspect angle of the sensor towards the moving targets constantly changes and the wavelength of the radar is very small, the Doppler shift f_d caused by the radial component changes very fast. The interference with the smeared signature and a car's shadow was a few frames in the observed examples. A possible tracking algorithm would have to threshold such ghost echos.

8.3 Achieved spatial resolution in CSAR mode

Spatial resolution of ground targets

An analysis of the achievable spatial resolution in high-resolution CSAR mode without the use of autofocus routines is given in Fig. 8.10. Therefore, the corner reflector placed on the grass at the northern exit of the parking place is analyzed, see Fig. 8.4 and zoomed-in in Fig. 8.10h. In contrast to the measurements of Fig. 8.11, the exact target height and thus the reference height of the object was not only measured by GPS but complemented with the SAR data. Since it is a strong target embedded in clutter, the height extraction is very reliable. The kurtosis operator of Chapter 5.2.3 was applied on a $2\,m^2$ rectangle with the corner in the center. With a height step size of 0.1 m in a small interval around the measured GPS height, the accurate corner height was estimated from the data to be 40 cm lower. Fig. 8.10 thus presents the measured resolution for range and azimuth as a function of φ_{az} at the calibrated corner height H_{opt}.

Dependent on φ_{az}, the pixel spacing was selected to 8 mm up to $\varphi_{az} = 10°$ and 4 mm for more extensive φ_{az} to meet the theoretically achievable very high resolution. Of course, this was only achievable in a reasonable time due to the highly parallel SAR processor. To put this into perspective, a $30\,m^2$ area then already corresponds to more than 50 million pixels. The 80 cm wide search window to measure the target's point spread function (PSF) was then interpolated again by a factor of 16. Fig. 8.10g compares the measured results with the theoretically achievable

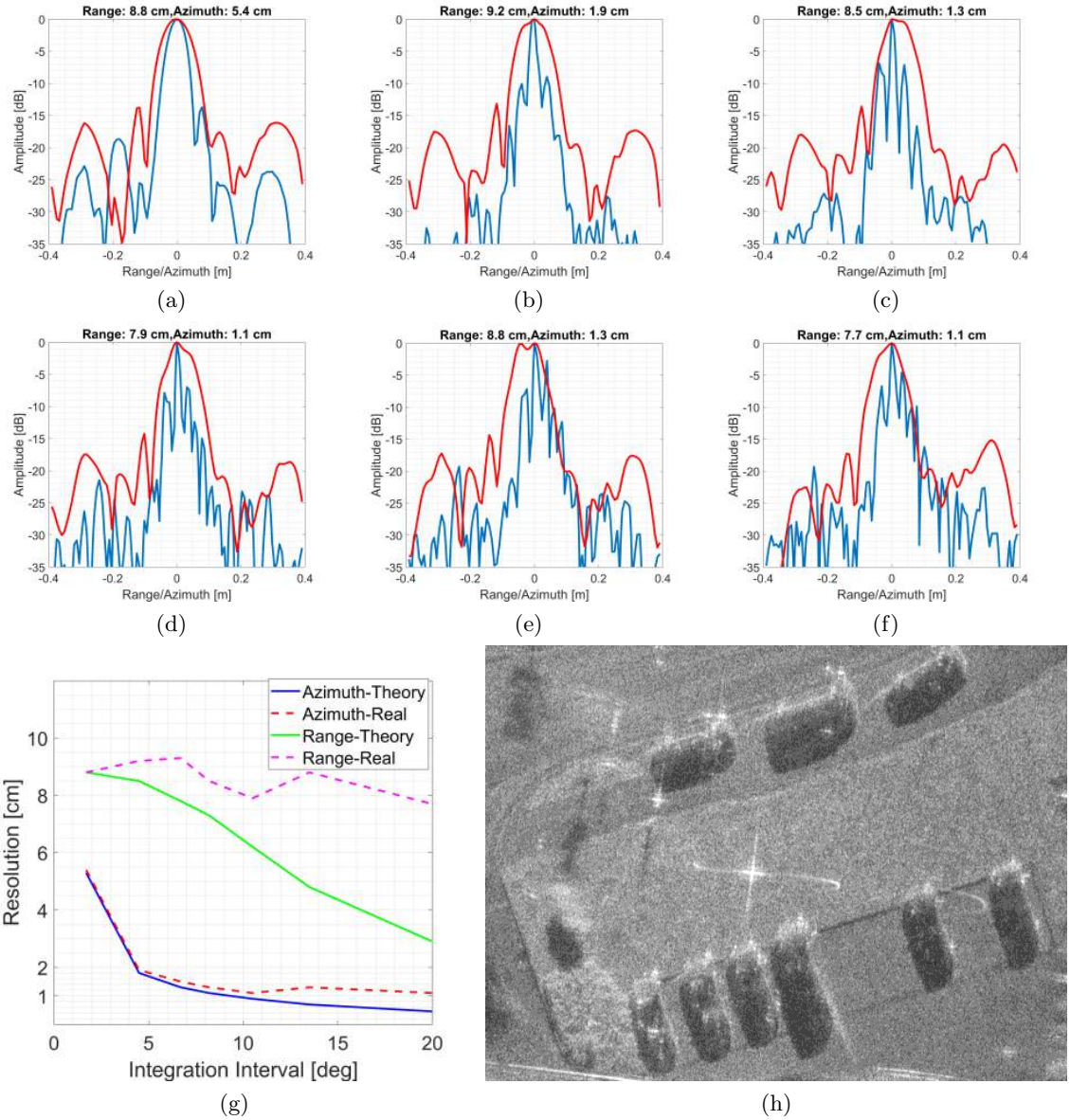

Figure 8.10: Measured spatial resolution of a corner as a function of the aspect integration interval φ_{az} after deriving the absolute height of the target. Azimuth resolution (blue), Range resolution (red). RF bandwidth is 2 GHz. a) $\varphi_{az} = 1.7°$, b) $\varphi_{az} = 4.5°$, c) $\varphi_{az} = 8°$, d) $\varphi_{az} = 10°$, e) $\varphi_{az} = 13.5°$, f) $\varphi_{az} = 20°$, g) measured spatial compared to theoretically achievable resolution, h) zoom of CSAR image from Fig. 8.4 with corner in the center focused at corner's reference height, $\varphi_{az} = 10°$, pixel spacing 8 mm.

resolution. The corner scene that was investigated is presented at reference height H_{opt} in very high resolution with $\varphi_{az} = 10°$ corresponding to $\delta_y = 1$ cm and $\delta_x = 8$ cm in Fig. 8.10h.

Comparison of the resolution of ground and high targets

Quantified analysis of the resolution of ground targets concerning their height is presented in Fig. 8.11, where the left corner reflector of Fig. 8.6 is evaluated. In contrast, analysis for simulated objects can be found in [Palm et al., 2019]. Compared to the previous data set in Fig. 8.10, in this data set, the RF bandwidth was only 1 GHz and the reference height was derived by GPS. To better visualize these findings with urban scene data, Fig. 8.11s and 8.11t present a zoom of the

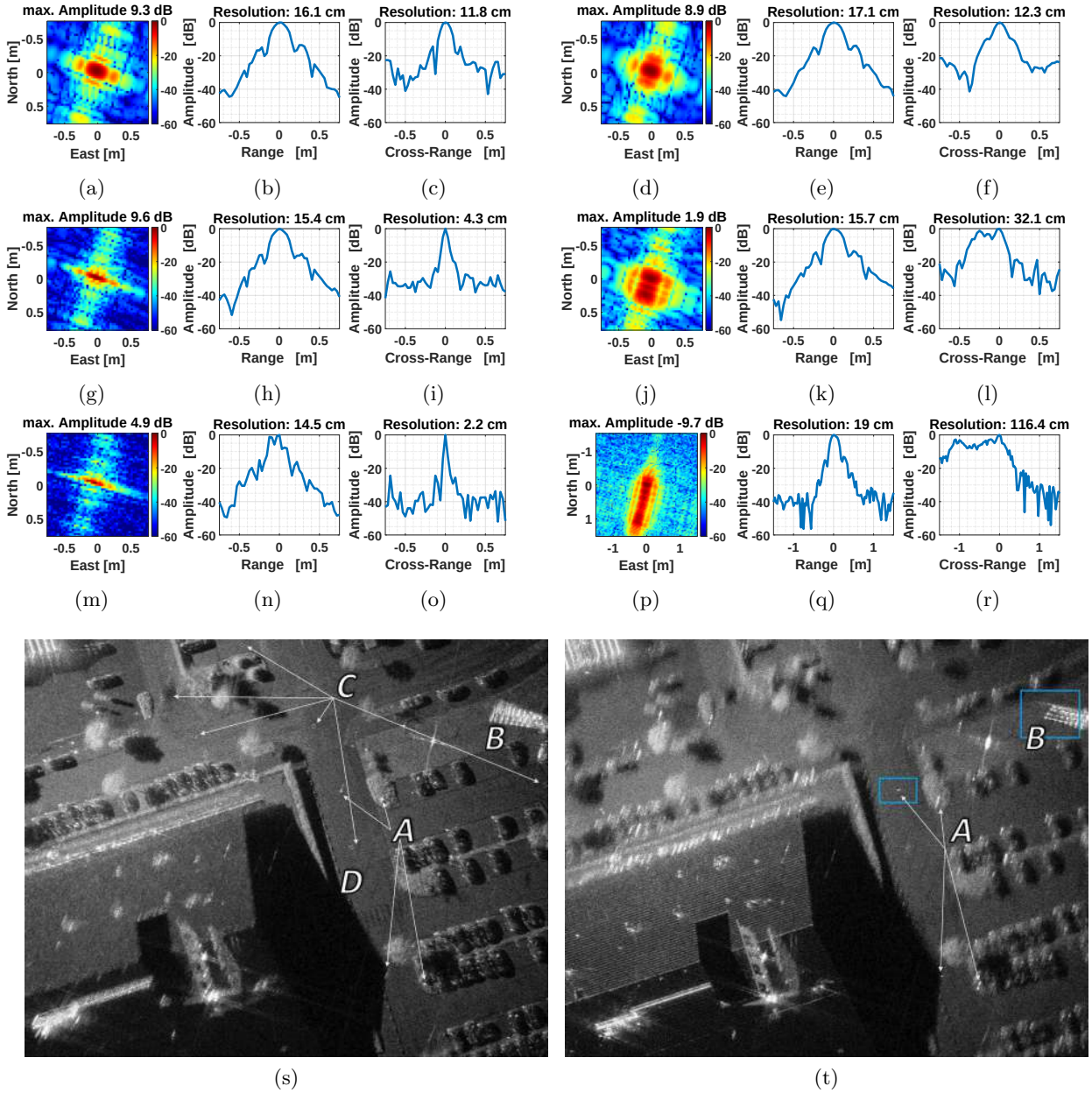

Figure 8.11: CSAR focusing of reflectors and an urban scene on different heights. Focusing at measured GPS height dh =0 m (left side) and dh = 10 m (right side). Aspect interval φ_{az} varies from $\varphi = 0.8°$ (ViCSAR mode) to $\varphi = 8.5°$ (HiRes mode), RF bandwidth is 1 GHz. a)-c) Target at dh = 0 m, $\varphi_{az} = 0.8°$, d)-f) dh = 10 m, $\varphi_{az} = 0.8°$, g)-i) dh = 0 m, $\varphi_{az} = 2°$, j)-l) dh = 10 m, $\varphi_{az} = 2°$, m)-o) dh = 0 m, $\varphi_{az} = 8.5°$, p)-r) dh = 10 m, $\varphi_{az} = 8.5°$. Peak signal loss of -0.8 dB in ViCSAR mode (first row). At $\varphi_{az} = 2°$ (2nd row), peak signal loss of -7.7 dB and azimuth resolution δ_y of 32 cm (4.3 cm ground target). At $\varphi_{az} = 8.5°$ (3rd row), peak signal loss of -14.6 dB and δ_y of 116 cm (2.2 cm for ground target). Due to the circular geometry, also δ_x is enhanced, s) $\varphi_{az} = 8.5°$, dh = 0 m, (δ_y = 2 cm for ground targets). Objects at ground (gully covers (C), street crosswalk (D)) are well focused, high structures like roofs are blurred, t) $\varphi_{az} = 8.5°$, dh = 10 m. Ground is blurred, high objects like roof, street lamp (A) or advertisement panel (B) (both blue rectangle) are in focus. Moving objects are no longer recognizable due to large φ_{az}.

urban area in very high-resolution mode ($\varphi_{az} = 8.5°$, 3 cm pixel spacing). On the left side, the data was focused at the reference height of the parking space while on the right side 10 m higher.

Thus, the result at 0 m height is a very high-resolution SAR image where all ground structures are in focus. Parked cars are nicely observable; even the gully covers (C) and paintings on the street like the crosswalk (D) in front of the building can be recognized. However, due to the large φ_{az}, moving cars are no longer visible (moving shadow smearing), and high structures like the roof are blurred. On the right side, all ground elements are defocused while high objects like parts of the roof, street lamps (A) (lamp base and lamp), or parts of the advertisement panel (B) are focused. The shape of the roof gable and small installations are imaged at very high resolution.

8.3.1 Discussion

Spatial resolution of ground targets

The experiments to determine the maximum spatial resolution further indicate that this can only be determined precisely if the height of the reference object is known precisely. In the resolution range that this work deals with, a height difference of several decimeters is sufficient to distort the measurements. The results show that a resolution in azimuth in the order of 1.1-1.3 cm is feasible for isotropic targets without the use of autofocus routines. However, the results only present the measurement within a partial area of the circular aperture of 20° of a single circle. In addition, the scene is in the main beam of the radar and therefore has a high SNR. At a different position on the circular path or if the flight movement is even more unsteady, the resolution capacity may be significantly worse.

The evaluation also indicates that from an angular interval of approx. 10°, no increase in resolution (neither azimuth nor range) is achieved compared with the theoretical resolution. This suggests that from this point onwards, the coherence is lost. To obtain more reliable statements about the resolution capability, many different isotropic targets whose heights have been precisely measured would have to be analyzed on many circular trajectories on different radii and in different weather and wind conditions. Then a statistical statement could be derived which order of magnitude is to be expected under different conditions. However, given this constellation of operating a small aircraft in a relatively turbulent flight condition, a resolution in the centimeter scale could not necessarily be expected. But it also demonstrates the quality of the most modern GPS/INS sensors, including dGPS post-processing software with the simultaneous implementation of a SAR processor optimized for such geometries and wavelengths.

Comparison of the resolution of ground and high targets

The results for the point target focusing at different heights are consistent with the derivations from Chapter 4.3. The cross-range resolution and the peak signal level (−0.4 dB) of a 10 m high target remain constant up to an azimuth integration of $\varphi_{max} = 0.8°$. The integration over a larger aspect interval significantly increases the resolution of the ground target in azimuth and range up to δ_y =2.2 cm and δ_x =12 cm at $\varphi_{az} = 8.5°$, respectively. However, in this data set, the height of the corner was derived only from GPS data that proved to be slightly erroneous in Fig. 8.10. Also, the RF bandwidth was limited to 1 GHz.

For high objects, the peak signal level and the resolution deteriorates considerably (−18.6 dB, δ_y =116 cm at 8.5°). On the one hand, this indicates that in unknown urban terrain, it is reasonable to limit the integration interval to a derived interval of φ_{max} or to a small multiply of it. All data in a fixed height interval is then sharply focused. On the other hand, this feature of focusing a specific height can be valuable if details of a scene shall be displayed in very high resolution or the actual height of an object is questionable in urban scenes. Therefore, choosing the proper aspect angle interval is a matter of application.

8.4 3d extraction in single-channel CSAR mode

This Section presents the results for 3d extraction of small point-like objects in Section 8.4.1 and for individual targets in Section 8.4.2 by applying the non-coherent tracking approach. The results for the 3d point cloud generation of urban scenes are shown in Section 8.4.3.

8.4.1 3d extraction of point-like objects

This Section presents the results of generating 3d information of objects by the proposed method of Chapter 5.1. The method evaluates the non-coherent tracking of backscattering energy flow in image sequences to derive height information. A corner field consisting of several scatterers at different heights is used to validate the proposed method and extract information of point-like objects. The scenario was also exploited to validate the proposed coherent 3d extraction methods of Chapter 5.2.2. The non-coherent method was further evaluated on several selected objects of the urban scene from the data acquisition indicated in Fig. 8.6 and Fig. 8.8.

Non-coherent 3d extraction of point-like objects

ViCSAR imaging results of the campaign from Fig. 7.4 showing the corner field are presented in Fig. 8.12. The resolution of the images is $\delta_y = 8\,\text{cm}$ and $\delta_x = 7.5\,\text{cm}$. The results for computing the 3d information of the corner field are presented in Fig. 8.13. It shows a zoom on the scene from one viewing angle with selected reflectors marked in Fig. 8.13a. Even the very tiny reflectors with 3 cm edge length (-5 dBsm) from Fig. 7.6 are observable in the center of the heliport. Five of the reflectors are placed on the ground at the reference height $dh = 0\,\text{m}$ (green circle), while the others are placed at altitudes ranging from 0.75 m up to 4.00 m. Computing the 3d positions by tracking the non-coherent energy flow, Fig. 8.13b presents a boxplot as a function of aspect integration and the computed height compared to ground truth. The tracking window size was set to $m = 7$ which corresponds to 0.9 m x 0.9 m with a 12.5 cm pixel spacing. The parameter η was set to -28 dB, ϵ to 0.3 m and $\lambda_{xx} = \lambda_{yy} = 0.25\frac{m}{deg} \cdot \varphi_s$.

An aspect tracking interval φ_s of only 2° results in a ±1 m height accuracy for all targets which is close to the theoretical limit derived in Section 5.1.4. The 3d accuracy increases rapidly

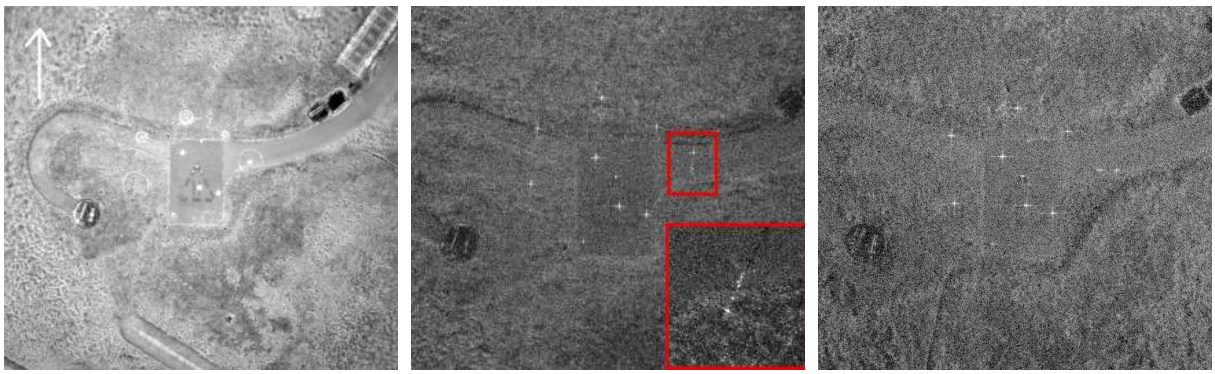

(a) (b) (c)

Figure 8.12: Selected ViCSAR imaging results. Zoomed-in view of the corner field from Fig. 7.6 located around a heliport with images orientated to the north. $\delta_x = 7.5\,\text{cm}$, $\delta_y = 8\,\text{cm}$. a) Non-coherent overlay of full 360° subaperture images, b) single look frame looking south. Tripod of Fig. 7.6c in red compared with a stripmap SAR image zoom with 2.5 cm resolution looking northeast, c) single look frame looking west.

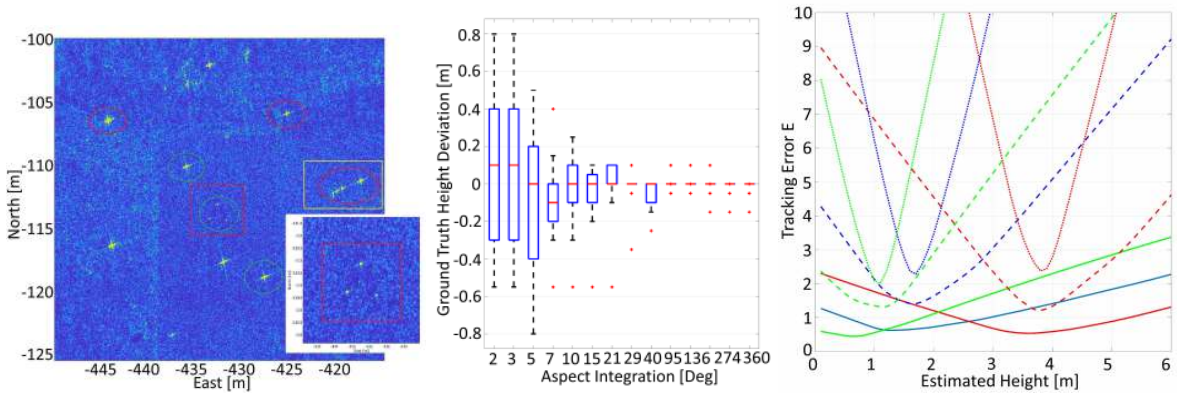

(a) (b) (c)

Figure 8.13: Corner field and computed 3d information with non-coherent method. a) Image frame of the corner field from aspect angle $\varphi = -117°$. Corners at the ground are marked with green circles. The red rectangle shows the zoom of the 3 cm edge length tiny corner. The tripod of Fig. 7.6c is marked with the orange rectangle, b) boxplot function of corners' height estimation compared to ground truth. Reliable results for all corners with an accuracy of 10 cm are achieved from $> 20°$, c) error tracking function for 3 targets (red circles in a)) at 1.70 m (blue), 3.75 m (red) and 1.10 m (green) height. Aspect interval is 5° (solid line), 10° (dashed line) and 20° (dotted line). The minimum of the function marks the estimated height of the scatterer.

at larger aspect intervals. With $\varphi_s = 10°$, the experiments show a ± 0.3 m accuracy and ≤ 0.1 m mean deviation. From an aspect interval $> 20°$, an accuracy of ± 0.1 m is reached.

In Fig. 8.13c, the error tracking function of equation 5.11 and 5.13, respectively, is presented for 3 individual targets. The focus is on the corners marked with the red circles in Fig. 8.13a that are located at a height dh of 3.75 m (red), 1.70 m (blue), and 1.10 m (green). Their mean SCR was 17 dB. φ_s was chosen to be 5° (solid line), 10° (dashed line) and 20° (dotted line). The minimum of the error function ΔE marks the estimated height of the object. With $\varphi_s = 5°$, the height error averages 0.4 m with poor resolution. With $\varphi_s = 10°$, the targets at $dh = 1.10$ m and 1.70 m already show their minima at the correct altitude, while the target at 3.75 m is located at 3.60 m. This is consistent with the derived minimum theoretic aspect interval of $\varphi_e = 8°$, while the height resolution at φ_e is expected to be still low. Tracking the target up to 20° clearly improves the height resolution resulting in the correct height estimation of all three targets on a 10 cm scale.

3d extraction of point-like objects with kurtosis operator

In Fig. 8.14, the results of the corner field for the validation of the proposed kurtosis method are presented. Eight image stacks with different $\varphi_{az} \in [0.6°, 1.2°, ..., 13°]$, each containing 45 CSAR images of the same scene at varying reference heights, were computed. The height step is set to $\Delta H = 0.1$ m and ranges from 0 m up to 4.50 m. Due to the much higher resolution compared to ViCSAR mode, the pixel spacing was set to 3 cm.

In Fig. 8.14a, the corner field is focused at ground level with a large aspect interval of $\varphi_{az} = 8.5°$ and $\varphi_m = -115°$. Due to the longer integration with $\varphi_{az} >> \varphi_{max}$, the scatterers at higher elevation (left side and tripod) are no longer sharply focused - in contrast to Fig. 8.13a - but gradually blur in accordance with the derived equation 4.35 in Chapter 4.3. For each object, the 3d coordinate was computed by using a 0.75 m x 0.75 m pixel matrix x_l, and this information was projected into the SAR image. Thus, the red points (scatter plot) mark the computed actual 3d positions of the corners in the image domain. The individual distance to the projected corner

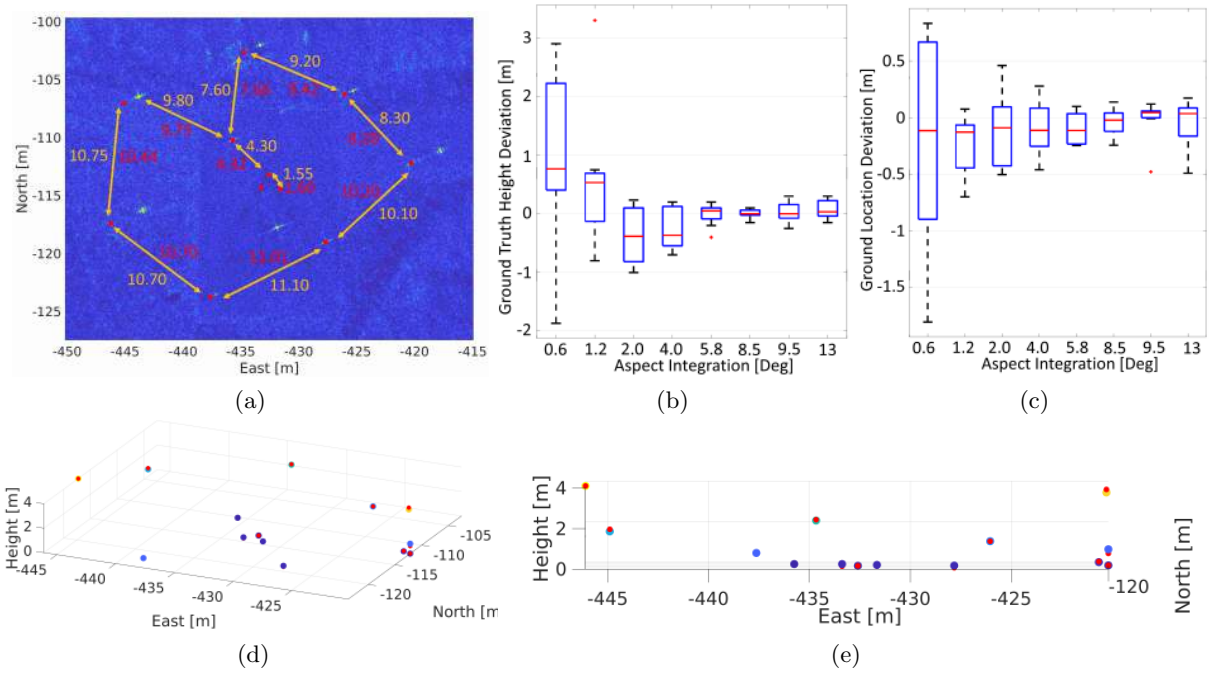

Figure 8.14: Corner field, statistics and computed 3d information with kurtosis method. a) SAR image of the scene with $\varphi_{az} = 8.5°$ at $dh = 0\,\text{m}$ and $\varphi_m = -115°$. Computed 3d position of each scatterer is projected into the SAR image as red points (scatter plot). Computed absolute ground distances of corners' 3d position in [m] included. Ground truth (red), computed distances (orange), b) boxplot as a function of ground truth height deviation and aspect integration. With $\varphi = 0.6° < \varphi_{max}$, no height information can be gained. Best accuracy is achieved with $\varphi_{az} = 8.5°$, c) boxplot as a function of ground location deviation and aspect integration, d) computed 3d position of each scatterer. Ground truth (red), computed position (colored), e) side view of d).

position indicates the level of foreshortening and reveals the object's height and the radar's line of sight. For example, the corner's position on the tripod (rightmost corner) corresponds nicely to the tripod's ground echo. The corner showing the largest projection at position (-443,-117)' m is the highest placed corner at 4 m height, see Fig. 7.6a. Further, the SAR image is supplemented with the computed absolute ground distances (orange) and measured ground truth distance (red) of the individual corners.

Analysis of the 3d accuracy in relation to the processed aspect interval is shown in Fig. 8.14b and 8.14c. The Figures show a boxplot of the height accuracy and the corner's absolute ground distances. As expected, it becomes apparent that a coherent integration of $\varphi_{az} < 1.2°$ does not lead to a reasonable 3d estimation since it is in the order of φ_{max}. Further, a side-looking view of the calculated 3d position with $\varphi_{az} = 8.5°$ is visualized in Fig. 8.14d and 8.14e. The ground truth information is marked in red while the computed position is marked in color. At the rightmost corner, besides the actual location of the scatterer, further elements of the tripod can be observed. Similar to the non-coherent approach, all scatterers are correctly located with a height accuracy of $< 20\,\text{cm}$.

8.4.2 3d extraction of selected objects in the image sequence

The accuracy of the non-coherent approach is further evaluated by retrieving 3d information from individual objects in urban scenes. In contrast to the corner field scenario, a potential scatterer region is manually marked in the video frames, and the energy flow is automatically

tracked over the complete aspect visibility. Targets are two different trees, a large corner reflector, an advertising tower, and three street lamps. The tracking windows were individually adapted without an automatic segmentation of the scene, which is not implemented. A $m = 7$ pixel window is chosen for the small objects (street lamp, corner), and a large window with $m = 40$ pixels for the more significant objects (trees, tower) with $\delta_p = 12.5\,\text{cm}$. The different objects are presented and marked with red circles in Fig. 8.15. The focusing height of the reference plane is chosen at the level of the parking space. Results are presented in Fig. 8.15 and Fig. 8.16.

The lamps are measured to be located at the height of 8.40 m up to 8.90 m. This corresponds to the LiDAR data where the lamps are measured in a range of 8.50 m up to 8.90 m. The corner is correctly computed at ground level; the high tree is computed at 8.80 m, the tower at 7.20 m, and the smaller tree at 6 m, see Fig. 8.15b. 3d locations of the objects can be examined in Fig. 8.15b, where the computed 3d coordinates are superimposed as red scatter points. The locations correspond to the center of the objects compared to Fig. 8.16b.

Besides extracting the 3d information, it is also possible to derive the signature of the object over the entire aspect visibility. The results of the marked objects are shown in Fig. 8.16a. The corner and the tower can be tracked over the entire circular trajectory; the trees have a tracking history of about 250° while the street lamps are only visible over a smaller aspect interval between 60° and 90°. The moving projection of the street lamp is most apparent as long as the projection is above asphalt (higher contrast). The typical corner reflector behavior with sharp signal spikes every 90° aspect change can be observed or the anisotropic scattering response of the metallic tower. However, the signal history of the trees (foliage) is much smoother, while the signal of the street lamps is significantly weaker and much shorter visible.

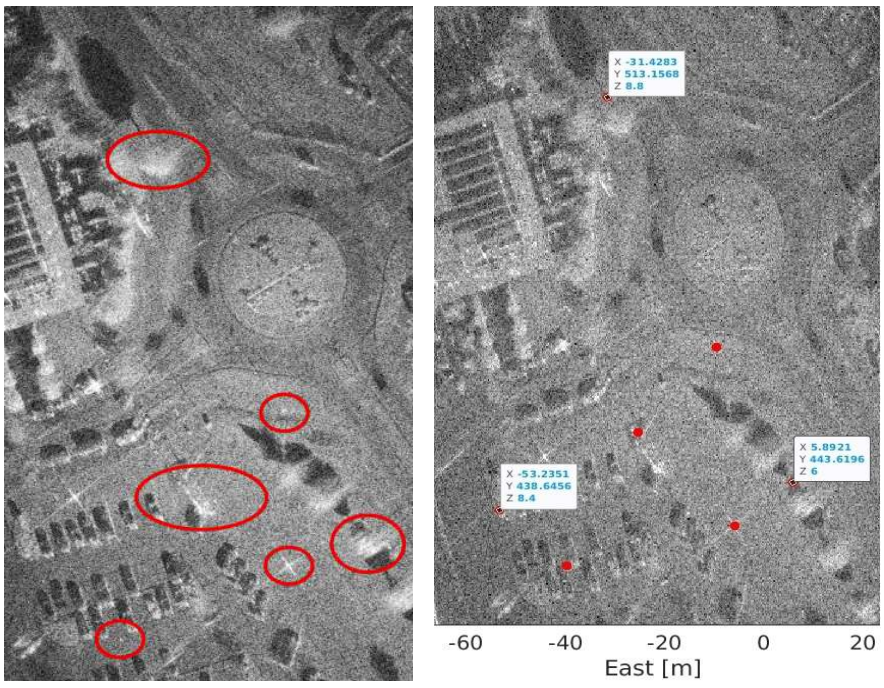

(a) (b)

Figure 8.15: Computing 3d information of manually selected objects in an urban scene with non-coherent approach. a) CSAR image frame with radar's viewing angle from south. Red circles mark the projected backscattering of several targets including trees, an advertising tower, two street lamps and a corner reflector, b) computed 3d position of marked objects as red scatter plot.

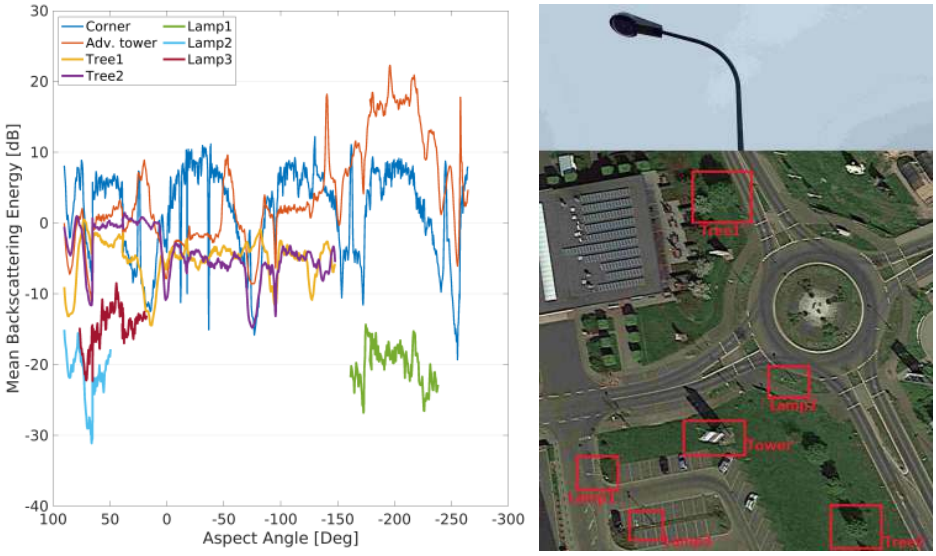

(a) (b)

Figure 8.16: Tracked signature of selected objects. a) Signature of objects from Fig. 8.15 over entire aspect visibility. Typical trihedral corner characteristic (blue) with sharp spikes every 90° is revealed. Street lamps have a short visibility of only 60° - 90°, b) aerial photo of scene (Google) and photo of street lamp.

8.4.3 3d point cloud generation of an urban scene

Preparation of the data set

The point cloud extraction method of Section 5.2.2 was evaluated for the urban scene indicated in Fig. 8.4. For extracting the 3d information, the 360° data set is divided into N = 20 corresponding image stacks with different mean aspect views, each covering an aspect interval of $\varphi_{az} = 8.5°$ to reconstruct the scene from all perspectives. To reduce the data size over the entire scene, for each mean aspect angle φ_m, a 3d image stack in a 1 m height step distance is computed with a pixel spacing of 3 cm. A step size of 10 cm would be too computationally and memory-intensive for the entire scene. The reference height $H_0 = 0$ m was extracted from the LiDAR data set and equals the lowest area of the parking space. Further, h_{max} was selected to 12 m corresponding to the highest objects in the scene. The results are then interpolated for the final height estimation in a 10 cm height step size as described in Section 5.2.2. Analyzing the corner results in Section 8.4.1, the coherent processing interval was set to $\varphi_{az} = 8.5°$ since this value showed optimal accuracy. Thus, range resolution is 7.5 cm, the achievable azimuth resolution of scatterers at correct elevation is below 3 cm. The size of the search filter matrix x_l was selected to $m = 30$, corresponding to 0.90 m x 0.90 m. Henceforth, the different point cloud fusion and 3d extraction methods from Chapter 5.2 correspond to (a) kurtosis operator (Ku), (b) spectrum operator (SP), and (c) weighted mean operator (WM).

To get a qualitative impression of the local 3d extraction, the response of the designed Ku operator shall be analyzed as an example. Therefore, a part of the roof area of the central building focused at different heights is presented in Fig. 8.17. It is easy to recognize that the integration interval of $\varphi_{az} = 8.5°$ already leads to a significant degradation in the image parts that are not at the processed focusing height of $H = 0$ m. While the lower objects are in focus at very high resolution, the backscattering energy of objects above the reference plane flows in the along-track direction. The response of the Ku metric shows that it is able to capture the energy flow that

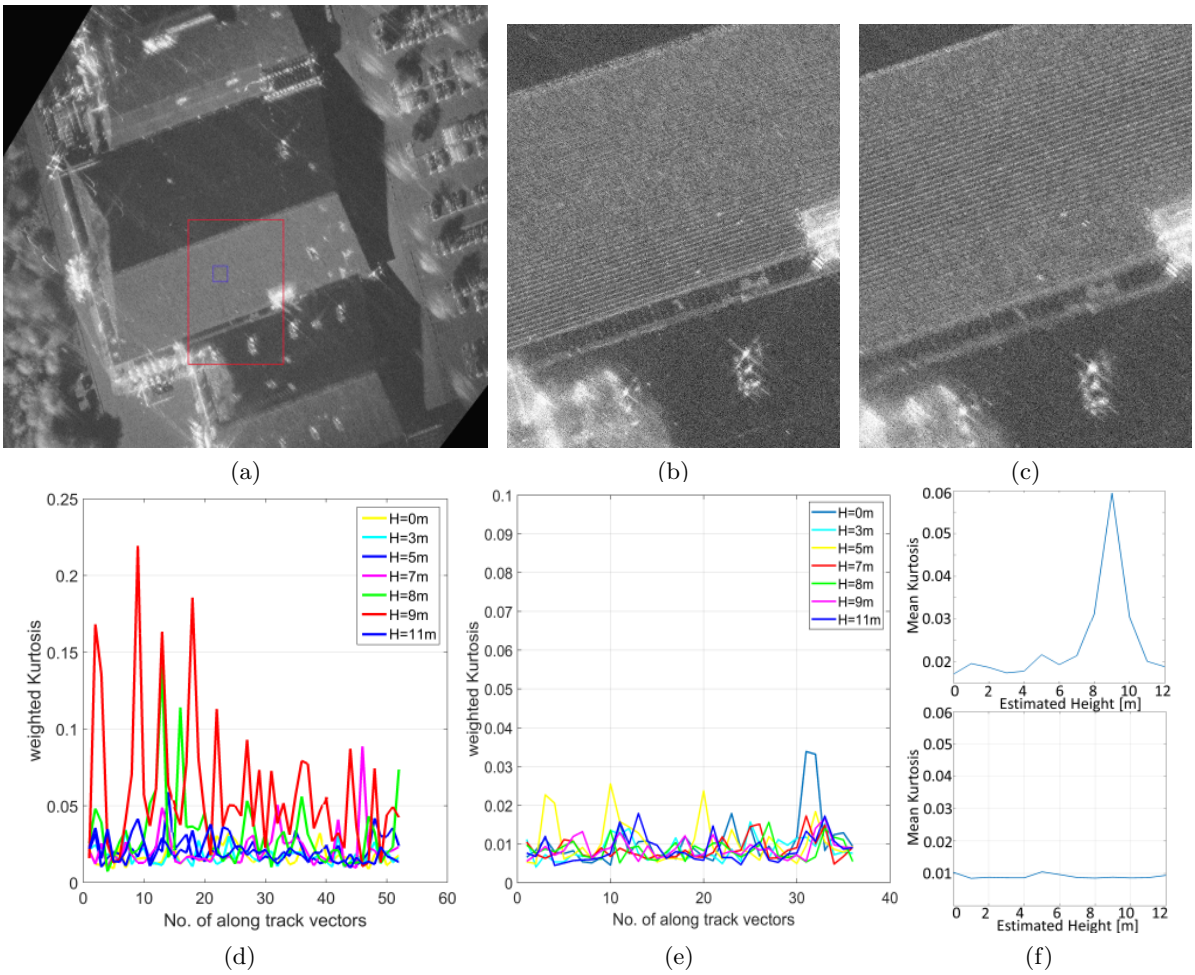

Figure 8.17: Zoom of imaged building and Ku metric results of the roof area. Radar's viewing direction is northeast. Due to the slope of the roof, only southern part is visible, northern part is shadowed. a) Zoom of the largest building processed at $H = 0\,\mathrm{m}$. Ground objects are well focused while the roofs of the buildings start to defocus. Due to some wind during data acquisition, the leaves appear smeared while the trees' shadows are focused, b) zoom on part of the roof (red square from a)) at $H = 5\,\mathrm{m}$. Lower roof part starts to get in focus, c) zoom at $H = 9\,\mathrm{m}$. Focus moves higher toward the center of the image, d) weighted kurtosis applied to the roof at 9 m height (blue rectangle in a)), e) weighted Ku applied to radar shadow, f) proposed metric $\vec{s}(H, \varphi)$ applied to roof area (top) and radar shadow (below). As the scatterers in the examined window are at similar height, the proposed metric nicely estimates the correct height of the roof.

is due to the reflection of the installed roof tiles. Although the backscattering characteristic is relatively low and there are no strong scatterers in the scene, the result obtained by the metric is unambiguous. Applying the operator in noisy areas like the radar shadow indicates that the response is an order of magnitude lower and, in particular, more evenly distributed, and can be thresholded. Responses passing the threshold are interpolated and selected as inputs for the proposed fusion process.

3d point cloud results for an urban scene

The global 3d point clouds of the urban scene derived by the different extraction methods and fused from the local clouds are presented in Fig. 8.18. Fig. 8.18a presents the results derived from the Ku operator and Fig. 8.18c from the SP operator. For the SP operator, high threshold levels

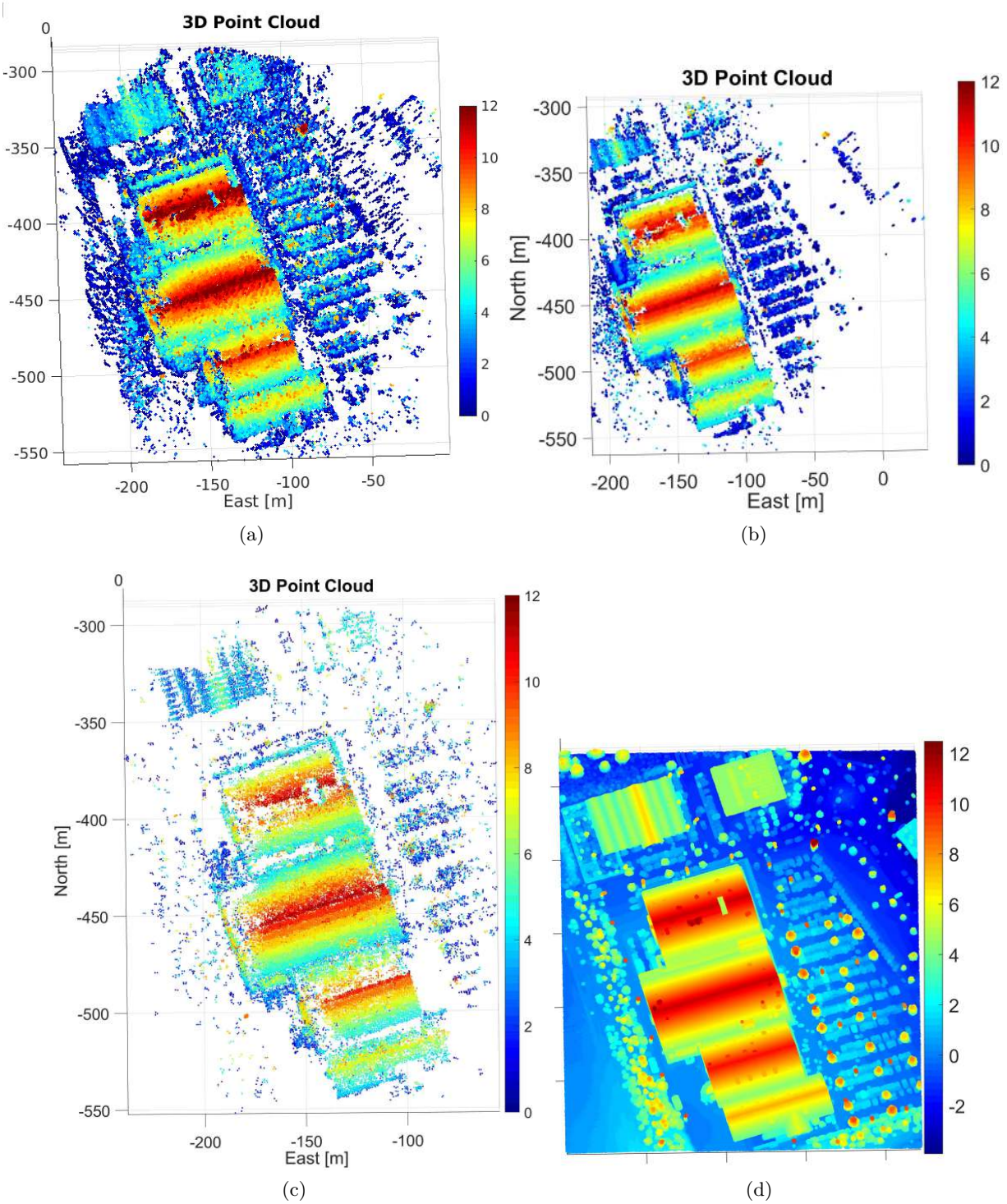

Figure 8.18: Computed 3d global point cloud of an urban scene compared to LiDAR. a) 3d point cloud derived with Ku operator, top view. Fusion of $N = 20$ aspect views. Height is color coded. Commercial buildings, parking area and infrastructure is observable. High spots aside the building are mainly from street lamps, b) point cloud derived by mean weighting factor method (WM). Local height extraction was realized by Ku operator. Noise level is significantly lower, c) point cloud derived by SP operator. Threshold levels are set significantly higher to reduce noise level, d) LiDAR point cloud (Source: Land NRW 2020 - Data licence Germany - Version 2.0).

were chosen as the focus was more on the precise extraction of valid areas and noise reduction. In Fig. 8.18b, the results from the WM method of Section 5.2.4 are shown, where the extracted spatial location of each 3d point corresponds to the maximum of the weighted mean from all views. Extracting local height information in this method was done with the Ku operator. However, only $N = 13$ views were chosen to limit the computational burden.

The result from transferring the computed point cloud of Fig. 8.18a for better presentation to a point cloud visualization software is shown in Fig. 8.19. Illustrated are the four commercial buildings in the scene's center, the parking space in front of the buildings, parts of the greenhouses in the north, and parts of the fuel station in the northeast. At the northern end of the parking

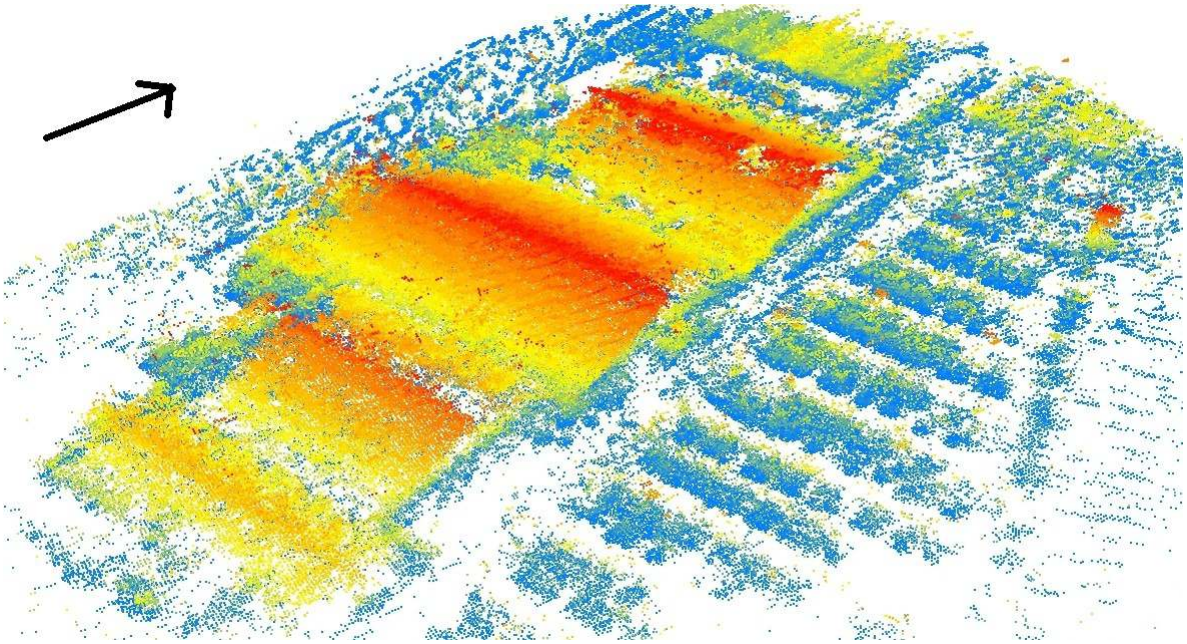

(a)

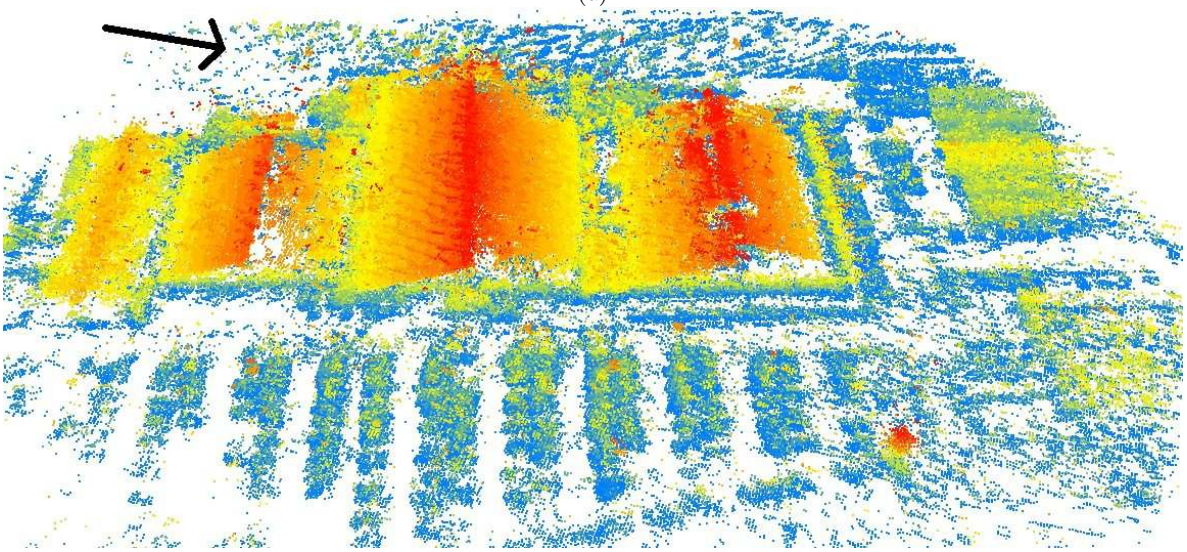

(b)

Figure 8.19: Computed 3d point cloud of the entire urban scene from different aspects shown in [Palm & Stilla, 2021]. Building structure and height of roofs are recognizable from all aspects, the arrow indicates north. a) View from southeast, b) view from east.

space, the 12 m high advertisement tower is located. The main central building also marks the center of the circular trajectory.

Besides the spatial information, observers might be interested in having information on the angular scattering characteristics. Fig. 8.20 reveals the mean aspect angle at which each locally derived 3d point from Fig. 8.18a is visible. Due to the buildings' similar roof inclination, a kind of preferential looking direction can be recognized. From various aspects, the roof is shaded, while from small intervals, it flashes. Yet, the edges and alignment of the roof tiles are nicely observable from some aspects. Thus, the northern roofs appear red and green while the southern appear pink and blue since these views apparently offer the best height extraction angular interval with respect to the flight trajectory. It is also recognized that the border areas of the circular spot are only visible from limited aspect angles.

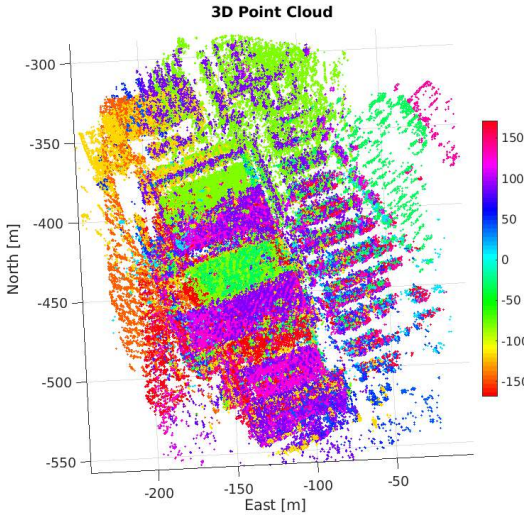

Figure 8.20: Color coded mean aspect angle that reveals the origin of each 3d point from Fig. 8.18a. Due to the roof inclination, a preferential looking direction can be observed in the roof area.

Quantitative results

Quantitative results are presented in Table 8.1, Table 8.2, and Fig. 8.21. The Figure shows a cross-section of a 15 m^2 roof area of the central building compared to the cross-section of the same area derived from the LiDAR. The radar cloud derived from the Ku method is fused with different numbers of aspect views N. For comparison, the profiles generated from the SP and WM operators are also shown. The accuracy deteriorates with larger N, which is synonymic to a larger number of fused subapertures. A best-fit plane of all points with the least square of the normal distance to the plane is calculated for evaluating the deterioration quality.

Table 8.1 presents the result for N, the standard deviation σ_r, the number of points P, and the derived roof angle γ compared to the LiDAR data set. The lowest $\sigma_r < 0.2$ m is achieved for $N = 1$, which is a factor of 10 compared to LiDAR. With increasing N, σ_r also increases to a maximum of 54 cm when all views are fused without any form of calibration, see Table 8.1.

However, further investigations indicated that the degradation in height is not arbitrary or random. Compared to the first 'master view', it was found that the local point cloud data from some aspect views showed a height offset H_{of} in the order of -0.5 m up to +0.7 m (height bias) in the data. This means that all points, e.g., in the second subaperture were 0.3 m too high compared to the first subaperture. Shifting the data from these subapertures by H_{of} could significantly improve the accuracy and reduce the σ_r of the data. Therefore, the height bias shift

in five and seven of the most relevant views is also presented in Fig. 8.21d and Fig. 8.21e. The quantitative analysis in Table 8.2 for the calibrated and shifted data indicates that a deviation of only $\sigma_r \leq 0.2\,\text{m}$ for the roof area can be reached even by fusing $N = 7$ views. The pitch of the roof γ is then derived with an accuracy of $< 0.25°$. Again, this value can only be achieved by shifting the data with H_{of}. But it should be noticed that nearly the same high accuracy is reached without any form of calibration by applying the WM approach, see Fig. 8.21g and Table 8.1. The point cloud density varies, of course, with N or the used threshold filters, but for the analyzed roof, it can reach 9 to 11 points per m^2.

Height accuracy can be further evaluated by Fig. 8.22. It shows a cross-section with a depth of 1 m through the building complex compared to LiDAR. The profile with Ku approach for N = 20 in Fig. 8.22a is compared to the WM method for N = 14 in Fig. 8.22b. Again, in [Palm & Stilla, 2021], it can be seen that in terms of height accuracy, the best results for non-calibrated data are achieved with only a few aspect views N. However, this only corresponds to a low point density. The derived maximum heights for all buildings of Fig. 8.22 are presented in Table 8.3. For N = 3, an accuracy of $< 0.5\,\text{m}$ can be reached for calculating the height of the roof ridge [Palm & Stilla, 2021]. A fusion of 20 aspect views still results in a height accuracy of $< 1\,\text{m}$ for Ku and SP approach and $< 0.6\,\text{m}$ for WM approach.

Objects that appear as smaller point targets in the scene, like street lamps, show relatively good height accuracies. In Fig. 8.22e, a street lamp extracted by Ku approach on the parking space is compared with LiDAR data for N = 1 in Fig. 8.22d. The height accuracy is further evaluated in Table 8.4 and shows promising results in terms of σ_r and the mean height μ of the object that can be derived in the range of 10 to 20 cm. Also, the number of extracted points P from the top

Table 8.1: Accuracy of the roof area with number of fused aspects N.

N	σ_r [m]	γ [deg]	P
1 Ku	0.18	15.36	759
3 Ku	0.19	15.31	769
6 Ku	0.24	15.30	808
9 Ku	0.32	15.09	1212
12 Ku	0.45	15.52	1473
15 Ku	0.52	15.55	2696
20 Ku	0.54	15.58	2736
20 SP	0.60	15.20	1107
14 WM	0.25	15.13	2160
LiDAR	0.02	15.01	2524

Table 8.2: Accuracy of the roof area calibrated to the 'master' view, see Fig 8.21.

N	σ_r [m]	γ [deg]	P
1 Ku	0.18	15.36	759
5 Ku	0.18	15.20	1205
7 Ku	0.20	15.25	2020

Table 8.3: Maximum roof height of the four buildings B1 to B4 (left to right) of Fig 8.22 and two street lamps L1/L2.

N	B1 [m]	B2 [m]	B3 [m]	B4 [m]	L1 [m]	L2 [m]
3 Ku	11.6	11.2	10	7.1	8.9	8.8
20 Ku	11.9	12	10.1	8.1	8.9	9.1
14 WM	10.6	11.1	9.8	8	8.6	8.5
LiDAR	11.2	11.2	10.2	7.5	8.9	8.7

Table 8.4: Mean height μ and σ_r of the street lamp from Fig. 8.22e and 8.22d.

N	σ_r [m]	μ [m]	P
1 Ku	0.25	8.70	12
9 Ku	0.32	8.56	16
20 Ku	0.37	8.37	27
LiDAR	0.10	8.78	12

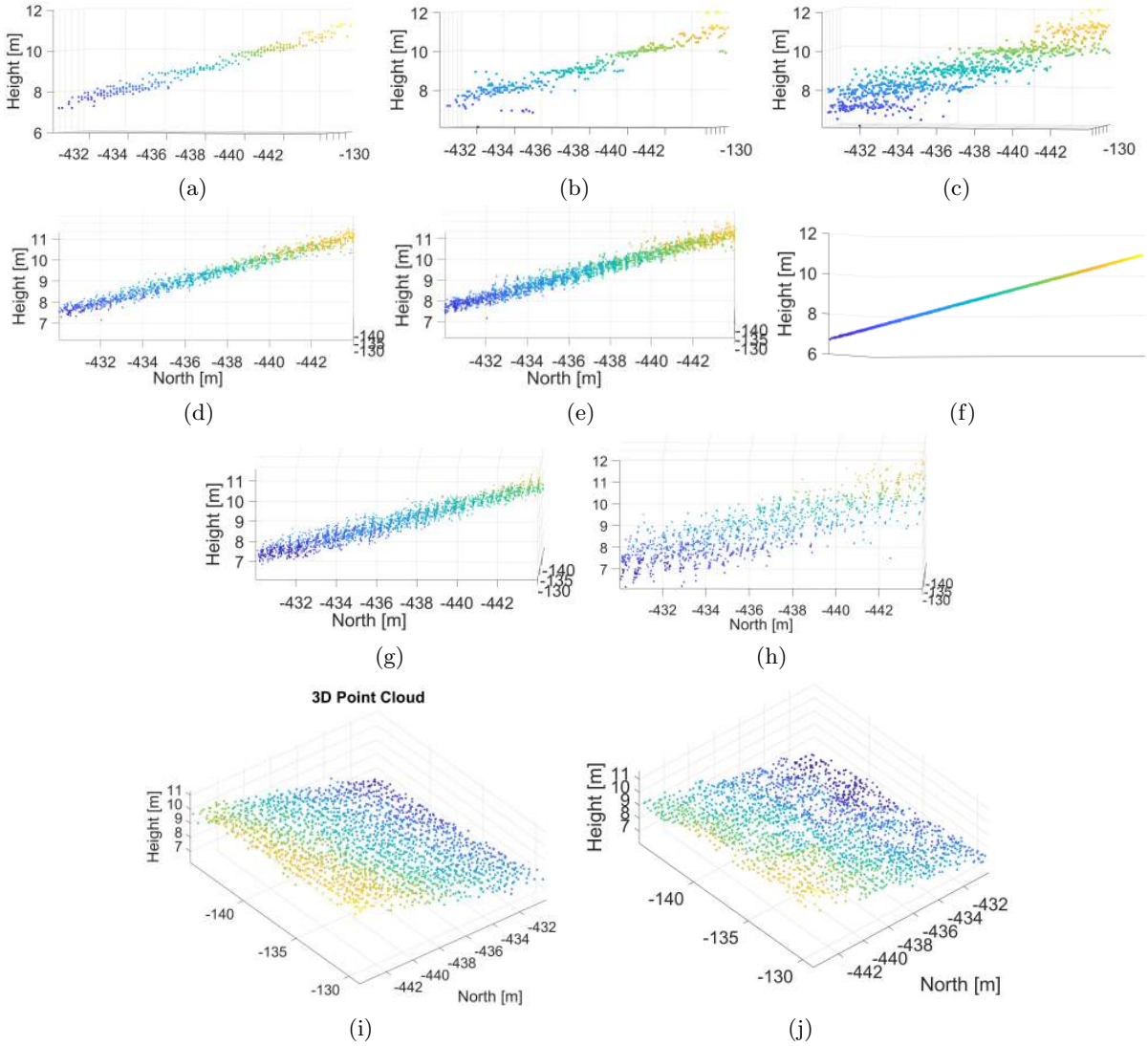

Figure 8.21: 3d point cloud profile and oblique view of the calibrated and non-calibrated roof area. Cross-section of a 15 m^2 roof area showing the roof pitch and point cloud density of the central building fused with a different number of aspect views N. Data derived with Ku method except for g), h) and j). a) N = 1, b) N = 9, c) N = 20, d) N = 5 most relevant views calibrated to 'master' view, e) N = 7 most relevant views calibrated to 'master' view, f) LiDAR derived profile of roof area, g) profile from WM approach with N=14, h) profile from SP operator approach with N = 20, i) oblique view of roof area with $N = 7$ most relevant, calibrated views. Area represents $P = 2020$ points which corresponds to 9 points per m^2, j) oblique view of area from WM approach.

of the street lamp corresponds to LiDAR-derived data. A summary of the height accuracies of the four buildings (B1,...,B4) and two street lamps (L1/L2) is shown in Table 8.3.

Further results for height accuracy validation by comparing the three different 3d extraction methods Ku, SP, and WM are presented in Table 8.5. Therefore, all 3d points associated with the entire building complex were validated with the LiDAR data set. The entire investigated building complex is shown in Fig. 8.23. The area corresponding to Fig. 8.23a is named 'all buildings', while the area corresponding to Fig. 8.23b is named 'Roof Area' in Table 8.5. Each extracted 3d point from the radar data was selected and evaluated with the corresponding match in the LiDAR data set by choosing the LiDAR point that showed the smallest spatial distance while both point

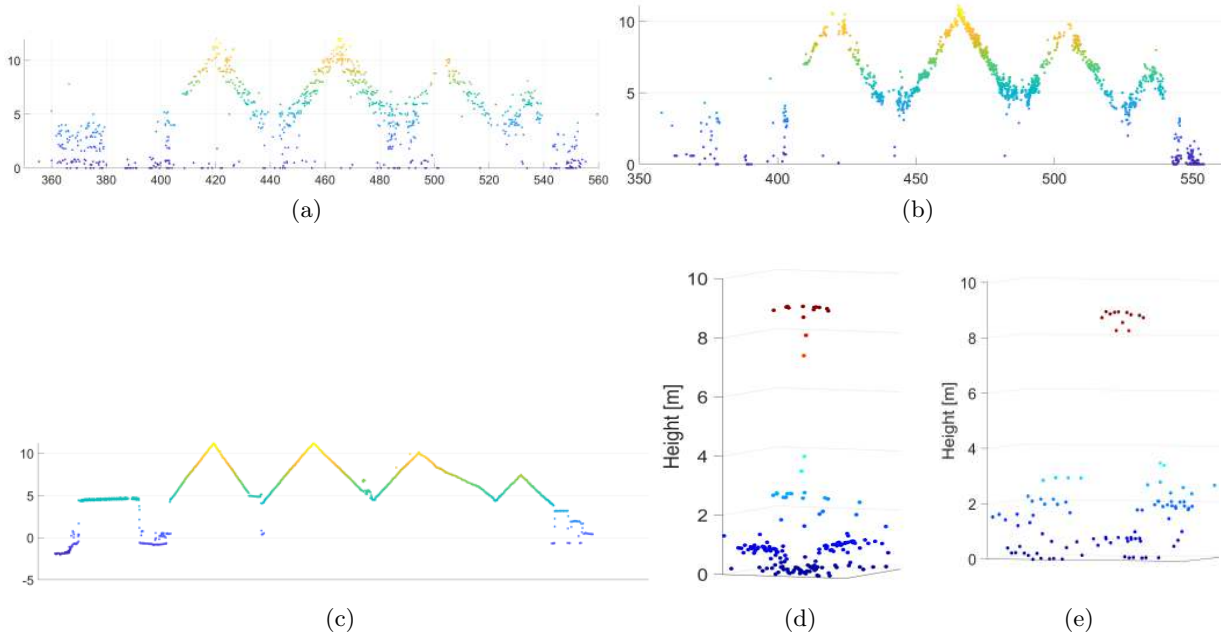

Figure 8.22: Comparing the building profile and street lamps derived from radar and LiDAR. Cross-section of 1 m depth of the buildings from the derived point cloud and qualitative comparison of a street lamp. a) Radar, fusion of N = 20 by Ku method, b) radar, fusion of N = 14 by WM method, c) LiDAR. The left object is the greenhouse followed by the four commercial buildings. Maximum height of all objects is presented in Table 8.3, d) LiDAR street lamp L1, e) street lamp L1 extracted with Ku approach with N = 1. Top height in LiDAR is 8.87 m while in radar 8.9 m. Objects appearing like small point targets show good correspondence.

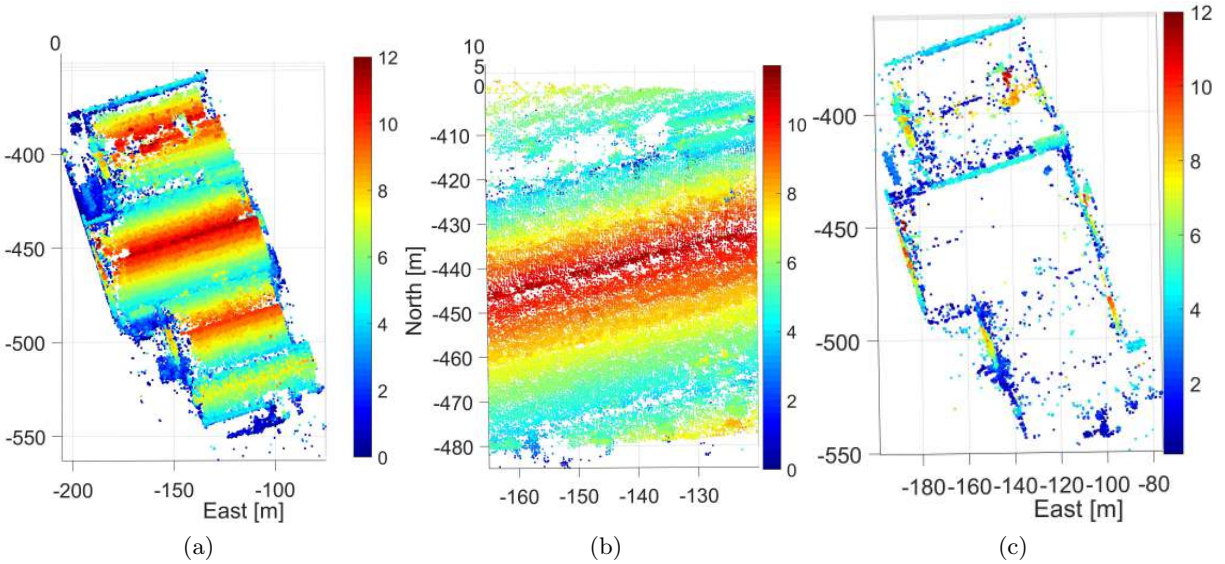

Figure 8.23: Validation of different point cloud extraction methods. Whole building complex area was validated with LiDAR data set. Results are presented in Table 8.5. a) 3d point cloud derived by WM approach showing the building complex scene (all buildings). This was the first area to be investigated, b) point cloud of larger roof area. This was the second scene to be investigated in Table 8.5, c) areas showing height errors of more than 2 m when validated with LiDAR.

Table 8.5: Height accuracy of the building and roof area from Fig. 8.23 using the three different extraction methods. Differentiation between points of low and high altitude.

	Kurtosis		Spectral		Weighted Mean	
Height	σ_r [m]	P	σ_r [m]	P	σ_r [m]	P
All buildings	2.41	140019	1.86	46300	1.81	140159
>5.0 m	1.54	81203	1.53	31755	1.37	84036
<5.1 m	3.02	58816	2.39	14525	2.36	56123
Roof area	1.42	51417	1.21	19030	0.99	51405
>5.0 m	1.06	37804	1.06	14030	0.68	37354
<5.1 m	1.85	13613	1.52	5000	1.51	14051

clouds were transferred in the WGS84 reference system. The validation was also separated on different height levels to differentiate the results further. This simplifies the discrimination of height areas that are possibly more problematic. 3d points that show a significant error in height can be marked and further visualized what is shown in Fig. 8.23c. Additionally, all 3d points are indicated that show a height error of more than 2 m compared to LiDAR.

3d point clouds of selected areas

The following results show 3d point clouds of more difficult areas, as typically the scene was located on the edge of the circular illuminated spot. Therefore, only a small number of aspect views could be acquired. The results for the area of the greenhouse (area (E) in Fig. 8.4) are presented in Fig. 8.24. From Fig. 8.18d, this building had a height ranging from 3 m to 7 m at the top, and data was only acquired with the radar at the northern part of the circular trajectory. Two subapertures from the circular data set could be evaluated that illuminated the area of the building. As Fig. 8.24 nicely indicates, these two subpertures are already sufficient to extract a reasonable level of 3d information and the object's dimensions. The main building in the center can be observed that also shows the largest height. Also, the noise level is relatively low considering the type of the building.

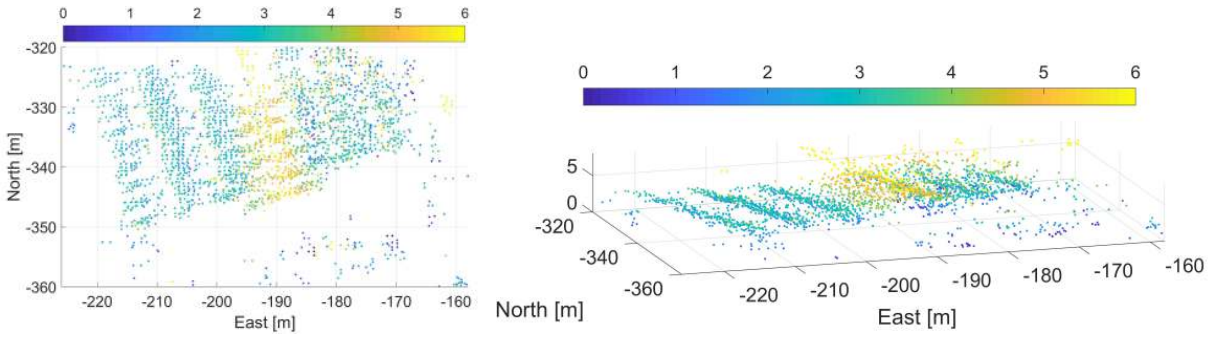

(a) (b)

Figure 8.24: 3d point cloud of the greenhouse area. a) Top view, b) oblique view.

The results for the gas station (area (D) in Fig. 8.4) are presented in Fig. 8.25. Also, this object was located at the northern edge of the illuminated spot, and only a small number of subapertures could be evaluated for 3d extraction. Additionally, this building had a flat roof that showed a high level of clutter characteristic. A large part of the right roof area was also

covered with solar panels, making this surface a challenging area. However, the results of Fig 8.25 indicate, that the extracted 3d points are spreading within 2-3 m around the true height of the building, which was measured to be at 4.5 m. Although the 3d reconstruction is far from perfect, there is a rough impression of the dimensions and the approximate height of the roof.

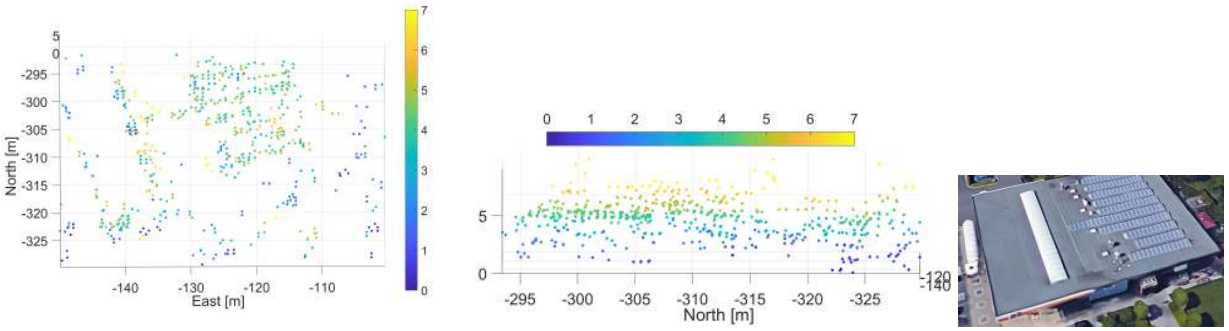

(a) (b) (c)

Figure 8.25: 3d point cloud of the gas station's roof (area (D) in Fig. 8.4). Challenging object since the flat roof showed clutter behavior. Building was on the outer border of the circular spot, rarely visible. True height is 4.5 m. Point clouds were derived with SP operator. a) Oblique view from above, b) profile view, c) aerial photo (Google).

Results for the extracted 3d point cloud of the northern building B1 (see Table 8.3) are presented in Fig. 8.26. Located inside the roof area is a small courtyard that complicates the 3d extraction since the smooth roof area has a more or less large hole that could lead to falsified height extractions in the vicinity. However, the results indicate that the developed method can handle such challenges and that even the courtyard dimensions are observable in the 3d point cloud. Furthermore, the profile view of Fig. 8.26b shows that also a part of the facade structure of the inner courtyard is indicated and could be reconstructed.

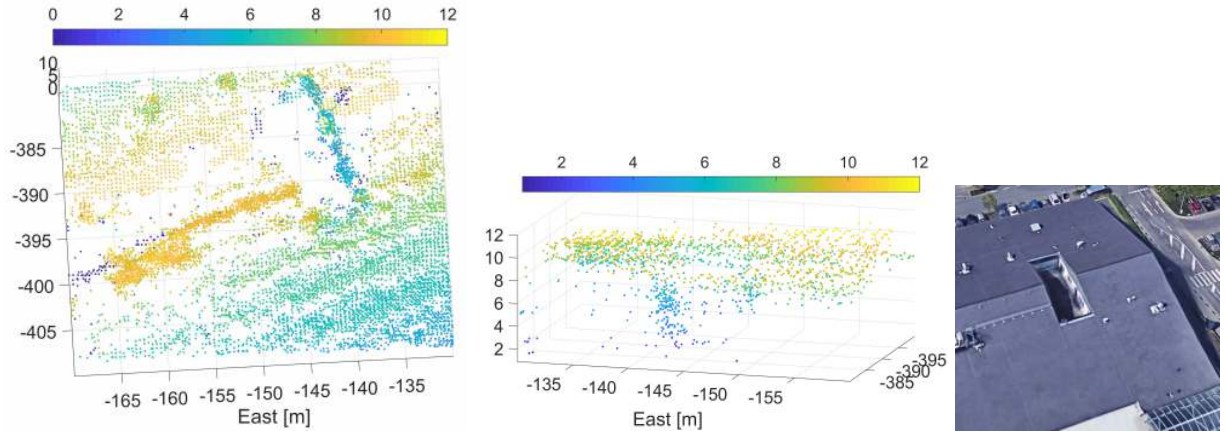

(a) (b) (c)

Figure 8.26: 3d point cloud of the northern building with the inner courtyard. Challenging roof surface. a) Top view derived by WM method. 3d information of roof surface and inner courtyard are extracted, b) same scene derived with SP operator. Side view from different direction to the south. Area and course of the wall of the inner courtyard are observable, c) aerial photo (Google).

Fig. 8.27 shows the rear side (the western side) of the central building (area (A) in Fig. 8.4). The focus shall lie on the extracted facade of the building. Besides the 3d extraction of the roof area, the facade's linear course is also reconstructed. The facade is even mapped relatively distinctly on a straight line without significant scattering. Thereby, a relatively exact dimension of the building from the rear side can be reconstructed.

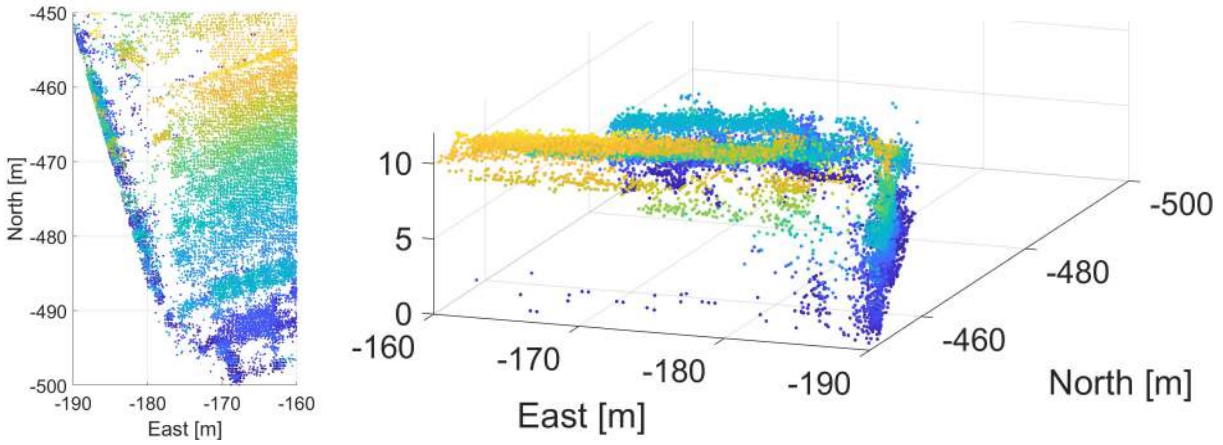

(a) (b)

Figure 8.27: 3d Point cloud with focus on the central building's facade (area (A) in Fig. 8.4). Derived with WM approach. a) Top view of the western side of the central building. The course of the facade in the point cloud is clearly observable, b) side view. Looking from the north to the south alongside facade.

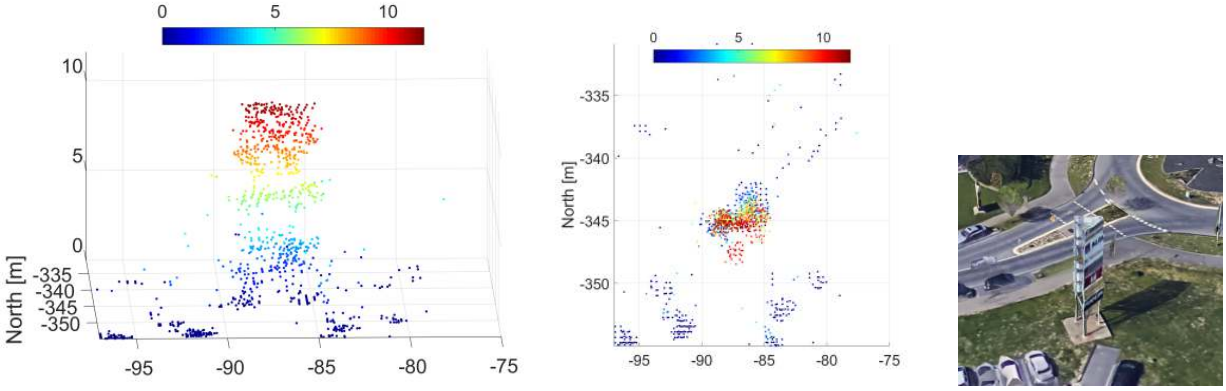

(a) (b) (c)

Figure 8.28: 3d point cloud of the 12 m high tower. Each side of the triangular object has a length of 3.5 m. Extracted with WM method. a) Side view, b) top view, c) aerial photo (Google).

The 3d point cloud of the metallic tower situated in the northern part of the scene is presented in Fig. 8.28. The tower has a length of 3.5 m and a height of 12 m. Also, this object was only illuminated within a smaller number of subapertures. The WM method resulted in a maximum height of 10.80 m while the Ku method was 12 m. The dimensions of the tower in the derived point cloud show that these are close to the actual length of 3.5 m, see Fig. 8.28b.

The results presented in Fig. 8.29 give a view of the parking area that is dominated by clutter. Best results are obtained here by applying the WM approach that is presented in Fig.8.29a and Fig.8.29b from two opposing views. While the Ku and SP approaches show a high noise level

in this area, this is not the case for the WM approach. However, on the other side, nearly all information, e.g., of trees, is removed, and only street lamps and parked cars remain observable.

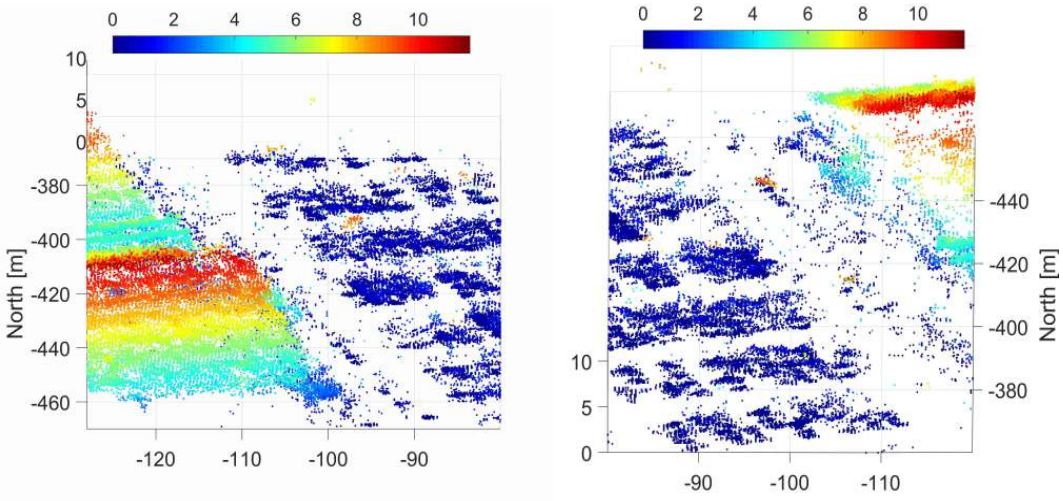

(a) (b)

Figure 8.29: 3d point cloud of the parking space in front of central building. a) Oblique view from the south. Only street lamps are observable as high targets. 3d information of trees are not or scarcely extracted, b) oblique view from the north toward the building's entrance area.

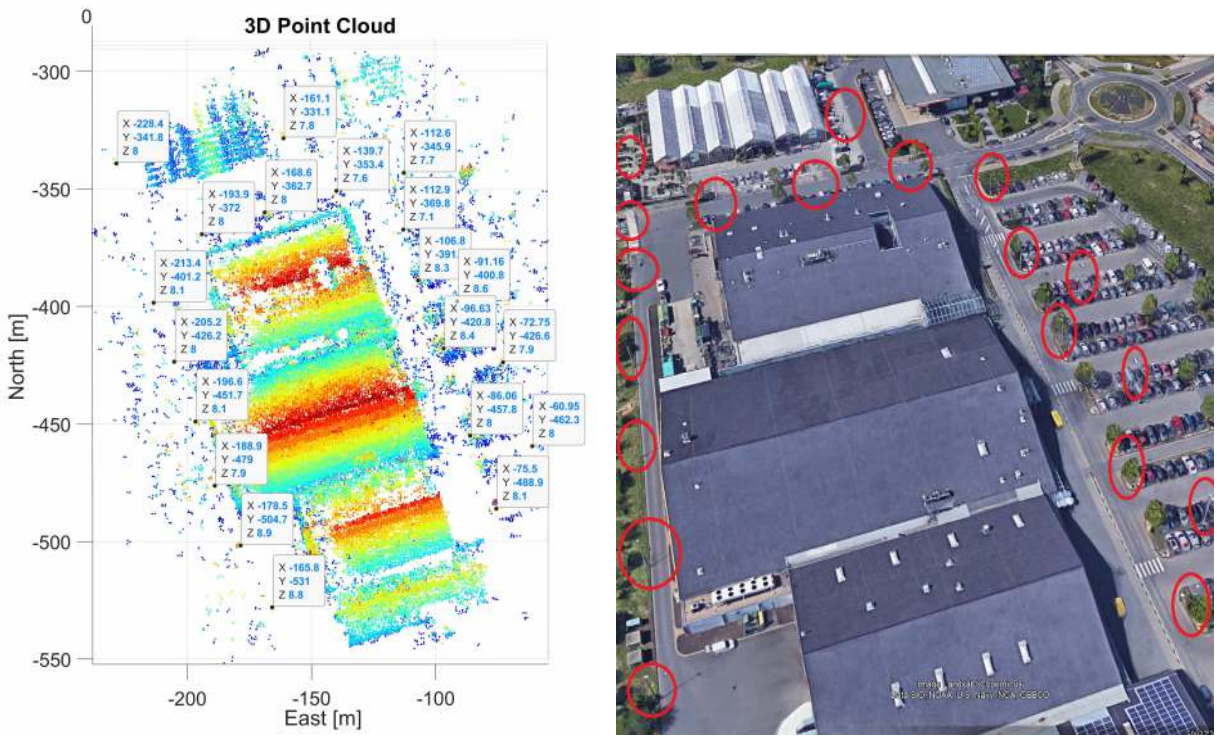

(a) (b)

Figure 8.30: Global 3d point cloud with highlighted street lamps. a) 3d point cloud derived with SP operator. Highlighted are several extracted street lamps with their corresponding heights and 3d coordinates, b) aerial photo of the urban scene with highlighted street lamps (Google).

The robust reconstruction of relatively small targets in the urban scene shall be presented in Fig. 8.30. It shows the 3d positions and the extracted height of multiple street lamps in the derived 3d point cloud in Fig. 8.30a. The location of these targets in an aerial image is presented in Fig. 8.30b. The derived height of these targets is relatively uniform over the entire urban scene. Compared to the LiDAR data from Fig. 8.18d, the height error was measured in the order of $\sigma_r = 0.5\,\mathrm{m}$.

Responses of the SP approach considering height extraction of trees are presented in Fig. 8.31. Further, the extraction of targets from only one aspect angle in a local point cloud is visualized along with a zoom on the selected area in the global point cloud.

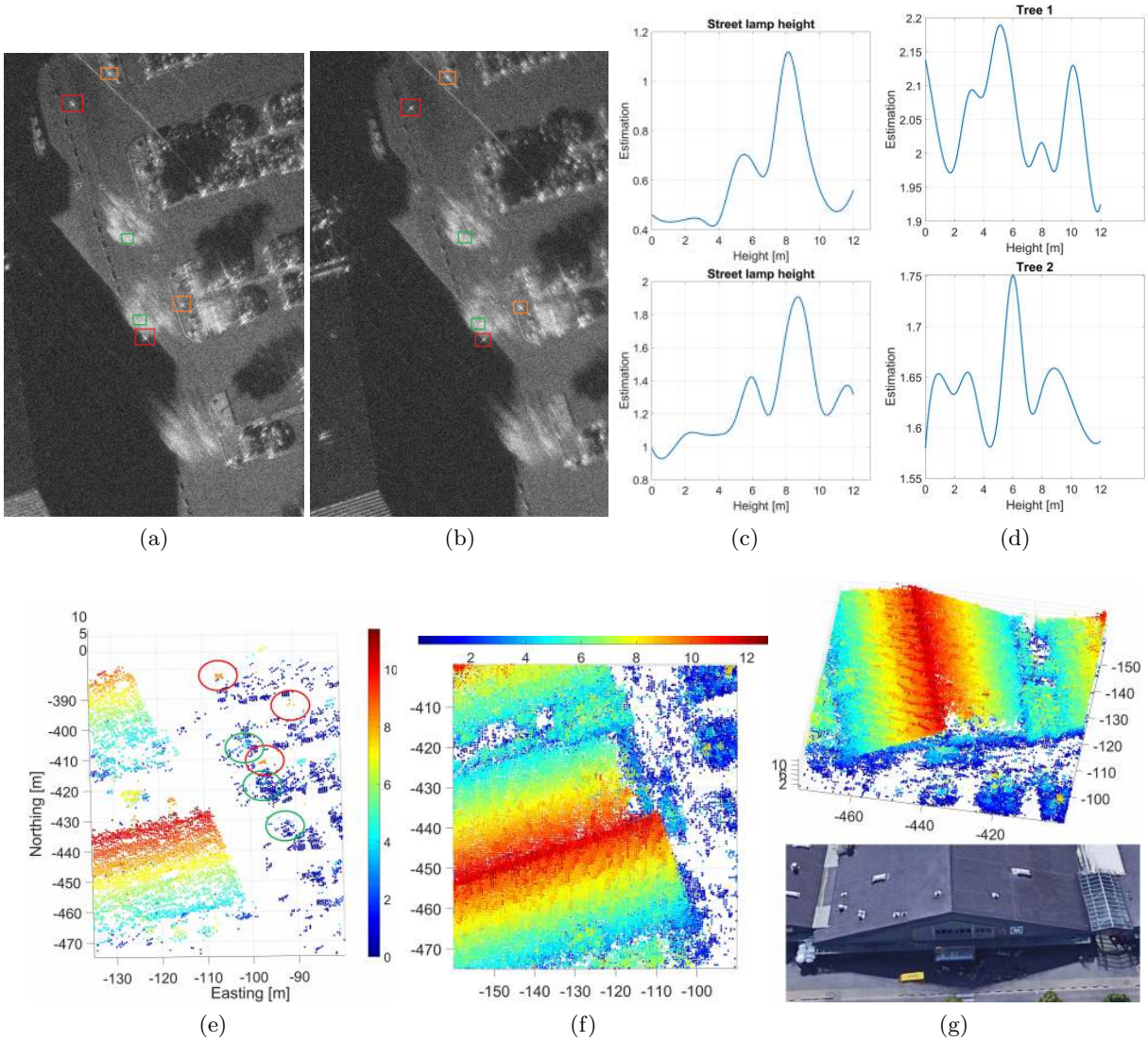

Figure 8.31: Height extraction and zoom of selected areas of the 3d point cloud. a) CSAR image, $\varphi_m = 50°$, $dh = 0\,\mathrm{m}$. Street lamp (red), lamp base (orange), treetop (green), b) equal view, $dh = 8\,\mathrm{m}$, c) estimated height of both lamps (north above, south below) with SP approach, d) estimated treetop height (north above, south below), e) zoom of extracted local 3d point cloud from $\varphi_m = 50°$ (one subaperture) with lamps (red) and trees (green) marked, f) top view of central building's entrance area in global 3d point cloud, g) frontal oblique view and aerial photo (Google).

Computational load of the proposed method

The SAR processor is parallelized, and time-consuming routines like the azimuth focusing are written in CUDA. The most significant amount of computation is due to the SAR processing of the extensive image stacks at different height levels ΔH with large φ_{az} in a 3 cm pixel spacing. Therefore, an Nvidia dgx station with four tesla v100 graphic cards with 5000 kernels each is used. Processing a SAR image stack of an area of $200\,\mathrm{x}\,200\,m^2$ at 16 different height levels and calculating the point cloud information from one specific viewing angle then takes 45 minutes with all four cards running at 99%. Twenty viewing angles approximately sum up to a computing time of one day. Non-coherent tracking in the image frames is significantly less computing-intensive as the focusing is carried out at only one height level with $\varphi_{max} < \varphi_{az}$, and the actual tracking is very fast.

Height ambiguities caused by the flight path or the objects' geometry

Evaluating an object under different flight conditions or a special geometry or backscattering property can lead to wrong height estimations. Two typical effects shall be shown here as examples. In Fig. 8.32, only the effect of down- or upward velocity $\vec{\mathbf{v}}_{sd}$ of the aircraft on the target's projection is indicated, while the actual flight parameters of a single aperture of size φ_{az} are analyzed. The same target's energy flow or smearing can differ significantly from two viewing angles if $\vec{\mathbf{v}}_{sd}$ varies that also affects the result of the proposed metric of that specific object. Two slightly different 3d estimations of the same target can therefore occur by a variation of $\vec{\mathbf{v}}_{sd}$.

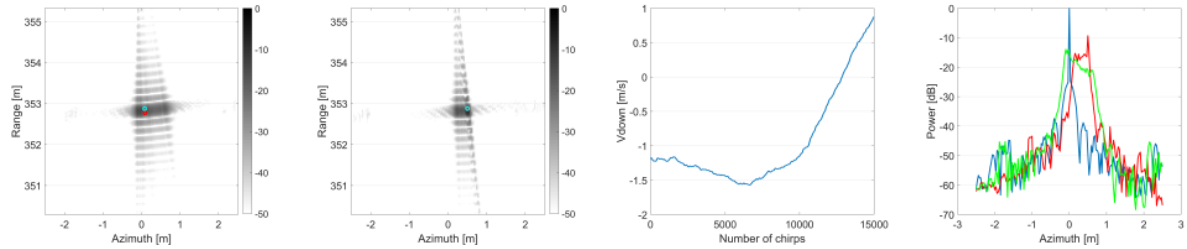

(a) (b) (c) (d)

Figure 8.32: Simulated point target projection using real experimental flight data of one synthetic aperture. Impact of Up/downward velocity $\vec{\mathbf{v}}_{sd}$. a) Projection of target at 5 m with $\vec{\mathbf{v}}_{sd}$, b) projection of target at 5 m with $-\vec{\mathbf{v}}_{sd}$, c) experimental Up/downward velocity $\vec{\mathbf{v}}_{sd}$ of one aperture, d) azimuth smearing. Positive $\vec{\mathbf{v}}_{sd}$ (green), negative $-\vec{\mathbf{v}}_{sd}$ (red), target at 0 m (blue).

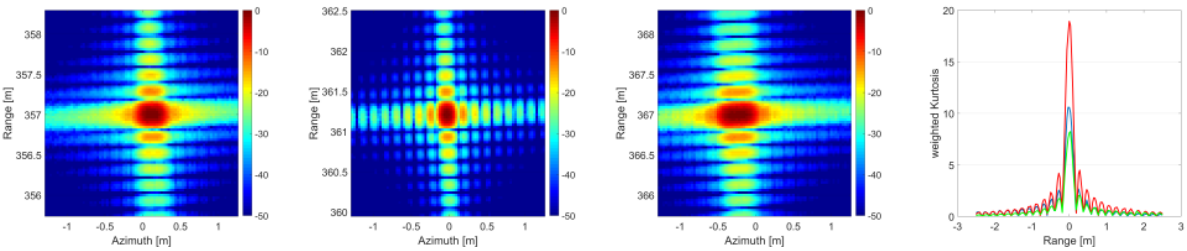

(a) (b) (c) (d)

Figure 8.33: 5 point targets at 0 m height aligned in 6 cm distance along a straight line with low angular persistence. Targets focused at different heights. a) Focused at correct height H=0 m, b) H=5 m, c) H=12 m, d) weighted kurtosis response (0 m (blue), 5 m (red), 12 m (green)).

Another example is the geometric shape and the object's alignment that can violate the assumed point target model. For example, a parked car can have multiple scatterers at a close distance aligned along a straight line at the front, the tires, or the rear. These may reflect in consecutive order at the same angle of incidence with short angular persistence. The backscattering flow in the final image will thus represent the model's response of a single point target at a different height as indicated in Fig. 8.33. Here, five ground targets aligned in 6 cm distance along a straight line with an angular persistence $< \varphi_{max}$ are focused at different heights. It is nicely observable that although these are five targets placed at the ground, the model estimates a single point target at 5 m height, see Fig. 8.33d. Due to the wrong height, the five targets then better coincide in one resolution cell.

8.4.4 Discussion

3d extraction of point-like objects

The non-coherent tracking approach shows high potential in efficiently extracting accurate 3d information of detached objects that appear as small point targets in the scene. Given such point-like targets, a small angular integration of only 2° can result in height accuracies of 1 m. Tracking larger aspect intervals between 10° and 20° can already reveal the height with an accuracy of 30 cm up to 10 cm, respectively. Analysis of the error function ΔE further indicates that the findings are consistent with the derived minimum theoretic aspect interval of φ_e. However, when interpreting these numbers, one has to consider that these were ideal targets like corner reflectors, and the sample was small. Nevertheless, objects in urban scenes often show only a small level of angular persistence but still significantly larger than 2°. Yet, the height resolution at this minimum angular interval φ_e is still very low, which means that 1.5 to 2 times the angular interval should be used for reliable height estimations.

For the larger coherent integration using the kurtosis method, similar results are indicated for smaller angular intervals as the non-coherent tracking. This is also expected applying the image spectral or weighted mean method. Consistent with the derivation of φ_{max}, height extraction with $\varphi_{az} < \varphi_{max}$ is not possible. An optimum in the data set can be found at $\varphi_{az} = 8.5°$ that is in the order of $10 - 20$ cm height accuracy. Further angular integration leads to poorer height estimates. Obviously, a more extensive φ_{az} leads to a loss of coherency in the SAR processing what is in accordance with Section 8.3. Therefore, the optimum value should be considered a kind of upper limit for further applications if the same conditions are applied.

By analyzing the exact projection of high objects on the focusing plane in the form of ellipses, it was noticed that the projection in ViCSAR mode could be counterclockwise to the sensor's movement. Although the platform was moving in parts with a higher or lower but always positive rotation angle rate, the projection could move partially counterclockwise due to the sink or climb rate $v_s \cdot \vec{e}_z \neq 0$.

More system specifically, given the three scatterers of Fig. 8.13c, the tracking accuracy of the proposed framework applied to the SAR data can be estimated from equation 5.14. With step size $n \approx 2$, a height resolution of $\delta h = 0.1$ m and $\varphi_e = 20°$, a filter response of $\delta E(0) = 2.24$ m and a mean $\delta E(\delta h) = 0.21$ m can be measured in Fig. 8.13c. With a pixel spacing of 12 cm the proposed algorithm's upper bound of the system's absolute mean tracking accuracy is estimated to $\frac{\delta E(0)}{n \cdot 20} \approx 5$ cm. Besides measurement errors of both the object's height and the platform's path, the implemented non-coherent tracking method can measure object movements in consecutive image frames below 5 cm in ViCSAR mode given the current processing parameters.

Non-coherent tracking of objects in image sequences

The tracking of man-made or natural objects in image frames indicates that the 3d location of the object's projection can efficiently be estimated. However, the computed heights from these objects do not show the exact maximum height but only correspond to the object's mean height of the entire object's projection, like the foliage for the tree. These values better specify the mean height of the moving backscatter energy of the entire object. Since the lower parts of trees with their trunks have a low backscattering signal, the mean height is shifted towards the treetop. The 12 m high tower reflects the radar signal more or less from the bottom to the top, leading to a computed mean height of 7.20 m which corresponds to the tower's center. Further, collecting object signatures is of great interest and can certainly be of benefit for classifying objects in the urban scene, particularly since objects of the dimension of a street lamp can be evaluated.

For deriving 3d information from a complete scene, however, an image segmentation would be very advantageous. In this case, e.g., the edges of a roof could be tracked and the extracted height assigned to the entire roof level. Without an image segmentation, the method relies on detached scattering centers that are evaluated. However, the superposition of several scattering objects within the search matrix is problematic since the energy flow of a single object can no longer be analyzed over a more extensive angular range.

3d point cloud generation of an urban scene

Results for the 3d urban mapping indicate a high level of detail that can be achieved for specific objects in the urban scene while clutter regions are hardly evaluable. From a qualitative perspective, the derived 3d information is certain of benefit when interpreting the exact location or dimension of an object or the type of roof structure of a building compared to only having the information from the SAR image. In addition, the circular acquisition allows a more or less shadow-free 3d reconstruction of specific objects from 360°. Considering time-critical applications, the data acquisition took only less than two minutes.

The 3d information of urban objects that show more a point-like behavior in the scene can be derived at accuracies in the range of some up to one decimeter. These include street lamps, the scatterer elements of a metallic tower, a car, or installed objects located on roofs. Comparatively good results for larger objects have been achieved at larger gabled roofs covered with roof tiles. Nearly the entire roof surface of the central building could be mapped in 3d with a point density of about nine points per square meter. One reason that may explain the good results with gabled roofs is that multiple scatterers there are located at nearly the same height in close vicinity. In addition, the edges of the roof tiles at some aspect intervals show a more point-like reflection that can be evaluated in the corresponding subapertures. Therefore, a large amount of the roof's 3d information was acquired from only a few aspects, but which aspects are beneficial is challenging to estimate in advance. For example, the partially good reconstruction of the facade of buildings was not initially expected, but the presence of dominant scatterers along the facade may have favored this.

Quantitative results showed that the absolute height of the rooftop could be derived with an accuracy of 30 cm up to 80 cm, depending on the extraction method. More interesting, the spreading σ_r of the reconstructed roof area compared to a least-square plane is in the order of 20 cm up to 60 cm that is a factor of 10 times more than LiDAR-derived roof surfaces. The accuracy also deteriorates with larger N, synonymic to a more significant number of fused subapertures. These findings are in accordance with [Duque et al., 2015]. However, it must be taken into account that the actual SAR raw data was focused on height steps of 1 m, and only the 3d results were interpolated on a 10 cm step size. Therefore, a 20 cm accuracy is very promising

and puts the relation to LiDAR into a better perspective. An investigation that may focus the entire scene on smaller height steps similar to the 10 cm height steps with the corner field data is therefore encouraging. However, this would significantly increase the computational load. The roof inclination γ could also be derived accurately with an $< 0.5°$ accuracy, and γ only marginally degrades by fusing more aspects. Knowing the exact value of γ can be valuable by deriving an optimal viewing angle to a specific roof area or for better segmentation or classification.

Best results for the complete building complex were derived by applying the WM fusion yielding a σ_r of 1.81 m for a data set of 140.000 points. While considering only the actual roof area, the best accuracy was derived for points above 5 m height with $\sigma_r = 0.68$ m analyzing more than 37000 points. This result includes part of the roof area that showed clutter behavior and height extraction there was prone to errors. It is noticeable that all operators show a higher accuracy for objects above 5 m height and worse accuracy for targets at lower elevations. Analysis of this effect in Fig. 8.23c indicates that erroneous areas are nearly all situated at the border of the building. One reason probably is that low areas at the border are more likely to be overlaid by several objects at different heights, e.g., facade areas. A second reason is the various materials in the scene. For example, the canopy at a lower height is made of glass, and also the transition between the adjacent buildings is of different material showing more clutter characteristics.

When comparing the different metrics for 3d extraction, the WM operator achieves the best results for the buildings as this method averages the information from all aspect views. Thus, height biases that are present in single subapertures are less relevant. On the other hand, information from e.g., trees, is removed as they might be only valid from a smaller aspect interval. Further, the computational burden is high. Ku and SP methods are similar at high altitudes, but SP shows higher accuracy for low targets. Also, SP showed slightly better qualitative results and lower noise levels in areas more challenging to reconstruct, but this might also be due to a higher applied threshold level. In particular, in the parking space area in Fig. 8.18c, with SP, it is better to assess areas that show only parked cars and regions that comprise trees.

Analysis of the fused aspects showed that derived 3d points from some aspects had a constant height bias. By calibrating the data, the relative accuracy could be increased up to 20 cm, which was also the lower bound for the WM operator. The causes may be manifold, e.g., a bad flight path measurement at the corresponding subaperture or errors from fusing the data from the local WGS84 reference system into the global point cloud reference system. Also, the focusing step size of 1 m may be too large. But most importantly, the deterioration of the height accuracy due to the fusion of multiple aspects is not a random process. Yet, it can be significantly reduced by extracting the offset bias.

As expected, objects located in the center of the circular trajectory could be reconstructed best. Yet, a relatively good 3d reconstruction was also achievable for objects placed at the edge of the spotlighted region. This is in accordance with the corner field experiments and indicates that only small angular visibility of $8° - 15°$ can already achieve a high level of 3d information. Furthermore, most street lamps at the northern or southern border of the scene were also extracted from only one single subaperture. Besides the spatial information, the presented approach can also collect angular scattering information that may help classify an object.

It should be noted, however, that the proposed methods are optimized to be applied in urban scenes with building heights below 20-25 m. If the buildings are significantly higher, the search matrix has to be enlarged to a size that would definitely reduce the accuracy of the derived 3d position. In addition, it would be even more complicated to follow the energy track of the original object.

Problems arise in areas that show clutter or volume scattering behavior like the gas station's roof, trees, or the parking area. In these regions, the height error can amount to several meters easily. If not handled with the WM method, these scene parts become rather noisy. Also, volume scatterers such as trees are challenging to recognize, and their 3d structure can only partially be observed in the point clouds if at all. There are also gaps in the roof reconstruction that might be due to dividing the circle in different arcs that do not always give the best view of the scene. In particular, the roof area near the facade causes problems and the area of the roof transition mentioned before. In addition, the signature of moving objects in the parking space area interferes, causing ghost targets. Beneficial would also be a kind of subaperture pre-selection since some aspects are significantly more valuable for height extraction than others.

Nevertheless, evaluating the amplitude images with the proposed metric is a struggle with ambiguities. The causes of incorrect height derivation are often violations against the proposed methods' model assumptions, e.g., the expectation of a persistent backscatter in the scene. If a smeared object on the image plane is really an object at the wrong focus height or only a smeared object at the correct height is difficult to estimate. One reason is that minor absolute position errors in the track measurement of fused aspect views can already lead to a higher point spreading. Further, the evaluation of the experimental data shows that the accuracy of the height extraction from a specific aspect angle depends not only on the radar's view or elevation angle but also on a large extent from the platform's flight path. Therefore, the same object observed under a different aspect angle forms a broader or narrower projection course, depending on the platform's current up or downward velocity. Ambiguities can also arise when multiple backscatterers with short angular persistence are geometrically arranged in such a way that they resemble the energy flow of a single target at a defined height as indicated in Fig. 8.33. An extension of the model to evaluate line targets would probably be beneficial.

A further problem is that the platform does not fly a perfect circular trajectory. Certain sections show a relatively high rotation angle rate, while others are flown instead more linearly. When it comes to the fusion of the entire circular data set, this means, that there might be a good viewing angle to the object. Still, while on a more linear flight path, the height resolution capability is limited or, at worst, not available. The concept works best when the platform ideally has a uniform angular rotation rate in all selected views that is rather likely at higher flight altitudes and larger radii.

8.5 Optimizing focusing process to the specific scene

Estimating an optimal viewing angle of the urban scene was done by deriving a surface model with equidistant step size from the 3d point cloud of Fig. 8.18a. A 1 m raster step size was applied on the point cloud setting the mean filter height as surface height. Further, a 4 m large rectangular low pass filter was applied on the surface model to smoothen the roof area, while in the last step, it was interpolated to a grid size of 3 cm for the refocusing process. The height threshold parameter η_r was set to 2.7 m, labeling areas above the threshold as roof areas while areas below the threshold are labeled as ground.

Results for the calculated optimal viewing angles φ_{vm} are presented in Fig. 8.34. All roof elements aligned to the mean northern or southern direction are summarized to one viewing direction. The normal vector $\vec{\mathbf{n}}_r$ of the roof area was derived by the least square approach at a 5 m step size. Areas indicated in dark blue (-50) are areas where no optimal viewing angle can be derived. These fields cause shadowing or foreshortening from all aspect views since high objects from multiple sides border them. Ground pixels with restricted views are indicated around the building complex. For instance, along the eastern facade, the best viewing angle is in the direction

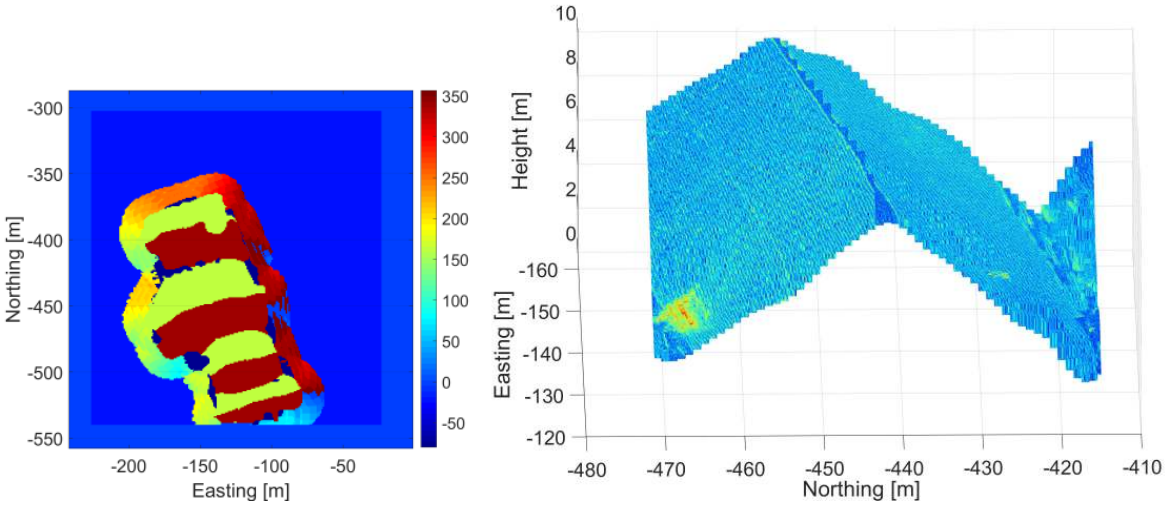

(a) (b)

Figure 8.34: Derived optimal aspect angle φ_{vm} in [deg] for buildings and refocused roof area. a) Derived φ_{vm} for high and ground pixels, b) part of central building's roof area refocused at φ_{vm} with $\varphi_{az} = 5°$ (2 cm resolution) on the derived surface model. Both sides of the roof can be focused with high resolution in the correct geometry.

of north-northwest ($330° - 360°$) or south-southeast. Pixels that do not show viewing restrictions are filled with information from a 'master view'.

Parts of the central building's roof area refocused on the smoothed 3d surface by selecting φ_{vm} is presented in Fig. 8.34b. Both roof sides can be focused directly in the optimized image geometry with δ_y =2 cm and $\varphi_{az} = 5°$. In the area of the roof transition and closer to the facade, the 3d structure appears more distorted but the gable roof's shape can be easily derived.

A SAR image with δ_y =2 cm of the complete building complex refocused with φ_{vm} on the surface model is presented in Fig. 8.35a. Since the complete 360° data set was only acquired for the center, focusing the borders was not always possible by applying φ_{vm}. Notice, the roof area is focused at consistent high resolution from higher to lower parts despite the circular flight path. Compared to a SAR image processed on a linear trajectory, the missing shadow areas next to the buildings are noticeable. Yet, all roof structures are visible and also the ground area next to the buildings is observable from all aspects. These areas are typically shadowed, show foreshortening, or are partly overexposed due to strong double bounce reflections. Similarly, the remote part of the roof is often shadowed from one aspect. The image, therefore, has some similarities with a top view of the scene. However, shadowed areas and substantial distortions are still visible along the roof area, particularly closer to the facade.

Even more information can be gained by manually superimposing the three most appropriate views from φ_{vm} in a colored SAR image while the data is refocused on the surface model. Fig. 8.35b and a zoom of the central building in Fig. 8.36a present the result of the fusion of the three aspect views $\varphi_m = 242°$ (green), $\varphi_m = 70°$ (red), and $\varphi_m = 20°$ (blue). Again, nicely observable is the very high resolution of the complete roof area of all four buildings. The dimensions of the building can be evaluated from the image along with small objects that are placed right next to the facade which is even more highlighted in Fig. 8.36a. White-colored objects like some roof installations are high targets visible from all aspect views. Since they are colored white, the 3d locations of their scatterers are most likely very accurate.

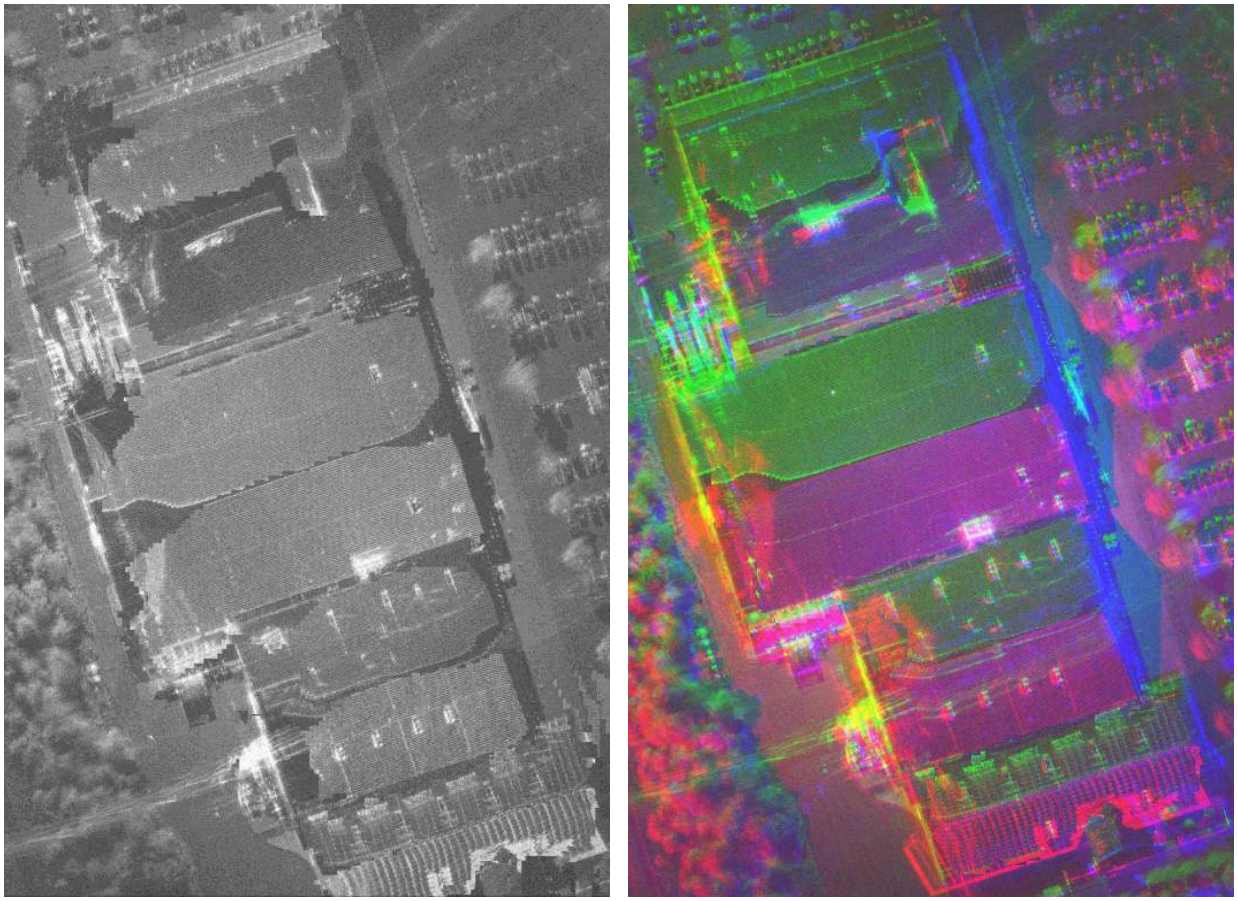

(a) (b)

Figure 8.35: SAR image refocused on the surface model by selecting optimal aspects φ_{vm}. a) Composed SAR image of the main buildings, where each pixel is focused from φ_{vm} derived from Fig. 8.34a, b) manual superposition of the three most appropriate views refocused on the surface model. Each color channel indicates a different aspect view.

On the eastern side of the facade, it is recognized that the shadowed area in the red channel is filled with information from green and blue. Even parts of the facade and the entrance area of the building are visible in the blue channel. The parking area is imaged on the flat plane geometry; therefore, the tree projections do not fit. Yet, the observer gets a high level of detailed 360° information of a spotlighted urban scene in a single image.

Further results of a manual superposition of the three most favorable aspect views of a planar region in a colored SAR image are presented in Fig. 8.36b. Unfortunately, this area was rather outside the circle, and only a limited number of aspect views were available. The focusing height of the different views is calibrated by extracting the exact 3d location of the corner reflector by the Ku operator of Section 5.2.3. The imaged area is the northern part of the parking area focused with δ_x =7.5 cm and δ_y =2 cm. Shadowed areas from parking cars or trees are supplemented with information from other views. As the scene is not static, each pixel $I(x, y, \varphi(T))$ is time-dependent, and thus changes over T are easily recognizable. For example, red arrows indicate two parked cars at the start of the circular trajectory. Still, they are disappeared at the end of the trajectory (red scattering) while one car newly arrived (green scattering).

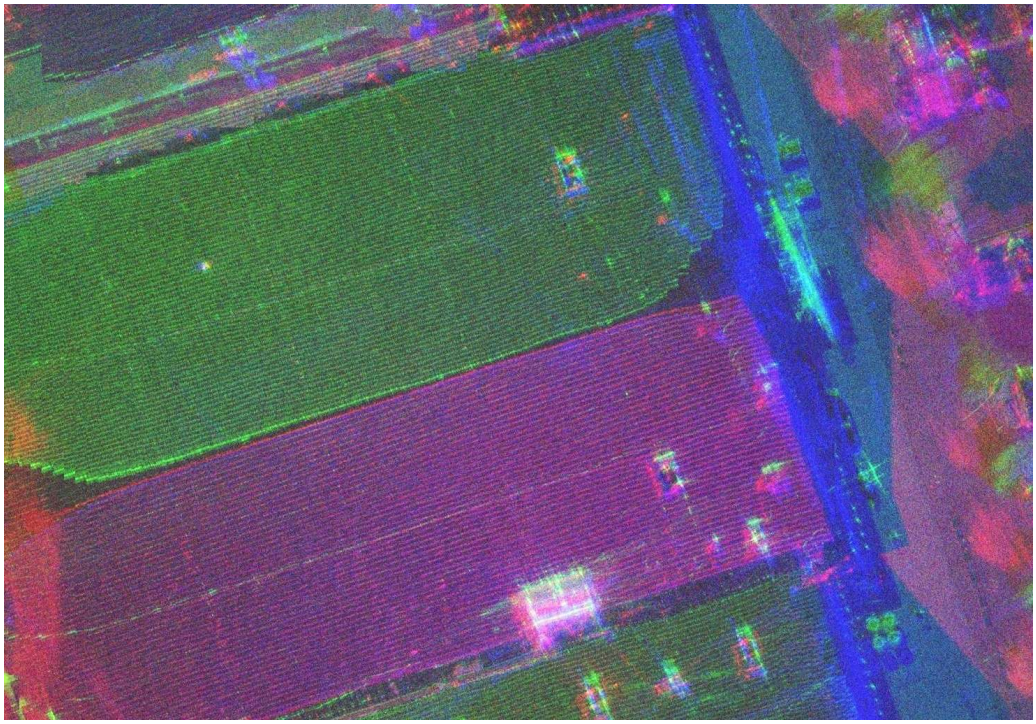

(a)

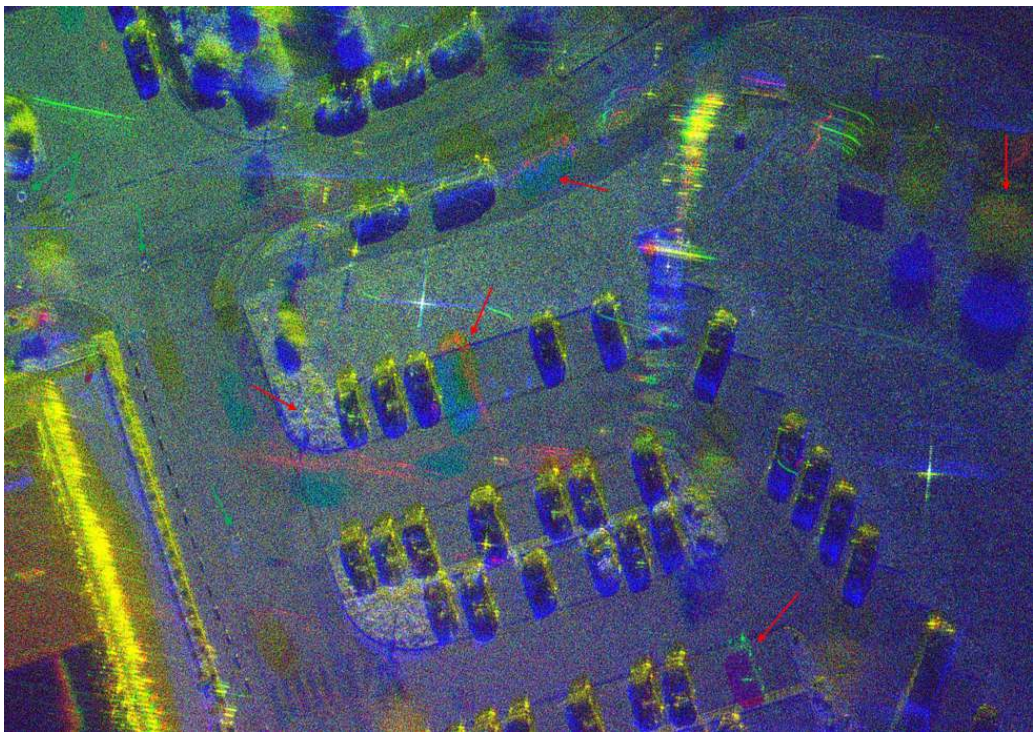

(b)

Figure 8.36: Superimposed SAR image of the three most appropriate views refocused on the derived 3d surface model. a) Zoom of the right side of the central building from Fig. 8.35b. High roof installations are visible from all 3 aspects and appear white. The entrance area and the objects placed directly beside the facade can be observed, b) the parking area with calibrated height. 7 cm x 2 cm resolution. Red arrows show parked cars that arrived or moved away during data acquisition, the base of a street lamp and tree foliage. Green arrows show gully covers.

8.5.1 Discussion

Extracting the scenes' 3d information is very valuable as focusing different aspect views in the correct image geometry becomes feasible. This allows a joint representation of information gathered from multiple aspects in a single SAR image with minor distortions. The results indicate that both sides of a large gabled roof can be mapped with only minor distortions in very high resolution in a single image. Despite the circular aperture, the entire roof area can be resolved at the same level of high resolution. Further, thanks to the unobstructed view right next to the facades from all sides, the dimension of a single building can be determined relatively accurately. When imaged from multiple aspects in a flat plane geometry, the roof area would be offset, shifted, and not fit together at the gable or ridge. Extracting the exact dimensions of an entire building would also be very challenging. However, an enhanced mapping of facades or trees is not possible with the currently proposed method.

Most image distortions happen in the vicinity of the facade or at the roof transition and are obviously due to erroneous height extractions. As detailed in Section 8.4.3, the 3d point cloud shows gaps in multiple areas, and further, the model of a smooth roof area is neglected at the ridge. Shadowed areas are due to wrong derivations of φ_{vm}, but this is most likely also due to inaccurate height estimations. There is the inner courtyard in the northern building, which complicates the 3d extraction and violates the model of a smooth roof area. Other distortion effects might also come from the data being focused on a pitched roof surface instead of a flat plane. On the other side, some derived object heights are indeed very accurate and result in scatterers that are mapped in white in the colorized images. In CSAR, the quality of the 3d information can be identified by the fused image.

At flat surface areas, the fusion of different aspect views can be realized in a flat plane, but it also requires a very precise absolute height extraction of the focusing plane. In addition to the very high resolution, changes during the data acquisition are observable in a single image.

8.6 Mobile radar mapping

The following Section presents the results for the ultra-high-resolution SAR imaging applied to street and facade mapping. The SAR images were processed with a resolution of $\delta_x = \delta_y = 5\,\text{mm}$ corresponding to a synthetic aperture length of $< 0.5\,\text{m}$ while the car was moving $20\,\frac{km}{h}$.

8.6.1 Street mapping

Results of the street mapping experiments are presented in Fig. 8.37. It shows a SAR image with a parking place covered with paving stones. Several small objects like screws, nails, bearing balls, and two tiny 30 mm edge-length corner reflectors (blue), similar to Fig. 7.6f, are placed in the scene to evaluate the system's performance. The phase profile of such a reflector in the raw data is indicated in Fig. 8.37c and Fig. 8.37d with the typical azimuth chirp characteristic. By converting the phase history to range history, a distance change of $\pm$ 2 cm within the coherent aperture can be measured, see Fig. 8.37e. The phase change from chirp to chirp from Fig. 8.37f reveals that trajectory stability of less than 0.15 mm is required to generate coherent data processing. Obviously, this is at the limit of modern GPS/INS units. The results in Fig. 8.37b present a manual measurement of the dimensions of a threaded screw in the focused image domain (red). It indicates that due to the derived imaging geometry, the dimensions of objects can be measured on a 1 cm resolution scale.

Further street mapping results are demonstrated in Fig. 8.38. A bus lane and parts of a road crossing and adjacent parking bays are mapped. The colored lane markings and labels have a

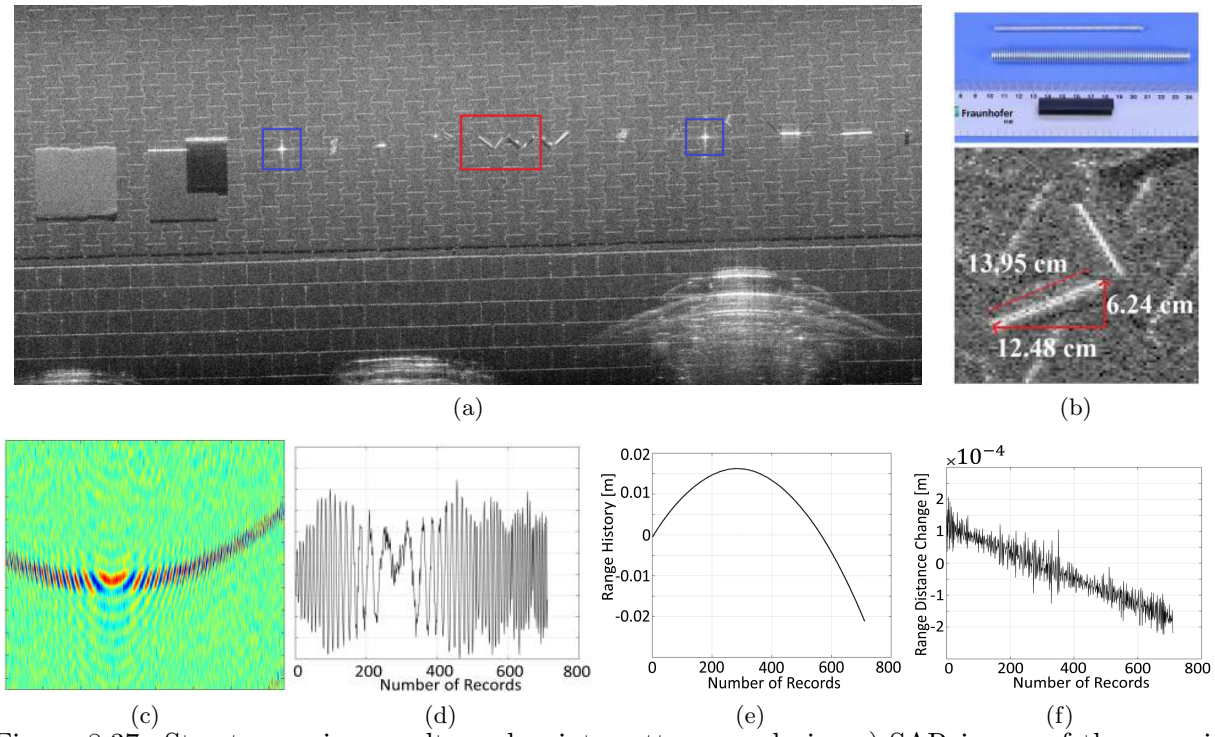

Figure 8.37: Street mapping results and point scatterer analysis. a) SAR image of the experimental setup that shows different metallic objects placed on a parking lane to test the sensor's resolution capacity and the proposed focusing strategy. Front side of parking cars at the bottom of the image, b) 30 cm^2 zoom of a threaded screw (red square in a)) and validation of the measured dimensions, c) range compressed raw data of a corner reflector, d) azimuth phase history (real part), e) phase converted to range history. Distance change of ±2 cm, f) range distance change < 0.15 mm for each chirp indicating the high GPS/INS requirements.

smooth surface and are less rough even at these high frequencies and therefore present a mirrored surface that makes these areas appear dark. Some lane markings can be recognized as already worn out or partially repaired. Further, the asphalt condition can be identified, and small cracks of several millimeters on the surface and the markings are observable. Obviously, cracks are best detectable if they run parallel to the acquisition geometry since the radar sensor can detect the edges well. They represent a better reflection at the angle of incidence applied.

More prominent objects such as gully covers are shown on the left and right part of the road images and even better in Fig. 8.39 and shall represent the high detail level. Typically, a very strong echo comes from the curbside and from the edges of paving stones. When observing the pattern of the paving stones from the rain gutter, it is possible to detect stones that are soiled with sand and parts which are clean due to the different roughness, see Fig. 8.38f. The asphalt itself is rough at this wavelength and shoes diffuse scattering.

The proposed method of adapted planes further ensures enhanced image geometry. For example, Fig. 8.39 shows a 3 m^2 zoom of a gully cover on the road from Fig. 8.38c. In Fig. 8.39a, the mean height of the image plane is chosen from the start of the image strip (flat plane model). Aside, in Fig. 8.39b, the height is determined by the proposed method. Although the resolution is only slightly better in Fig. 8.39b due to the fact that the trajectory at this section was nearly linear, the imaged object's dimensions are significantly improved. The dimensions of the gully cover in the SAR image of Fig. 8.39b are measurable as 0.78 m x 0.76 m, however in Fig. 8.39a as 0.96 m x 0.75 m. The gully cover's real diameter was measured to be 0.78 m, see Fig. 8.39c, which

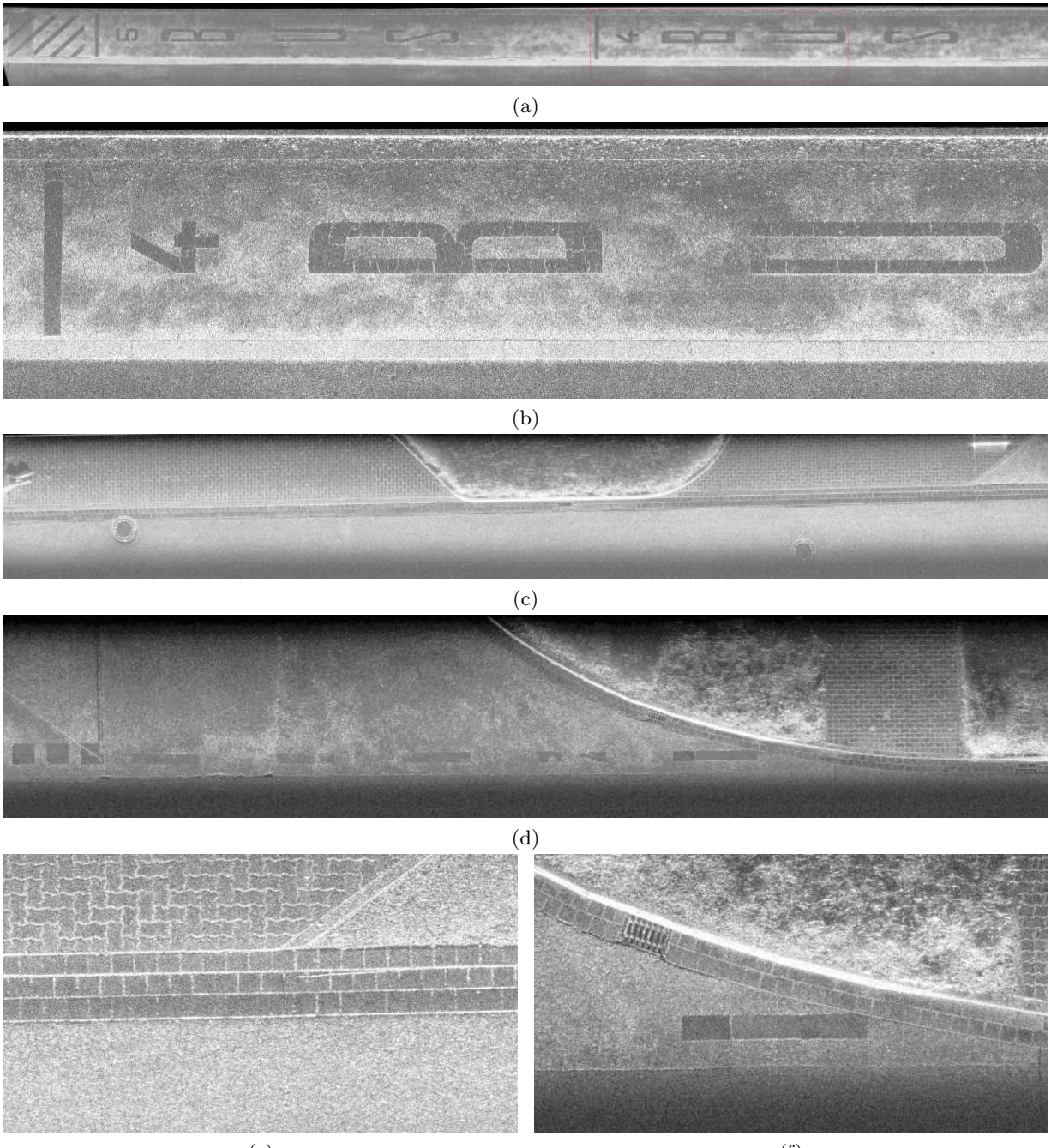

(a) (b) (c) (d) (e) (f)

Figure 8.38: Street mapping SAR imaging results. Images are sections of considerably longer strips. a) Bus lane beside the road. Letters on the surface are well resolved due to the surface's different roughness characteristics, b) zoom of the letters. Small cracks in the painting are visible in the image, c) a street with adjacent parking lane and vegetation. The pattern and size of the paving stones are observable. Different types of gully covers are present and altering asphalt background. On the left side is a standing road sign on the lane, d) one side of a road intersection. The condition of the asphalt and the lane markings can be recognized. Some markings are worn out, cracks in the asphalt down to several millimeters are visible, e,f) details from image c) and d) to visualize the quality of the results. The patterning of stones is well observable. In f), parts of the rain gutter are soiled with sand and appear slightly smeared that is due to the different roughness compared to clean stones.

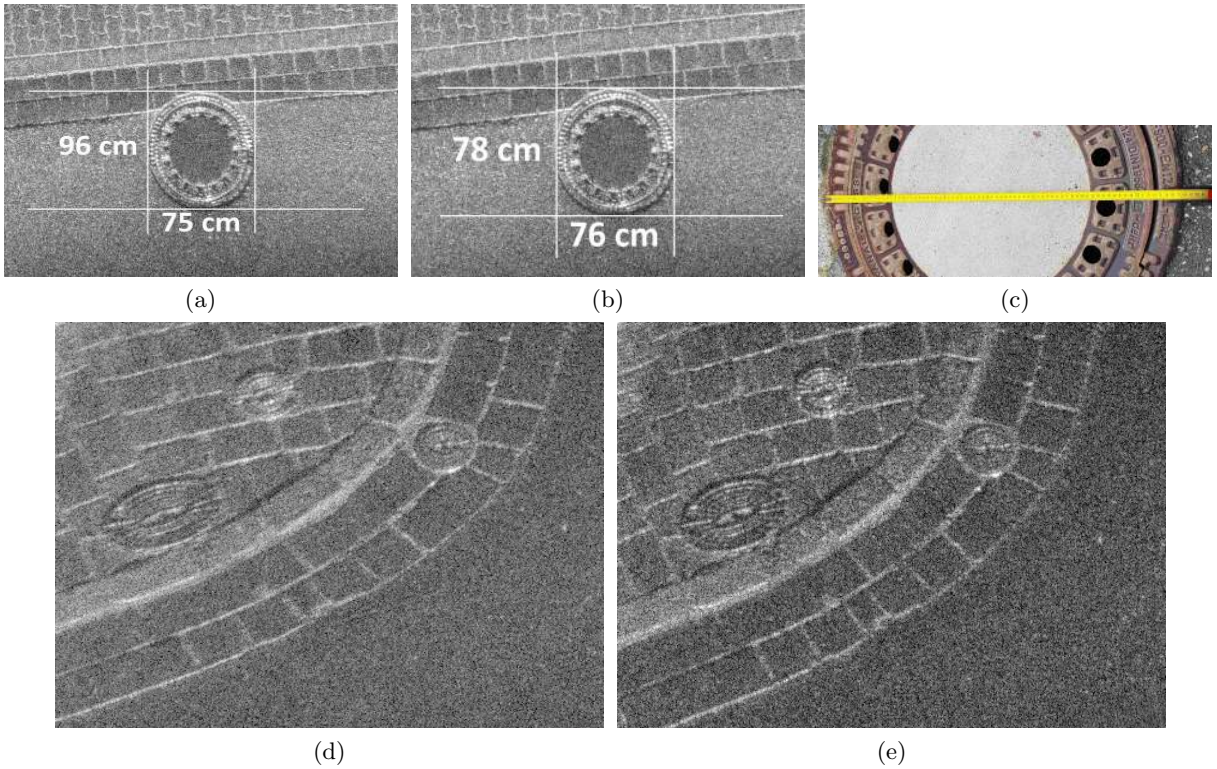

Figure 8.39: Comparison of image distortions and blurring effects in SAR images. a) $3\,m^2$ zoom of gully cover from Fig. 8.38c focused with the flat plane model with height chosen from the start of the path. Due to the slightly sloped road, the height at the gully cover's position is $\sim 50\,\text{cm}$ too low, causing a distorted geometry in range dimension and slight blurring, b) focusing on the adapted plane method. Geometric distortion is highly reduced, c) photo, indicating a radius of 78 cm, d) $1.5\,m^2$ zoom of street area located on a curved, downward sloping road focused with flat plane geometry, e) area focused with proposed method. Due to the curved street, the image sharpness is improved.

is very close to the value in the SAR image. The distortion in Fig. 8.39a is due to the fact of non precise height information - in this case a deviation of $dh \approx 50\,\text{cm}$.

Similar effects can also be observed in Fig. 8.39d. This data set was taken on a curved, downward-sloping street where the path of the car for several ten meters could be approximated to be on a circular track with 40 m radius. Besides the discussed geometrical distortions by using the flat plane model with an estimated mean height, the presented method also enhances the focusing performance in Fig. 8.39e by means of contrast and sharpness. Blurring in the image caused by the non-linear movement and wrong height is reduced.

Finally, Fig. 8.40 shows the author lying on a parking site on a blanket. Again, each individual paving stone can be clearly recognized, and the size of the stone is correctly measured with 20 cm x 15 cm. The body of the person shows a very high level of detail. Stronger echos are from the head, forearm, and fingers. It is possible to recognize whether and in which way arms and legs are extended, and the fingers can be counted individually. At this frequency, parts of the clothes and the blanket are transparent, revealing the paving stones below the blanket or a mobile phone below a jersey, see [Palm et al., 2018]. More experimental results of subcentimeter mobile mapping can be found in [Palm et al., 2016a,b, 2019].

Figure 8.40: SAR image of the author at 300 GHz. Person is lying on the stomach with the head down on a blanket on paving stones. Through the transparent blanket, the pattern of the stones is visible. All fingers are clearly indicated.

8.6.2 Facade mapping

Three different facade styles mapped at close range are presented in Fig. 8.41 to analyze the backscattering characteristic. In Fig. 8.41a, the first floor of the entire facade of a half-timbered house is presented. Since the facade's orientation and the image plane's orientation are slightly shifted ($d\vartheta < 0$), the facade moves slowly into the image plane. This can be observed in particular on the course of the windows, which are not exactly horizontal.

The facade's highly detailed square-framed timbered work can nicely be identified due to the different backscattering characteristics compared to the rough wall plaster. It can be observed that the wooden beams are slightly offset from the masonry, and the backscattering further reveals different workmanship of the masonry. The glass of the windows appears dark as the transmitted radar wave is reflected away (mirror effect). Due to the oblique view from below, window benches cause shadowing while multipath effects and strong echoes on top of the windows can be observed. The strong horizontal echo from the top of the building is due to the rainwater pipe, which can also be seen on the building's right side.

Similar effects can be observed in Fig. 8.41b, which shows two adjoining houses connected with an archway. Again, the shape and dimensions of the windows and their double-bounce effects are clearly visible. The wall plaster of the right building was much smoother, which led to a very homogenous backscattering behavior in the SAR image. The course of the rainwater pipe on the left side of the building is observable, and again, the double bounce effects due to the direct view into the roof projection. On the right side of the left building, a tree stands in front of the facade. The branches and leaves seem to partially protrude into the focusing plane, since a flat plane model obviously does not fit a standing tree.

In Fig. 8.41c, the brick facade of two houses is presented. The houses are situated next to each other but show a slightly different orientation angle that can easily be observed in the SAR image through the course of the windows and bricks. Due to the fine resolution, each brick stone

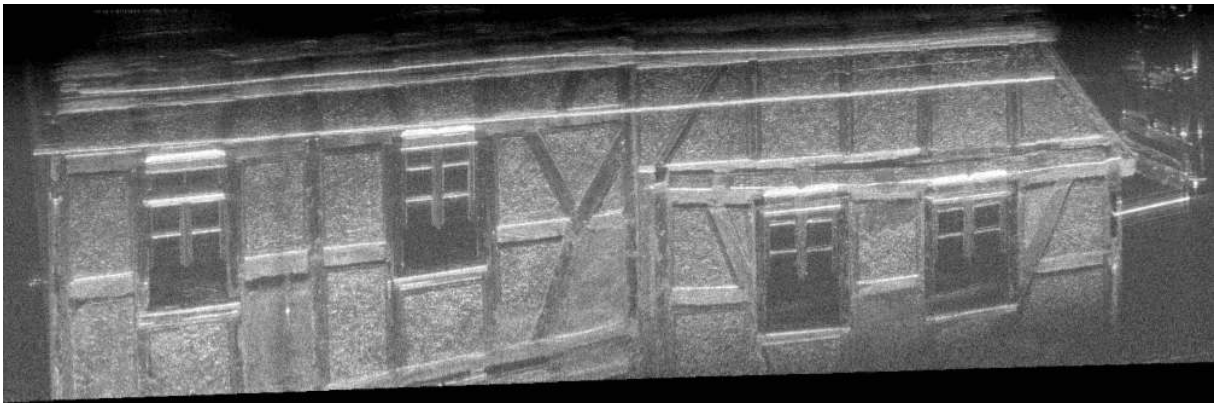

(a)

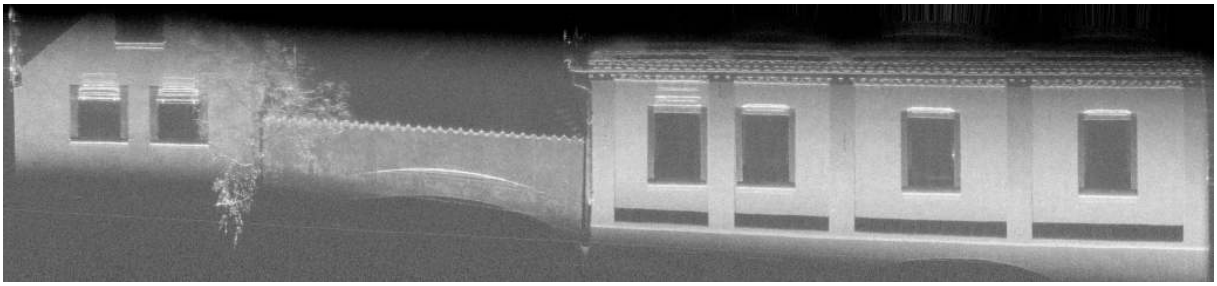

(b)

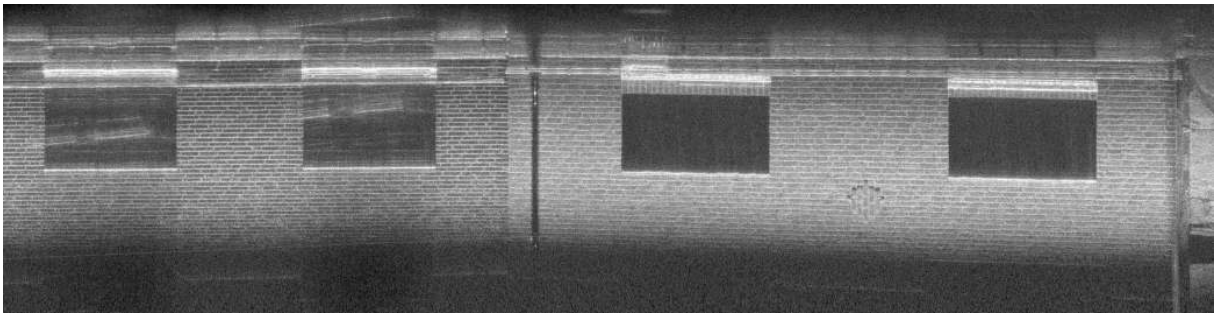

(c)

(d)

(e)

(f)

Figure 8.41: SAR images of facades with 5 mm resolution. a) First floor of the half-timbered house. The orientation of the facade is slightly offset from the focusing plane. The backscattering characteristic reveals different materials, b) first floor of two adjoining houses with more homogenous wall plaster connected with an archway. A tree is standing in front of the left facade, c) brick facade of two adjoining houses with slightly different orientation, d) photo of the half-timbered house, e) photo of two adjoining houses, f) photo of the brick facade.

can be counted or the fixations of the rainwater pipe. In addition, the rotated geometry causes the range resolution to increase at higher elevations.

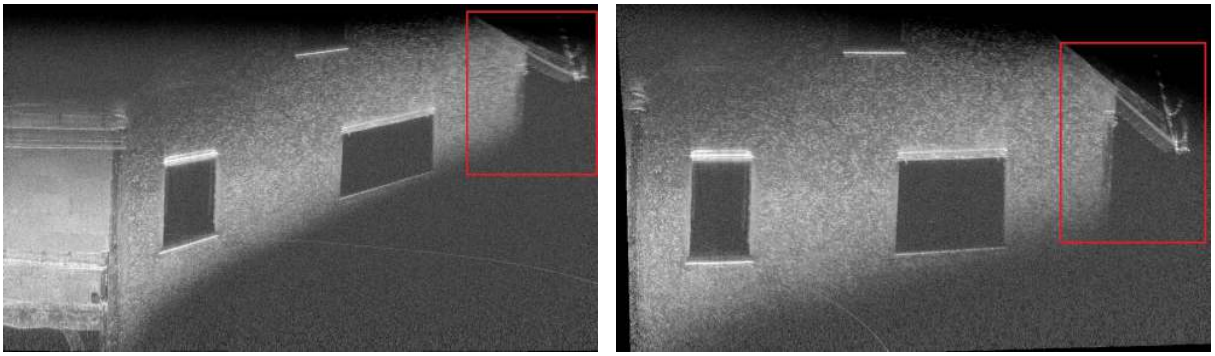

(a) (b)

Figure 8.42: SAR image of facade mapped on adapted focusing plane. a) Sloping facade mapped on wrong imaging geometry, b) facade mapped on adapted imaging plane rotated by $\vartheta = 11°$.

The height ΔH and width ΔL of one window of each facade were further evaluated and compared with measurements from a laser rangefinder. With a pixel spacing in the SAR image of 2 mm, the edge position of the windows was determined manually. Table 8.6 compares the results that, similar to Section 8.6.1, show that a measurement in the centimeter scale is possible. With 5 cm, the most significant deviation affects the half-timbered house that also shows the largest orientation shift ($d\vartheta < 0$), according to Chapter 6.2.

Table 8.6: Window size ΔH x ΔL measured (center) and extracted from the SAR image (right).

	Laser	SAR
window Fig. 8.41a	1.09m x 0.78m	1.14m x 0.74m
window Fig. 8.41b	1.12m x 0.76m	1.16m x 0.78m
window Fig. 8.41c	1.06m x 1.98m	1.03m x 1.98m

The effect of adapting the facade orientation ϑ in a second iteration alongside a window as proposed in Section 6.2 is presented in Fig. 8.42. In this case, the window height of the window furthest to the left was extracted manually since the facade begins to disappear into the depths of the image plane. It shows that the adapted facade with $d\vartheta = 11°$ is now much better aligned to the building and, more importantly, the focusing quality is also improved. This is indicated along the rain pipe and the eaves marked in red.

8.6.3 Discussion

The level of detail resolved in the SAR images is exceptionally high. The street images show consistent high focusing quality and contrast over the entire image strip by applying the proposed method of 'focusing on adapted planes'. Adapting the geometry is particularly important in curved street sections or when objects in the image shall be precisely measured. Very small scale object details can be resolved, and various types of different asphalt pavement or lane markings are observable in very high resolution with minor geometric distortions. Diffuse scattering dominates at these small wavelengths, and only highly smooth surfaces like lane markings show specular reflections. The potential to measure the dimension of objects on a centimeter or even millimeter scale in the processed SAR images might be valuable for subsequent image processing steps and can lead to new applications. For instance, change detection applications to register small-scale

objects are particularly conceivable. Further, the road surface is ideally suited for backprojection SAR since smaller sections can be ideally approximated as flat planes, and no shadow formation is expected from high objects. On the other hand, diffuse scattering behavior provides little information for further autofocus algorithms.

Due to the currently limited sensor height and the sensor's limited output power, the image strips typically have a swath width of only 4 m to 6 m. In addition, the platform's speed is also still limited due to the high RF bandwidths, which results in high data rates. Great effort must also be attached to a very precise path measurement in the form of dGPS postprocessing of the data that can handle the more challenging conditions such as start-stop problems or reduced coverage by GPS satellites in urban environments. Compared to the real-time GPS/INS data used initially, there were significant differences in quality in the image data, especially since the determined GPS altitude information was too imprecise. The importance of a correct fast time Doppler correction at this very high frequency is further indicated in [Palm et al., 2018]. However, the relatively stable movement of a car compared to a small aircraft is beneficial.

In the context of facade mapping, the SAR images also show a very high level of detail by using the proposed method. Therefore, the evaluation of the actual height and width of small facade elements such as windows, masonry, or rainwater pipes can be achieved very precisely and cannot be compared with airborne SAR applications. However, the model assumes the facade is situated next to the street and oriented along with it. This is by no means the case for all facades. Further, if the distance to the facade cannot be determined precisely enough, the image quality suffers. At last, the evaluation of the course of the facade from the SAR data is exhausting, and the subsequent adaptation by the manual estimation of object sizes only provides limited enhancement. This characteristic severely restricts the proposed method for operational applications.

9 Conclusion

This thesis indicates for the first time the feasibility of processing high-resolution airborne W-band FMCW SAR data acquired from circular trajectories. To the author's knowledge, in the course of this work, the first W-band FMCW SAR sensor designed explicitly for this acquisition geometry was created, operated on a small aircraft, and its data evaluated. It can be stated that the application of such a sensor concept on a circular trajectory provides valuable information of an urban scene both in terms of urban mapping and urban monitoring. Operated on a single-channel and single path configuration, SAR images with very high spatial resolutions of the urban scene can be achieved, information gathered from different aspects jointly presented, and 3d information of specific urban objects extracted.

9.1 Answering the research questions

a) What spatial resolution can be achieved over an illuminated urban area without autofocus methods on a circular trajectory with a W-band SAR on a small aircraft?

A general statement on the spatial resolution of a W-band sensor over urban areas without autofocus routines cannot be derived. The resolution to be achieved in CSAR depends particularly on the length of the of the object's visibility within the synthetic aperture, on the knowledge of the exact height of the object in the spatial domain, and on parameters that compromise the ability of long coherent processing. This corresponds notably to wind or thermal lift that affects the precise measurement of the flight path. However, if the height of an object or area is known or if this information can be extracted from the CSAR data by applying a method proposed in this thesis, then the evaluated experiments indicate that azimuth resolutions in the order of 1.1 cm-1.3 cm are feasible over urban areas. Again, it should be mentioned that this number is derived by the evaluation of a partial flight path of a single circular trajectory. Therefore, to obtain a statistically more reliable statement, many different circular flights would have to be evaluated, even with varying conditions of weather and different targets.

The results also indicate that from an angular interval of approx. 10° the coherence most likely is lost. In other words, to achieve a CSAR image that also shows a range resolution of 1-2 cm, an RF bandwidth of approx. 8-10 GHz would be necessary for this constellation. This can undoubtedly be achieved in the near future and is already possible with the current sensor, but it fails at the moment due to very high data rates. For the height accuracy of up to 0.2 m-0.6 m achieved at pitched gabled roofs, this would correspond to spatial resolutions of 2-3 cm in these areas.

If the height of the targets to be imaged in the urban scene is unknown, this thesis has given an analytical derivation of the maximum resolution and maximum angular integration interval φ_{max}. If targets up to a height of 10 m in an urban scene shall be focused sharply, a spatial resolution of 10 cm is feasible. Up to now, the limited output power of the W-band sensor allows only small areas with a diameter of less than 150 m to be mapped with one circular trajectory.

b) How can a joint representation of the 360° full-aspect SAR imaging be realized and represented substantially?

This work has proposed two methods to jointly represent the entire aspect 360° data. The first approach is by generating a video sequence of the urban scene in the presented ViCSAR mode [Photogrammetry and Remote Sensing - TUM, 2020]. The CSAR geometry is particularly suited for video monitoring since the same area can constantly be observed for a longer time, revealing immediately small changes and dynamic events. Further, the aspect-dependent scattering characteristics, the maximum aspect visibility, or the aspect that offers a reliable 3d estimation of urban objects can become apparent. It was noticed that a high anisotropic backscattering behavior characterizes gabled roofs, whereas flat roofs typically do not.

Most interesting is that W-band ViCSAR may open up another exciting field of research: the ground moving target indication (GMTI) by shadow tracking of moving objects. So far, little attention has been paid to this monitoring capability of CSAR processing. Small moving cars, buses, trucks and even pedestrians located at favorable clutter backgrounds can be monitored due to the very short 'illumination time per image'. The fact that asphalt shows rough surface characteristics is very beneficial and, in the first place, enables shadow monitoring. This property will likely be of interest for many applications since the exact location, the dimension, the direction, and the speed of moving objects with even low SCR can be immediately recognized by an observer in the form of moving images.

A second approach to jointly represent different views is optimizing the focusing process to the specific scene. With knowledge of 3d information, in a 2nd iteration, the data can be refocused from optimal aspect angles in the correct imaging geometry. This procedure offers the fused representation of multiple aspects in a single SAR image without significant distortions common with flat plane imaging geometry. However, this requires very precise and dense 3d information, which is challenging to extract over a large area with a single-channel SAR. Further, large roof areas or flat surfaces are suitable for this method, whereas areas with trees or smaller objects are not suitable for the proposed method. Hence, there is still a lot of research to be done in order to optimally fuse the multiple aspects into a single SAR image in the future. However, it is expected that subaperture processing remains an important topic in future CSAR experiments over urban areas.

c) How can the potentially large azimuth bandwidth, which increases rapidly over a small aspect interval, be exploited to extract 3d information, and which accuracy can be achieved with such a radargrammetric evaluation of single-channel, single-pass data to obtain a 3d point cloud?

The benefit of creating large azimuth bandwidths due to only minor aspect changes can be exploited in more than one way to extract 3d information. With the design of highly overlapping subapertures, a continuous image sequence in high resolution offers the possibility of tracking projected scatterer information in consecutive image frames. This allows a very efficient form of a height extraction process, and height accuracies of up to 10 cm could be demonstrated with ideal, point-like objects. Yet, it is rather challenging to apply the method on large urban scenes where observers are not only interested in evaluating isolated scattering centers. However, it is possible to estimate the 3d location of a tree trunk bearing foliage and the geometrical center of the vegetation that may coincide with the mean height of the tree by following the projection of the foliage in the image sequence.

Promising 3d point cloud results could be derived by operating with considerably larger subapertures and locally extracting the 3d information from a derived image stack. By a subsequent fusion, a global 3d point cloud can be designed that reveals the urban scene from a 360° perspective that allows extracting the proper dimensions, the location, and 3d information of specific

objects. Applied to real data sets, quantitative results indicated that height accuracies of up to 18-60 cm can be reached in roof areas covered with roof tiles depending on the fused aspects and calibration. Furthermore, the roof's pitch angle could even be extracted with an accuracy of $< 0.4°$. For 3d point clouds that cover large building complexes, a height accuracy between 1.80 m to 2.40 m is feasible, depending on the 3d extraction method. Also, the 3d position of very small objects like street lamps could be extracted with a very high level of detail (0.2-0.5 m accuracy) or even facade information. The gabled roofs and areas with point-like scattering behavior proved to be well suited for extracting 3d information, but only from limited aspects. Therefore, it is crucial to fuse information from individual subapertures from as many aspects as possible. Even better accuracies are expected to be derived if the focusing height step size from currently 1 m is adapted to significantly smaller step sizes of one decimeter. However, this would increase the computational load considerably when evaluating a complete urban scene.

Problematic is the height extraction of clutter regions or areas with volume scattering behavior. Further, improving the 3d accuracy requires the determination of the origin of the constant height bias that was investigated from different aspects. Removing this error would significantly reduce the height deterioration caused by fusing multiple aspects. However, it remains rather unlikely that the high level of height accuracy that is achieved with a LiDAR system in good weather conditions can be achieved with a single-channel mmW SAR sensor.

d) To what extent can SAR measurements in the lower terahertz frequency domain from a car-borne mobile radar mapping system be processed and which details of the urban scene can be resolved?

The level of detail that can be reached in the context of mobile radar mapping sets new standards in close-range radar imaging. To the author's knowledge, the first operational SAR images in the mobile mapping context at frequencies in the lower terahertz domain were presented in the course of this thesis. The spatial resolution of these SAR images is in the range of 5 mm. On the one hand, the ultra-high-resolution is based on the considerable RF bandwidth that systems at these frequencies can emit. On the other hand, the application of advanced processing techniques and the use of high precision GPS/INS provides the potential to focus the data with an extremely high level of detail. This high detail level is indeed a bit of a surprise as one could initially have assumed that an autofocus method was vital. Potentially, the diffuse scattering of the rough surface causing a form of 'natural multilook process' is beneficial.

The 1 mm wavelength is well suited for urban areas applications. Since it interacts very nicely with small-scale objects, imaging tiny cracks in the street, individual paving or brick stones, or different asphalt or facade surfaces is feasible. In addition, areas like streets that show specular behavior at lower transmit frequencies like P- or X-band in airborne SAR experiments can be imaged with ultra-high resolution showing clutter characteristics.

Applying backprojection methods for SAR focusing in urban areas, the scene needs to be modeled precisely. This is more convenient for man-made or artificial objects such as streets or facades but difficult for vegetation. Therefore, the street mapping geometry is well suited for applying SAR imagery at these wavelengths since a planar region is illuminated without objects that may cause shadowing. The system currently is limited by low output power and the associated short range of less than 25 m. Also, the measuring depth of 5-12 m only allows a small area to be illuminated at a comparatively low platform speed below 40 km/h. Further, the low installation height of the antenna and the downwards or upwards directed illumination have only allowed imaging one street lane or the upper one to two floors of a house.

Probably, an additional sensor would be beneficial in urban scenes; for example, it seems promising to investigate the combination of radar and LiDAR. The LiDAR could then derive the

facade's geometry while the SAR sensor could provide an ultra-high resolution imaging on the derived 3d surface. The high-precision path measurement of the synthetic aperture also remains a considerable effort. Due to the fact that in the experiments no odometer was used, bad coverage and low accessibility of GPS satellites along with stop and go events in urban environments were problematic when deriving a high precision trajectory that is needed to focus the data in a millimeter resolution. Nevertheless, much effort has to be taken to calculate an optimal trajectory at these wavelengths. Therefore, it would not be surprising that further increases in image resolution potentially at even higher radar frequencies are more restricted by too high requirements on the GPS/INS sensors than on the radar.

9.2 Outlook

9.2.1 Possible future applications

The circular data acquisition and evaluation of urban scenes may open up many new applications, and the methods proposed in this thesis are indeed just a beginning. Up to now, most users of radar remote sensing work with SAR imaging products. High-resolution SAR videos are less established but can potentially offer new applications. Circular trajectories are very suitable for this form of visualizing information since the same area can continuously be monitored. In particular, the dynamics in a complex urban scene can be represented differently by a SAR video, and some properties are better highlighted. Thus, a CSAR with high carrier frequencies would probably be beneficial in the area of time-critical information acquisition like surveillance or disaster management applications. Future developments should ensure that the scene information is available to the observer in real-time to further increase the advantage of the 'all-weather' capability.

The 3d extraction of urban scenes with high-resolution CSAR will remain a challenging field of research in the future. The investigated height accuracies of up to 10 cm for point scatterers or up to 18-60 cm for gabled roof areas are very likely only a first development step. Significant improvements may be expected with multi-channel sensors that offer multi-baseline processing. Similar, multi-circular trajectories at different heights are promising. The CSAR geometry also offers the possibility to focus data from optimal aspects in the proper imaging geometry if 3d information is available or could be derived.

Different methods on the 3d extraction and, in particular, the 360° fusion process are to be expected. Probably, similar to the WM approach, more statistically advanced methods similar to [Schmitt & Stilla, 2014b] are promising to fuse locally derived 3d information. Combining classical approaches based on cross-correlation criteria like [Zhang et al., 2018] should also be considered. Further, aspect views should be preselected as the quality of the local generated 3d information varies significantly. Only a few aspects correspond to the majority of derived 3d information, partly due to the platform not flying an ideal circular trajectory. Also, a radiometric calibration might be promising since areas viewed from different aspects are more comparable. Concerning the currently restricted output power, it is foreseeable that in the near future a significant increase in output power at W-band can be expected, in particular, driven by the communications industry.

Carborne applications might detect small cracks on streets or detect and monitor tiny metallic objects on airport runways. The proposed street mapping method could be expected to be implemented operationally on a larger scale since the model is very robust. However, this does not apply to the facade focusing. The model of assuming a facade facing the street in the immediate vicinity and aligned in orientation is much more prone to errors.

If we look more into the future, there will be very likely drone carried systems with frequencies of 300 GHz, or even higher. Such drones may be able to fly into narrow street canyons revealing tiny materials on roads or facades with subcentimeter resolution. This thesis could already highlight to some extent which image qualities are then to be expected.

9.2.2 Subsequent research work

Subsequent to this work, new questions arise. First, the indication of moving objects by their shadow in the ViCSAR sequence raises the question to what extent a refocus of the signature of the vehicles is possible. Regarding the sensor's single-channel constellation, a method could be investigated based on evaluated parameters from the tracked shadows. Thus, the signature would add an additional interesting parameter to the interpretability of the CSAR videos.

Second, real-time ViCSAR processing would open further exciting applications. One scientific question would be the level of real-time change detection capability that such a configuration may offer. Considering multiple circular flights on the same trajectory, the same urban area is constantly illuminated, allowing to detect small changes immediately.

Third, further research on the 3d extraction and fusion of circular data in urban areas is promising. Here, a combination of interferometric with radargrammetric methods evaluating multi-circular passes at different heights would clearly be of great interest.

At last, the quality of the ViCSAR image registration is highly dependent on precise flight data. On the other hand, this may allow the design of an autofocus approach that evaluates the potential mean shift (bias) of all image pixels in the video sequence.

Bibliography

Altshuler EE, Marr RA (1988) A comparison of experimental and theoretical values of atmospheric absorption at the longer millimeter wavelengths. IEEE Transactions on Antennas and Propagation, 36 (10): 1471–1480.

Austin CD, Ertin E, Moses RL (2011) Sparse signal methods for 3-D radar imaging. IEEE Journal of Selected Topics in Signal Processing, 5 (3): 408–423.

Axelsson SRJ (2004) Beam characteristics of three-dimensional SAR in curved or random paths. IEEE Transactions on Geoscience and Remote Sensing, 42 (10): 2324–2334.

Bamler R, Eineder M (2005) Accuracy of differential shift estimation by correlation and split-bandwidth interferometry for wideband and delta-k SAR systems. IEEE Geoscience and Remote Sensing Letters, 2 (2): 151–155.

Barron JL, Fleet DJ, Beauchemin SS (1994) Performance of optical flow techniques. International Journal of Computer Vision, 12 (1): 43–77.

Borgmann B, Schatz V, Hammer M, Hebel M, Arens M, Stilla U (2021) MODISSA: a multipurpose platform for the prototypical realization of vehicle-related applications using optical sensors. Applied Optics, 60 (22): F50–F65.

Budillon A, Evangelista A, Schirinzi G (2011) Three-Dimensional SAR Focusing From Multipass Signals Using Compressive Sampling. IEEE Transactions on Geoscience and Remote Sensing, 49 (1): 488–499.

Budillon A, Johnsy A, Schirinzi G (2017) Extension of a fast GLRT algorithm to 5D SAR tomography of Urban areas. Remote Sensing, 9: 844.

Cantalloube H (2018) Circular SAR imaging of not planar targets. Limitations of the 'Height from Focus' paradigm. In: IEEE International Geoscience and Remote Sensing Symposium, IGARSS 2018: 3671–3674.

Cantalloube H, Colin E (2006) Airborne SAR imaging along a circular trajectory. In: 6th. European Conference on Synthetic Aperture Radar, EUSAR 2006: 16–18.

Cantalloube H, Colin-Koeniguer E, Oriot H (2007) High resolution SAR imaging along circular trajectories. In: IEEE International Geoscience and Remote Sensing Symposium, IGARSS 2007: 850–853.

Cantalloube HMJ, Nahum CE (2010) Multiscale local Map Drift driven Multilateration SAR Autofocus using fast Polar Format Image Synthesis. In: 8th European Conference on Synthetic Aperture Radar: 1–4.

Caris M, Stanko S, Palm S, Sommer R, Pohl N (2015) Synthetic aperture radar at millimeter wavelength for UAV surveillance applications. In: IEEE 1st International Forum on Research and Technologies for Society and Industry Leveraging a better tomorrow (RTSI): 349–352.

Chen L, An D, Huang X, Zhou Z (2017) A 3D Reconstruction Strategy of Vehicle Outline Based on Single-Pass Single-Polarization CSAR Data. IEEE Transactions on Image Processing, 26 (11): 5545–5554.

Cooper KB, Dengler RJ, Llombart N, Bryllert T, Chattopadhyay G, Schlecht E, Gill J, Lee C, Skalare A, Mehdi I, Siegel PH (2008) Penetrating 3-D imaging at 4- and 25-m range using a submillimeter-wave radar. IEEE Transactions on Microwave Theory and Techniques, 56 (12): 2771–2778.

Cooper KB, Dengler RJ, Llombart N, Thomas B, Chattopadhyay G, Siegel PH (2011) THz imaging radar for standoff personnel screening. IEEE Transactions on Terahertz Science and Technology, 1 (1): 169–182.

Cumming IG, Wong FH (2005) Digital processing of synthetic aperture radar data: Algorithms and implementation. Boston: Artech House Inc.

Curlander JC, McDonough RN (1991) Synthetic Aperture Radar - Signals and Signal Processing. New York, NY, USA: John Wiley & Sons.

Damini A, Balaji B, Parry C, Mantle V (2010) A videoSAR mode for the X-band wideband experimental airborne radar. In: Algorithms for Synthetic Aperture Radar Imagery XVII, 7699: 135–145.

de Paul OV (2007) Remote Sensing: New Applications for Urban Areas. Proceedings of the IEEE, 95 (12): 2267–2268.

Duersch MI, Long DG (2015) Analysis of time-domain back-projection for stripmap SAR. International Journal of Remote Sensing, 36 (8): 2010–2036.

Duque S, Breit H, Balss U, Parizzi A (2015) Absolute Height Estimation Using a Single TerraSAR-X Staring Spotlight Acquisition. IEEE Geoscience and Remote Sensing Letters, 12 (8): 1735–1739.

Dzwonkowski P (2016) High resolution inverse synthetic aperture radar demonstrator utilizing low-teraherz band: A practical implementation using common laboratory equipment and commercial off the shelf elements. In: 17th International Radar Symposium (IRS): 1–4.

Ehlers M (2005) Urban Remote Sensing: New Developments and Trends. In: Proceedings of URS 2005: 14–16.

Ellum C, El-Sheimy N (2002) Land-based mobile mapping systems. Photogrammetric engineering and remote sensing, 68 (1): 13–17.

Ender J (1993) AER - ein experimentelles Mehrkanal-SAR. In: 8. Radar Symposium der DGON (German Institute of Navigation), 1993: 120–125.

Ertin E, Austin CD, Sharma S, Moses RL, Potter LC (2007) GOTCHA experience report: three-dimensional SAR imaging with complete circular apertures. In: Algorithms for Synthetic Aperture Radar Imagery XIV, Proc. SPIE, 6568: 9–20.

Ertin E, Moses RL, Potter LC (2008) Interferometric Methods for 3-D Target Reconstruction with Multi-Pass Circular SAR. In: 7th European Conference on Synthetic Aperture Radar: 1–4.

Ertin E, Potter LC, Moses RL (2006) Enhanced imaging over complete circular apertures. In: Fortieth Asilomar Conference on Signals, Systems and Computers, 2006: 1580–1584.

Essen H, Biegel G, Sommer R, Wahlen A, Johannes W, Wilcke J (2008) High Resolution Tower-Turntable ISAR with the Millimetre Wave Radar COBRA (35 / 94 / 220 GHz). In: 7th European Conference on Synthetic Aperture Radar: 1–4.

Feger R, Haderer A, Stelzer A (2017) Experimental verification of a 77-GHz synthetic aperture radar system for automotive applications. In: IEEE MTT-S International Conference on Microwaves for Intelligent Mobility, ICMIM 2017: 111–114.

Ferretti A, Prati C, Rocca F (2000) Nonlinear subsidence rate estimation using permanent scatterers in differential SAR interferometry. IEEE Transactions on Geoscience and Remote Sensing, 38 (5): 2202–2212.

Frey O, Magnard C, Ruegg M, Meier E (2009) Focusing of airborne synthetic aperture radar data from highly nonlinear flight tracks. IEEE Transactions on Geoscience and Remote Sensing, 47 (6): 1844–1858.

Frey O, Werner C, Hajnsek I, Coscione R (2018) A car-borne SAR system for interferometric measurements: Development status and system enhancements. In: IEEE International Geoscience and Remote Sensing Symposium, IGARSS 2018: 6508–6511.

Frölind PO, Ulander LM, Gustavsson A, Stenström G (2012) VHF/UHF-band SAR imaging using circular tracks. In: IEEE International Geoscience and Remote Sensing Symposium, IGARSS 2012: 7409–7411.

Froelind P, Ulander LMH, Gustavsson A (2008) First results on VHF-band SAR imaging using circular tracks. In: 7th European Conference on Synthetic Aperture Radar, EUSAR 2008: 1–4.

Fu W, Ma J, Chen P, Chen F (2020) Remote Sensing Satellites for Digital Earth, (pp. 55–123). Singapore: Springer.

Gamba P, Herold M (2009) Global Mapping of Human Settlement: Experiences, Datasets, and Prospects. Boca Raton, Florida: CRC Press.

García-Rubia JM, Riera JM, Garcia-del-Pino P, Benarroch A (2013) Attenuation Measurements and Propagation Modeling in the W-Band. IEEE Transactions on Antennas and Propagation, 61 (4): 1860–1867.

Gehrung J, Hebel M, Arens M, Stilla U (2017) An approach to extract moving objects from MLS data using a volumetric background representation. ISPRS Annals of Photogrammetry, Remote Sensing and Spatial Information Sciences, IV-1/W1: 107–114.

Gernhardt S, Bamler R (2012) Deformation monitoring of single buildings using meter-resolution SAR data in PSI. ISPRS Journal of Photogrammetry and Remote Sensing, 73: 68–79.

Goel K, Adam N (2012) Three-Dimensional Positioning of Point Scatterers Based on Radargrammetry. IEEE Transactions on Geoscience and Remote Sensing, 50 (6): 2355–2363.

Gu X, Valdes-Garcia A, Natarajan A, Sadhu B, Liu D, Reynolds SK (2015) W-band scalable phased arrays for imaging and communications. IEEE Communications Magazine, 53 (4): 196–204.

Guo H, Dou C, Zhang X, Han C, Yue X (2016) Earth observation from the manned low Earth orbit platforms. ISPRS Journal of Photogrammetry and Remote Sensing, 115: 103–118.

Gurgel KW, Schlick T (2009) Remarks on Signal Processing in HF Radars using FMCW Modulation. In: International Radar Symposium, IRS 2009: 45–50.

Huelsmeyer C (1905) Verfahren, um entfernte metallische Gegenstaende mittels elektrischer Wellen einem Beobachter zu melden. German Patent, No. DE165546C.

Ishimaru A, Chan TK, Kuga Y (1998) An imaging technique using confocal circular synthetic aperture radar. IEEE Transactions on Geoscience and Remote Sensing, 36 (5): 1524–1530.

Kallfass I, Henneberger R, Sommer R, Harati P, Dilek SM, Schoch B, Eisenbeis J, Marahrens S, Palm S, Tessmann A (2019) High system gain E-band link in a wideband aircraft-to-ground data transmission. In: IEEE International Conference on Microwaves, Antennas, Communications and Electronic Systems, COMCAS 2019: 1–5.

Kim S, Fan R, Dominski F (2018) ViSAR: A 235 GHz radar for airborne applications. In: IEEE Radar Conference, RadarConf18: 1549–1554.

Kinghorn A, Nejman A (2009) PicoSAR- an advanced lightweight SAR system. In: European Radar Conference, EuRAD 2009: 168–171.

Kremer J, Hunter G (2007) Performance of the streetmapper mobile LiDAR mapping system in real world projects. Photogrammetric Week 2007, : 215–225.

Krozer V, Loffler T, Dall J, Kusk A, Eichhorn F, Olsson RK, Buron JD, Jepsen PU, Zhurbenko V, Jensen T (2010) Terahertz imaging systems with aperture synthesis techniques. IEEE Transactions on Microwave Theory and Techniques, 58 (7): 2027–2039.

Lewark UJ, John L, Wagner S, Tessmann A, Leuther A, Zwick T, Kallfass I (2015) Ultra-broadband W-band frequency multiplier-by-twelve MMIC. In: 10th European Microwave Integrated Circuits Conference, EuMIC 2010: 5–8.

Li Y, Wang T, Liu B, Yang L, Bi G (2017) Ground moving target imaging and motion parameter estimation with airborne dual-channel CSSAR. IEEE Transactions on Geoscience and Remote Sensing, 55 (9): 5242–5253.

Liebe HJ, Manabe T, Hufford GA (1989) Millimeter-wave attenuation and delay rates due to fog/cloud conditions. IEEE Transactions on Antennas and Propagation, 37 (12): 1617–1612.

Lillesand TM, Kiefer RW, Chipman JW (2004) Remote Sensing and Image Interpretation, volume 5. New York, USA: John Wiley & Sons.

Lin Y, Hong W, Tan W, Wang Y, Wu Y (2011) Interferometric Circular SAR Method for Three-Dimensional Imaging. IEEE Geoscience and Remote Sensing Letters, 8 (6): 1026–1030.

Lin Y, Hong W, Tan W, Wang Y, Xiang M (2012) Airborne circular SAR imaging: Results at P-band. In: IEEE International Geoscience and Remote Sensing Symposium, IGARSS 2012: 5594–5597.

Lv Z, Li X, Zhang B, Wang W, Zhu Y, Hu J, Feng S (2016) Managing Big City Information Based on WebVRGIS. IEEE Access, 4: 407–415.

Madry S, Pelton JN (2013) Electro-optical and Hyper-spectral Remote Sensing, (pp. 729–738). New York, NY: Springer.

Magnard C, Morsdorf F, Small D, Stilla U, Schaepman ME, Meier E (2016) Single tree identification using airborne multibaseline SAR interferometry data. Remote Sensing of Environment, 186: 567–580.

Marston TM, Kennedy JL (2016) Volumetric acoustic imaging via circular multipass aperture synthesis. IEEE Journal of Oceanic Engineering, 41 (4): 852–867.

Massonnet D, Rabaute T (1993) Radar interferometry: limits and potential. IEEE Transactions on Geoscience and Remote Sensing, 31 (2): 455–464.

Matzler C, Rosenkranz P, Battaglia A, Wigneron JP (2006) Thermal microwave radiation: applications for remote sensing, volume 52. The Institution of Engineering and Technology (IET).

Photogrammetry and Remote Sensing - TUM (2020) Airborne circular W-band SAR - Test area WachtbergKreisel [Video]. [Online]. Available: `https://www.youtube.com/watch?v=cwDjJqtx_og` and `https://www.youtube.com/watch?v=D59hBaNwJXE`.

Meta A (2006) Signal processing of FMCW Synthetic Aperture Radar data. PhD thesis, Electrical Engineering, Mathematics and Computer Science, TU Delft.

Moreira A, Prats-Iraola P, Younis M, Krieger G, Hajnsek I, Papathanassiou K (2013) A Tutorial on Synthetic Aperture Radar. IEEE Geoscience and Remote Sensing Magazine (GRSM), 1 (1): 6–43.

Nations U (2019) World Urbanization Prospects: The 2018 Revision. United Nations - Department of Economic and Social Affairs, Technical Report.

Oloumi D, Ting JW, Rambabu K (2016) Design of pulse characteristics for near-field UWB-SAR imaging. IEEE Transactions on Microwave Theory and Techniques, 64 (8): 2684–2693.

Oppenheim AV, Buck JR, Schafer RW (1999) Discrete-Time Signal Processing; 2nd ed. Prentice-Hall signal processing series. Upper Saddle River, NJ: Prentice-Hall.

Otten M, van Rossum W, van der Graaf M, Vlothuizen W, Tan R (2014) Multichannel imaging with the AMBER FMCW SAR. In: 10th European Conference on Synthetic Aperture Radar, EUSAR 2014: 1–4.

Palm S, Maresch A, Stilla U (2013) Investigation on circular mapping by FMCW-SAR on small airplanes. ISPRS - International Archives of the Photogrammetry, Remote Sensing and Spatial Information Sciences, XL-1/W1 (1): 281–286.

Palm S, Oriot H, Cantalloube H (2012) Radargrammetric DEM extraction over urban area using circular SAR imagery. IEEE Transactions on Geoscience and Remote Sensing, 50 (11): 4720–4725.

Palm S, Pohl N, Stilla U (2015) Challenges and potentials using multi aspect coverage of urban scenes by airborne SAR on circular trajectories. ISPRS - International Archives of the Photogrammetry, Remote Sensing and Spatial Information Sciences, XL-3/W2: 149–154.

Palm S, Sommer R, Caris M, Pohl N, Tessmann A, Stilla U (2016a) Ultra-High Resolution SAR in Lower Terahertz Domain for Applications in Mobile Mapping. In: 2016 German Microwave Conference (GeMiC): 205–208.

Palm S, Sommer R, Hommes A, Pohl N, Stilla U (2016b) Mobile Mapping by FMCW synthetic aperture radar operating at 300 GHz. ISPRS - International Archives of the Photogrammetry, Remote Sensing and Spatial Information Sciences, XLI-B1: 81–87.

Palm S, Sommer R, Janssen D, Tessmann A, Stilla U (2019) Airborne circular W-band SAR for multiple aspect urban site monitoring. IEEE Transactions on Geoscience and Remote Sensing, 57 (9): 6996–7016.

Palm S, Sommer R, Pohl N, Stilla U (2016c) Airborne SAR on circular trajectories to reduce layover and shadow effects of urban scenes. In: Remote Sensing Technologies and Applications in Urban Environments, Proc. SPIE, 10008: 179–186.

Palm S, Sommer R, Stilla U (2018) Mobile radar mapping - subcentimeter SAR imaging of roads. IEEE Transactions on Geoscience and Remote Sensing, 56 (11): 6734–6746.

Palm S, Sommer R, Tessmann A, Stilla U (2019) Ultra-high resolution imaging of facades and vertical infrastructure by carborne SAR and airborne CSAR. ISPRS Annals of Photogrammetry, Remote Sensing and Spatial Information Sciences, IV-2/W7: 129–136.

Palm S, Stilla U (2021) 3-D Point Cloud Generation From Airborne Single-Pass and Single-Channel Circular SAR Data. IEEE Transactions on Geoscience and Remote Sensing, 59 (10): 8398–8417.

Palm S, Wahlen A, Stanko S, Pohl N, Wellig P, Stilla U (2014) Real-time onboard processing and ground based monitoring of FMCW-SAR videos. In: 10th European Conference on Synthetic Aperture Radar, EUSAR 2014: 1–4.

Paparoditis N, Papelard JP, Cannelle B, Devaux A, Soheilian B, David N, Houzay E (2012) Stereopolis II: A multi-purpose and multi-sensor 3D mobile mapping system for street visualisation and 3D metrology. Revue française de photogrammétrie et de télédétection, (200): 69–79.

Peters ST, Schroeder DM, Haynes MS, Castelletti D, Romero-Wolf A (2021) Passive Synthetic Aperture Radar Imaging Using Radio-Astronomical Sources. IEEE Transactions on Geoscience and Remote Sensing (In Press), : 1–16.

Pinheiro M, Prats P, Scheiber R, Nannini M, Reigber A (2009) Tomographic 3D reconstruction from airborne circular SAR. In: IEEE International Geoscience and Remote Sensing Symposium, IGARSS 2009: 21–24.

Ponce O, Prats P, Rodriguez-Cassola M, Scheiber R, Reigber A (2011) Processing of circular SAR trajectories with fast factorized back-projection. In: IEEE International Geoscience and Remote Sensing Symposium, IGARSS 2011: 3692–3695.

Ponce O, Prats-Iraola P, Pinheiro M, Rodriguez-Cassola M, Scheiber R, Reigber A, Moreira A (2014) Fully polarimetric high-resolution 3-D imaging with circular SAR at L-Band. IEEE Transactions on Geoscience and Remote Sensing, 52 (6): 3074–3090.

Ponce O, Prats-Iraola P, Scheiber R, Reigber A, Moreira A (2016) First airborne demonstration of holographic SAR tomography with fully polarimetric multicircular acquisitions at L-Band. IEEE Transactions on Geoscience and Remote Sensing, 54 (10): 6170–6196.

Quay R, Brückner P, Tessmann A, Ture E, Schwantuschke D, Dammann M, Waltereit P (2017) Hetero-integrated GaN MMICs: hot islands in a (silicon) ocean. In: Integrated Nonlinear Microwave and Millimetre-wave Circuits Workshop, INMMiC 2017: 1–3.

Rambour C, Budillon A, Johnsy AC, Denis L, Tupin F, Schirinzi G (2020) From Interferometric to Tomographic SAR: A Review of Synthetic Aperture Radar Tomography-Processing Techniques for Scatterer Unmixing in Urban Areas. IEEE Geoscience and Remote Sensing Magazine, 8 (2): 6–29.

Reigber A, Lombardini F, Viviani F, Nannini M, Martinez del Hoyo A (2015) Three-dimensional and higher-order imaging with tomographic SAR: Techniques, applications, issues. In: IEEE International Geoscience and Remote Sensing Symposium, IGARSS 2015: 2915–2918.

Reigber A, Moreira A (2000) First demonstration of airborne SAR tomography using multibaseline L-band data. IEEE Transactions on Geoscience and Remote Sensing, 38 (5): 2142–2152.

Ribalta A (2011) Time-domain reconstruction algorithms for FMCW-SAR. IEEE Geoscience and Remote Sensing Letters, 8 (3): 396–400.

Ruault du Plessis O, Dreuillet P (2013) The ONERA airborne multi-frequency SAR imaging systems. In: International Conference on Radar: 85–90.

Schmitt M, Magnard C, Stanko S, Ackermann C, Stilla U (2013) Advanced high resolution SAR interferometry of urban areas with airborne millimetrewave radar. Photogrammetrie, Fernerkundung, Geoinformation, 6: 603–617.

Schmitt M, Stilla U (2011) Fusion of airborne multi-aspect InSAR data by simultaneous backward geocoding. In: Proc. Joint Urban Remote Sensing Event, JURSE 2011: 53–56.

Schmitt M, Stilla U (2014a) Generating point clouds of forested areas from airborne millimeter wave InSAR data. In: IEEE Geoscience and Remote Sensing Symposium: 1–4.

Schmitt M, Stilla U (2014b) Maximum-likelihood estimation for multi-aspect multi-baseline SAR interferometry of urban areas. ISPRS Journal of Photogrammetry and Remote Sensing, 87: 68–77.

Shi B, Leong SW, Mulya A, Luo B, Wang W (2015) Electronic beam steering using PLL array for radar applications in W-band. In: IEEE 5th Asia-Pacific Conference on Synthetic Aperture Radar, APSAR 2015: 274–276.

Skolnik MI (1980) Introduction to Radar Systems. New York: McGraw Hill Book Co., 2 edition.

Soergel U (2010) Review of Radar Remote Sensing on Urban Areas. Dordrecht: Springer.

Soergel U, Michaelsen E, Thiele A, Cadario E, Thoennessen U (2009) Stereo analysis of high-resolution SAR images for building height estimation in cases of orthogonal aspect directions. ISPRS Journal of Photogrammetry and Remote Sensing, 64 (5): 490–500.

Soumekh M (1996) Reconnaissance with slant plane circular SAR imaging. IEEE Transactions on Image Processing, 5 (8): 1252–1265.

Stanko S, Johannes W, Sommer R, Wahlen A, Wilcke J, Essen H, Tessmann A, Kallfass I (2011) SAR with MIRANDA - Millimeterwave radar using analog and new digital approach. In: European Radar Conference, EuRAD 2011: 214–217.

Stilla U (2012) Urban remote sensing by ultra high resolution SAR. In: IEEE International Geoscience and Remote Sensing Symposium: 5406–5409.

Stilla U, Gamba P, Juergens C, Maktav D (2011) Preface. In: Joint Urban Remote Sensing Event - JURSE 2011: V–VI.

Stilla U, Hedman K (2010) Feature Fusion Based on Bayesian Network Theory for Automatic Road Extraction, (pp. 69–86). Dordrecht: Springer.

Stilla U, Soergel U, Thoennessen U (2003) Potential and limits of InSAR data for building reconstruction in built up-areas. ISPRS Journal of Photogrammetry and Remote Sensing, 58: 113–123.

Tessmann A, Leuther A, Hurm V, Massler H, Wagner S, Kuri M, Zink M, Riessle M, Stulz HP, Schlechtweg M, Ambacher O (2014) A broadband 220-320 GHz medium power amplifier module. In: IEEE Compound Semiconductor Integrated Circuit Symposium, CSICS 2014: 1–4.

Tessmann A, Massler H, Lewark U, Wagner S, Kallfass I, Leuther A (2011) Fully integrated 300 GHz receiver S-MMICs in 50 nm metamorphic HEMT technology. In: IEEE Compound Semiconductor Integrated Circuit Symposium, CSICS 2011: 1–4.

Thiele A, Thoennessen U, Cadario E, Schulz K, Soergel U (2006) Building recognition from multi-aspect high-resolution interferometric SAR data in urban areas. In: Zelnio EG, Garber FD (eds) Algorithms for Synthetic Aperture Radar Imagery XIII, 6237: 13 – 20.

Thome F, Leuther A, Schlechtweg M, Ambacher O (2018) Broadband High-Power W-Band Amplifier MMICs Based on Stacked-HEMT Unit Cells. IEEE Transactions on Microwave Theory and Techniques, 66 (3): 1312–1318.

Ture E, Brückner P, Alsharef M, Granzner R, Schwierz F, Quay R, Ambacher O (2017) First demonstration of W-band Tri-gate GaN-HEMT power amplifier MMIC with 30 dBm output power. In: IEEE MTT-S International Microwave Symposium, IMS 2017: 35–37.

Ulander LMH, Frölind PO, Gustavsson A, Ragnarsson R, Stenström G (2017) Airborne passive SAR imaging based on DVB-T signals. In: IEEE International Geoscience and Remote Sensing Symposium, IGARSS 2017: 2408–2411.

Ulander LMH, Hellsten H, Stenstrom G (2003) Synthetic-aperture radar processing using fast factorized back-projection. IEEE Transactions on Aerospace and Electronic Systems, 39 (3): 760–776.

Vu VT, Sjogren TK, Pettersson MI, Hellsten H (2010) An Impulse Response Function for Evaluation of UWB SAR Imaging. IEEE Transactions on Signal Processing, 58 (7): 3927–3932.

Wang H, Chen Z, Zheng S (2017) Preliminary research of low-RCS moving target detection based on Ka-Band video SAR. IEEE Geoscience and Remote Sensing Letters, 14 (6): 811–815.

Watson GN (1995) A Treatise on the Theory of Bessel Functions. Cambridge University Press.

Weber R, Tessmann A, Zink M, Kuri M, Stulz HP, Riessle M, Massler H, Maier T, Leuther A, Schlechtweg M, Kallfass I (2011) A W-Band x12 frequency multiplier MMIC in waveguide package using quartz and ceramic transitions. In: IEEE Compound Semiconductor Integrated Circuit Symposium, CSICS 2011: 1–4.

Weiss MA (2001) Productive cities and metropolitan economic strategy. Paper presented to the United Nations International Forum on Urban Poverty (IFUP). Fourth International Conference, Marrakech, Morocco.

Wells L, Sorensen K, Doerry A, Remund B (2003) Developments in SAR and IFSAR systems and technologies at sandia national laboratories. In: IEEE Aerospace Conference Proceedings, 2: 1085–1095.

Westfall PH (2014) Kurtosis as Peakedness, 1905 - 2014. R.I.P. The American Statistician, 68 (3): 191–195.

Wiley CA (1954) Pulsed Doppler radar methods and apparatus. U.S. Patent, No. 3,196,436.

Wu B, Gao Y, Ghasr MT, Zoughi R (2018) Resolution-based analysis for optimizing subaperture measurements in circular SAR imaging. IEEE Transactions on Instrumentation and Measurement, 67 (12): 2804–2811.

Yamaguchi H, Kajiwara A, Dozono S, Nishiyama F, Tanaka T (1997) A study on 94 GHz band millimeter-wave RCS characteristics: numerical comparison with 35 GHz. In: Proceedings of the 1997 IEEE National Radar Conference: 172–177.

Zhang J, Suo Z, Li Z, Zhang Q (2018) DEM generation using circular SAR data based on low-rank and sparse matrix decomposition. IEEE Geoscience and Remote Sensing Letters, 15 (5): 724–728.

Zhou J, Shi Z, Fu Q (2015) Three-dimensional scattering center extraction based on wide aperture data at a single elevation. IEEE Transactions on Geoscience and Remote Sensing, 53 (3): 1638–1655.

Zhu S, Zhang Z, Liu B, Yu W (2016) Three-dimensional high resolution imaging method of multi-pass circular SAR based on joint sparse model. In: 11th European Conference on Synthetic Aperture Radar, EUSAR 2016: 1–5.

Zhu XX, Shahzad M (2014) Facade Reconstruction Using Multiview Spaceborne TomoSAR Point Clouds. IEEE Transactions on Geoscience and Remote Sensing, 52 (6): 3541–3552.

Danksagung

Einen besonderen Dank möchte ich an dieser Stelle meinem Doktorvater Prof. Uwe Stilla für die langjährige Unterstützung und die wissenschaftliche Begleitung meines Dissertationsthemas aussprechen. Dies war sowohl für meine private wie auch berufliche Entwicklung ein sehr erfahrungsreicher Prozess. Neben den vielen lehrreichen fachlichen Diskussionen bin ich ihm besonders dafür dankbar, mir geduldig beigebracht zu haben, wie man wissenschaftliche Texte oder Präsentationen optimal strukturiert, und kompakt, aber dennoch detailliert, ausführt.

Meinen weiteren Dank möchte ich an Prof. Joachim Ender ausdrücken. Neben seiner Funktion als dritter Gutachter und langjähriger Institutsdirektor des Fraunhofer FHR hat er mir gerade zu Beginn der Arbeit wertvolle Ideen und Denkanstöße gegeben. Damit hat er an entscheidenden Stellen meine Forschung in die, meiner Meinung nach, richtige Richtung gelenkt.

Genauso möchte ich mich bei Prof. Uwe Sörgel als zweiten Gutachter bedanken. Seine konstruktiven Anmerkungen führten insbesondere zum Ende der Arbeit zu weiteren Verbesserungen des finalen Manuskriptes. Zuletzt gilt mein Dank ebenfalls Prof. Roland Pail für die Übernahme des Vorsitzes des Prüfungsausschusses.

Neben dem Prüfungsvorsitzenden und den Gutachtern möchte ich gerne weiteren Personen, mit denen ich während meiner Doktorarbeit zusammengearbeitet habe, danken. Zunächst möchte ich Hélène Oriot (ONERA, Palaiseau) nennen, welche mich noch als Student der RWTH betreute, mir überhaupt erst Einblicke in das Themenfeld Circular SAR ermöglichte, und damit meine Neugier für dieses Thema weckte. Bei den Kollegen am Fraunhofer FHR möchte ich drei Kollegen hervorheben: Insbesondere möchte ich mich bei Rainer Sommer bedanken, der über viele Jahre Arbeit in den Sensor investiert hat und dabei immer leidenschaftlich engagiert war ein funktionierendes und optimales Radarsystem für die vielen Experimente dieser Arbeit bereitzustellen. In vielen Stunden gemeinsamer Laborarbeit konnte ich von ihm einiges an Hardwarewissen erlernen. Ähnliches gilt für Alfred Wahlen, von dessen umfangreichen und detaillierten Radarwissen ich zu Beginn meiner Arbeit sowohl hard- als auch softwareseitig profitierte. Zuletzt möchte ich noch Daniel Nöthen danken, welcher mir durch seine umfassenden Programmierkenntnisse eine große Hilfe bei der softwareseitigen Umsetzung vieler rechenintensiver Prozesse war.

Dank gilt auch den vielen anderen aktiven und ehemaligen Kollegen der Abteilung HRA wie insbesondere Stephan Stanko, Nils Pohl sowie dem leider bereits verstorbenen Helmut Essen. Mit den Kollegen der Abteilung verbinde ich unzählige interessante Gespräche und fruchtbare Diskussionen sowie abwechslungsreiche und kurzweilige Messkampagnen. Dabei gilt auch ein Dank unserem Piloten, Frank Vervoorst, welcher unermüdlich und geduldig die zirkularen Datensätze auf diversen Trajektorien erflog.

Zuletzt möchte ich natürlich meiner gesamten Familie für ihre Unterstützung Danke sagen. Dies gilt für meine Eltern, welche mich auf meinem Werdegang immer unterstützt haben. Insbesondere möchte ich mich aber bei meiner Frau Aline bedanken, welche mir beim Fertigstellen der Arbeit immer wieder den Rücken freigehalten hat und mir in diversen Situationen den nötigen Zuspruch gegeben hat.